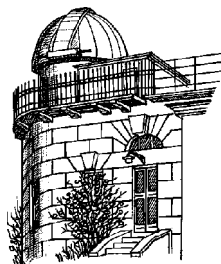# ODESSA ASTRONOMICAL PUBLICATIONS

Volume 27 Issue 1
(2014)

FOREWORD

This regular issue of the journal contains the publication of reports of the 14-th International Gamow Conference-School: "Astronomy and beyond: Astrophysics, Cosmology, Cosmomicro-physics, Astroparticle Physics, Radioastronomy, and Astrobiology".

The Conference-School was devoted to 110-th anniversary of George Gamow, a prominent physicist and astrophysicist of XX century. George Gamow was born in Odessa, where he studied at high school and University, and where he became interested in physics and astronomy.

The theory of alpha and beta decay and nuclear reactions as the basis of stellar energy, the hot Universe model with the prediction of the CMB and the expansion of the Universe, deciphering the genetic code, all this showed the breadth and universality of his method of research.

The Gamow's annual conference-schools have become an attractive meeting place for scientists of different ages and scientific fields. The topics of the conference reflects modern advances in cosmology, astrophysics, gravitation, high energy and astroparticle physics, and in the study of the Sun and the solar system.

Among the undoubted achievements of the George Gamow jubilee year is the first in the history of mankind landing of the probe Philae on the nucleus of the comet Churyumov-Gerasimenko, which contains the primary matter of the solar system.

M.I.Ryabov, A.I.Zhuk

CONTENTS

Subsection Virtual observatories are practice of application

RADIO-ASTRONOMY

SUN AND SOLAR SYSTEM

PLENARY SESSION

THE LHC AND THE DISCOVERY OF THE HIGGS BOSON: 50 YEARS OF HIGGS MECHANISM

C. Royon

CEA/IRFU/Service de physique des particules,
CEA/Saclay, 91191 Gif-sur-Yvette cedex, France

ABSTRACT. We describe briefly the ATLAS detector and some of the physics results on QCD, top physics and.the Higgs boson discovery that lead to the Nobel Prize of Physics in 2013. We finish the short report by a new method to look for extra-dimensions in the universe.

Keywords: LHC, ATLAS, Higgs boson

1. The Large Hadron Collider and the ATLAS experiment

1.1. The Large Hadron Collider

The Large Hadron Collider is now the most energetic collider that has ever been built. It collides proton with a center-of-mass energy of 7 TeV (2011), 8 TeV (2012) and will restart next year with an energy of 13 TeV. It allows studying the internal structure of nuclei in terms of quarks and gluons. In relation with cosmology, the LHC proton proton collider reproduces the conditions in the universe less than 10^{-10} seconds after the big-bang or a temperature higher than 10^{15} degrees which could lead to a sign of dark matter candidates. For comparison, the heavy ion mode of the LHC probes a time of about 10^{-9} seconds after the big-bang or a temperature above 10^{12} Kelvin.

Before the start of the LHC, the standard model of particle physics was almost complete with the discovery of the six quarks (up, down, charm, strange, top and bottom) and leptons (electron, muon and tau with their associated neutrinos) and the photon, gluon, and Z/W bosons responsible for the electromagnetic, strong and weak interactions. But the Higgs boson responsible for the existence of mass in the standard model of particle physics was still elusive despite the active searches at LEP and at the Tevatron.

The LHC as we mentioned already is now the largest accelerator on earth with a circonference of 27 km, located underground at a depth varying between 50 to 100 m. The weight is of the order of 38,000 tons, and the typical magnetic field of the order of 8.3 T. The typical energy per beam stands at 400 MJ (let us re-

call that 1 MJ melts 2 kg of copper), and the power consumption of the LHC is about 120 MW (as a comparison, a city such Ann Arbor in the US consumed 190 MW in 2008).

As many accelerators, the LHC is composed of dipole magnets that keep the beam in circular orbits, quadrupole and sextupole magnets that focus the beams and radiofrequency cavities that accelerate the beams. The LHC is one of the hottest spot in the universe: when two proton beams collide, they reach a temperature of about 10^{17} degrees over a minuscule area (for comparison the temperature in the sun's core is about 10^7 degrees) and it creates a condition similar to that 10^{-13} second after the big-bang., It is one of the hottest spots in the universe today. Ironically, the LHC is at the same time one of the coolest places on earth. LHC beams are kept in orbit by superconducting electromagnets operating at a temperature of 1.9 K. It takes about one month to cool down and needs about 10,000 tons of liquid nitrogen and 100 tons of liquid helium to cool and to keep it cold. The LHC is also one of the largest instrument on earth in order to track particles with micron precision over a lenth of 50 m with about 100 million electronic readout channels. These detectors are analogous to digital cameras but taking pictures at a rate of 40,000,000 per second and they are sensitive to light and other radiations.

1.2. The ATLAS and CMS detectors

Many experiments coexist in the LHC: Alice, ATLAS, CMS, TOTEM, LHCb, Moedal, LHCf. We will concentrate in this report of the two generic ones namely ATLAS and CMS. As an example, a sketch of the ATLAS detector is shown in Fig. 1. It is made of different subdetectors: the pixel, semiconductor and transition radiation detectors that allow to reconstruct the point of interaction and the tracks of charged particles, the calorimeters that allow to measure the position and energy of leptons and hadrons, and the largest one, the muon chambers that allow to detect and measure muons. In comparison, the CMS is more compact and weights more than the Eiffel tower in Paris. The
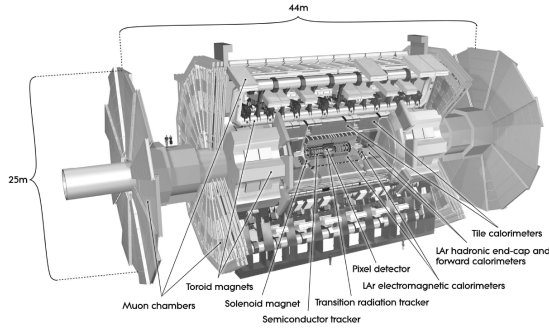
Figure 1: Sketch of the ATLAS detector

ATLAS collaboration is composed of about 3000 scientists from 174 institutes and 38 countries. The ATLAS inner detector alows precise tracking and vertexing with a resolution of $\sigma_{p_T}/p_T \sim 3.8\ 10^{-4} p_T (GeV) \oplus 0.05$. The ATLAS calorimeter is composed of two parts, the electromagnetic Pb-Lar one, with a resolution of $\sigma_E/E = 10\%/\sqrt{(E)} \oplus 0.7\%$ and the central hadronic Fe/Scintillator Tiles one, and the forward Cu/W-Lar one with a resolution of $\sigma_E/E \sim 50\%/\sqrt{E} \oplus 3\%$. The muon detector is made of an air-core toroid system with a bending power of 1 to 7.5 Tm instrumented with gas chambers which leads to a resolution σ_{p_T}/p_T of 2-3% below 200 GeV and 10% at 1 TeV.

In addition, special care was put on the trigger in ATLAS. Protons collide at a rate of 40 MHz and among these, a tiny fraction ($5\ 10^{-6}$) is recorded since not all collisions are interesting and it is not practical to record all of them. The event selection is performed through a multi-level trigger system: the level 1 (hardware) rate is 75 kHz, level 2 (firmware) 3 kHz, and level 3 (software) 200 Hz. This leads to a huge data volume of 320 MB per second or 3PB a year. To give some feeling, the data recorded by each LHC experiment would fill 2,000,000 DVDs per year. In order to analyse this huge volume of data, hundreds of thousands of computers through over the world are connected as a world-wide computing grid.

2. LHC physics

2.1. Rediscovering the standard model: jet measurements

Before looking for discoveries such as the Higgs boson or physics beyond the standard model, it is fundamental to be able to recheck the standard model predictions (what has been discovered in previous experiments) in order to show that the detector is well understood. When a proton collides with another proton at the LHC, the actual collision occurs between quarks
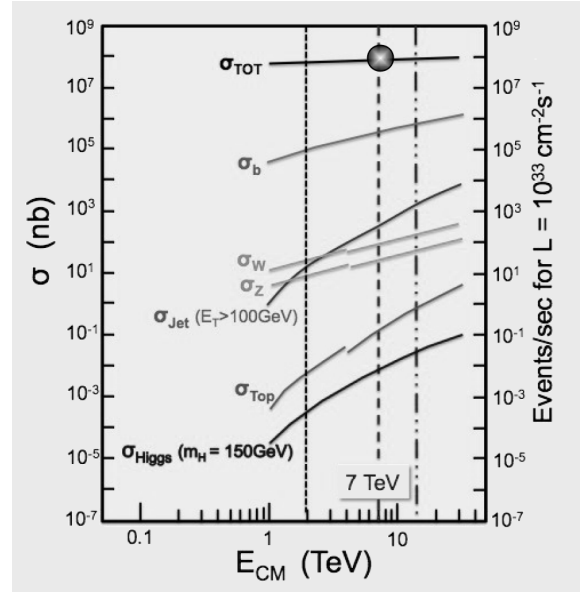
Figure 2: Different physics topics at the LHC
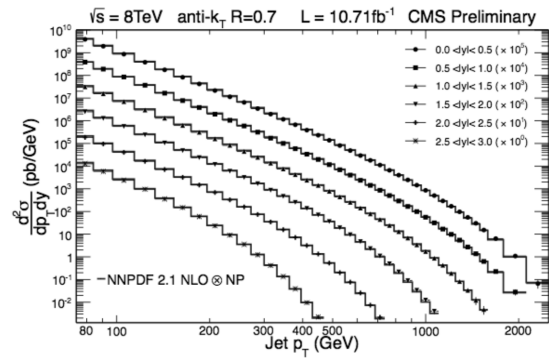
Figure 3: Jet cross section measurements as a function of jet p_T in different rapidity bins

and gluons inside the nuclei, and the cross section of produced objects in the final state will be sensitive to the internal structure of the proton.

The cross section values for different processes at the LHC are shown in Fig. 2. The largest cross section is the total cross section whereas the W/Z, top quark, and Higgs cross sections are respectively about 6, 8 and 10 orders of magnitude below. We already understand the difficulty to look for the Higgs boson since backgrounds will stand orders of magnitude above our signal.

The jet cross section as a function of jet p_T in different domains of rapidity corresponding to different angular regions in the CMS detector is shown in Fig. 3. This measurement is sensitive the proton structure in terms of quarks and gluons. The measurement is in good agreement with NLO order QCD calculations
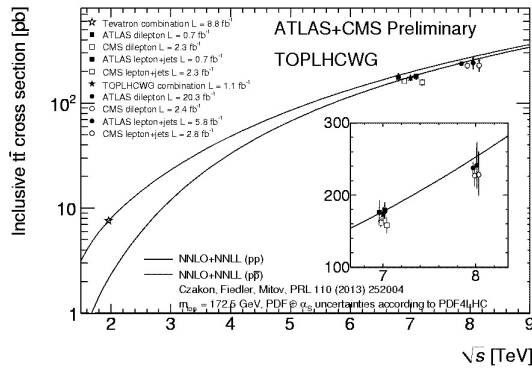
Figure 4: $t\bar{t}$ production cross section measured by the ATLAS and CMS collaborations as a function of the center-of-mass energy compared to NNLO calculations

Figure 5: Scheme to look for the Higgs boson in the $\gamma\gamma$ decay channel at the LHC

displayed as a full line [1], and allows constraining further the proton structure in terms of quarks and gluons.

2.2. Top quark physics

The second standard model measurement that we mention is related to the top qaurk production that was recently discovered at the Tevatron [2]. In about 85% of events, the $t\bar{t}$ events are gluon-induced processes at the LHC. The selection of $t\bar{t}$ events can be performed in different ways. The top quark decays in a bottom quark and a W boson, that itself can decay into two jets or one lepton (electron, muon or tau) and a neutrino. Typically, the signature of a $t\bar{t}$ will be two b-jets originating from the top quark decays, and two Ws that can lead to two leptons (one electron and one muon or two electrons or two muons as an example) and missing transverse energy due to the undetected neutrinos. The $t\bar{t}$ production cross section measured by the ATLAS and CMS collaborations [3] is found to be in good agreement with NNLO cross section calculation as shown in Fig. 4.

3. The discovery of the Higgs boson

Before discussing the processes that lead to the discovery of the Higgs boson at the LHC by the ATLAS and CMS experiments, let us describe the ideas of the Higgs mechanism. Let us imagine a room full of journalists quietly chattering, it is analogous to the space filled only with the Higgs field. A well-known person (the President, Albert Einstein...) enters in the room. This creates a disturbance as he moves through the room and attracts a group of journalist with each step. This increases the resistance to movement of that

famous person. In other words, that person acquires mass just like a particle moving through the Higgs field. Something different might happen in the same room full of journalists: a rumor crosses the room, "the Higgs boson has been discovered", for instance. In that case, it creates the same kind of clustering but this time between the journalists themselves. In this analogy, these clusters are the Higgs particles. Of course, this is just an image to illustrate the Higgs mechanism and the real field theory explanation how particles acquire mass was proposed separately by Higgs, Englert and Brount about fifty years ago [4].

At the LHC, the Higgs boson is mainly produced by two gluons originating from the protons. Depending on its mass, the Higgs boson can decay into $b\bar{b}$ (mainly at low masses), WW and ZZ (at higher masses), in $\gamma\gamma$, $t\bar{t}$, $\tau\tau$... At the LHC, all channels were obviously considered while looking for the Higgs boson. We will restrict ourselves to two golden channels of the Higgs boson decay, namely the $\gamma\gamma$ and ZZ ones. The $\gamma\gamma$ channel has a low branching ratio (typically 0.2% for a Higgs boson mass of 126 GeV) but leads to a clean signal of two photons in the ATLAS detectors. In the case of the ZZ decay, this channel is even cleaner when each of the Z boson decays leptonically into electrons or muons. It corresponds only to a branching ratio of 0.014% but leads to a very clean signal with very low background of 4 leptons in the final state (2 muons and 2 electrons, or 4 muons or 4 electrons).

The method to observe the Higgs boson in the $\gamma\gamma$ decay channel is illustrated in Fig 5. The background is due to the standard model production of two photons which is a steeply falling distribution as a function of the diphoton mass. If the Higgs boson decaying into two photons exists, it should appear as a small bump

in this distribution provided the production cross section is high enough. This is indeed what was observed in the ATLAS and CMS experiments [5] as shown in Fig. 6. Both ATLAS and CMS collaborations discovered a peak at about 126 GeV in the steeply falling diphoton mass distribution. It is necessary to look in other channels to know if this peak is really due to the existence of the Higgs boson and not to another particle. As an example, the results in the ZZ channel is shown in Fig. 7 and leads to the same conclusion, namely an object compatible with the Higgs boson has been observed in the 4 lepton channel at about the same mass as in the diphoton one. This important result lead to the discovery papers of a Higgs boson-like particle [5] which received more than 3200 citations in about 2 years and lead to the Nobel Prize of Physics to Higgs and Englert (Brout sadly passed away about 1 year before the anouncement of the discovery).

More recent results show that this Higgs boson-like particle has all characteristics (spin, couplings...) so far of the standard model Higgs boson, with a mass of $M_H = 125.35 \pm 0.37$ (stat) ± 0.18 (syst) GeV (ATLAS) and $M_H = 125.03^{+0.26}_{-0.27}$ (stat) $^{+0.13}_{-0.15}$ (syst) (CMS) [6]. More data at a higher center-of-mass energy of 13 TeV and also more statistical precision in the rarest decay channels with more integrated luminosity will confirm this result or show some interesting differences with respect to the standard model in a near future when the LHC restarts next year. It is worth mentioning that many decay channels have been looked at now such as $\gamma\gamma$, ZZ, WW, $\tau\tau$, $b\bar{b}$, $Z\gamma$... as well as different Higgs boson production mechanism (gluon-gluon as already mentioned, or vector bosn fusion, associate production with a vector boson, and associate production with $t\bar{t}$).

4. The future: looking for extra-dimension in the universe

We will finish this short report by mentioning a recent proposal to look for the existence of extra-dimensions in the universe by looking especially at the 4 photon couplings at the LHC [7]. We live in a four dimension of space time but gravity might live in extradimensions, and we aim to probe this idea predicted especially by string theories at the LHC. If extra-dimensions are discovered at the LHC, this might lead to major changes in the way we see the world.

The process that we want to study is shown in Fig. 8. It corresponds to $\gamma\gamma$ productions via photon exchanges. Two photons are produced in the final state that can be detected in the ATLAS and CMS detectors and two intact protons are also produced. They can be measured in dedicated detectors located far away from the interaction point (220 m) from the CT-PPS and AFP projects in the CMS/TOTEM and ATLAS collaborations respectively. The two photons in the final state
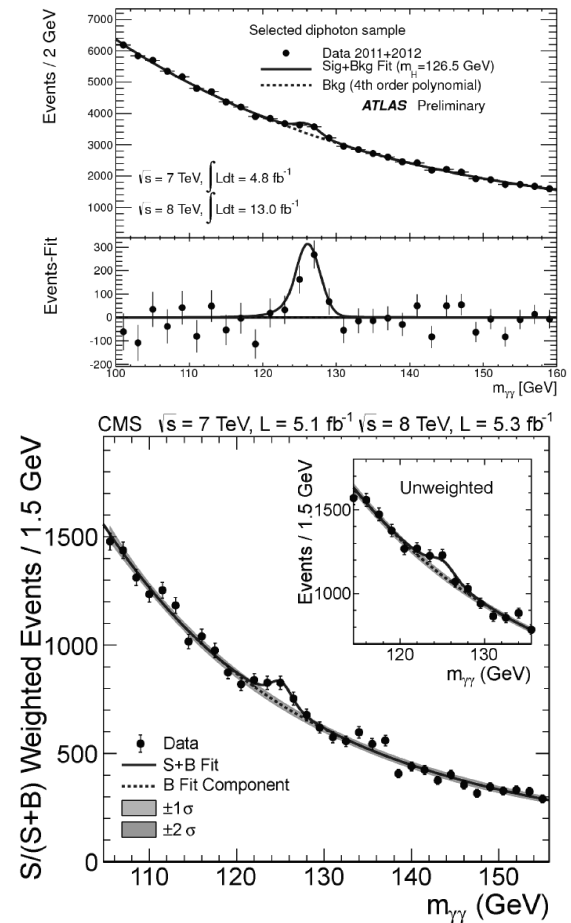
Figure 6: Higgs boson discovery in the diphoton channel at the LHC
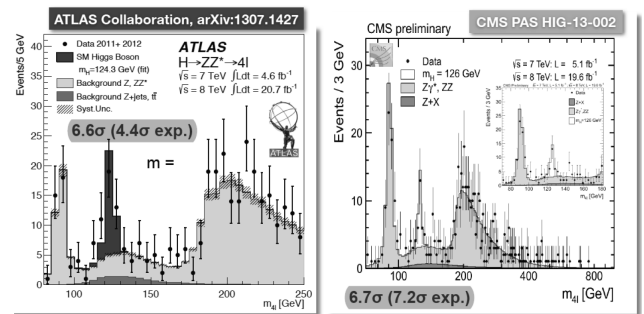
Figure 7: Higgs boson discovery in the ZZ channel at the LHC
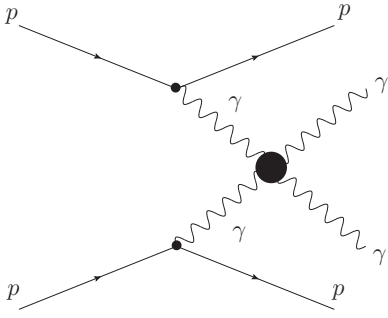
Figure 8: Diphoton production via photon exchange processes at the LHC

Figure 9: Ratio of the diphoton masses computed from the two photons measured in ATLAS/CMS or from the intact proton information as measured by CT-PPS or AFP. For the signal the ratio is close to 1 whereas it is flatter for the pile up background.

appear at high momentum transverse and high masses. The $\gamma\gamma\gamma\gamma$ couplings are predicted by extra-dimension and composite Higgs models. The anomalous couplings was predicted to be of the order of 10^{-14}-10^{-13} for a large range of models. The fact that the event is exclusive, namely that we observe two high mass photons in ATLAS/CMS and two intact protons in AFP or CT-PPS allows suppressing completely the background, including all pile up background up to a pile up of 100. This is due to the fact that the system is completely constrained: the mass and the rapidity of the photon system computed using the photons or the intact protons must be the same within resolution as shown in Fig. 9. After these requirements, the typical sensitivity was found to be $\sim 10^{-14}$ reaching the values expected from generic extra-dimension models [7]. Without tagging the protons and without benefitting from the exclusive requirements, such a reach would not be feasible at the LHC High luminosity and energy at the LHC will thus lead especially to unprecedented sensitivity on quartic $\gamma\gamma\gamma\gamma$ anomalous couplings that, if discovered, might be the sign of the existence of extra-dimensions in the universe, which would be a major discovery.

To conclude, after a brief description of the LHC machine and the ATLAS detector, we described two important SM measurements, namet the jet and $t\bar{t}$ production cross sections that are in agreement with SM expectations. The discovery of the Higgs boson by the ATLAS and CMS experiments was definitely one of the main results at the LHC, that might lead to additional fundamental discoveries such as the existence of extra-dimensions in the universe in a near future.

References

1. ATLAS Coll.: 2012, *Phys. Rev. D*, **86**, 014022; CMS Coll.: 2013, *Phys. Rev. D*, **87**, 112002.
2. D0 Coll.: 1995, *Phys. Rev. Lett.*, **74**, 2632; CDF Coll.: 1995, *Phys. Rev. Lett.*, **74**, 2626.
3. ATLAS Coll.: 2012, *Phys. Rev. D*, **90**, 072004; CMS Coll.: 2014, *J. High Energy Phys.*, **02**, 024.
4. Englert F., Brout R.: 1964, *Phys. Rev. Lett.*, **13**, 321. 37.; Higgs P.W.: 1964, *Phys. Lett.*, **12**, 132. 38; Higgs P.W.: 1964, *Phys. Rev. Lett.*, **13**, 508.
5. ATLAS Coll.: 2012, *Phys. Lett. B*, **716**, 1; CMS Coll.: 2012, *Phys. Lett. B*, **716**, 30.
6. ATLAS Coll.: https://twiki.cern.ch/twiki/bin/view/AtlasPublic/HiggsPublicResults; CMS Coll.: https://twiki.cern.ch/twiki/bin/view/CMSPublic/PhysicsResultsHIG
7. Fichet S., von Gersdorff G., Kepka O., Lenzi B., Royon C., Saimpert M.: 2014, *Phys. Rev. D*, **89**, 114004; Chapon E., Kepka O., Royon C.: 2010, *Phys. Rev.*, **D81**, 074003; Kepka O., Royon C.: 2008, *Phys. Rev. D*, **78**, 073005.

PREHEATING THE UNIVERSE AFTER INFLATION

I.V. Rudenok[1], Yu.V. Shtanov[1,2], S.I. Vilchinskii[1]

[1] Department of Physics, Taras Shevchenko National University,
64/13 Volodymyrska St., Kiev 01601, Ukraine
igrudenok@gmail.com, sivil@univ.kiev.ua
[2] Bogolyubov Institute for Theoretical Physics,
14-b Metrologichna St., Kiev 03680, Ukraine
shtanov@bitp.kiev.ua

ABSTRACT. Inflationary stage is followed by particle production in the background of an oscillating inflaton field, which process is called preheating. For sufficiently strong couplings between the inflaton and matter fields, it is known to proceed non-perturbatively, with parametric resonance playing crucial role for bosonic fields. The evolution of the occupation numbers for fermions is non-perturbative as well. In the Minkowski space, parametric resonance for bosons and non-perturbative effects for fermions would still persist even in the case of weak coupling. In particular, the energy density of created bosons would grow exponentially with time. However, the situation is quite different in the expanding universe. We give a simple demonstration how the conditions of the expanding universe, specifically, redshift of the field modes, lead to the usual perturbative expressions for particle production by an oscillating inflaton in the case of weak couplings. The results that we obtain are relevant and fully applicable to the Starobinsky inflationary model.

Keywords: Inflation; preheating; Starobinsky model

1. Introduction

Consider a scalar field ϕ (to be later associated with the inflaton) of mass M interacting with a light scalar field φ of mass $m_\varphi \ll M$ with the interaction Lagrangian density

$$\mathcal{L}_{\text{int}} = -\sigma \phi \varphi^2 \,, \qquad (1)$$

where σ is a constant of dimension mass. Suppose that the homogeneous field $\phi(t)$ is classically oscillating in the neighborhood of its minimum at $\phi = 0$ with amplitude ϕ_0, while the field φ is in the vacuum state. In the Minkowski space, this initial condition would lead to production of φ-particles via parametric resonance.

For sufficiently small values of σ, namely, for

$$\sigma \phi_0 \ll M^2 \,, \qquad (2)$$

the resonance will be most efficient in the first narrow resonance band centered at the frequency

$$\omega_{\text{res}} = \frac{M}{2} \qquad (3)$$

(see Shtanov, Traschen and Brandenberger, 1994). Within the resonance band, the mean particle occupation numbers grow with time according to the law

$$N_k = \frac{1}{1 - \Delta^2/\sigma^2 \phi_0^2} \sinh^2 \lambda t \,, \qquad (4)$$

where

$$\lambda = \frac{1}{M} \sqrt{\sigma^2 \phi_0^2 - \Delta^2} \,, \qquad \Delta = \omega_k^2 - \omega_{\text{res}}^2 \,, \qquad (5)$$

and $\omega_k = \sqrt{m_\varphi^2 + k^2} \approx k$ is the frequency of the mode of the field φ. The width of the resonance band is determined by the condition that the expression under the square root in (5) is nonnegative.

The total particle number, as well as the energy density of the φ-particles, in Minkowski space grows asymptotically exponentially with time, in contrast to the expectations based on the naïve perturbation theory, where it grows with time only linearly.

There are several important modifications in the case of expanding universe. Firstly, the amplitude of the oscillating inflaton gradually decreases with time as $\phi_0 \propto a^{-3/2}$, where a is the scale factor. Secondly, the frequency of the mode of the scalar field φ is redshifted:

$$\omega_k = \sqrt{m_\varphi^2 + \frac{k^2}{a^2}} \approx \frac{k}{a} \,, \qquad (6)$$

where k now is the comoving wave number. Nevertheless, the theory of parametric resonance is still applicable if the evolution of the relevant quantities occurs adiabatically:

$$\left| \dot{\phi}_0/\phi_0 \right| = \frac{3}{2} H \ll M \,, \qquad (7)$$

where $H \equiv \dot{a}/a$ is the Hubble parameter, and

$$\left| \dot{\lambda}/\lambda \right| \ll \lambda \,, \qquad (8)$$

In this case, one can replace law (4) by an approximate expression (Shtanov, Traschen and Brandenberger, 1994)

$$N_k \simeq \sinh^2 \int \lambda \, dt \qquad (9)$$

as long as the mode with the comoving wave number k remains within the resonance band.

If the adiabaticity condition (8) does not hold, and the parametric resonance, therefore, does not develop, then one usually employs the Born approximation for the total width Γ_φ of decay of a ϕ-particle into a pair of φ-particles:

$$\Gamma_\varphi = \frac{\sigma^2}{8\pi M} \,. \qquad (10)$$

However, if this naïve formula does not work in the Minkowski space (as argued above), one may wonder why it works in the case of expanding universe.

Similar issues can be raised about the production of fermionic particles. Although there is no parametric resonance in this case, still the picture of creation of particle pairs by an oscillating *classical* field is quite different from that based on the usual perturbation theory (Greene and Kofman, 1999, 2000). Nevertheless, in the case of expanding universe, one often uses the Born formula for the total width of decay of ϕ into a pair $\psi, \overline{\psi}$:

$$\Gamma_\psi = \frac{\Upsilon^2 M}{8\pi} \qquad (11)$$

where Υ is the Yukawa coupling of the scalar field ϕ to the fermionic field ψ. (The widths (10) and (11) in the Born approximation in the background of an oscillating classical field in the Minkowski space are calculated, e.g., in Shtanov, Traschen and Brandenberger, 1994.)

The purpose of this letter is to clarify the formulated issues and to justify equations (10) and (11) in the case of expanding universe. Our results will be applicable, in particular, to the Starobinsky inflationary model (Starobinsky, 1980), as we will show below.

2. Inflaton decay in the expanding universe

We derive the rates of the inflaton decay into (scalar) bosons and fermions in the expanding universe using the method of Bogolyubov coefficients. For more details, see Rudenok, Shtanov and Vilchinskii, 2014.

A scalar field φ with mass m_φ interacting with the inflaton ϕ via coupling (1) obeys the equation of motion

$$\Box \varphi + \left(m_\varphi^2 + 2\sigma\phi \right) \varphi = 0 \,. \qquad (12)$$

For the mode $\chi_k = a^{3/2} \varphi_k$ with the comoving wave number k, at the preheating stage, we have the equation (see, e.g., Shtanov, Traschen and Brandenberger,

1994)

$$\ddot{\chi}_k + \Omega_k^2 \chi_k = 0 \,, \qquad (13)$$

where

$$\Omega_k^2(t) = \omega_k^2(t) + 2\sigma\phi(t) - \frac{9}{4} H^2 - \frac{3}{2} \dot{H} \,, \qquad (14)$$

and ω_k is given by (6). At the preheating stage, the inflaton field evolves as

$$\phi(t) = \phi_0(t) \cos Mt \,, \qquad (15)$$

where the amplitude $\phi_0(t) \propto a^{-3/2}(t)$ slowly decreases with time due to the universe expansion as a consequence of the adiabaticity condition (7).

Using equation (5), and taking into account that inflaton-field oscillations mainly occur in the regime $\phi_0 \ll M_{\rm P}$, one can see that the adiabaticity condition (8) is violated for weak coupling satisfying (2). It is this case that will be under study in the present paper.

As a consequence of non-stationarity of the external field ϕ and of the metric, the quantity Ω_k in (13) is a function of time. In the case $\Omega_k = {\rm const}$, the solution for φ_k would maintain its positive-frequency character, i.e., $\varphi_k \sim e^{{\rm i}\Omega_k t}$ for all t. The time-dependence of Ω_k results in the mixing of frequencies, hence, in particle production of the field φ. In the case under consideration, the resonance band is passed so quickly that parametric resonance does not develop, and particle occupation numbers are small. Therefore, in calculating them, one is justified to use perturbation theory.

The mixing of frequencies is considered in a standard way by looking for solutions of the field equation in the form (Grib, Mamayev and Mostepanenko, 1994)

$$\varphi_k(t) = \frac{1}{\sqrt{\Omega_k}} \left[\alpha_k(t) e^{{\rm i} \int_{t_0}^t \Omega_k(t')dt'} \right.$$
$$\left. + \beta_k(t) e^{-{\rm i} \int_{t_0}^t \Omega_k(t')dt'} \right] \,, \qquad (16)$$

$$\dot{\varphi}_k(t) = {\rm i} \sqrt{\Omega_k} \left[\alpha_k(t) e^{{\rm i} \int_{t_0}^t \Omega_k(t')dt'} \right.$$
$$\left. - \beta_k(t) e^{-{\rm i} \int_{t_0}^t \Omega_k(t')dt'} \right] \,, \qquad (17)$$

where $\alpha_k(t)$ and $\beta_k(t)$ are the Bogolyubov coefficients satisfying the relation

$$|\alpha_k|^2 - |\beta_k|^2 = 1 \,. \qquad (18)$$

In terms of these coefficients, the average occupation numbers in the corresponding modes are given by $N_k = |\beta_k|^2$. Substituting expressions (16), (17) into (13), one obtains the system of equations for α_k and β_k,

$$\dot{\alpha}_k = \frac{\dot{\Omega}_k}{2\Omega_k} e^{-2{\rm i} \int_{t_0}^t \Omega_k(t')dt'} \beta_k \,, \qquad (19)$$

$$\dot{\beta}_k = \frac{\dot{\Omega}_k}{2\Omega_k} e^{2{\rm i} \int_{t_0}^t \Omega_k(t')dt'} \alpha_k \,, \qquad (20)$$

with the initial conditions $\alpha_k = 1$, $\beta_k = 0$. Treating this system perturbatively, in the first order, we

replace α_k by unity in (20). Then, leaving only the resonant term in this equation, we use the stationary-phase approximation to evaluate the coefficient β_k (see Rudenok, Shtanov and Vilchinskii, 2014):

$$\beta_k = \frac{\sigma M \phi_0(t_k)}{4\omega_k^2(t_k)} \sqrt{\frac{\pi}{|\dot{\omega}_k(t_k)|}} = \frac{\sigma \phi_0(t_k)}{M^{3/2}} \sqrt{\frac{2\pi}{H(t_k)}}, \quad (21)$$

where the moment of time t_k is defined by the stationary-phase relation $\omega_k(t_k) = M/2$, which is just the moment of passing through the center of the resonance band for the k-mode.

The process of particle production can be pictured as follows. A mode with sufficiently high wave number k undergoes redshift till it reaches the resonance region. After passing through the narrow resonance band, it becomes filled with particles with average occupation numbers given by (21), which, in our approximation, remain subsequently constant. The modes with wave number smaller than $k_{\min} = Ma(t_0)/2$, where t_0 is the moment of the beginning of particles creation, will never pass through the resonance region due to the redshift and will be free of particles in our approximation.

In this picture, the energy density $\rho_\varphi(t)$ of the created particles at any moment of time is given by

$$\rho_\varphi(t) = \frac{1}{a^4(t)} \int \frac{d^3k}{(2\pi)^3} k |\beta_k|^2$$
$$\times \theta(k - k_{\min}) \theta(Ma(t) - 2k), \quad (22)$$

where $\theta(x)$ is the Heaviside step function.

By comparing the time derivative of this energy density with the equation for the evolution of the energy density ρ_φ of continuously created relativistic particles,

$$\dot{\rho}_\varphi = -4H\rho_\varphi + \Gamma_\varphi \rho_\phi, \quad (23)$$

we determine the effective rate of particle production Γ_φ:

$$\Gamma_\varphi \rho_\phi = \left. \frac{k^3 |\beta_k|^2 M \dot{a}}{4\pi^2 a^4} \right|_{k=Ma/2}. \quad (24)$$

Hence, using (21) and relation $\rho_\phi = \frac{1}{2} M^2 \phi_0^2$, we get the standard expression (10) for the quantity Γ_φ.

Consider now the case of fermions. In a curved space-time, one uses the covariant generalization of the Dirac equation:

$$[i\gamma^\mu(x)\mathcal{D}_\mu - m]\psi(x) = 0, \quad (25)$$

where $\gamma^\mu(x) = h_{(a)}^\mu(x)\gamma^a$, with γ^a being the usual constant Dirac matrices, and $h_{(a)}^\mu(x)$ is a pseudo-orthonormal tetrad.

We consider the typical case where the spinor field ψ interacts with the inflaton field ϕ through the Yukawa coupling

$$\mathcal{L}_{\text{int}} = \Upsilon \phi \overline{\psi} \psi. \quad (26)$$

This leads to the appearance of the effective time-dependent fermion mass in equation (25):

$$m(t) = m_\psi - \Upsilon \phi(t). \quad (27)$$

The Bogolyubov transformation in this case is performed in a usual way as described, e.g., in Grib, Mamayev and Mostepanenko, 1994. The first-order perturbation-theory solution for the Bogolyubov coefficient β_k has the form

$$\beta_k = \frac{\Upsilon M}{4i} \int_{t_0}^t \frac{\phi_0(t')}{\omega_k(t')} e^{2i \int_{t_0}^{t'} \omega_k(t'')dt'' - iMt'} dt', \quad (28)$$

where

$$\omega_k = \sqrt{m_\psi^2 + \frac{k^2}{a^2}} \approx \frac{k}{a}. \quad (29)$$

Higher-order corrections to this perturbative solution are small under the condition (Shtanov, Traschen and Brandenberger, 1994)

$$\frac{\Upsilon \phi_0}{M} \ll 1, \quad (30)$$

which is assumed to be the case.

By using the stationary-phase approximation, we obtain, similarly to (21) (see Rudenok, Shtanov and Vilchinskii, 2014),

$$\begin{aligned} \beta_k &= -\frac{\Upsilon M \phi_0(t_k)}{4\omega(t_k)} \sqrt{\frac{\pi}{|\dot{\omega}_k(t_k)|}} \\ &= -\frac{1}{2} \Upsilon \phi_0(t_k) \sqrt{\frac{2\pi}{MH(t_k)}}. \end{aligned} \quad (31)$$

Then, repeating the reasoning of the case of bosons, and taking into account the four spin polarizations of particles and anti-particles, we get the final result for the production rate of fermions Γ_ψ, which coincides with (11).

3. The Starobinsky model

Historically, one of the first inflationary models was the model suggested by Starobinsky in 1980. It is motivated by the necessity to consider local quantum corrections to the Einstein theory of gravity. The simplest such correction represents the term proportional to the second power of the Ricci scalar in the action of the model, so that the full gravitational action reads as

$$S_{\text{g}} = -\frac{M_{\text{P}}^2}{2} \int d^4x \sqrt{-g} \left(R - \frac{R^2}{6\mu^2} \right), \quad (32)$$

where

$$\mu = 1.3 \times 10^{-5} M_{\text{P}} \quad (33)$$

is a constant with indicated value required to explain the inflationary origin of the primordial perturbations (Faulkner et al., 2006).

A conformal transformation $g_{\mu\nu} \rightarrow \chi^{-1} g_{\mu\nu}$, with $\chi = \exp\left(\sqrt{\frac{2}{3}} \frac{\phi}{M_{\rm P}}\right)$ transforms the theory (32) into the usual Einstein gravity with a new special scalar field ϕ (the scalaron):

$$S_{\rm g} = -\frac{M_{\rm P}^2}{2} \int d^4 x \sqrt{-g} R$$
$$+ \int d^4 x \sqrt{-g} \left[\frac{1}{2} g^{\mu\nu} \partial_\mu \phi \partial_\nu \phi - V(\phi)\right], \quad (34)$$

where

$$V(\phi) = \frac{3\mu^2 M_{\rm P}^2}{4} \left[1 - \chi^{-1}(\phi)\right]^2 \quad (35)$$

is the arising field potential.

The scalaron universally interacts with other fields present in the theory. At the preheating stage, we can employ the relation

$$|\phi/M_{\rm P}| \ll 1. \quad (36)$$

Without taking into account the back-reaction of the mater fields on the dynamics of the scalaron field, its behavior at the stage of preheating is approximately described by the Klein–Gordon equation

$$\Box \phi + \mu^2 \phi = 0, \quad (37)$$

and by the oscillatory regime (15) with mass $M = \mu$.

Due to condition (36) and assuming also that $m_\varphi \ll \mu$, one can obtain an approximate equation for a scalar field φ minimally coupled to gravity in the original frame (32):

$$\Box \varphi + \left[m_\varphi^2 - \frac{\mu^2 \phi}{\sqrt{6} M_{\rm P}}\right] \varphi = 0. \quad (38)$$

This is just equation (12) with

$$\sigma = -\frac{\mu^2}{2\sqrt{6} M_{\rm P}}, \quad (39)$$

Thus, the theory of Sec. 2 is applicable here, and the particle production rate is given by (10):

$$\Gamma_\varphi = \frac{\sigma^2}{8\pi M} = \frac{\mu^3}{192\pi M_{\rm P}^2}, \quad (40)$$

which coincides with equation (7) of Gorbunov and Panin, 2010.

For the fermions, we derive the decay rate (11):

$$\Gamma_\psi = \frac{\Upsilon^2 M}{8\pi} = \frac{\mu m_\psi^2}{12\pi M_{\rm P}^2}, \quad (41)$$

which, up to a factor four (possible account of the spin states), coincides with equation (8) of Gorbunov and Panin, 2010.

4. Discussion

Particle production in the background of an external classical oscillating field is one of the key processes describing the stage of preheating after inflation. In Minkowski space, it would be dominated by the parametric resonance in the lowest resonance band, no matter how small is the coupling between the inflaton and bosonic matter fields. The energy density of the created particles would grow exponentially with time, in contrast to the usual perturbation-theory expectations.

The specific features of the expanding universe, surprisingly, restore the validity of the usual Born formula in the case of sufficiently weak coupling. The reason is that every particular mode of the field to be excited, due to redshift, quickly passes the resonance zone, resulting in small occupation numbers.

It is also important that couplings (1) and (26) were linear in the inflaton field ϕ, so that we also had $N_k = |\beta_k|^2 \propto \phi_0^2 \propto \rho_\phi$. These are precisely the types of coupling responsible for the decay of a ϕ-particle, justifying the interpretation of (10) and (11) as decay rates.

We have shown that the results of the present paper are fully applicable to one of the most successful inflationary models — the Starobinsky model.

References

Linde A.D.: 1990, *Particle Physics and Inflationary Cosmology* (Harwood, Chur, Switzerland).

Traschen J.H., Brandenberger R.H.: 1990, *Phys. Rev. D*, **42**, 2491.

Kofman L., Linde A.D., Starobinsky A.A.: 1994, *Phys. Rev. Lett.* **73**, 3195.

Shtanov Y., Traschen J.H. and Brandenberger R.H.: 1995, *Phys. Rev. D*, **51**, 5438.

Greene P.B., Kofman L.: 1999, *Phys. Lett. B*, **448**, 6.

Greene P.B., Kofman L.: 2000, *Phys. Rev. D*, **62**, 123516.

Starobinsky A.A.: 1980, *Phys. Lett. B*, **91**, 99.

Grib A.A., Mamayev S.G., Mostepanenko V.M.: 1994, *Vacuum Quantum Effects in Strong Fields* (Friedmann Laboratory Publishing, St.-Petersburg).

Faulkner T. et al.: 2006, *Phys. Rev. D*, **76**, 063505.

Gorbunov D.S., Panin A.G.: 2011, *Phys. Lett. B,* **700**, 157.

Rudenok I., Shtanov Y., Vilchinskii S.: 2014, *Phys. Lett. B,* **733**, 193.

SOLAR CYCLES – TO UPDATING BASIC PARAMETERS

M. I. Ryabov

Odessa observatory "Uran-4" of Radio astronomical Institute NANU
ryabov-uran@ukr.net

ABSTRACT. Examining daily and monthly averages of solar activity index of the northern and southern hemispheres on the total area of spots-Sp (12-24 cycles, 1874-2014), the Wolf numbers-W (22-24 cycles, 1992-2014). Application of band pass filtering based on Wavelet analysis shows that «Northern» and «Southern» cycles have their own start time, rise phase, the phases of decline, maximum and minimum. The formation of each cycle on all indices of activity is determined as a result of the combined effect of the long-period and short-periodic processes.

Introduction

This paper continues the cycle of studies [1-3] of the properties of "Northern" and "Southern" cycles of activity according to daily and monthly average values of indexes of summary area sunspots groups -Sp, and Wolf numbers – W. In the paper [1] we show a significant difference in the dynamics of the development of Northern and Southern hemispheres on the smoothed values space groups of spots for 12-23 cycles of activity. Based on the application of wavelet analysis we identified extended "periods" and power global spectra of the power of the activity of the northern and southern hemispheres for the daily index values of Sp and W in the 23rd cycle of solar activity [2-3].

Method of data analysis

Method of application of an expanded version of wavelet analysis is described in [2]. On the basis of data obtained with the use of band-pass Wavelet filter we defined the regularities of the "11-year" cycle, cycles of average length (1-7 years) and periods of less than a year.

Results of the investigation

Allocation of 11-year-old "Northern" and "Southern" cycles of activity allows to determine their minima, maxima, phases of rise and fall , and cycles duration . General view of the cycles is presented in Figure 1, and the numerical results in Table 1.
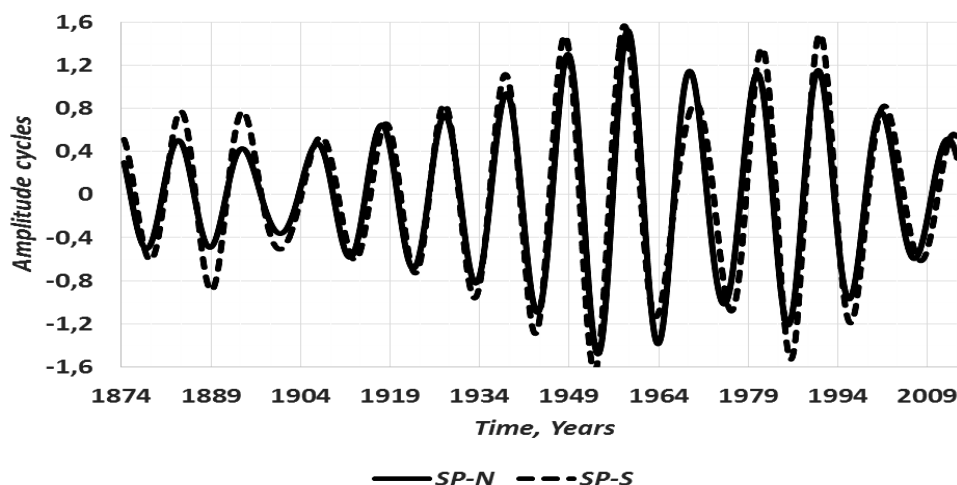
Figure 1: The dynamics of the "11-year" cycles of Northern and Southern hemispheres of the Sun.

Table 1 (advanced cycles of activity are shown in bold)

Cycle	N min	N max	Long. N cycle	S min	S max	Long. S cycle
12	**1878,17**	1883,50	10,66	1878,84	1883,92	10,21
13	**1888,83**	1894,25	11,75	1889,04	1894,25	11,50
14	**1900,58**	1906,00	11,67	**1900,54**	1907,42	12,54
15	**1912,25**	1917,58	10,67	1913,09	1918,29	10,12
16	**1922,92**	1928,17	10,41	1923,21	1928,09	9,96
17	1933,33	1938,50	10,34	**1933,17**	1938,17	10,12
18	1943,67	1948,83	10,16	**1943,29**	1948,25	9,96
19	1953,83	1958,83	10,00	**1953,25**	1958,21	10,25
20	1963,83	1969,17	11,09	**1963,50**	1970,08	12,67
21	**1974,92**	1980,50	10,75	1976,17	1981,29	9,92
22	**1985,67**	1990,75	10,25	1986,08	1991,00	10,04
23	**1995,92**	2001,25	10,91	1996,13	2001,79	11,79
24	**2006,83**	2012,50		2007,92	2013,04	

According to the reviewed data, duration of the "N" cycles varies in the range from 10 up to 11.75 years, and S cycles from 9.92 to 12.67 years. The 11-year cycle is the dominant period. Considering it as a trend and the removal of original data using the filtering method, it allows to determine the dynamics of development of average length and short periods. The result of filtering for each hemisphere is shown in Figure 2.

From Fig. 2 you can see that in the northern hemisphere there is a merger and separation of periods ranging from 1 to 5 years. Activity maximum in the 19th cycle of activity. At the same time in the southern hemisphere local area of increased activity dominates, with a maximum gain of its manifestation in 18-cycle activity. The original dynamics is illustrated by the results of Fourier filtering strip for periods of 3-5 years in the northern hemisphere and 4-7 years in the South. Periods of "pitching" the data intervals in the northern hemisphere 15-22 cycles of activity (see Figure 3) and in the southern hemisphere in 18-20 cycles can be observed.
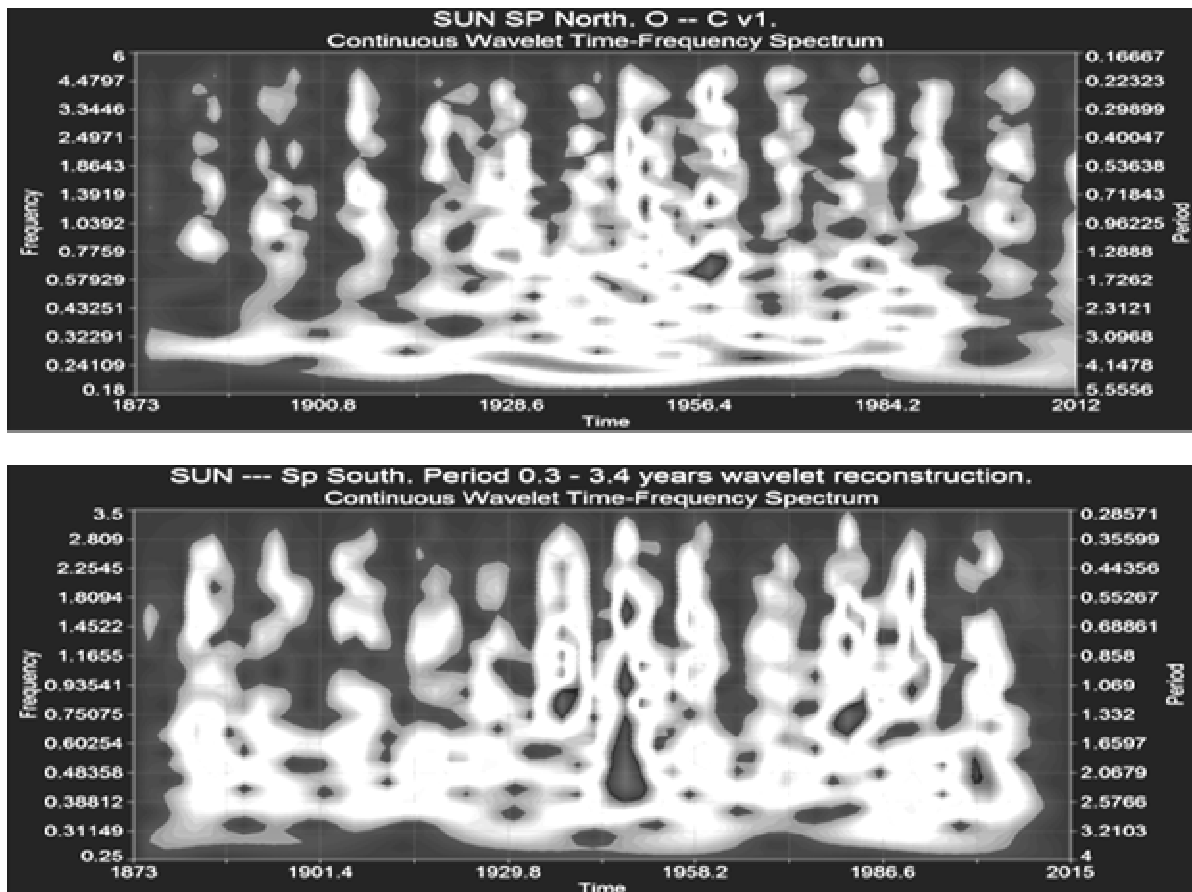
Figure 2: Wavelet spectra of N and S of the hemispheres of the Sun when the 11-year "cycle include
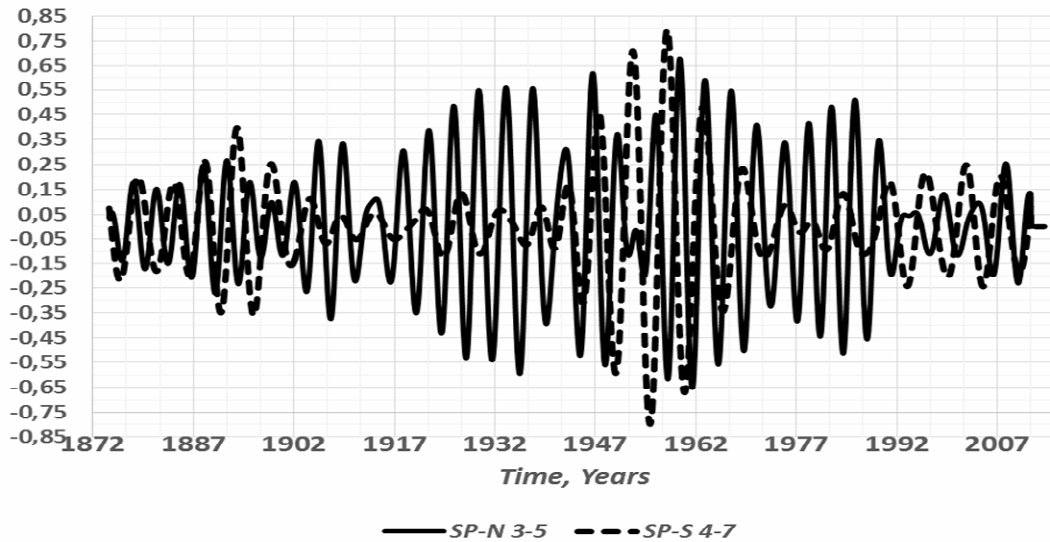
Figure 3: Dynamics of development of the activity periods (3-5 years) for Northern and (4-7 years) for Southern hemispheres of the Sun
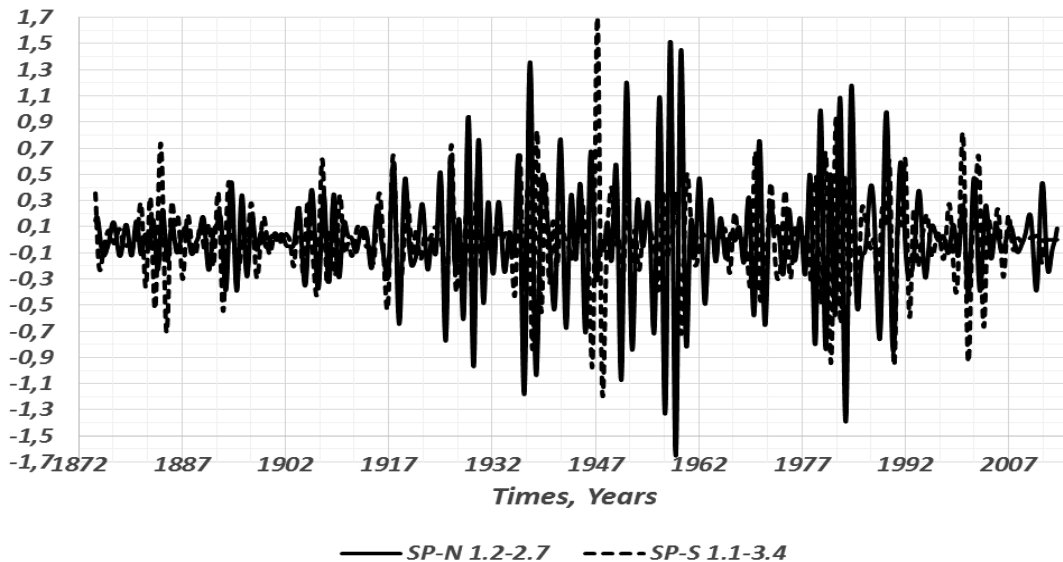
Figure 4: Dynamics of development of the activity periods (2-2.7 years) for Northern and (1.1-3.4 years) for Southern hemispheres of the Sun

At the same time, considering the dynamics of shorter periods in the Northern hemisphere (1.2-2.7 years), and in Southern (1.1-3.4 years) correspond more to show activity during periods of growth, peak and off-peak with different ratios of amplitudes (see Figure 4).

Conclusion

The formation of each cycle on all indices of activity is determined as a result of the combined effect of the long-period and short-periodic processes. Presented processes in the transition from cycle to cycle show merger, separation, modulation, and recurrent decay. Manifestation of abnormal activity in the rise phase, peak and decline cycle is formed by both intensifying objects in the processes, time and "Spectra periods" which are markedly different in the northern and southern hemispheres. Time intervals of activity in the northern and southern hemispheres are significantly different. The main conclusion is that the study of nature and development of the solar cycle modelling can be justified only on the basis of consideration of the activity of the northern and southern hemispheres particularly including their interaction while forming the global activity complexes.

Reference

1. Ryabov M.I. et al.: 2009, *Cycles activity on the Sun and stars*, 121.
2. Ryabov M.I. et al.: 2013, *Solar and solar-Earth connections physics*, 235.
3. Ryabov M.I. et al.: 2013, *Odessa Astron. Publ.*, **26/2**, 276.

ON THE SEPARATION OF SOLAR AND LUNAR CYCLES

N. S. Sidorenkov [1], T. S. Zhigailo [2]

[1] Hydrometeorological Research Center of the Russia Federation, Moscow, Russia Federation
sidorenkov@mecom.ru
[2] Odessa State Environmental University, Odessa, Ukraine

ABSTRACT. The synodic rotation period of the Sun nearly coincides with the sidereal rotation period of the Moon (27.3 days). The 11-year cycle of solar activity coincides with the eclipse cycle Tritos. The secular cycle of solar activity is close to the 93-year lunar cycle. Due to these coincidences, the cause of monthly, 11-year, and secular periods and their super harmonics in terrestrial processes is attributed to the Sun by solar-terrestrial researchers and to lunisolar tides by geophysicists. The possibilities of separating the solar and lunar cycles by applying spectral analysis, examining frequency differences, and detecting beats and resonances are discussed in this talk.

Key words: solar and geomagnetic activity; lunar months, lunisolar tides, beats of oscillations, cycles of eclipses, lunar perigee and apogee.

Introduction

The angular velocity of the Sun's rotation decreases with increasing heliographic latitude. The sidereal rotation period of the Sun is equal to 25 days at the equator and increases to 35 days as the poles are approached. Its average value is taken to be 27 days. With the same period, the Moon and Earth rotate about their common center of mass (barycenter). Moreover, the 11- and 90-year periods of solar activity coincide with the eclipse cycle Tritos (equal to 10.91 years or 135 synodic months. Table 1) and with the 93-year cycle of beats in the amplitudes of the perigee and nodal tides. Due to these coincidences, the cause of monthly, 11-year, and secular periods and their super harmonics in terrestrial processes is attributed to the Sun by solar-terrestrial researchers and to lunisolar tides by geophysicists. The possibility of separating the solar and lunar cycles by applying the spectral analysis, examining the frequency differences, and detecting the beats and resonances is discussed in this paper.

Geomagnetic activity

At present the *aa* geomagnetic activity index has gained much popularity. The *aa* index is calculated from the three-hourly index *A* measured at two antipodal magnetic observatories, Hartland (United Kingdom) and Canberra (Australia), which are located at an identical distance from the geomagnetic equator (at a geomagnetic latitude of ± 50). These observatories have the longest series of observations (since 1868). Accordingly, there is a continuous time series of the *aa* index from 1868 until now. The most complete description of the *aa* index can be found in IAGA Bulletin 33.

We have constructed the spectrum of the series of daily *aa* values from 1868 to 2008 (Fig. 1). The analysis of the *aa* spectrum shows that long-time oscillations of the geomagnetic activity are associated with the solar activity (the peaks near periods of 11 and 5.2 years). The high-frequency part of the spectrum (periods < 1 year) has peaks at the lunisolar tide periods (182, 27, 13.6, 9, and 7 days). This result can be caused by the lunisolar tides affecting the motion of the plasma in the ionosphere and the magnetosphere, thereby resulting in the geomagnetic variations analogous to the solar daily and lunar daily variations.

Of course, the 27-day cycle of geomagnetic activity can arise because of the 27-day recurrences of the active domains on the solar disk due to the Sun's rotation about its axis and the Earth's motion around the Sun. However, the other high-frequency peaks, including the semiannual one, agree perfectly with the spectrum of lunisolar tides.

In addition to the 11-year and 5-year periods seen in Fig. 1, the solar activity exhibits a 22-year magnetic cycle and a secular cycle of about 90 years.

Lunisolar cycles

The Moon and the Earth rotate around the barycenter of the Earth--Moon system with a monthly period. The Earth's orbit is 1/81 as large as the Moon's. Moreover, since we are on the Earth, we cannot observe its rotation. That is why it took several thousand years for humans to realize the Earth's annual rotation around the Sun. The monthly rotation of the Earth is nearly unobservable, but on a scale of 1 to 81, it repeats all features of the Moon's rotation. For this reason, in what follows we consider the monthly rotation of the Moon.

There are the synodic (29.53 days), sidereal (27.32 days), anomalistic (27.55 days), draconic (27.21 days), and other months. The perigee of the lunar orbit moves from west to east with a period of 8.85 years. The plane of the lunar orbit precesses. As a result, the lunar nodes rotate along the ecliptic from east to west (against the Moon's motion) with a period of 18.61 years. The Earth--Moon system rotates around the Sun with an annual period of 365.24 days. Naturally, all these fundamental periods of the Moon's and Earth's monthly and annual rotation have super harmonics and sub harmonics.
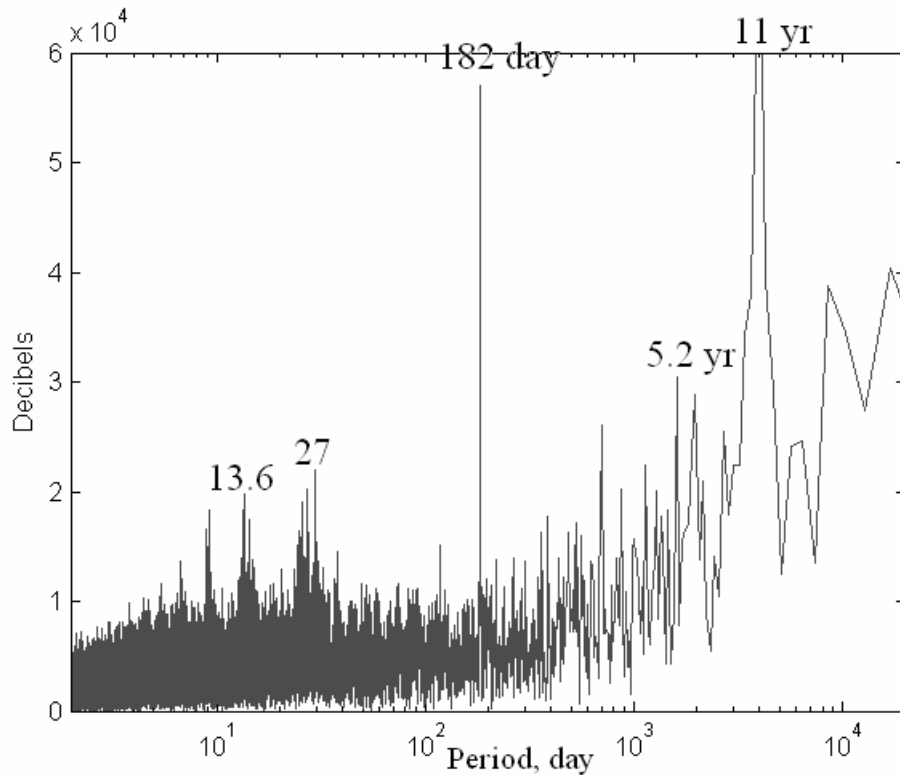
Figure 1: Spectrum of the *aa* geomagnetic activity index.

Table 1: The durations of some eclipse cycles (http://en.wikipedia.org/wiki/Eclipse_cycle)

cycle	solar days	synodic months	solar years	anomalistic months
Fortnight	14.77	0.5	0.040	0.536
Month	29.53	1	0.081	1.072
Semester	177.18	6	0.485	6.43
Lunar year	354.37	12	0.970	12.861
Octon	1387.94	47	3.80	50.371
Octaeteris	2923.53	99	8.00	106.100
Tritos	3986.63	135	10.91	144.681
Saros	6585.32	223	18.03	238.992
Metonic cycle	6939.69	235	19.00	251.853
Inex	10571.95	358	28.94	383.674
Exeligmos	19755.96	669	54.09	716.976
Callippic cycle	27758.75	940	76.00	1007.411

The interference of oscillations with slightly different frequencies gives rise to beats. The most pronounced is the beat generated by the frequencies corresponding to the synodic and anomalistic months:

$$\frac{1}{27.55455} - \frac{1}{29.53059} = \frac{1}{411.78}$$

The period of 411.78 days is called the Full Moon Cycle (FMC). Additionally, there is a specific FMC equal to 14 synodic months or 413.3733 days. Three and a half specific FMCs make up exactly four years. Three and a half FMCs also make up nearly four years. As a result, geophysical, meteorological, and oceanological tidal phe-nomena exhibit the four-year cyclicity (Sidorenkov and Sumerova, 2012a). A small difference between the specific (synodic) and perigee FMCs gradually accumulates and leads to smaller amplitudes of tidal phenomena. The interference of these two cycles generates beats:

$$\frac{1}{27.21222} - \frac{1}{27.55455} = \frac{1}{2190.344} \rightarrow \frac{1}{5.997\,yr}$$

The tidal effects are amplified when the moment of the monthly orbit perigee coincides with the perihelion of the annual orbit. These situations generate oscillations of ter-restrial processes with periods of 31/62/93/186 years (Wilson, 2013):

$$8.847 \times 3.5 = 30.96 \approx 31 \; yr$$
$$8.847 \times 7 = 61.93 \approx 62 \; yr$$
$$8.847 \times 10.5 = 92.89 \approx 93 \; yr$$
$$8.847 \times 21 = 185.79 \approx 186 \; yr$$

The cycles of 93 and 186 years are amplified because they are multiples of the cycle of the regression of nodes

$$18.6 \times 5 = 93 \; yr$$
$$18.6 \times 10 = 186 \; yr$$

The lunisolar tides repeat with a period of 355 days, which is known as the tidal year. This period is also manifested as a cycle of repeated eclipses. Meteorological characteristics (pressure, temperature, cloudiness, etc.) vary with a period of 355 days. The interference of these tidal oscillations and the usual annual 365-day oscillations generates beats in the annual amplitude of meteorological characteristics with a period of about 35 years (Sidorenkov and Sumerova, 2012b). The quasi 35-year variations in cloudiness lead to oscillations of the radiation balance over terrestrial regions. As a result of these quasi-35-year beats, the climate, for example, over European Russia alternates between "continental" with dominant cold winters and hot summers (such as from 1963 to 1975 and from 1995 to 2014) and "maritime" with frequent warm winters and cool summers (such as from 1956 to 1962 and from 1976 to 1994).

It was found in (Litvinenko, 2012) that the recurrence of eclipses is related to the features of the annual variation in air temperature anomalies. Examples of recurring features in the temperature anomaly distribution in cycles of saros and exeligmos were presented. It was found that anomalously cold years occur when the eclipses are observed in the polar regions. Clearly, these interrelations cannot arise due to the very short instants when the direct solar radiation is screened by the Moon. The effect probably arises due to certain configurations of the celestial bodies, the positions of the lines of nodes and apses of their orbits, and the orientations of their rotation axes and the Earth's magnetic field that develop in the Sun--Earth--Moon system in the years of certain eclipses and influence the flow of solar and space plasmas toward the Earth.

The causes of the catastrophic floods occurring in the summer of 2013 were analyzed in (Sidorenkov and Chazov, 2015). It was shown that these phenomena were related to the fact that, over the entire year 2013, the Moon was found near the perigee in the Southern Hemisphere and near the apogee in the Northern Hemisphere. The Moon moves rapidly at the perigee and slowly at the apogee. As a result, in each lunar month in 2013, the Moon stayed within the Southern Hemisphere of the celestial sphere for 10--11 days and within the Northern Hemisphere for about 17 days. Accordingly, the tidal waves generated by the moon in the Earth's atmosphere moved at a varying zonal speed, completing a half-revolution over 10 and 17 days alternately. This nonuniformity in the motion of tidal waves led to the development of stable blocking systems in the atmosphere, to the anomalously intense precipitation, and to flooding in the summer of 2013.

Conclusions

The periods of the lunar and solar cycles are known with astronomical and astrophysical accuracy, respectively (the latter is the several orders of magnitude less than the former).

The lunar cycles can be detected from the periods of beats in their amplitudes, from their frequency modulations, and their clearer manifestations at time intervals multiple of the solar year.

The dependence of meteorological processes on the tidal oscillations of the Earth's rotation rate (i.e., on the modulus of the Moon's declination and parallax), the relation of climate characteristics to the cyclicity of eclipses (i.e., to the orientation of the Moon's line of nodes), and the relation of droughts and floods to features of the perigee position (i.e., to the orientation of the apses of the Moon's and Earth's orbits) suggest that the responses of the climate system, biosphere, and noosphere to space impacts depend more not on the solar activity and gravitational tides but rather on the mutual configurations of the bodies in the Sun--Earth--Moon system (more precisely, in the entire solar system), on the positions of their lines of nodes and apses, and on the orientations of their rotation axes and the Earth's magnetic field with respect to the flow of the solar wind and space plasma. The situation depends on varying conditions affecting the flow of plasma to the Earth.

References

Litvinenko L.N.: 2012, In book: Sistema "Planeta Zemlya". Moscow: LENAND. 2012. P. 292-304 (in Russian).

Sidorenkov N.S.: 2009, The interaction between Earth's rotation and geophysical processes. WILEY-VCH Verlag GmbH & Co. KGaA, Weinheim, 2009. 317 pp.

Sidorenkov N.S., Sumerova K.A.: 2012a, *Proceed. of Hydrometcentre of Russia*, **348**, 195.

Sidorenkov N.S. and Sumerova K.A.: 2012b, Temperature Fluctuation Beats as a Reason for the Anomalously Hot Summer of 2010 in the European Part of Russia. ISSN 1068-3739, Russian Meteorology and Hydrology, 2012, Vol. 37, № 6, P. 411.

Sidorenkov N.S., Chazov V.V., Petrov V.N.: 2015, Reasons of the floods in 2013. In book: "Planeta Zemlya". Moscow: LENAND. 2015. P. ? (in Russian).

Wilson I.R.G.: 2013, *The Open Atmospheric Science Journal*, **7**, 51.

http://en.wikipedia.org/wiki/Eclipse_cycle

GRAVITATIONAL MICROLENSING AND EXTENDED SOURCE MODELS

V.M. Sliusar, V.I. Zhdanov

Astronomical Observatory, Taras Shevchenko National University of Kyiv
Observatorna str., 3, Kyiv, Ukraine
vitaliy.slyusar@gmail.com; valeryzhdanov@gmail.com

ABSTRACT. We perform statistical simulations of light curves of extended microlensed sources having different brightness distribution in the source plane. We generated a set of realizations of lensing point mass system that takes into account an external shear; these include 12000 point masses which are uniformly distributed in the lens plane. The list of the circular symmetric source models used includes gaussian, limb-darkening, power law and Shakura-Sunyaev accretion disk models observed face-on. We estimated difference η between the amplification curves (an analog of the light curves) for these different source models. This difference appears to be considerable, in some cases it amounts up to $\sim 10\%$. However, the effect of the shear within limits $\gamma = 0 \div 0.5$ is not considerable, though it leads to some diminishing of η.

Keywords: galaxies, quasars, gravitational lensing
PACS 98.62.Sb

1. Introduction

In this paper we study the light curves of an extended microlensed source in extragalactic gravitational lens systems (GLSs). Microlensing processes induce a considerable brightness variations of the source images; this is observed in a number of real extragalactic GLSs (Schneider et al., 1992), which have several macro-images of one quasar.

Sometimes a considerable brightness enhancement in some micro-image occurs which is referred to as a high amplification event (HAE); it is associated with an intersection of the GLS caustic by the source. One of important applications of HAE deals with a possibility to study a light distribution over the source. Since a pioneering paper by Grieger, Kayser and Refsdal (1988) this question has been analyzed in a number of papers, as theoretically and observationally (for a review see, e.g., Mortonson, 2005; Zhdanov et al, 2012; Alexandrov & Zhdanov, 2011). The determination of the source profile from observational data is an incorrect mathematical problem and to solve it one needs some additional assumptions about this profile and, possibly, about the mass distribution in the gravitational lens system. Anyway, it is often claimed (see, e.g., Mortonson, 2005) that under some general conditions the only characteristic, that can be presently derived from typical light curve measurements in GLS, is the source size. This question needs further statistical studies with various assumptions about the source model.

In particular, one of the questions concerns the accuracy that is needed in order to distinguish different fiducial source models in GLS using the light curves. These questions were discussed by Alexandrov et al, 2011; Sliusar et al, 2009; Sliusar et al, 2013. However the consideration of these papers has been limited mainly to the shearless distributions of masses. The present paper continues this line taking into account the effect of non-zero external shear γ.

2. The model

We use the same source models as Sliusar et al, 2009; Sliusar et al, 2013; these models can be uniquely characterized by the half-brightness radius $R_{1/2}$, which is different from the size parameter R below. The simplest and most widely used is Gaussian model (GS):

$$I_G(r) = \pi^{-1} R^{-2} \exp\left[-(r/R)^2\right].$$

Limb-darkening (LD) model is:

$$I_{LD}(r) = (q+1)\pi^{-1} R^{-2}\, \Xi(r/R; q),$$

where $\quad \Xi(\xi; q) = \Theta(1-\xi^2)(1-\xi^2)^q, \quad q \geq 0.$
The power-law (PL) models ($p > 1$):

$$I_{PL}(r) = (p-1)\pi^{-1} R^{-2}\left[1 + r^2/R^2\right]^{-p}.$$

The accretion disk (AD) of Shakura-Sunyaev (1973) has the (normalized) brightness distribution $I_{AD}(r) = 3R\theta(r-R)(2\pi r^3)^{-1}[1 - \sqrt{R/r}]$, R being the radius of the inner edge of the accretion disk.

Here we assume zero optical depth of a continuous matter. In this case the lens equation is as follows:

$$\mathbf{y} = \mathbf{A}\mathbf{x} - \sum_{i=1}^{N} R_i^2 \frac{\mathbf{x} - \mathbf{x}_i}{|\mathbf{x} - \mathbf{x}_i|^2} \qquad (1)$$

where $\mathbf{x}_i$ is the angular position of the i-th microlens on the sky, R_i is its angular Einstein ring radius; $\mathbf{A} = diag\{1 - \gamma, 1 + \gamma\}$ is the 2-dimensional external shear matrix.

To simulate the light curves we have used the "ray-shooting" method with direct calculation of each deflection angles. The parameters of numerical simulations along with are as follows. The total number of point masses is about 12000. The masses of the point lenses were distributed according to the Salpeter law in the interval $0.2 \sim 10\,M_{Sun}$ with index -2.35. The microlens positions were chosen in a random way with uniform distribution over the lens plane. The length of source trajectory has been chosen long enough to have enough the caustic crossings events (far from the boundaries of the field), and the size of the microlensing field was chosen large enough to avoid boundary effects. As a rule we generated hundred realisations of the microlensing field and, correspondingly, 100 light curves. To compare the light curves for different source models we used the relative difference

$$\eta = 2 \max_t \left(\frac{|K_i(t) - K_j(t)|}{K_i(t) + K_j(t)} \right) \qquad (2)$$

where $K_i(t)$ and $K_j(t)$ is amplification for i-th and j-th model respectively along the trajectory of source, which moves uniformly.

3. Results

We present the results of simulations for source models with the same half-brightness radius $R_{1/2} = 0.21$. The index for the "long range" PL model was $p = 3/2$; Shakura-Sunyaev (1973) accretion disk also corresponds to this class of the power-law asymptotic dependence for large distances from the center. For LD model we have chosen $q = 1$.

The results are mainly analogous to that of Alexandrov et al, 2011; Sliusar et al, 2009; Sliusar et al, 2013; see also Zhdanov et al (2012). We do not see a considerable changes of η for different value of the shear from the interval $\gamma = 0 \div 0.5$. However, there is a tendency of diminishing η with γ, which is slightly different for different directions of the source motion. We expect that this tendency will be even larger for larger values of γ.

We note that the maximum difference between the light curves corresponding to different models is within the reach of the photometrical measurements. However it must be taken into account that (i) this is a statistical result "in principle", which appeals to a long-term observations, and (ii) we used simplified source models that can differ greatly from the real source picture. For

Table 1: Relative difference η between the light curves for different source models. Motion of the source is orthogonal to the direction of the shear. The accuracy of statistical simulation for η is < 0.002.

Models	$\gamma = 0.1$	$\gamma = 0.3$	$\gamma = 0.5$
GS-PL	0.101	0.095	0.059
GS-LD	0.089	0.078	0.033
GS-AD	0.097	0.088	0.049
PL-LD	0.117	0.103	0.059
PL-AD	0.041	0.042	0.040
LD-AD	0.120	0.105	0.056

Table 2: Relative difference η between light curves with different source models. Motion of the source is directed along the direction of the shear. The accuracy of statistical simulation for η is < 0.002.

Models	$\gamma = 0.1$	$\gamma = 0.3$	$\gamma = 0.5$
GS-PL	0.103	0.089	0.052
GS-LD	0.083	0.069	0.028
GS-AD	0.098	0.082	0.040
PL-LD	0.115	0.098	0.050
PL-AD	0.044	0.042	0.038
LD-AD	0.117	0.099	0.044

more detailed information the probability distributions of η must be added; this requires additional and longer statistical simulations.

The above results concern a comparison of different models with the same $R_{1/2}$. However, in reality we do not know what radius should be used and one may ask why not to fit a light curve with a different size parameters of different models. Therefore, we must check whether we can replace one model with a different one with some other source parameters to get better fitting. This check has been carried out by Sliusar (2013); it has been shown that, at least for the involved values of the parameters, the results are almost the same as for the models with equal $R_{1/2}$.

References

Alexandrov A.N., Sliusar V.M., Zhdanov V.I.: 2011, *Ukrainian Journ. Phys.*, **56**, 389.

Alexandrov A.N., Zhdanov V.I.: 2011, *MNRAS*, **417**, 541.

Grieger B., Kayser R., Refsdal S.: 1988, *Astron. Astrophys.*, **194**, 54.

Mortonson M.J., Schechter P.L., Wambsganss J.: 2005, *ApJ*, **628**, 594.

Schneider P., Ehlers J., Falko E.E.: 1992, *Gravitational Lenses* (New York, Springer).

Shakura N.I., Sunyaev R.A.: 1973, *Astron. Astrophys.*, **24**, 337.

Sliusar V.M., Alexandrov A.N., Zhdanov V.I.: 2009, *Visnyk KNU (Astronomy)*, No. **45**, 29.

Sliusar V.M., Zhdanov V.I., Alexandrov A.N.: 2013, *Journ. Phys. Stud.*, **16**, No. **3**, 3904.

Zhdanov V., Alexandrov A., Fedorova E., Sliusar V.: 2012, *ISRN Astron. Astrophys.*, **2012**, ID 906951.

COSMOLOGY, COSMOMICROPHYSICS AND GRAVITATION

DIFFERENT APPROACHES FOR DARK MATTER HALOS OF CLUSTERS OF GALAXIES

R. Brilenkov [1], M. Eingorn [2], A. Zhuk [3]

[1] Department of Theoretical Physics, Odessa National University,
 st. Dvoryanskaya 2, 65082 Odessa, Ukraine, *ruslan.brilenkov@gmail.com*
[2] CREST and NASA research centers,
 North Carolina Central University, Duhram, NC, U.S.A.
 maxim.eingorn@gmail.com
[3] Astronomical Observatory, Odessa National University,
 Shevchenko Park, 65014, Odessa, Ukraine, *ai.zhuk2@gmail.com*

ABSTRACT. To describe the density profile of dark matter halos of clusters of galaxies, we compare the approach based on the Schwarzschild-de Sitter metric with a recently developed mechanical one (discrete cosmology inside the cell of uniformity). In the first approach, the cosmological effects are completely incorporated into the cosmological constant, while in the second one the scale factor enters directly the corresponding equations. Hence, in the latter case we can take into account the effect on the density profiles not only the cosmological constant, but also other material components. Thus, we can evaluate how this dynamic impact is considerable and testable.

Key words: Dark matter; galaxy cluster.

1. Introduction

It is known, that our expanding Universe is well described by the isotropic and homogeneous Friedmann model on scales larger than the cell of uniformity which is of the order of 190 Mpc. The modern realization of this scenario is the ΛCDM model. However, according to astronomical obsevations, there is no clear evidence of spatial homogeneity inside the cell of uniformity. Here, the Universe consists of a set of discrete inhomogeneities (galaxies, groups and clusters of galaxies) which disturb the background Friedmann model. Hence, on such scales, classical mechanics of discrete objects provides more adequate approach than hydrodynamics.

2. Halo density profiles

According to the mechanical approach developed in the recent series of papers [1-3], the radius R_H of the zero acceleration sphere around a cluster of galaxies of the mass m is:

$$R_H{}^3 = \frac{G_N m}{\ddot{a}/a}, \frac{\ddot{a}}{a} = H_0^2\left(-\frac{1}{2}\Omega_M\frac{a_0^3}{a^3} + \Omega_\Lambda\right) > 0,$$

where the second formula represents the well-known second Friedmann equation for the scale factor a(t); dots denote the derivatives with respect to synchronous time t. We consider the late-time accelerated expansion of the Universe. Therefore, $\ddot{a}/a > 0$. In accordance with the standard ΛCDM model, the Universe is filled with the nonrelativistic dark matter (DM) characterized by the average rest mass density $\overline{\rho}$ (being constant in the comoving reference frame) and the dark energy represented by the cosmological constant Λ. We focus our attention on the isothermal profile which is spherically symmetric density profile of dark matter in halo of the form

$$\rho(R) = \rho_1\left(\frac{R_1}{R}\right)^2, \rho_1 = const, R_1 = const, \rho_1 = \rho(R_1)$$

For this distribution, the gravitational potential is

$$\Phi_{\Lambda CDM}(R) = -\frac{\ddot{a}}{a}\left(\frac{R^2}{2} - R_H^2 + \frac{R_H^3}{R}\right) + 4\pi G_N\rho_1 R_1^2\ln\frac{R}{R_H} -$$

$$-4\pi G_N\rho_1 R_1^2\left(1 - \frac{R_H}{R}\right) - \frac{G_N m}{R_H}$$

Here, we use the discrete cosmology approach where the background metrics is the Friedmann one. On the other hand, if the background metric is the Schwarzschild-de Sitter one, we obtain:

$$\Phi_\Lambda(R) = \frac{8\pi G_N}{3}\rho_\Lambda\left(\frac{R_\Lambda}{R}\right)^2\ln\frac{R}{R_\Lambda} - \frac{4\pi G_N}{3}\rho_\Lambda - \frac{G_N m}{R_\Lambda}$$

Obviously, this expression is quite different from the previous one.

3. Conclusions

We found gravitational potentials for the isothermal halo density profiles in the case of two different approaches. This gives us an opportunity to consider motion of test massive bodies taking into account both gravitational attraction to inhomogeneities and cosmological expansion of the Universe. The comparison with observations should allow us to determine which approach best fits the experimental data.

References

Eingorn M., Zhuk A.: 2012, arXiv:1205.2384.
Eingorn M., Kudinova A., Zhuk A.: 2013, arXiv:astro-ph/1211.4045.
Eingorn M., Zhuk A.: 2014, arXiv:astro-ph/1309.4924.

COSMOLOGICAL PERTURBATIONS IN PRESENCE OF SCALAR FIELDS

A.Yu. Burgazli[1], M.V. Eingorn[2], A.I. Zhuk[3]

[1] Department of Theoretical Physics, Odessa National University
42, Pastera Str, Odessa 65082 Ukraine, *dtp@onu.edu.ua*

[2] North Carolina Central University, Durham, United States
1801 Fayetteville Rd, Durham, NC 27707, USA

[3] Astronomical Observatory, Odessa National University
T.G.Shevchenko Park, Odessa 65014 Ukraine, *astro@paco.odessa.ua*

ABSTRACT. We investigate the role of the scalar field assuming its presence at late stages of the Universe evolution together with dust presented by a system of an arbitrary number of gravitating masses (galaxies, groups of galaxies and clusters of galaxies) and the cosmological constant in the framework of the theory of scalar cosmological perturbations. In particular, we discuss the case of the homogeneous scalar field and its possible influence on the gravitational potentials representing metric perturbations. We also focus attention on the interconnection between the astrophysical problem and the cosmological one in the scalar field presence.

Key words: Dark energy, gravitational potential, inhomogeneous Universe, perturbations, phantom, scalar fields, quintessence

1. Introduction

The acceleration of the Universe expansion was discovered little bit more than a decade years ago and was awarding of the Nobel Prize in 2011. There are a large number of attempts to explain the reasons of the acceleration and the most prefable model for today is the ΛCDM model. There the cosmological constant is responsible to answer for the accelerated expansion. However, there are problems connected with the Λ term like the regulation mechanism which can not offset naturally huge vacuum energy down to the cosmologically acceptable value and to solve the conjuction problem of close magnitudes of the non-compensated remnants of the energy density and vacuuam energy of the Universe at present stage of evolution.

But the possibility of the scalar fields introducing as a matter source is well-known and it could help to solve the problems with the cosmological constant.

In previous work [1] we studied scalar fields in the form of perfect fluids. These fluids were considered as barotropic fluids with the linear equation of state (EoS) $p = \omega\rho$ ($\omega < 0$ is the parameter of the equation of state). We showed that, to be compatible with the scalar field perturbations theory, the parameter of the equation of state should be $\omega = -1/3$ and this perfect fluid should be clustered. Such fluids are called quintessence and phantom for $-1 < \omega < 0$ and $\omega < -1$, respectively. Usually they have a time varying parameter ω of the equation of state, but the models with constant ω are also popular for consideration.

In particular, the value $\omega = -1/3$ corresponds to the frustrated network of cosmic strings and $\omega = -2/3$ to the frustrated network of domain walls, but the last one is ruled out for our work.

2. The models with constant ω

The investigation of the viability of the models with constant ω is of interest to answer the question whether such models are an alternative to the cosmological constant. We consider the compatibility of these models with the scalar perturbations of the Friedmann-Robertson-Walker metrics. In the conformal Newtonian gauge, such perturbed metrics is

$$ds^2 \approx a^2 \left[(1 + 2\Phi)d\eta^2 - (1 - 2\Psi)\gamma_{\alpha\beta}dx^\alpha dx^\beta \right], \quad (1)$$

where scalar perturbations $\Phi, \Psi \ll 1$ and, following the standart argumentation, we can put $\Phi = \Psi$.

We consider the Universe at late stages of its evolution when galaxies, clusters and groups of galaxies are already formed (also the peculiar velocities of inhomogeneties are much less than the speed of light) and deep inside of the cell of uniformity where the Universe is highly inhomogeneous. The perturbations of perfect fluids with $\omega = const$ are purely adiabatic, i.e. the dissiparive processes are absent. We neglect the

the contribution of radiation, therefore, the Friedmann equations read

$$\frac{3\left(\mathcal{H}^2 + \mathcal{K}\right)}{a^2} = \kappa \overline{T}_0^0 + \Lambda + \kappa \overline{\epsilon} \qquad (2)$$

and

$$\frac{2\mathcal{H}' + \mathcal{H}^2 + \mathcal{K}}{a^2} = \Lambda - \kappa \omega \overline{\epsilon}, \qquad (3)$$

where $\mathcal{H} \equiv a'/a \equiv (da/d\eta)/a$ and $\kappa \equiv 8\pi G_N/c^4$ (c is the speed of light and G_N is the Newton's gravitational constant), $\overline{T}^{ik}$ is the energy-momentum tensor of the average pressureless dustlike matter.

We show that the only one value $\omega = -1/3$ is possible for the model with constant parameter of the equation of state to be compatible with the scalar perturbations theory [2, 3]. For $\omega = -1/3$ the equation of the gravitational potential and the fluctuation of the energy density of the perfect fluid read, respectively:

$$\Delta\varphi + \left(3\mathcal{K} - \frac{9\pi G_N}{c^4}\varepsilon_0 a_0^2\right)\varphi = 4\pi G_N(\rho - \overline{\rho}) \qquad (4)$$

and

$$\delta\epsilon = \frac{2\epsilon_0 a_0^2}{c^2 a^3}\varphi. \qquad (5)$$

We investigate the dependence on the curvature parameter $\mathcal{K}$ and showed that reasonable expressions of the conformal gravitational potential φ exist for any sign of $\mathcal{K}$. If the perfect fluid is absent, the hyperbolic space is preferred.

3. The models with time-varying ω

We consider the case of fluids with the varying parameter ω (e.g., scalar fields with arbitrary potentials). The system of the equations of scalar perturbations, following the standart argumantation $\Phi = \Psi$ and taking into account the possible contributions of the spatial curvature as well as of the dust, read:

$$\Delta\Phi - 3\mathcal{H}(\Phi' + \mathcal{H}\Phi) + 3\mathcal{K}\Phi = \frac{\kappa}{2}a^2\delta\epsilon_{dust} -$$

$$\frac{\kappa}{2}\left[(\phi_c')^2\Phi - \phi_c'\varphi' - m^2 a^2\phi_c\varphi\right], \qquad (6)$$

$$\partial_i\Phi' + \mathcal{H}\partial_i\Phi = \frac{\kappa}{2}\phi_c'\partial_i\varphi, \qquad (7)$$

$$\frac{2}{a^2}\left[\Phi'' + \mathcal{H}\Phi' + \Phi\left(2\frac{a''}{a} - \mathcal{H}^2 - \mathcal{K}\right)\right] =$$

$$\kappa\left[-\frac{1}{a^2}(\phi_c')^2\Phi - \phi_c'\varphi' - m^2\phi_c\varphi\right]. \qquad (8)$$

Considering of the case $\varphi = 0$ gives the result for the potential:

$$V = \frac{\beta^2}{a^2} + C, \qquad (9)$$

where $\beta = \phi_c'$.

Taking into account the possible contributions of radiation also, we obtained the Friedmann equations

$$\frac{2\mathcal{H}' + \mathcal{H}^2 + \mathcal{K}}{a^2} = \Lambda - \kappa p_{rad} - \kappa p_{\varphi}, \qquad (10)$$

$$\frac{3(\mathcal{H}^2 + \mathcal{K})}{a^2} = \Lambda + \kappa\epsilon_{dust} + \kappa\epsilon_{rad} + \kappa\epsilon_{\varphi}. \qquad (11)$$

From the equation (6), including the contribution of radiation, and the Friedmann equations it follows the equation for definition of the field's fluctuation and gravitational potential.

$$\Delta\Phi - 3\mathcal{H}(\Phi' + \mathcal{H}\Phi) + 3\mathcal{K}\Phi =$$

$$\frac{\kappa}{2}\frac{\delta\rho c^2}{a} - \frac{\kappa}{2}\left[(\phi_c')^2\Phi - \phi_c'\varphi' - a^2\frac{dV}{d\phi}(\phi_c)\varphi\right]. \qquad (12)$$

4. Conclusions

We considered the Universe on the late stage of its evolution and deep inside of the cell of uniformity. Supposing that the Universe contains also the cosmological constant and a perfect fluid with a negative parameter of the equation of state ω, we investigated scalar perturbations of the FRW metrics due to inhomogeneities. We have got that, to be compatible with the theory of scalar perturbations in the case of constant parameter of EoS, this fluid should be clustered and should have the parameter parameter of the equation of state $\omega = -1/3$. It is concentrated around the inhomogeneities and results in screening of the gravitational potential. Such perfect fluid neither accelerates not decelerate the Universe, but the presence of it helps to resolve the Seeliger paradox for any sign of the spatial curvature parameter $\mathcal{K}$. Such perfect fluid can be simulated by scalar fields with the corresponding form of the potentials as well as by the frustrated network of topological defects.

For the scalar fields with the arbitrary potentials (and dust and radiation as additional matter sources) we got the equation for the defenition of the field's fluctuation and gravitational potential. It gives us possibility to study the dynamics of inhomogeneities of the Universe inside of the cell of uniformity.

References

Burgazli A.Yu., Eingorn M.V., Zhuk A.I.: 2014, *astro-ph/1301.0418v2*.

Eingorn M., Zhuk A.I.: 2012, *JCAP*, **09**, 026.

Eingorn M., Zhuk A.I.: 2014, *JCAP*, **09**, 024.

ENVIRONMENTAL PROPERTIES OF GALAXIES AT $Z < 0.1$ FROM THE SDSS VIA THE VORONOI TESSELLATION

D.V. Dobrycheva[1*], O.V. Melnyk[2,3], I.B. Vavilova[1], A.A. Elyiv[1,3]

[1] Main Astronomical Observatory of the NAS of Ukraine, Kyiv, Ukraine
[2] Astronomical Observatory, Taras Shevchenko National University of Kyiv, Ukraine
[3] Dipartimento di Fisica e Astronomia, Universita di Bologna, Italy
*daria@mao.kiev.ua

ABSTRACT. The aim of our work was to investigate the environmental density of galaxies from the SDSS DR9 at $z < 0.1$ using the 3D Voronoi tessellation. The inverse volume of the Voronoi cell was chosen as a parameter of local environmental density. We examined a density of given bright galaxy taking into account its faint satellites located in the Voronoi cell. We found that with the increase of total galaxy density around the central bright galaxy, the probability that it has the early type is increasing.

Key words: data analysis; surveys; galaxies.

1. Introduction

Many studies have confirmed that galaxy morphology and environment are correlated. The fraction of the early type galaxies is higher in regions with elevated concentrations of galaxies, while the late type galaxies predominate in the general field (Dressler 1980; Einasto et al. 2003, Blanton et al. 2005, Vavilova et al. 2009). However, the basic galaxy properties at first depend strongly on galaxy mass (nature) and then on their environments (nurture; Peng et al. 2010). In this work we examined an environmental density of galaxies from SDSS DR9 at $z < 0.1$ using 3D Voronoi tessellation (Melnyk et al. 2006; Elyiv et al. 2009; see, also, Kim et al. 2000; Ramella et al. 2001; Wilman et al. 2010; Way et al. 2011; Soares-Santos et al. 2011; Zaninetti 2012).

2. Sample and Method

The detail description of the studied galaxy sample was presented in Dobrycheva (2013). We note here that the initial sample included 724 000 objects from SDSS DR9 with $z < 0.1$. After the removing of stars and duplicates as well as applying the limits on redshift, $0.02 < z < 0.1$, and apparent magnitude, $m_r < 17.7$, the studied sample contains 260 000 galaxies.

The application of the Voronoi tessellation requires that the galaxy sample should be as much homogeneous as possible. By this reason we limited the
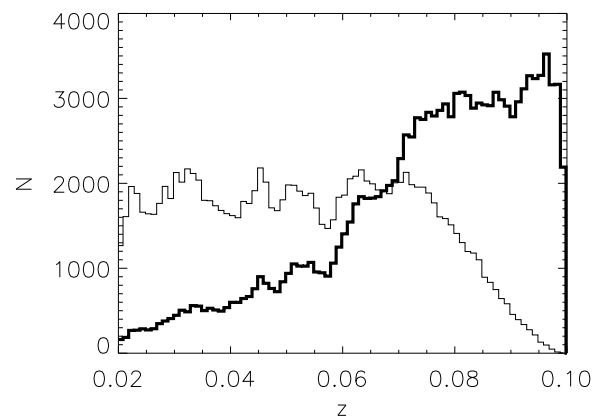
Figure 1: The redshift distribution for the central bright galaxies (thick line) and faint satellites (thin line).

SDSS sample by the absolute magnitude $M_r < -20.7$ ($N \sim 124000$). Then, for these bright central galaxies we applied 3D Voronoi tessellation method. We examined the properties of the environment near the central bright galaxies taking into account its faint satellite galaxies with $M_r > -20.7$ ($N \sim 136000$). Their distributions by z are shown in Fig. 1.

The absolute galaxy magnitude was corrected for the Galactic absorption *ext* by Schlegel et al. (1998) and K-correction $K(z)$ according to Chilingarian (2010): $M_r = m_r - 5 * log(V/H_0) - 25 - K(z) - ext$. We characterised the local environment density of galaxies by the inverse value of the Voronoi cell volume: $N = (n+1)/V$, where $n+1$ is the total number of galaxies (n faint and 1 bright galaxies) inside the Voronoi cell having the volume V. All galaxies from the studied sample were morphologically classified according to the criteria proposed by Melnyk et al. (2012) using the colors $(g - i)$ and inverse concentration $R50/R90$ indices.
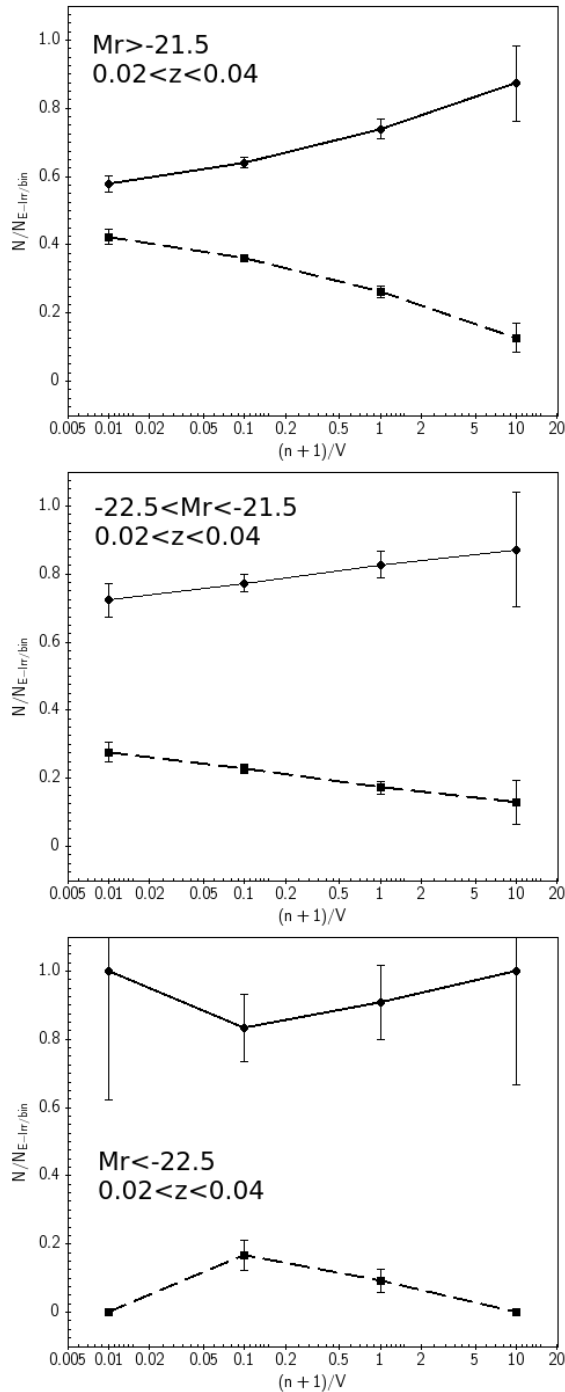
Figure 2: Distribution of galaxies according to their environmental density in the Voronoi cells: $(n + 1)/V$, where n is the number of faint satellite galaxies with $M_r > -20.7$, V is the volume of Voronoi cell. Types of $E - S0$ (solid line) and $Sa - Irr$ (dotted line) correspond to the central bright galaxies, which are the nuclei of the corresponding Voronoi cells. Number of galaxies in each bin is normalized by the total number of central bright galaxies $E - Irr$ in the corresponding bin $(n + 1)/V$. The absolute magnitude ranges noted in the figures correspond to the central bright galaxies.

3. Results

Fig. 2 shows the distribution of the early $E - S0$ (solid line) and $Sa - Irr$ (dashed line) type central bright galaxies by the inverse value of the Voronoi cell volume in four intervals: $(n + 1)/V < 0.01$, $0.01 < (n + 1)/V < 0.1$, $0.1 < (n + 1)/V < 1$, $(n + 1)/V > 1$. The number of galaxies is normalized to the total number of galaxies $E - Irr$ in the sample in the corresponding range of $(n + 1)/V$. We were able to analyse the environmental density of galaxies only in the $0.02 < z < 0.04$ interval because of the number of faint galaxies are dramatically decreases with z (Fig. 1). Namely, we clearly see in Fig. 2 that with increasing the environmental density, the proportion of the early type central galaxies is increasing, while the proportion of the late type galaxies is decreasing.

It allows to conclude that the early type galaxies are located in denser environments than the late type galaxies; moreover, the brighter the central galaxies, the greater the proportion of early types in the subsample. The detailed comparison of the environmental density of galaxies versus the magnitude, color, and morphological type of the central bright galaxy is presented in Dobrycheva et al. (2015).

References

Blanton M.R., Eisenstein D., Hogg D.W. et al.: 2005, *Aph. J.*, **629**, 143.

Chilingarian I., Melchior A.-L., Zolotukhin I.: 2010, *MNRAS*, **405**, 1409.

Dobrycheva D.V.: 2013, *Odessa Astron. Publ.*, **26**, 187.

Dobrycheva D.V., Melnyk O.V., Elyiv A.A. et al.: 2015, *Astrophysics, in prep.*

Dressler A.: 1980, *Aph. J.*, **236**, 351.

Einasto M., Einasto J., Muller V. et al.: 2003, *A&A*, **401**, 851.

Elyiv A.A., Melnyk O.V., Vavilova I.B.: 2009, *MNRAS*, **394**, 1409.

Kim R.S.J., Strauss M.A., Bahcall N.A.: 2000, *ASP Confer.Ser.*, **200**, 422.

Melnyk O.V., Dobrycheva D.V., Vavilova I.B.: 2012, *Astrophysics*, **2**, 293.

Melnyk O.V., Elyiv A.A., Vavilova I.B.: 2006, *Kinemat. Fiz. Nebesn. Tel*, **22**, 283.

Peng Y.-J., Lilly S.J., Kovac K.: 2010, *Aph.J.*, **721**, 193.

Ramella M., Boschin W., Fadda D. et al.: 2001, *A&A*, **368**, 776.

Schlegel D.J., Finkbeiner D.P., Davis M.: 1998, *Aph.J.*, **500**, 525.

Soares-Santos M., de Carvalho R.R., Annis J. et al.: 2011, *Aph.J.*, **727**, 45.

Vavilova I.B., Melnyk O.V., Elyiv A.A.: 2009, *Astron. Nachr.*, **330**, 1004.

Way M.J., Gazis P.R., Scargle J.D.: 2011, *Aph.J.*, **727**, 48.

Wilman D.J., Zibetti S., Budavri T.: 2010, *MNRAS*, **406**, 1701.

Zaninetti L.: 2012, *RMxAA*, **48**, 209.

THE ASYMMETRIC DRIFT AND THE ROTATION CURVE OF THE GALAXY

O.Golubov[1,2,3]

[1] Institute of Astronomy of V. N. Karazin Kharkiv National University,
35 Sumska Str., 61022, Kharkiv, Ukraine, *golubov@astron.kharkov.ua*
[2] School of Physics and Technology, V. N. Karazin Kharkiv National University,
Svobody Sq. 4, 61022, Kharkiv, Ukraine
[3] Department of Aerospace Engineering Sciences, University of Colorado at Boulder,
429 UCB, Boulder, CO, 80309, USA.

ABSTRACT. Asymmetric drift in the solar neighbourhood is studied by the means of the RAVE data. The asymmetric drift correction is applied to the SDSS data to measure the rotation curve of the Milky Way in the extended solar neighbourhood. The rotation curve is flat between 7 and 10 kpc. Via fitting this flat rotation curve, and the inner rotation curve determined through tangent point method, density model of the Milky Way is constructed.

Key words: Galaxy: dynamics – Galaxy: disk

1. Introduction

The rotation curve of the Milky Way provides a powerful tool for constraining the density model of our galaxy.

Here for our studies we use two data samples: over 600,000 stars from RAdial Velocity Experiment, or RAVE (Siebert et al. 2011) and over 20,000 stars from Sloan Digital Sky Survey, or SDSS (Lee et al. 2011). For both samples we have spectroscopic data, which allow to reconstruct stellar models and thus to measure distances to the stars via photometric parallaxes. Knowing also radial velocities from spectroscopy, coordinates on the celestial sphere and proper motions, we have all 3 spatial coordinates and all 3 components of velocity necessary for our analysis.

In Section 2 we discuss the asymmetric drift, which must be accounted for to construct the rotation curve. In this analysis we use the RAVE data sample. In Section 4 we apply the asymmetric drift correction to the SDSS data to construct the rotation curve of the Milky Way in the extended solar neighbourhood. In Section 5 we use the rotation curve to get the density model of the Milky Way. Finally, in Section 6 we outline the major results of our work.

2. Asymmetric Drift

The asymmetric drift is the difference between the mean rotation velocity v_φ of a stellar population and the actual circular velocity v_c. It is governed by the Jeans equation

$$v_c^2 = \bar{v}_\phi^2 + \sigma_\phi^2 - \sigma_R^2 - \frac{R}{\rho}\frac{\partial\left(\rho\sigma_R^2\right)}{\partial R} - R\frac{\partial\left(\overline{v_R v_z}\right)}{\partial z} \quad (1)$$

where R, φ, and z are cylindrical coordinates, v_R, v_φ, and v_z are corresponding velocities, σ_R, σ_φ, and σ_z are velocity dispersions, and ρ is stellar density.

To simplify the equation, we use several assumptions:
1. Exponential disc with the radial scale length R_d;
2. Constant shape of the velocity ellipsoid, $\sigma_R \sim \sigma_\varphi \sim \sigma_z$;
3. Stellar density proportional to squared velocity dispersion, $\rho \sim \sigma_R^2$, which together with the former assumption corresponds to constant thickness of the stellar disc;
4. Alignment of principal axes of velocity ellipsoid with coordinate directions of spherical coordinates.
5. The asymmetric drift is small, $\left|v_c - \bar{v}_\varphi\right| << v_c$.

These assumptions allow to re-write Eq. (1) in the following way

$$\bar{v}_\varphi = v_c - \left(\frac{2R}{R_d} - 2 + \frac{\sigma_\varphi^2}{\sigma_R^2} + \frac{\sigma_z^2}{\sigma_R^2}\right)\frac{\sigma_R^2}{2v_c} \quad (2)$$

According to our assumptions, the term in the brackets does not depend on σ_R. Thus if we plot $\bar{v}_\varphi$ as function of σ_R^2, we must get a linear dependence.

Equation (2) was applied by Golubov et al. (2013) to the RAVE data sample. The data were binned in metallicities, and each metallicity had its own dependence of the asymmetric drift on σ_R^2. All these dependences were consistent with the linear law Eq. (2) with different scalelengths R_d for different metallicities. The best fit local standard of rest velocity was in a good agreement with Dehnen & Binney (1998). If we assumed the local standard of rest by Schönrich et al. (2010) instead, the scalelengths R_d appeared to depend on σ_R^2.

3. Rotation Curve

The asymmetric drift correction studied in Section 2 is applied to the SDSS data sample from Lee et al. (2011). The applicability of this correction is checked via comparing the asymmetric drift measured for three different metallicity bins of the SDSS sample to the corresponding metallicity bins of RAVE. The asymmetric drift follows the same trend, which justifies the same asymmetric drift correction.

This results into a rotation curve at Galactocentric radii 7 kpc $< R <$ 10 kpc. The rotation curves built for three populations of different metallicities are consistent with each other. The rotation curve is flat (Golubov & Just 2013a, Golubov et al. 2012), and does not demonstrate any dips similar to the ones assumed by Sofue et al. (2009).

4. Density Model

We apply the rotation curve to construct the density model of the Milky Way. When fitting the density model, we constrain ourselves with the local stellar density and dark matter density in the solar neighbourhood, as they were determined by Just & Jahreiß (2010). The rotation curve used for fitting is composed of the inner rotation curve determined via tangent point method, supplemented by flat rotation curve in the extended solar neighbourhood (Golubov & Just 2013a).

As the result of such fitting we get a density model of the Milky Way, consisting of Dehnen bulge, exponential disc with a hole, and flattened cored isothermal dark matter halo. Using NFW profile instead of cored isothermal halo is also consistent with the data, although provides a slightly worse fit (Golubov & Just 2013b).

5. Results

RAVE data were used to study the asymmetric drift. They were consistent with the linear dependence of $\bar{v}_\phi$ on

σ_R^2, and better consistent with the old local standard of rest by Dehnen & Binney (1998), than with the new one by Schönrich et al. (2010). Dependence of the asymmetric drift on metallicity was also analysed, resulting into smaller radial scalelength for more metal-poor populations.

The rotation curve turned to be flat in the extended solar neighbourhood.

We have built a density model of the Milky Way, which was flat in the extended solar neighbourhood, consistent with the inner rotation curve derived by tangent-point method, and with the local density constraints.

References

Dehnen W. & Binney J.J.: 1998, *MNRAS*, **298**, 387.
Golubov O. et al.: 2013, *A&A*, **557**, 92.
Golubov O. & Just A.: 2013a, *Proceedings of the International Astronomical Union*, **295**, 231.
Golubov O. & Just A.: 2013b, *Proceedings of the International Astronomical Union*, **292**, 101.
Golubov O. et al.: 2012, *EPJ Web of Conferences*, **19**, id.01006.
Just A. & Jahreiß H.: 2010, *MNRAS*, **402**, 461.
Just A. et al.: 2012, *EPJ Web of Conferences*, **19**, id.01007.
Lee Y.-S. et al.: 2011, *ApJ*, **738**, 187.
Schönrich R. et al.: 2010, *MNRAS*, **403**, 1829.
Siebert A. et al.: 2011, *AJ*, **141**, 187.
Sofue et al.: 2009, *PASJ*, **61**, 283.

MORPHOLOGICAL TYPES OF 254 RICH PF GALAXY CLUSTERS

E.A. Panko[1], A.M. Andrievsky[2], A.V. Gotsulyak[2]

[1] V.O. Suckomlinsky Nikolaev National University,
Nikolaev, Ukraine *panko.elena@gmail.com*

[2] Astronomical Department, Odessa National University, Odessa, Ukraine

ABSTRACT. We determined the morphological types for 254 rich galaxy clusters from the PF Catalogue of Galaxy Clusters and Groups. The data set contains the PF galaxy clusters, which have no ACO coinciding ones. The applied morphological scheme was combined of the prevalent classifications, such as Bautz-Morgan, Rood-Sastry etc approaches. We assigned the morphological types using numerical criteria and taking into consideration concentration to the cluster center, the signs of preferential direction or plane in the cluster, and the positions of the brightest galaxies. The features of the data set are discussed.

Key words: Galaxies: clusters: morphological types.

1. Introduction

The morphological types of galaxy clusters resulting from their outward appearance are physically related to the clusters and their member galaxies. It was reflected in different morphological schemes beginning from Abell (1958) and Zwicky et al.(1961-1968) papers. The classification characteristics took into consideration several different parameters: cluster richness (number of galaxies within a specific limiting magnitude), the central concentration, the presence of bright galaxies in the center of the cluster, the presence of peculiar galaxies, etc. The prevalent Bautz-Morgan (BM) classification scheme (Bautz & Morgan, 1970) is based on the relative contrast (dominance in extent and brightness) of the brightest galaxy to other galaxies in the cluster, ranging from type I to III in decreasing order of dominance. The Rood-Sastry (RS) system (1971) classifies clusters based on the geometry of the distribution of the ten brightest members (from cD, to binary B, core C, line L,flat F, and irregular I). The Rood-Sastry and Bautz-Morgan schemes are in agreement and complement each other. López-Cruz at al. (1997) and López-Cruz & Gaztanaga (2001) introduced the definition of a cD cluster, the complement to this class is called a non-cD cluster.

Panko (2013) proposed the morphological scheme accordingly to features of "The Catalogue of Galaxy Clusters and Groups" (Panko & Flin, 2006, hereafter PF). The morphological scheme combines the prevalent BM and RS approaches. The new scheme bases on the numerical criteria and takes into consideration both concentration to the cluster center and the signs of the presence of preferential direction or plane (hereafter flatness). Addition parameter – the role of Bright Cluster Members or cD galaxy presence was included to scheme too. The new morphological scheme was tested in the region $11° \times 16°$ centered to supercluster SCL 184 (Einasto et al., 1997) and contained 175 PF galaxy clusters with different richness (Panko, 2013).

2. Rich PF galaxy clusters and their morphology

The PF Catalogue was constructed on Münster Red Sky Survey Galaxy Catalogue (Ungrue et al., 2003, hereafter MRSS) as the observational basis. MRSS galaxies have no redshifts, unfortunately. Nevertheless, the list of clusters with all MRSS galaxies in the each cluster field allows to study the large-scale structures properties by statistical methods. From comparison positions of PF and ACO clusters (Abell, Corwin, Olowin, 1989) for 1056 PF objects with different richness BM morphological types were assumed. But only 247 such clusters are rich and have number of galaxies in its field ($N_g \geq 100$).

Panko et al. (in preparation) determined the morphological types according Panko (2013) criteria for the 247 rich PF galaxy clusters having assumed BM types. The map of galaxy positions in rectangular coordinates was constructed for each cluster. The new types were assigned corresponding to concentration (C - compact, I - intermediate, and O - open), flatness (L - line, F - flat, and no symbol if no indication of flatness is present), and the role of bright galaxies (cD or BG if the BCM role is significant). Other peculiarities were noted as P. The designations can be combined, for example CFcD or ILP. From analysis of the each
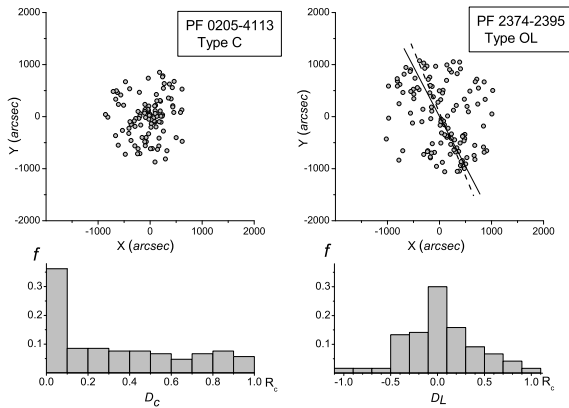
Figure 1: Galaxy clusters C and OL type and distribution of distance from cluster center D_c and from preferential line D_L of galaxies in the clusters (dashed line). The direction of the major axis od the PF 2374-2395 best-fitted ellipse is shown as solid line.

type frequencies it was shown:

– the sign of the flatness type is independent of concentration;

– role of BCMs is strongly connected with cluster concentration: the number of cD clusters is greatest in C-type;

– for L and F clusters a correlation between position angle for the major axes of the best-fit ellipse and the direction of the preferred plane was noted.

254 rich clusters without analogues in ACO catalogue were classified by the same way in present paper. Two cluster maps and their distribution of crucial distances in fractions of the mean cluster radius R_c are shown in Fig. 1. For C type cluster the distance from cluster center is decisive factor, and for PF 0205-4113 36% of galaxies placed inside of $0.1R_c$. For OL type cluster the distance to preferential line (dashed line in Fig. 1) is selected as decisive factor and 30.5% of galaxies concentrate in the $0.1R_c$ wide strip centered to the line. The direction of preferential line and major axis of the cluster best-fitted ellipse are close one to another, according to expectations.

The general difference in morphology of the two data sets is the frequency of clusters with strong structure. The number of C and LF types is significantly less between clusters without ACO analogues. We can explain it by the observational selection: open galaxy clusters in the magnitude range from 14^m to $18.^m3$ were lost.

3. Conclusion

We determined the morphological types using the numerical criteria for 254 rich PF galaxy clusters without ACO analogues. All types founded in another data set – 247 rich PF galaxy clusters having ACO analogues – are present in the new data set too. All criteria are correct and can be used in future work. The presence of preferential plane or direction in some clusters is statistically significant. Full rich PF cluster list with morphological types contains more than 500 clusters, so we obtain expanded observational basis for statistical research.

References

Abell G.O.: 1958, *ApJS*, **3**, 211.
Abell G.O., Corwin H.G., Olowin R.P.: 1989, *ApJS*, **70**, 1.
Bautz P. & Morgan W.W.: 1970, *ApJ*, **162**, L149.
Einasto M., Tago E., Jaaniste J., et al.: 1997, *A&AS*, **123**, 119.
López-Cruz O., Yee H.K.C., Brown J.P., et al.: 1997, *ApJ*, **475**, L97.
López-Cruz O., Gaztanaga E.: 2001, *arXiv:astroph/ 0009028*.
Panko E.: 2013 *Odessa Astr. Publ.*, **26**, 90.
Panko E. & Flin P.: 2006, *J. Astr. Data*, **12**, 1.
Panko E., Bajan K., Flin P. et al.: (*in preparation*). In: IAUS 308 "The Zeldovich Universe. Genesis and Growth of the Cosmic Web". Eds.: R. van de Weygaert, S. Shandarin, E. Saar, J. Einasto.
Rood H.J., Sastry G.N.: 1971, *PASP*, **83**, 313.
Ungrue R., Seitter W.C., Duerbeck H.W.: 2003, *J. Astr. Data*, **9**,1.
Zwicky F., Herzog E., Wild P. et al.: 1961-1968, Catalogue of Galaxies and of Clusters of Galaxies, Pasadena, California Institute of Technology, on-line data: *http://vizier.cfa.harvard.edu/viz-bin/ VizieR?-source=VII/190*.

THE ELLIPTICITIES OF GALAXIES IN GALAXY CLUSTERS OF DIFFERENT MORPHOLOGICAL TYPE

Elena Panko[1] and Piotr Flin[2]

[1] Kalinenkov Astronomical Observatory, Nikolaev National University,
Nikolaev, Ukraine, *panko.elena@gmail.com*
[2] Institute of Physics, Jan Kochanowski University,
Kielce, Poland, *sfflin@cyf-kr.edu.pl*

ABSTRACT. The distribution of galaxy ellipticities was analyzed for 207 rich PF galaxy clusters found in the Münster Red Sky Survey Galaxy Catalogue. Clusters with BM types from a comparison with the ACO catalogue were also classified on the new scheme. The new morphological types take into consideration concentration towards the cluster center, indications of a preferential direction or plane, and the role of the brightest cluster galaxies. Differences in the distribution of galaxy ellipticities for individual clusters are statistically significant, in contrast to the average distribution of ellipticities for galaxies belonging to clusters of different morphological type. Two types of galaxy ellipticity distribution were found: single-mode and bimodal. The distributions apparently reflect different contributions from spiral and elliptical galaxies. The shapes of galaxies in individual clusters appear to relate to local conditions.

Key words: Galaxies: clusters: morphological types, galaxies: ellipticities.

1. Introduction

Rich clusters of galaxies are the most massive virialized systems known, and provide a powerful tool for the study of galaxy formation. The morphology of clusters has been studied mainly relative to bright member galaxies, with the main classification schemes by Bautz & Morgan (1970, BM) and Rood & Sastry (1971, RS) describing the relative contrast between the brightest galaxy and other galaxies in the cluster, or to the geometrical distribution of the ten brightest members, respectively. Both schemes complement each other.

From studies of 122 rich Abell clusters, van Kampen & Rhee (1990) found an alignment of cD-galaxies with their surroundings, while López-Cruz & Gaztañaga (2001) showed that cD clusters and non-cD clusters are different dynamically. Sandage & Hardy (1973) found that BM types and the absolute magnitudes of Brightest Cluster Members (BCM) are independent of cluster richness; they therefore concluded that BM types were defined by initial conditions at the onset of cluster formation rather than by later evolution. Panko et al. (2009) analyzed the relative orientations of BCM and their parent clusters for 1056 PF clusters and found statistically significant alignments in BM I clusters. Godłowski et al. (2010), using data for 97 PF galaxy clusters, also found a weak dependence of galaxy velocity dispersion with BM type for the parent cluster.

In a survey paper, Bahcall (1996) collected common properties for clusters and superclusters of galaxies. In particular, she noted the difference between the typical galactic content of clusters and the different morphological types. In regular clusters (BM types I, I-II, and II) the galactic content E:S0:Sp is 3:4:2, for intermediate clusters (BM II and II–III) the E:S0:Sp content is 2:5:3, and for open clusters (BM II–III, III) the E:S0:Sp content is 1:2:3. The distribution of galaxy ellipticities was examined by us, since it can be an indicator of the galactic content in rich clusters.

2. Observational Basis

The Münster Red Sky Survey Galaxy Catalogue (Ungrue et al. 2003, hereafter MRSS) is a large scale galaxy catalogue in the red spectral region that covers an area of 5000 square degrees to a limit of $\sim 18^{\mathrm{m}}.3$. Various parameters were determined for each galaxy image, including ellipticity. The morphological types and redshifts of the galaxies were not established.

The Catalogue of Galaxy Clusters and Groups (Panko & Flin 2006, hereafter PF) was constructed from MRSS galaxies. By comparison with the ACO catalogue (Abell, Corwin & Olowin 1989) a list was created of PF clusters of different richness that have ACO analogues, and accordingly BM types. Only 247 rich PF clusters with $N_{\mathrm{g}} \geq 100$ were in the list. Panko (2013) proposed an integrated morphological scheme to study PF galaxy clusters. The primary designations are based on numerical criteria and take
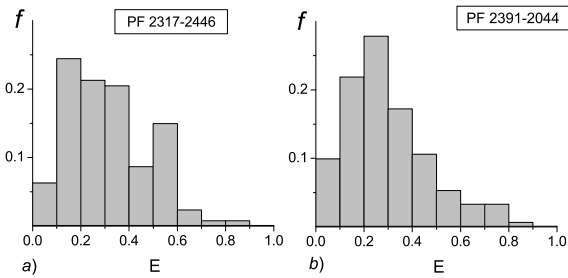
Figure 1: Bimodal and single-mode distribution of galaxy ellipticities in PF clusters of intermediate type.

Figure 2: Median distributions of galaxy ellipticities in C, I, and O clusters of L and F type.

into consideration the parameters: concentration to the cluster center (C = compact, I = intermediate, and O = open), the presence of a preferential direction or plane, hereafter flatness (L = line, F = flat, and no sign of flatness = without symbol), and the role of Bright Galaxies (cD and BG). Peculiarities are noted as P. Combined morphological types, such as CF, OFcD, IF, OF, etc., also exist. Such types were determined for 247 PF clusters by this scheme.

3. The Distribution of Galaxy Ellipticities

The distribution of galaxy image ellipticities was analyzed for individual rich PF clusters according to their morphology, excluding from the data set 40 clusters with peculiarities. An additional 207 clusters were divided into subsets containing both C, I, and O clusters of L and F type, with pure and combination types possible, such as CcD, OFBG, etc. An additional division into subsets according to BM type was also studied.

All subsets contain two kinds of ellipticity distributions: bimodal (Fig. 1a) and single-mode (Fig. 1b). Maximum frequency in single-mode clusters corresponds to bin 0.2–0.3. For bimodal clusters the main peak occurs in bin 0.1–0.2, with a secondary maximum in bins 0.4–0.6. The difference between distributions is statistically significant. The first case appears to occur in E-rich clusters, and the second in S-rich clusters. The same ellipticity distributions based on Galaxy Zoo classifications of galaxies were found by Hoyle et al. (2012); they note the difference between bulge-dominated and disk-dominated clusters. Fasano et al. (2000) found the trends in S0:E and S0:S indicated a morphological evolution; as redshift decreases, the S0 (lenticular) population tends to grow at the expense of regular spiral galaxies.

Weak signs of bimodality in the mean distributions are noted in O and IL types (Figs. 2a, 2b), but the global average distributions for all morphological types are identical (Fig. 2d). It seems that the E:S ratio in rich PF clusters does not depend on cluster morphology.
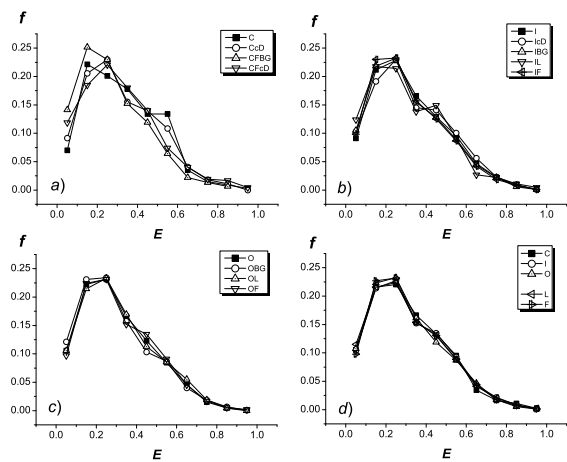
4. Conclusions

Two statistically significant types of distributions were found from analyses of galaxy ellipticities in rich galaxy clusters of different morphological type: single-mode and bimodal. The first type is present in E-rich clusters, while the second is found in S-rich clusters. Both distributions are present in all morphological types. The shapes of galaxies in individual clusters therefore appear to relate to local conditions.

References

Abell G.O., Corwin H.G., Olowin R.P.: 1989, *ApJS*, **70**, 1.
Bahcall N.: 1997, arXiv:astro-ph/9611148.
Bautz P. & Morgan W.W.: 1970, *ApJ*, **162**, L149.
Fasano G., Poggianti B., Couch W.J et al.: 2000, *ApJ*, **542**, 673.
Godłowski W., Piwowarska P., Panko E., et al.: 2010, *ApJ*, **723**, 985.
Hoyle B., Masters K.L., Nichol R.C., et al.: 2012, *MNRAS*, **423**, 3478.
López-Cruz O. & Gaztañaga E.: 2000, *ASPC*, **218**, 247.
Panko E.: 2013 *Odessa Astr. Publ.*, **26**, 90.
Panko E. & Flin P.: 2006, *J. Astr. Data*, **12**, 1.
Panko E., Juszczyk T., Flin P.: 2009, *AJ*, **138**, 1709.
Rood H.J. & Sastry G.N.: 1971, *PASP*, **83**, 313.
Sandage A. & Hardy E.: 1973, *ApJ*, **183**, 743.
Ungrue R., Seitter W.C., Duerbeck, H.W.: 2003, *J. Astr. Data*, **9**,1.
van Kampen E. & Rhee G.: 1990, *IAU Colloq.* **124**, 255.

NEUTRINO IN GRAVITATIONAL FIELD

R.M. Plyatsko, M.T. Fenyk

Pidstryhach Institute for Applied Problems in Mechanics and Mathematics
of NASU, 3-b Naukova Street, Lviv, 79060, Ukraine, *plyatskor@gmail.com*

ABSTRACT. The spin-gravity coupling for highly relativistic fermions according to the classical Mathisson-Papapetrou and quantum Dirac equations is considered. It is stressed that the behavior of fermions in the highly relativistic regime in the gravitational field is significantly different as compare to usual situations. Possible corrections to the known general relativistic Dirac equation for more adequate description of fermions in strong gravitational fields are discussed. Some numerical estimates for neutrinos with nonzero mass that is interesting in astrophysics are presented.

Key words: Dirac and Mathisson-Papapetrou equations: highly relativistic spin-gravity coupling: Lorentz-violating spinor.

The equation for a quantum particle with spin 1/2 in the gravitational field is known since 1929 when the usual Dirac equation was generalized for curved spacetime in general relativity [1]. The corresponding (in a certain sense) equations for a classical (nonquantum) spinning particle are eight years "younger" and are known as Mathisson-Papapetrou (MP) equations [2].

The traditional form of MP equations is

$$\frac{D}{ds}\left(mu^\lambda + u_\mu \frac{DS^{\lambda\mu}}{ds}\right) = -\frac{1}{2}u^\pi S^{\rho\sigma}R^\lambda_{\ \pi\rho\sigma}, \quad (1)$$

$$\frac{DS^{\mu\nu}}{ds} + u^\mu u_\sigma \frac{DS^{\nu\sigma}}{ds} - u^\nu u_\sigma \frac{DS^{\mu\sigma}}{ds} = 0, \quad (2)$$

where $u^\lambda \equiv dx^\lambda/ds$ is the particle's 4-velocity, $S^{\mu\nu}$ is the tensor of spin, m and D/ds are, respectively, the mass and the covariant derivative with respect to the particle's proper time s, and $R^\lambda_{\ \pi\rho\sigma}$ is the Riemann curvature tensor. The MP equations are considered with some supplementary condition and most often the condition $S^{\mu\nu}u_\nu = 0$ or $S^{\mu\nu}P_\nu = 0$ are used, where P_ν is the particle's 4-momentum (in general, P_ν is not parallel to u_ν). In the linear spin approximation the corresponding solutions of the MP equations coincide at the two these conditions. It is important that the MP equations can be used for the investigation of spinning particle motions with any velocity relative to the source of the gravitational field (for example, Schwarzschild's

or Kerr's black hole), up to the speed of light, similarly as the geodesic equations are used for a fast moving spinless particle.

The MP equations can be written in terms of the tetrad quantities comoving with the spinning particle [3]. It follows from this representation that in the concrete case of particle motion in Schwarzschild's background, when the particle's spin is orthogonal to the plane determined by the direction of particle motion and the radial direction, the absolute value of the particle 3-acceleration relative to geodesic free fall as measured by the comoving observer is proportional to γ^2, where γ is the relativistic Lorentz factor as calculated by the tangential particle velocity relative to the Schwarzschild mass. It means that there is significant difference in the reaction of a spinning particle on the gravitational field when its velocity is much less than the velocity of light (with γ of order 1) and is very close to this velocity ($\gamma \gg 1$). From the point of view of the comoving observer, the deviation of a spinning particle from the geodesic free fall is caused by the gravitomagnetic components of the moving Schwarzschild source.

Moreover, the strong action of gravity on a highly relativistic spinning particle is not only in the expression for the local accelerate of this particle relative to a spinless particle but in the trajectories of the spinning particle as compare to the corresponding geodesic trajectories as well [4]. Indeed, if the spinning particle posses the velocity relative to Schwarzschild's mass which corresponds to the γ-factor of order $1/\sqrt{\varepsilon_0}$, where $\varepsilon_0 \equiv |S_0|/(mM)$ (here $|S_0|$ and m are, respectively, the values of the particle's spin and mass; M is the Schwarzschild mass), its orbits that begin in the space region near $1.5r_g$ can significantly differ from the corresponding geodesic orbits. This result follows from the MP equations in the linear spin approximation, i. e. is common at the conditions $S^{\mu\nu}u_\nu = 0$ and $S^{\mu\nu}P_\nu = 0$. In addition, according to the exact MP equations at condition $S^{\mu\nu}u_\nu = 0$ the essentially nongeodesic highly relativistic orbits of the spinning particle are allowed for the radial coordinate r which is much greater than $1.5r_g$ and the necessary value of the γ-factor is proportional to $\sqrt{r}$. Some of these orbits show the significant attractive action of the spin-gravity coupling on a particle and others are caused

by the significant repulsive action, dependently on the spin orientation.

By the numerical estimates for an electron in the gravitational field of a black hole with three of the Sun's mass the value $|\varepsilon_0|$ is equal to 4×10^{-17}. Then the necessary value of the γ-factor for the realization of some highly relativistic circular orbits by the electron near this black hole is of order 10^8. This γ-factor corresponds to the energy of the electron free motion of order 10^{14} eV. Analogously, for a proton in the field of such a black hole the corresponding energy is of order 10^{18} eV. For the massive black hole those values are greater: for example, if M is equal to 10^6 of the Sun's mass the corresponding value of the energy for an electron is of order 10^{17} eV and for a proton it is 10^{21} eV. Note that for a neutrino near the black hole with three of the Sun's mass the necessary values of its γ-factor for motions on the highly relativistic circular orbits correspond to the neutrino's energy of the free motion of order 10^5 eV. If the black hole's mass is of order 10^6 of the Sun's mass, the corresponding value is of order 10^8 eV. So, some particles in cosmic rays posses a sufficiently high γ-factor for motions on the significantly nongeodesic orbits near black holes. Concerning neutrinos, perhaps, the corresponding effects of the highly relativistic spin-gravity coupling can be registered by the IceCube neutrino detector.

By the way, concerning the possible behavior of a highly relativistic neutrino in Schwarzschild's background we point out paper [5] where some solutions of the MP equations at the condition $S^{\mu\nu}P_\nu = 0$ are studied. The conclusion is formulated that gravitation can accelerate neutrinos to the superluminal motion due to their spin. In this context we stress that 1) this effect is not allowed by the MP equations at the condition $S^{\mu\nu}u_\nu = 0$ and 2) it is shown in [6] that the condition $S^{\mu\nu}P_\nu = 0$ is not adequate for the description of spinning particle motions with the velocity relative Schwarzschild's mass which is greater than some critical value that is close to the velocity of light.

Naturally, the MP equations can be used for description of fermions in the gravitational field only in situations when their quantum properties are not important. Here we stress that the general relativistic Dirac equations is not appropriate for fermions in some highly relativistic regime as well.

It is shown in many papers that in the linear spin approximation the MP equations follow from the general relativistic Dirac equation as some classical approximation (see, e. g. [7]). Here we draw attention to the fact that the exact MP equations (i. e., their nonlinear in spin terms) cannot be obtained from this Dirac equation in principle. Why? To answer this question we recall that the main step in obtaining the general relativistic Dirac equation in the curved spacetime consists in introduction the notion of the parallel transport for spinors as a generalization of this notion for tensors.

Whereas according to the MP equations the spin of a test particle is transported by Fermi:

$$\frac{Ds^\mu}{ds} = u^\mu \frac{Du_\nu}{ds} s^\nu, \qquad (3)$$

where D/ds is the covariant derivative. It follows from (3) that only in the linear spin approximation the Fermi transport coincides with the parallel transport. Therefore, to satisfy the principle of correspondence between the Dirac equation and the exact MP equations, at first sight, it is necessary simple to introduce and use the Fermi transport for spinors in some corrected Dirac equation. However, it is impossible without the Lorentz invariance violation. In this context we note that many papers are devoted to the violation of Lorentz invariance from different points of view, for example, in the context of the Standard-Model Extension by V. A. Kostelecky and co-authors [8, 9] and, probably, the key words *Lorentz-violating spinor* first appeared only last year [9]. One can hope that just in the framework of this approach the necessary corrected Dirac equation will be obtained.

References

1. Fock V., Ivanenko D.: 1929, *Z. Phys.*, **54**, 798; Fock V: *Z. Phys.*, **57**, 261; Weyl H.: 1929, *Proc. Natl. Acad. Sci. USA*, **15**, 323.

2. Mathisson M.: 1937, *Acta Phys. Pol.*, **6**, 163; Papapetrou A.: 1951, *Proc. R. Soc. A*, **209**, 248.

3. Plyatsko R.: 1998, *Phys. Rev. D*, **58**, 084031; Plyatsko R., Bilaniuk O.: 2001, *Class. Quant. Grav.*, **18**, 5187.

4. Plyatsko R.M., Vynar A.L.: 1982, *Sov. Phys. Dokl.*, **27**, 328; Plyatsko R.: 2005, *Class. Quant. Grav.*, **22**, 1545; Plyatsko R., Stefanyshyn O.: 2008, *Acta Phys. Pol. B*, **39**, 23; Plyatsko R., Stefanyshyn O., Fenyk M.: 2010, *Phys. Rev. D*, **82**, 044015; Plyatsko R., Fenyk M.: 2012, *Phys. Rev. D*, **85**, 044015; Plyatsko R.M., Fenyk M.T.: 2012, *Odessa Astron. Publ.*, **25**, 138; Plyatsko R., Fenyk M.: 2013, *Phys. Rev. D*, **87**, 044019.

5. Hojman S.A., Asenjo F.A.: 2013, *Class. Quant. Grav.*, **30**, 025008.

6. Plyatsko R.M, Stefanyshyn O.B., Fenyk M.T.: 2011, *Class. Quant. Grav.*, **28**, 195025.

7. Obukhov Yu., Silenko A., Teryaev O.: 2009, *Phys. Rev. D*, **80**, 064044; Obukhov Yu.N., Silenko A.J., Teryaev O.V.: 2011, *Phys. Rev. D*, **84**, 024025; Obukhov Yu.N., Silenko A.J., Teryaev O.V.: 2013, *Phys. Rev. D*, **88**, 084014; Obukhov Yu.N., Silenko A.J., Teryaev O.V.: 2014, *Phys. Rev. D*, **89**, 041501.

8. Kostelecky V. A., M. Mewes M.: 2013, *Phys. Rev. D*, **88**, 096006.

9. Bonder Y.: 2013, *Phys. Rev. D*, **88**, 105011.

DETERMINATION OF DARK MATTER TYPE BY X-RAY SOURCES STATISTICS

A.V. Tugay

Astronomy and Space Physics Department, Faculty of Physics,
Taras Shevchenko National University of Kyiv,
Glushkova ave., 4, Kyiv, 03127, Ukraine, *tugay.anatoliy@gmail.com*

ABSTRACT. The current cosmological model includes cold dark matter, which consists of massive nonrelativistic particles. There are also some observational and theoretical evidences for warm dark matter. The existence of warm DM can be examined by measuring of the galaxy clusters density profiles and accurate counting of dwarf galaxies. In this work I suppose that DM haloes are well traced by X-ray gas in clusters, groups, pairs and even single galaxies. The type of DM is inspected with the Xgal sample of 5021 X-ray emitting galaxies observed by XMM-Newton. The selection bias of this sample is also analyzed.

Key words: Cosmology: dark matter; X-rays: galaxies.

1. Introduction

Assumptions about the nature of dark matter (DM) can be divided into warm and hot dark matter. Massive neutrino was considered as the main candidate to hot DM up to 2001 and then it was excluded from DM candidates. The difference between cold dark matter (CDM) and warm dark matter (WDM) is concerned with the mass value of a DM particle (m_{DMP}). WDM particles became nonrelativistic after nucleosynthesis but before recombination, so their mass should lie in 3 eV - 30 keV interval. In the papers of Boyarsky et al. (2014) and Bulbul et al. (2014) there was found an X-ray emission line that can be the evidence of WDM particle decay with the 7 keV mass. Relativistic DM smooth initial density fluctuations are at any scale less than free-streaming length of a DM particle. Thus, WDM model predicts the lack of dwarf galaxies that can be checked by the astronomical observations. The relation between m_{DMP} and the protogalaxy mass at free-streaming scale (M_{FS}) can be derived from Pauli principle (Dodelson, Widrow, 1994):

$$M_{FS} \equiv \frac{4\pi\rho}{3}\left(\frac{\lambda_\nu}{2}\right)^3 \approx \frac{3 \cdot 10^{15} M_\odot}{\Omega_{DM}}\left(\frac{30eV}{m_{DMP}}\right)^2 \quad (1)$$

We can expect the deficit of galaxies with the mass less than M_{FS}. The one from the possibilities to estimate this mass is the consideration of extragalactic X-ray sources statistics. Galaxy clusters, groups and single galaxies can be the sources of the X-ray emission. All these structures are believed to form in a single DM halo. The proportionality of the X-ray luminosity and the mass of a DM halo is assumed in this paper. This allows us to estimate m_{DMP} and the type of DM by the luminosity function of the extragalactic X-ray sources.

2. Sample

The Xgal sample (Tugay, 2013) contains 5021 extragalactic sources from XMM-Newton observations archive. These sources are mostly Seyfert galaxies, galaxy clusters and QSOs (Tugay, 2014); the part of the starburst galaxies is very small (Tugay, Vasylenko, 2011). The sample doesnt have very large dispersion of the optical luminosities (Fig. 1), so we can find the minimal mass of a DM halo from the constant optical M/L ratio and some limiting value of X-ray luminosity. The following parameters were found for Xgal sample:

1. $r = F_u/F_x$ (see corresponding distributions in Tugay (2012)). The value $lg(r) = 2.38 \pm 1.07$ was found for the whole sample. The reasons of using this relation instead of the optical fluxes are the selection bias (clearly visible at Fig. 1) and larger absorption in the optical band.

2. The deficit of low luminosity X-ray galaxies can be noticed from Fig. 2. Sources with $F_x < 10^{-13} erg/s$ were rejected to avoid the bias from the most luminous ones. Average luminosity $lg(L_X) = 40.35 \pm 1.25$ was found for the rest of the sample. Limiting luminosity corresponding to M_{FS} and m_{DMP} was estimated as lower bound of 1σ interval of L_X distribution. $lg(L_{edge}) = 39.1 \pm 0.6$ was found by this method.
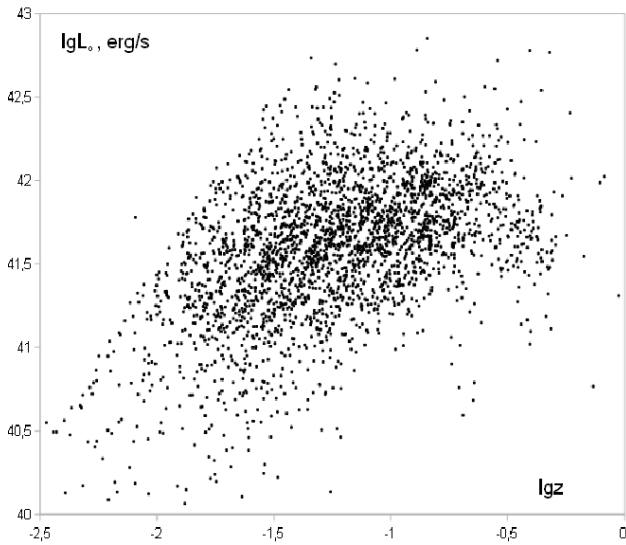
Figure 1: Distribution of optical u-band luminosities of SDSS galaxies from redshift.
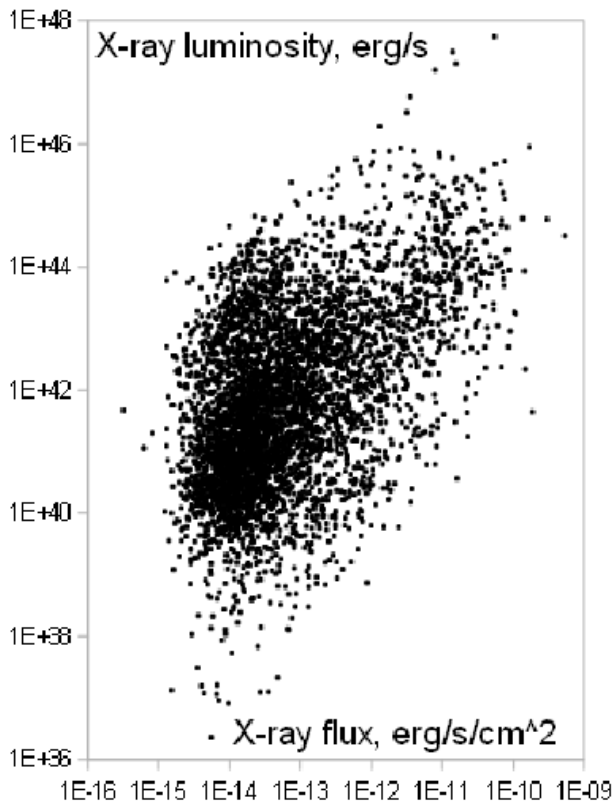
Figure 2: Distribution of X-ray luminosities of Xgal objects from X-ray flux.

3. The mass of a WDM particle

The mass of a DM particle was calculated from (1):

$$m_{DMP} = 6keV\sqrt{\frac{1.2 \cdot 10^{45} erg/s}{rKL_{edge}}} \qquad (2)$$

The optical mass-to-luminosity ratio $K = M/L = 140 \pm 40$ was taken from (Hradecky et al., 2000) for galaxy clusters. Real ratio may lie in the interval from 70 to 1500 for some clusters, so all estimations are very rough. The resulting value is
$m_{DMP} = 8 \div 120 keV$; $\overline{m_{DMP}} = 31 keV$

4. Conclusion

Warm and cold dark matter can not be distinguished by the distribution of X-ray luminosities. The main problem seems to be large dispersion of M/L and optical/X-ray ratios. Nevertheless, obtained estimation is close to the results of Boyarsky et al. (2014) and Bulbul et al. (2014) by the order of magnitude.

References

Boyarsky A. et al: 2014, *http://arxiv.org/abs/1402.4119*.

Bulbul E. et al: 2014, *Astrophys. J.,* **789**, 13. *http://arxiv.org/abs/1402.2301*.

Dodelson S., Widrow L.M.: 1994, *Phys. Rev. Lett.,* **72**, 17. *http://arxiv.org/abs/hep-ph/9303287*.

Hradecky V. et al: 2000, *Astrophy. J.,* **543**, 521. *http://arxiv.org/abs/astro-ph/0006397*.

Tugay A.V., Vasylenko A.A.: 2011, *Odessa Astron. Publ.,* **24**, 72.

Tugay A.V.: 2012, *Odessa Astron. Publ.,* **25**, 142. *http://arxiv.org/abs/1311.4333*.

Tugay A.V.: 2013, *Adv. Astron. and space Phys.,* **3**, 116. *http://arxiv.org/abs/1311.4337*.

Tugay A.V.: 2014, *IAU Symp.,* **304**, 168.

ASTROPHYSICS

DETERMINATION OF SIZE OF THE EMITTING REGION IN ECLIPSING CATACLYSMIC VARIABLE STARS

I.L.Andronov [1], K.D.Andrych [2]

[1] Department "High and Applied Mathematics, Odessa National Maritime University, Mechnikova Str., 34, 65029, Odessa, Ukraine, *tt_ari @ ukr.net*
[2] Department of Astronomy, Odessa National University, Shevchenko Park, 65014, Odessa, Ukraine, *katyaandrich@gmail.com*

ABSTRACT. The dependencies of the phase of eclipse of the white dwarf's centre and the durations of the ascending and descending branches of the light curve on the binary system's parameters were computed using the spherically-symmetric approximation and the more accurate model of the elliptical projection onto the celestial sphere of the companion (red dwarf) that fills its Roche lobe. The parameters of eclipses in the classical eclipsing polar OTJ 071126+440405 = CSS 081231:071126+440405 were estimated.

Keywords: Stars: variable – stars: binary – stars: cataclysmic

1. Introduction

Interacting binary stars are natural laboratories with extreme conditions that are inaccessible in terrestrial laboratories. There are many different processes that allow to determine physical characteristics of binary systems using methods for mathematical modeling of observations.

Especially useful are studies of eclipsing variables, particularly, eclipsing cataclysmic variables, which allow to determine some physical parameters from photometric observations only.

On the New Year night 31.12.2008, Denisenko and Korotkiy (2009) discovered the unique eclipsing polar (OTJ 071126 + 440405) in the Camelopardalis constellation. The light curve shows that the system has a very short duration of the ascending and descending branches of the primary minimum, what indicates a very small size of the radiation source.

Our theoretical work has been done for interpreting the observational data.

2. Effective Dimensions of the Stars

The simplest classical approach is to apply a model of spherical stars not only in Algol-type systems (Shulberg, 1971; Tsessevich, 1980; Chinarova, 2006), but also in cataclysmic systems (Shafter A., 1984; Horne, 1985; Downes et al., 1986; Garnavich et al., 1990 and, more recently, Aungwerojwit et al., 2012), assuming that the red dwarf (which fills its Roche lobe and thus is tidally distorted) is spherical.

Typically, the radius of this sphere R_2 is defined as

$$R_2 = \left(\frac{3V}{4\pi}\right)^{1/3},$$

where V is the volume of the Roche lobe, which may be estimated from a suitable approximation of Eggleton (1983)

$$\frac{R_2}{A} = \frac{Cq^{2/3}}{Dq^{2/3} + \ln(1 + q^{1/3})},$$

where $q = M_2/M_1$ is the mass ratio, M_1 – the mass of the compact primary, M_2 – the mass of the secondary which fills its Roche lobe. The values of the coefficients were adopted to be $C=0.49$ and $D=0.6$. The asymptotical approximations for this formula are $R_2/A = Cq^{1/3}$ for $q \ll 1$ and $R_2/A = C/D$ for $q \gg 1$. This expression is a good approximation also for intermediate values of q.

However, the Roche lobe is definitely not spherical, having the largest size along the line of centers, and the smallest in the "polar" direction (along the rotational axis).

For our task – modeling of entry/exit time (duration of the descending/ascending branch of the light curve) at the eclipse as functions of the parameters of the binary system (including the size of the white dwarf). We have chosen two models: the popular model of "spherical" red dwarf, and much more accurate model of it's elliptical projection onto the celestial sphere (there is assumed that red dwarf filed it's Roche lobe)

3. Calculating the Size of the Emitting Area

Let us consider a cataclysmic binary system, in which red and white dwarf obscure each other. Because these systems are very close (have a small orbital period), they have circular orbits, and this facts greatly simplifies the calculation. For convenience, we consider a coordinate system with its center in the red dwarf, so the white dwarf rotates around it.

The center of the white dwarf during its orbital motion shows an ellipse. The coordinates x and y can be expressed as:

$$x = A \cdot \sin 2\pi\varphi, \quad y = B \cdot \cos 2\pi\varphi, \quad B = A \cdot \cos i,$$

where φ is the phase expressed in units of the orbital period P, thus a multiplier of 2π is needed for conversion to radians. It rises to unity that mean the system made full rotation.

Here A and B correspond to minor and major axis of ellipse, which is the projection of the circular orbit of a radius A on the picture area (an area that passes through the center of the first stars perpendicularly to the line of sight). Inclination of the orbit i is the angle between the line of sight and the rotation axis of the binary system.

The distance between the centers of the stars can be calculated by the Pythagorean theorem. Taking into account the above formulas, it may be written in the following form:

$$R^2 = A^2(1 - \cos^2 2\pi\varphi \cdot \sin^2 i).$$

After some transformations, we get the following form of the same equation, which is convenient to determine the phase corresponding to the projected distance R:

$$2\pi\varphi = \arccos\left(\frac{\sqrt{1 - \dfrac{R^2}{A^2}}}{\sin i}\right)$$

We consider that, at the time of internal contact, the distance between the centers equals to the difference in the stellar radii, and at point of external contact – to sum of their radii. Obviously, for convenience, one can use the relative values of the stellar radii.

The phases of contacts were calculated as well as the phase difference between external and internal contacts, which corresponds to the length of ascending (or descending) branch of the eclipse and is measured in units of the orbital period. Results are presented in Fig.1 and Fig.2, where the radius of the white dwarf and the inclination of the orbit were fixed, respectively.

As in cataclysmic binary systems one of the stars – the red dwarf – fills its Roche lobe, it is deformed. To within a few hundredths of a percent profile stars can be approximated to an ellipse (Andronov, 1992).

The limb of the red dwarf indicated in Fig. 3 by a red line. The ellipse – like curves N_1 and N_2 are the locuses of points distant from the limb of the red dwarf by the radius of the white dwarf. Coordinates of these points can be calculated by these formulas, respectively.
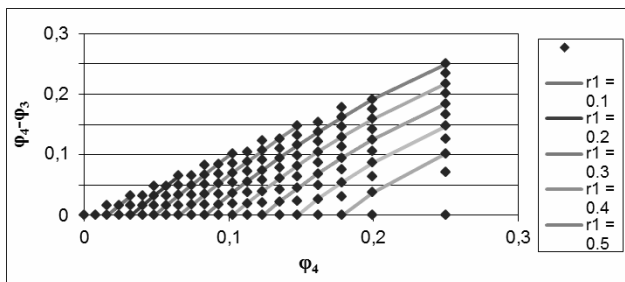

Figure 1: Phase of the external contact and the duration of the ascending branch of the light curve for different pairs of values of the relative radii r_1 and r_2, varying in increments of 0.05 in the range $0 \leq r_2 \leq r_1 \leq (1 - r_2)$. Inclination $i = 90°$.
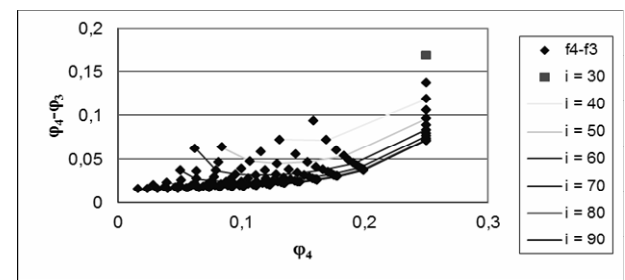

Figure 2: Phase of the external contact and the duration of the ascending branch of the light curve for different pairs of values of the relative radius r_1, which varies in increments of 0.05 in the range $0 \leq r_2 \leq r_1 \leq (1 - r_2)$, and inclination of the orbit from 30° to 90° in steps of 5°. The parameter $r_2 = 0.05$.
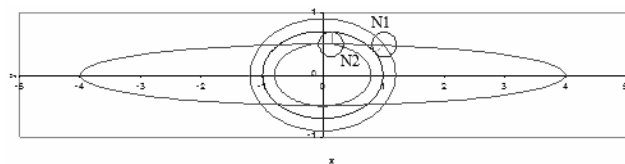

Figure 3: Scheme of internal and external contacts in eclipse

For the calculation of the contact points, it is necessary to solve the following system of equations:

$$\begin{cases} x_1 = x + R_2 n_x = A \cdot \sin 2\pi\varphi \\ y_1 = y + R_2 n_y = B \cdot \cos 2\pi\varphi \end{cases}$$

Let the phase of crossing the center of the white dwarf by the limb of the red dwarf that is φ_e. This phase can be calculated respectively to these formulas for the elliptical and spherical approximations.

In the case, if $r_2 \rightarrow 0$,

$$\varphi_e \rightarrow (\varphi_{in} + \varphi_{ex})/2$$

$$\sin^2 2\pi\varphi_e = \frac{\dfrac{b^2}{A^2} - \cos^2 i}{\dfrac{b^2}{a^2} - \cos^2 i}$$

If $b = a = r_e$:

$$\sin^2 2\pi\varphi_e = \frac{\dfrac{r_e^2}{A^2} - \cos^2 i}{\sin^2 i}$$

Andronov (1992) got coefficients for determining the radius of the object in the orbital (a/A) and polar (b/A) plane (that is the plane passing through the center line and the axis of rotation of the system), following the Eggleton's (1983) form. In his work, they are denoted as $\sin\theta(0°)$ ($C=0.4990$, $D=0.5053$) and $\sin\theta(90°)$ ($C=0.4394$, $D=0.5333$), respectively. The elliptic approximation for other angles is correct within 0.2% and 0.5%, respectively. For better accuracy, we used linear interpolation for the ratio of precise/fit values.

We adopted the mass ratio of $q=0.3$ in this system. Then we obtain the following values of the parameters: $r_e/A=0.28103$, $a/A=0.27216$, $b/A=0.26219$.

In Fig. 4, the duration of the eclipse depending on the inclination for both models is shown.
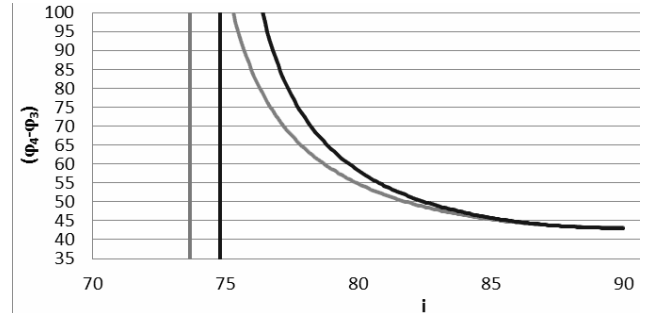
Figure 4: Duration of the ascending/descending branch $\varphi_4-\varphi_3$ (in seconds) as a function of inclination i for the models of circle (blue) and ellipse (red). The vertical lines show limiting values of i.
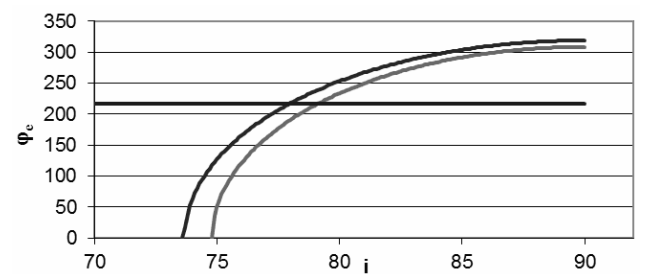

Figure 5: The dependence of the phase φ_e of the eclipse of the white dwarf center (expressed in seconds) on inclination for the models of circle (blue) and ellipse (red). The horizontal line shows the observed value.

To determine the duration of the entrance/exit of the eclipse, φ_e and the corresponding errors for all parameters, we write the system of conditional equations:

$$T_1 = T_0 + C_1 + P \cdot E - U - V$$
$$T_2 = T_0 + C_1 + P \cdot E - U + V$$
$$T_3 = T_0 + C_1 + P \cdot E + U - V$$
$$T_4 = T_0 + C_1 + P \cdot E + U + V$$

where T_0 is an initial epoch,

C_1 – correction to the initial epoch,

P – period,

E – number of cycle,

U – the time between crossing the center of the red dwarf limb by the white dwarf and the middle of eclipse,

V – half the length of the ascending / descending branches of the light curve.

From the observations, we have the following values: T_1, T_2, T_3, T_4, E, T_0.

Moments of contacts were obtained from the observations obtained by Dr. Sergey V. Kolesnikov using the 2.6 m telescope named after G.A.Shajn in the CrAO.

Table 1: The moments of eclipse contacts

BJD, 2400000+	Types of contacts	BJD, 2400000+	Types of contacts
54946.19335	1	54949.20429	1
54946.19340	2	54949.20435	2
54946.19836	3	54949.20932	3
54946.19842	4	54949.20937	4

The parameters were determined in the Excel using the method of the least squares. We have determined the period of the system: P=117.18292±0.00014 min.

Parameters such as mass and mass ratio of the stars in this system were taken from the works of other authors, who used not only photometric observations. Details are discussed by Andronov et al. (2014). Considering the phase of the eclipse for white dwarf's center, we obtain two values for inclination of the orbit for the elliptical (i=79.1177±0.0075°) and the spherical approximations (i=77.1231±0.0029°).

According to the observations, we obtained the duration of the entrance/exit of the eclipse (descending/ascending branches of the light curve): 4.752±0.306 seconds.

We compared this value to that expected for a white dwarf of the accepted mass of M_1=0.543$M_\odot$, corresponding to q=0.3 and M_2=0.163$M_\odot$. From the dependence "mass – radius" for white dwarfs (Andronov and Yavorskiy 1990), we obtained the radius of the white dwarf. Using our calculations for inclination of the orbit, we obtain the duration of the entry/exit (time between external and internal contact) of 63.2 seconds for the elliptical approximation, which is by 13.3 times more than the expected value for the white dwarf.

The Fig. 6 shows two models: the red dwarf, white dwarf at the phase of eclipsing center and the emitting region. Red line shows the elliptical model for the red dwarf, the violet line – circular model. The visible trajectories of the center of the white dwarf for different values of inclination of the orbit are shown. Vertical lines show different values of the parameter φ_e, including what is observed. From the cross point

of the ellipse, one may determine inclination. Also the white dwarf and the emitting area are shown in the same scale.
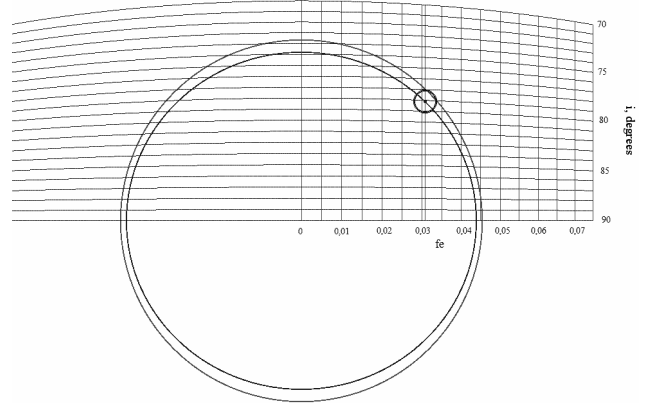
Figure 6: The scheme of eclipse preserving the scale for the numerical values of the model system OTJ 071126 + 440405.

4. Conclusions

- The dependencies of the phase of eclipse of the white dwarf's centre and the durations of the ascending and descending branches of the light curve on the binary system's parameters were computed using the spherically – symmetric approximation.

- Similar computations were performed with the more accurate model of the elliptical projection onto the celestial sphere of the companion (red dwarf) that fills its Roche lobe.

- The parameters of eclipses in the classical eclipsing polar OTJ 071126+440405 were estimated.

- The duration of entering/exiting the eclipse is shown to be 13.3 times shorter than the theoretical predictions. Hence, the emitting region is markedly smaller (~1300 km) as compared to the white dwarf's diameter. That is supposed to be the "hot spot" region.

References

Andronov I.L.: 1992, *A&AT*, **2**, 341.
Andronov I.L.: 2008, *JPS*, **12**, 2902.
Andronov I.L. et al.: 2014, in preparation.
Andronov I.L., Yavorskij Yu.B.: 1990, *CAOSP*, **20**, 155.
Aungwerojwit A. et al.: 2012, *ApJ*, **758**, 1.
Chinarova L.L.: 2006, *Binary Stars and their Evolution* (in Russ.), Odessa, ONU, 56 pp.
Denisenko D., Korotkiy S., 2009: *VSNET-alert*, **10870** http://ooruri.kusastro.kyoto-u.ac.jp/mailarchive/vsnet-alert/10870
Downes R.A. et al.: 1986, *ApJ*, **301**, 240.
Eggleton P.P.: 1983, *ApJ*, **268**, 368.
Garnavich P.M. et al.: 1990, *ApJ*, **365**, 696.
Horne K. : 1985, *MNRAS*, **213**, 129.
Shafter A.: 1984, *AJ*, **89**, 1555.
Shulberg A.M., 1971: *Close Binary Stellar Systems with Spherical Components* (in Russ.), Moscow, Nauka, 246pp.
Tsessevich V.P.: 1980, *Variable Stars and their Observations* (in Russ.), Moscow, Nauka, 176pp.

MODELLING OF MOTION OF BODIES
NEAR TRIANGULAR LAGRANGIAN POINTS

O.A.Bobrov

Department of Astronomy, Odessa National University,
Shevchenko Park, 65014, Odessa, Ukraine, *oleg_bobrov@ukr.net*

ABSTRACT. In this paper, we consider a system of three bodies connected by gravity, two of which are of comparable mass (the Sun and Jupiter), and the third is negligible and it is located in one of the triangular Lagrange points (restricted 3 – body problem). We used the equations of motion in a planar coordinate system that rotates together with massive bodies. Several programs have been written in the programming environment Pascal ABC, in order to build the trajectory of a small body, to indicate the osculating orbit around a massive body, to display equipotential surfaces.

Key words: Stars: binary – celestial mechanics – Solar system – asteroids

1. Introduction

Triangular Lagrangian points are important for planetary systems and planetary satellites. For example, asteroids are located close to this points of the Sun – Jupiter system. They move along the same orbit as Jupiter, in front and behind it, and are called, respectively, the Greeks and the Trojans. Similar asteroids were also found at Neptune, Uranus, Mars and Earth. There are very sparse clusters of interplanetary dust in the triangular points of the Earth-Moon system, so called Kordylewski clouds. Thus the study of the stability of the trajectories of small space objects near the triangular Lagrange points is interesting and relevant task.

2. Calculations

In the rotating coordinate system, the potential is:

$$P = -\frac{GM_1}{r_1} - \frac{GM_2}{r_2} - \frac{w^2 r_3^2}{2} \qquad (1),$$

where M_1, M_2 – the masses of massive bodies, r_1, r_2 – the distance from a point A to them, w – the angular velocity of the coordinate system r_3 – the distance from a point to the axis of rotation.

Here the first two terms correspond to the gravitational potential of all bodies, and the third – the potential of centrifugal force.

Let the first body be at the origin of the Cartesian coordinate system, the plane of rotation – in the plane XY, the second body – on the axis OX (in the positive part). Then X, Y – coordinates of the third body X', Y' – the velocity of the third body X'', Y'' – the acceleration of the third body, a – the distance between the massive bodies;

R_1, R_2 – distance from the third body to the first and second bodies; w – the angular velocity of the system

$$w = \sqrt{\frac{G(M_1 + M_2)}{a^3}} \qquad (3)$$

Let the rotation system of two bodies directed conterclockwise at right-handed coordinate system.

In order to simplify computing, we scaled coordinates in units of a, velocity in units $a \cdot w$, acceleration in units of $a \cdot w^2$, mass in units of the total mass $M_1 + M_2$. Then $m_2 = 1 - m_1$. The equations of motion in projections (e.g. Subbotin, 1968, Andronov, 1990):

$$R_1 = \sqrt{X^2 + Y^2} \qquad (4)$$

$$R_2 = \sqrt{(X-1)^2 + Y^2} \qquad (5)$$

$$X'' = -\frac{X m_1}{R_1^3} - \frac{(X-1) m_2}{R_2^3} + X - m_2 + 2Y' \qquad (6)$$

$$Y'' = -\frac{Y m_1}{R_1^3} - \frac{Y m_2}{R_2^3} + Y - 2X' \qquad (7)$$

First term is the gravity law for the first and second bodies. Other forces appear because the coordinate system rotates. The third term – the centrifugal force, and the fourth term – the Coriolis force. We integrated these equations using the Runge – Kutta method of 4th order.

Strict concept of stability motion is a complicated mathematical concept. But we used, an intuitive concept of stability. If a sufficiently long period of time the Trojan body will not leave the area near the Lagrange point, the motion in our understanding is considered stable. This area is considered as a region, where the potential energy of the Trojan body is higher than the one at the Lagrange point (located behind the second body). Using the dichotomy method, by this criterion we determined the maximum speed value in different directions.

Fig.3 shows the speed limit for Lagrange points L_4 and L_5, where the angle is measured from the axis OX in the rotation direction of the system. We can see that the two graphs are symmetrical and shifted relatively to each other. The bodies at different Lagrangian points, moving out in the same direction, are under the effect of Coriolis force directed the same. This force is directed in one case to the small body, and the other – from the small body, so we must introduce different directions of the reference angle. Then it was introduced the system of reference angle where the graphs for different points coincide. The direction of velocity 0° - direction of orbital motion at the Lagrangian point.The angle is measured at the point L_5 in the direction of rotation second body, and at the point L_4 - backwards. The body, which has a direction parallel to the direction at first body, has the greatest speed limit.

In opposite, a body, which has perpendicular direction of motion, has a lower limit speed.
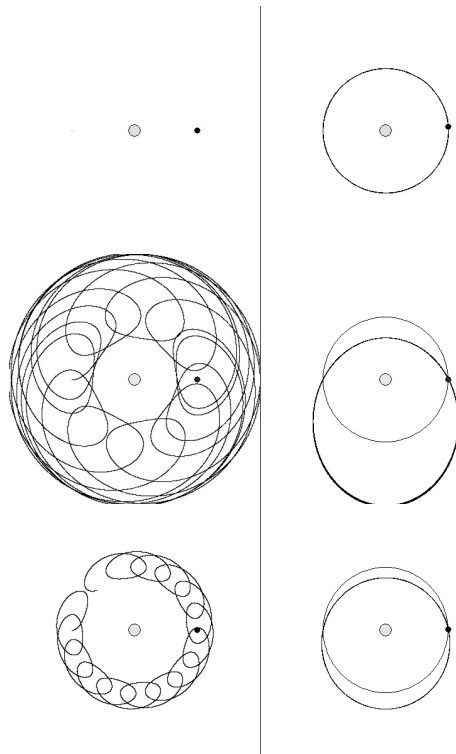
Figure 1: Example of motion in the rotating coordinate system without affecting the second body, a computer simulation. Left − the motion relative to the second body, right − in the inertial reference system.
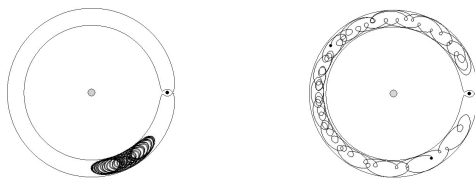
Figure 2: The greatest speed limit is the steady motion of a body around a Lagrange point, and the minimum − motion at all area.
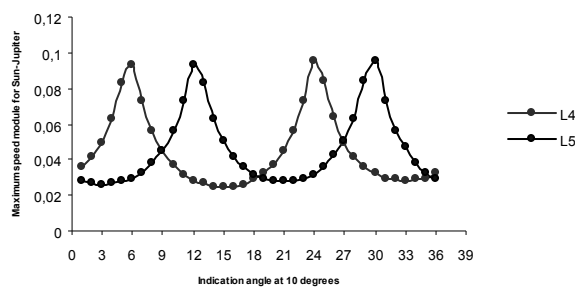
Figure 3: The dependence of the speed limit on flying of the Sun − Jupiter system (in the same frame of reference edges). The time of motion is 20 orbital periods.

3. Conclusions

We determined maximum speed, at which a small body leaves the neighborhood of the triangular Lagrangian points for the Sun-Jupiter system and the Earth-Moon system, as well as its dependence on the velocity direction of the body at the Lagrangian point. For different Lagrangian points, opposite directions for reference angle between the velocity vector and the line of centers of mass

bodies were introduced (clockwise in one point and conterclockwise in another). With this choice of measuring direction angles, the graphs of limiting velocities almost coincided. This can be explained by the fact that the body in different Lagrange points with the same initial velocity vector have the same effect of the Coriolis force. However, at one point, this force will be directed to the second body (Jupiter), and another − from the second body.
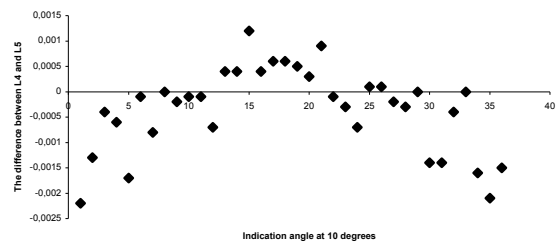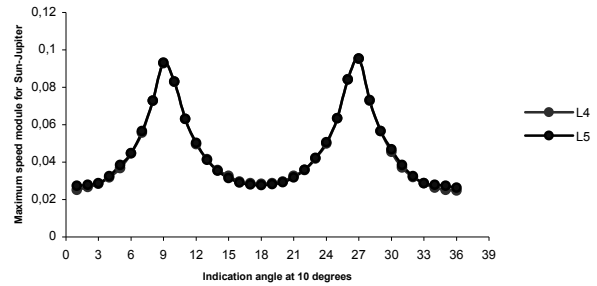
Figures 4, 5: The dependence of the speed limit on the direction flying of Sun − Jupiter system (up) and the difference between the two graphs (bottom).
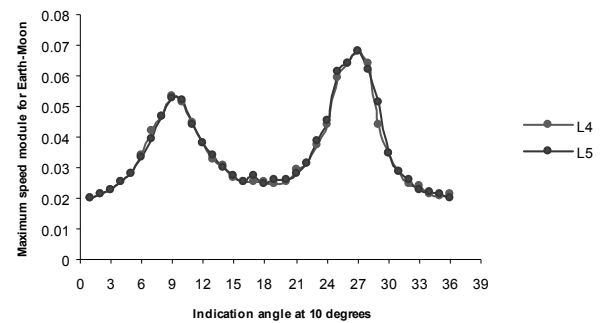
Figure 6: The dependence of the speed limit on the direction flying of Earth − Moon system.

References

Andronov I.L.: 1991, *Stroenie i Evoluciya Peremennykh Zvyozd* (in Russian), Odessa, 84 p.

Subbotin M.F.: 1968, *Vvedenie v Teoreticheskuyu Astronomiyu* (in Russian), Moscow, Nauka.

GAMMA RAY BURST FOLLOW-UPS WITH BOOTES-4

Sergey Guziy[1], Alberto J. Castro-Tirado[2,3], Martin Jelínek[2], Javier Gorosabel[2], Petr Kubánek[4], Ronan Cunniffe[2], Oscar Lara-Gil[2], Juan C. Tello[2], Soomin Jeong[2], Samantha R. Oates[2], Youdong Xu[2], Dolores Pérez-Ramírez[5], Chenzou Cui[6], Yufeng Fan[7] , Chuanjun Wan[7], Jinming Bai[7] and I. Kheyfets[1]

[1] Astronomical Observatory, Nikolaev National University, Nikolska 24, Nikolaev, Ukraine
[2] Instituto de Astrofísica de Andalucía (IAA-CSIC), P.O. Box 03004, E-18080, Granada, Spain
[3] ISA-UMA, Universidad de Málaga, Spain
[4] IP-ASCR Praha, Czech Republic
[5] Universidad de Jaén, Campus Las Lagunillas, Jaén, Spain
[6] National Astronomical Observatory, Chinese Academy of Sciences, Beijing 100012, China
[7] Yunnan Astronomical Observatory, CAS Kunming 650011, Yunnan, China

ABSTRACT. The Burst Observer and Optical Transient Exploring System (BOOTES), is a global robotic observatory network, which started in 1998 with Spanish leadership devoted to study optical emissions from gamma ray bursts (GRBs) that occur in the Universe. We present shot history and current status of BOOTES-4 telescope. Some details of 38 GRBs followed-up with BOOTES-4 are discussed.

Key words: Gamma ray burst: follow-up, optical transient

1. Introduction

The Burst Observer and Optical Transient Exploring System (BOOTES), started in 1998 as a Spanish-Czech collaboration devoted to study optical emissions from gamma ray bursts (GRBs). The first BOOTES robotic astronomical station was located at INTA's Estación de Sondeos Atmosféricos in Centro de Experimentación de El Arenosillo, a dark-sky site near Mazagón (Huelva), center owned by the Instituto Nacional de Técnica Aerospacial (INTA). The second observing station was opened in 2001 and it is located at the Estación Experimental de La Mayora (dubbed BOOTES-2), 240 km apart. The latter is run by the Consejo Superior de Investigaciones Científicas (CSIC). In 2009 BOOTES expanded abroad, with the third station (BOOTES-3) being installed in Blenheim (South Island, New Zealand). The fourth one (BOOTES-4) has been deployed in 2011 at the Lijiang Astronomical Observatory (Yunnan, China).

2. BOOTES-4 location, instruments and science

For many astrophysical problems it is necessary that photometric and astrometric observations be carried out over a long period of time. In the case of transient events, it is especially important to have continuous monitoring for several hours or even days after the event. The successful implementation of the BOOTES project requires the installation of telescopes in varying timezones. BOOTES-4 installed at the Lijiang Astronomical Obser-

vatory, Yunnan, China (Lat: 26°41'43"N, Long: 100°01'47"E, Elev: 3231m), deliberately chosen as being at an intermediate longitude between Spain and Mexico. It was officially opened on 20 March 2012 (See Figure 1).

Figure 1: BOOTES-4 telescope

Similarly to the BOOTES-1,2,3 stations, its dome is controlled by electrical motors which are controlled automatically according to the existing weather conditions.

The BOOTES-4 station has the next instruments:

- MET Ritchey-Chrétien reflector telescope (0.6m, f/8) with very fast slewing speed (> 100 deg/s) and easy rescheduling;
- EMCCD narrow field camera (clear, Sloan u',g',r',i' and UKIRT Z and Y -band filters): 10'x10' FOV (fast readout <1s);
- All-sky camera (CASANDRA-4): 180º FOV.

Main science with BOOTES-4 station is:

- The observation of the GRB error box simultaneously to the GRB occurrence;
- The detection of optical flashes (OTs) of cosmic origin;

- The monitoring of high-energy targets in different optical, as ground-based support for the ESA's *International Gamma-Ray Laboratory (INTEGRAL);*
- The monitoring of several objects (bright AGNs/QSOs, old GRB positions, etc.).

3. GRBs with BOOTES – 4

GRBs are indeed one of the main scientific goals of BOOTES. We know that GRBs arise at cosmological distances (with mean redshift $z \sim 2.5$ and redshifts in the range ~0.01 to ~ 10), with huge isotropic equivalent radiated energy, and small timescales (in the range few ms to 10^2 s), thus implying a small emitting region. The spectrum is non-thermal and relativistic outflows ($\Gamma > 100$) are involved. A frequent assumption is that short and long GRBs (with the short ones representing 1/3 of the overall GRB population) are due to different progenitors leading to the same succession of events: formation of a compact object and ejection of a relativistic outflow which produces the (long-lasting) afterglow at other wavelengths. Main program for BOOTES-4 system is observations optical counterparts for gamma ray burst: open and monitoring OT in different filters.

GRBs observations with BOOTES-4 was started in February 2012 and continue till present days. For the period from 2012 to 2013 was 38 real-time follow-ups, with 6 detections of the OA and 32 observations with upper limit, 4 pulications (GCN circulars and other). Some examles presented on Figures 2,3,4,5.
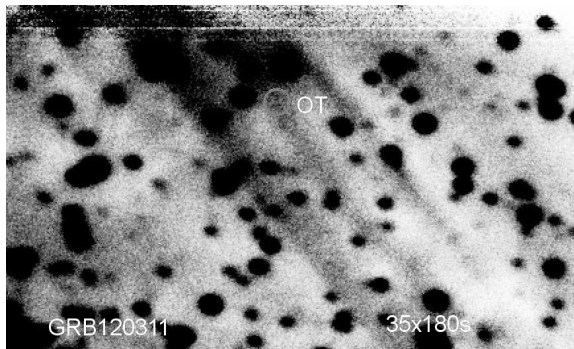
Figure 2: GRB 120311A - optical transient in the SWIFT XRT error box obtained with BOOTES-4 telescope in 13.66 hours after the burst. On the picture 35 coadded unfiltered images taken with 180s exposure each.
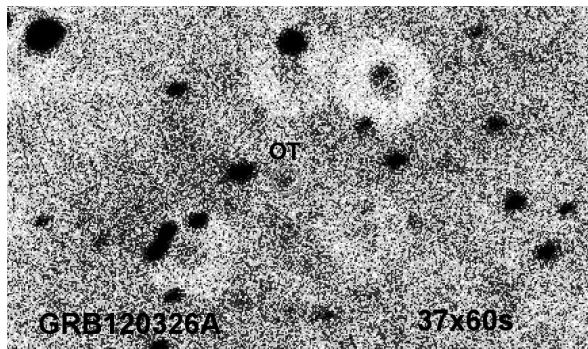
Figure 3: GRB 120326A. The observations started 10.7 hours after the GRB trigger. On the picture 37 coadded images taken with 60s exposure each.
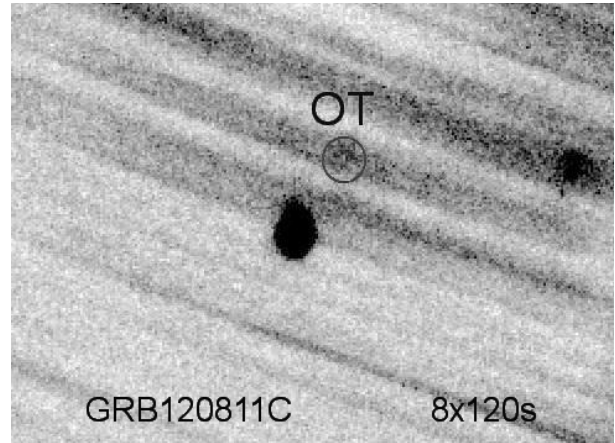
Figure 4: GRB 120811C. The observations started 34 min. after the GRB trigger with bad weather condition. On the picture 8 coadded unfiltered images taken with 120s exposure each. The afterglow was detected in the combined image with magnitude as 19.1 ± 0.3
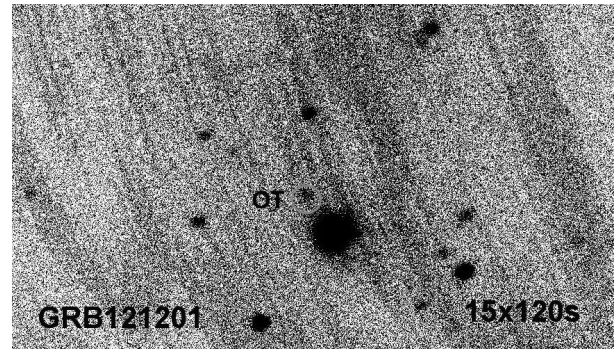
Figure 5: The GRB 121201A. The observations started 3 sec. after the GRB trigger. On the picture 15 coadded unfiltered images taken with 120s exposure each. The afterglow was detected in the combined image.

4. Conclusion

Multiwavelength observations (photometry, spectroscopy, polarimetry) are ideal to better understand the GRB diversity. As on Oct. 1 2013, the number of GRBs followed-up at the BOOTES-4 stations is 38, with 6 optical counterpart detections and 32 upper limits reported (the rest being too crowd fields or unusable due to dew, low airmass, unfocused images,...), altogether leading to 4 publications.

Installing the remaining BOOTES stations will help in continuous monitoring for some celestial sources, building more precise light curve for the targets. More detailed information about the BOOTES network can be seen in *http://bootes.iaa.es*.

EXPLOSIVE NUCLEOSYNTHESIS
AT STRONG STELLAR MAGNETIZATION

V. N. Kondratyev[1,2], Yu. V. Korovina[,3]

[1] Physics Department, Taras Shevchenko National University of Kyiv,
    03022-UA Kyiv, Ukraine, *vkondrat@univ.kiev.ua*
[2] Bogolubov Laboratory of Theoretical Physics, JINR,
    141980-RU Dubna, Russia
[3] Moscow Institute of Open Education, 125167-RU Moscow, Russia

ABSTRACT. Synthesis of iron group nuclides is considered for the ultra-magnetized astrophysical plasma in supernovae. Magnetic modification of nuclear structure is shown to shift maximum of nucleosynthesis products towards smaller mass numbers enhancing titanium yield. The results are corroborated with an excess of ^{44}Ti revealed from the INTEGRAL mission data for yang supernova remnants at a field strength ranging up to 10 teratesla.

Keywords: Stars: supernovae, magnetic field. – Nucleosynthesis: abundances.

1. Introduction

Supernovae (SN) represent promising candidates for synthesis of heavy atomic nuclei and renewing other nuclear components. Nuclides produced in such processes contain an information on matter structure and explosion mechanisms. In this contribution we analyze possibilities for using radionuclides to probe internal regions of respective sites. Magnetization of hot dense plasma makes plausible explosion mechanism and can leave its trace at nucleosynthesis (cf., e.g., (Kondratyev, 2012; 2014) and refs.therein). We reveal radiatioactivity and volume of ^{44}Ti in SN remnant (SNR) Cassiopeia A (CAS A) and SN1987A from the INTEGRAL data. The observational data are compared to theoretical predictions while accounting for an influence of astrophysical environment on creation and decay of ^{44}Ti in SNR.

2. Radionuclides probing the explosion active region

Radioactive nuclides synthesized at SN events provide an opportunity to probe the interior active nuclear reaction regions. Created at the SN explosions radioisotopes can be observed by registration of characteristic gamma-lines, accompanying their radioactive transitions. The decay chain ^{44}Ti$\rightarrow$ ^{44}Sc$\rightarrow$ ^{44}Ca gives rise to the emission of lines with energies 67.9 keV and 78.4 keV (from ^{44}Sc*) and 1157 keV (from ^{44}Ca*) of approximately the same intensity. The ^{44}Ti half-life period of about 60 years allows to evaluate the mass of this isotope in SNR.
We analyze the data obtained by the INTEGRAL IBIS/ISGRI and SPI detector systems. As is described, e.g., by Kondratyev (2012) we analyze the Sciences Windows (scw) of type pointing from catalog VIRGO (http://virgo.bitp.kiev.ua). Here we discuss further results from processing of extended data sets accumulated during a period from 2002 to 2012. The total effective exposure time is about 1.5 Ms. The respective image-mosaics for

vicinity of SNR CAS A in various energy ranges of registered photons are presented in Fig. 1. The color (brightness) is proportional to the gamma-quanta flux: as larger the flux as brighter (lighter) the color of a pixel. For the first range the confidence level (i.e., ratio signal/noise) reaches the level of 40, for other energy intervals it exceeds 5 indicating reliable registration. As discussed, see (Kondratyev, 2004a; 2012; 2014) and refs therein, respective energy spectra display peaks at energies 67.9 and 78.4 keV, i.e. characteristic lines of ^{44}Sc, with total flux 10^{-4} photons/cm^2/s.
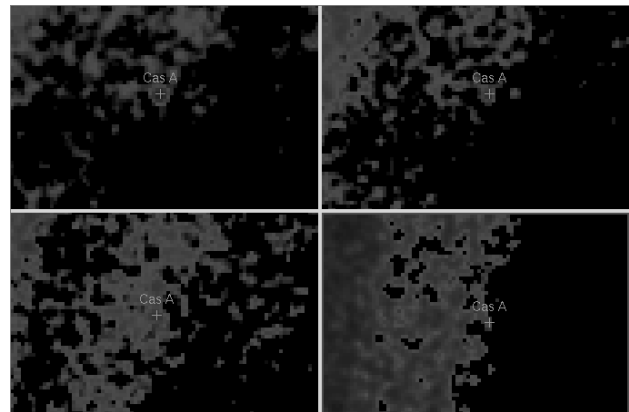
Figure 1: Direction (pixel number) dependence of the registered gamma-ray flux at different energy ranges. top: left – 20–62 keV, right – 62–72 keV, bottom: left – 72–82 keV; right – 82-100 keV; for vicinity of SNR CAS A, (J2000) R.A. 350.86°, decl. 58.81°, indicated by cross.

The corresponding flux of ^{44}Ca characteristic line revealed from INTEGRAL SPI detector system data is 0.5×10^{-4} photons/cm^2/s (Kondratyev, 2012a) displaying, thereby, very good agreement with ^{44}Sc results.

Table 1. ^{44}Ti initial mass M_{Ti}, in Solar masses M_{Sun}, for young Type II SNe.

SNR	$M_{\text{Ti}}[10^{-4} M_{\text{Sun}}]$
CAS A	$\left(3.3^{+0.9}_{-0.7}\right)$
SN1987A	3.1 ± 0.8

Accounting for a distance to SN CAS A, half-life time of isotope and an averaged over lines isotropic emission of gamma-radiation we get a mass of initially synthesized ^{44}Ti at SN explosion. Table 1 compares the results with

the one obtained by Grebenev et al. (2012) for SN1987A. The values show good agreement and exceed considerably predictions of SN models without magnetic effects. It is worthy to notice here that such a trend is met for other objects (cf., (Magkotsios et al., 2010) and refs. therein), as well.

3. Explosive synthesis of magnetized nuclei

The nuclear statistical equilibrium (NSE) approach is used very successfully for a description of abundance of iron group and nearby nuclides for over half a century, cf. (Kondratyev, 2004, 2012, 2014). We briefly recall that at NSE conditions abundance of i-th nuclear particle Y_i (e.g., nucleons, nuclei, electrons) at a temperature T is determined by the respective chemical potential from the condition of entropy S extremum. At considered parameters of SN plasma, i.e. magnetic field strengths $H < 100$ teratesla, the yield Y_i of atomic nucleus i is mainly determined by corresponding binding energy B_i as: $Y_i \sim \exp\{-B_i/kT\}$. Respectively, the dependence of relative output for nucleosynthesis products $y = Y(H)/Y(0)$ on magnetic field strength H is defined by a change of binding energy $\Delta B(H)$ in a field.. The normalized yield ratio $[i/j] = y_i/y_j$ with exponential accuracy can be written as

$$[i/j]\,(H) \sim \exp\{(\,\Delta B_j - \Delta B_i\,)/kT\}. \tag{1}$$

Since magnetic effects are determined by nuclear shell structure (Kondratyev, 2002; 2004; 2012; 2014) we identify magnetic field dependence of binding energy $\Delta B(H)$ with a change of shell correction energy C (i.e. $\Delta B(H) = C(H) - C(0)$) and use Eq. (1) to examine features of nuclide composition in ultra-magnetized astrophysical plasmas. As is shown in Fig. 2 the often considered yield ratio [Ti/Ni] displays oscillations as a function of field strength due to magic-antimagic switching in nuclear structure. At weak fields the portion of Ti grows in conjuction with observations.
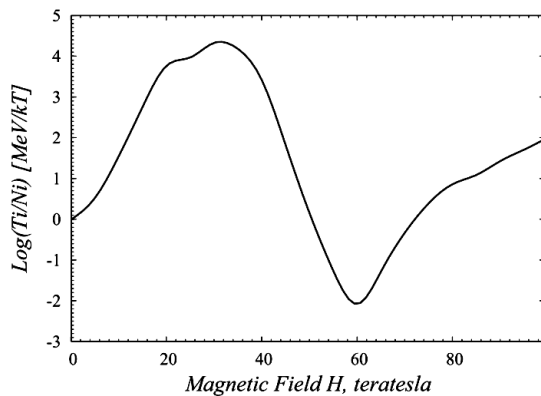
Figure 2: Magnetic field dependence of yield ratio ^{56}Ni and ^{44}Ti.

As can be seen in Fig. 2, at a typical freezing temperature of 0.1 MeV, for a formation of atomic nuclei at an expansion of nuclear matter in a jet at large entropy, magnetic effects can enhance up to an order of magnitude the yield of an isotope ^{44}Ti at a field strength from 1 to 10 teratesla. We remark that such a field ensures (Kondratyev, 2014) noticeable contribution of magnetic energy within shock wave front to total energy associated with blowing up the star material. Furthermore, magnetic pressure radial gradient is comparable with gravitational force, i.e., $dH_n^2/dR \sim 8\pi\,GM\,n(R)/R^2$, where M denotes the mass within neutrino sphere of radius R, with respective stellar matter density $n(R)$, and gravitational constant G.

4. Conclusion

We investigated an effect of the ultra-magnetized astrophysical plasma in supernovae on synthesis of chemical elements at conditions of nuclear statistical equilibrium. For iron group nuclides the magnetic modification of nuclear structure shifts a maximum of nucleosynthesis products towards smaller mass numbers approaching titanium. Direct signals of ^{44}Ti radioactive decay in the gamma-spectra and volume of the isotope in supernova remnants Cassiopeia A and SN1987A revealed from the INTEGRAL IBIS/ISGRI and SPI observational data are analyzed. Magnetic effects in nucleosynthesis are favorably compared to observational results at a field strength achieving 10 teratesla.

References

Grebenev S.A. et al.: 2012, *Nature,* **490**, 373.
Kondratyev V.N.: 2002, *Phys. Rev. Lett.,* **88**, 221101.
Kondratyev V.N.: 2004, *Phys. Rev.* C, **69**, 038801.
Kondratyev V.N et al.: 2004a, *Proc. 54th Intern.Symp. on Nuclear Spectroscopy and Structure of Atomic Nuclei* (Belgorod, Russia), p. 83.
Kondratyev V.N.: 2012, *Phys. Atom. Nucl.*, **75**, 1368.
Kondratyev V.N.: 2012a, *EPJ Web of Conf.* **38**, 17008.
Kondratyev V.N.: 2014, *EPJ A.* **50**, 7.
Magkotsios, G. et al.: 2010, *ApJS*, **191**, 66.

REVERBERATION MEASUREMENT OF THE INNER RADIUS OF THE DUST TORUS IN NGC 4151 DURING 2008-2013

V. L. Oknyansky [1], N. V. Metlova [1], O. G. Taranova [1], V. I. Shenavrin [1], B. P. Artamonov [1], C. M. Gaskell [2], Di-Fu Guo [3]

[1] Sternberg Astronomical Institute, Moscow M.V. Lomonosov State University, Moscow, Russian Federation, oknyan@mail.ru
[2] Department of Astronomy and Astrophysics, University of California, Santa Cruz, USA
[3] School of Space Science and Physics, Shandong University, Weihai, China

ABSTRACT. We investigate the correlation between infrared (*JHKL*) and optical (*B*) fluxes of the variable nucleus of the Seyfert galaxy NGC 4151 using partially published data for the last 6 years (2008-2013). Here we are using the same data as in Oknyansky et al. (2014), but include also optical (*B*) data from Guo et al. We find that the lag of flux in all the infrared bands is the same, 40 ± 6 days, to within the measurement accuracy. Variability in the *J* and *K* bands is not quite simultaneous, perhaps due to the differing contributions of the accretion disk in these bands. The lag found for the *K* band compared with the *B* band is not significantly different from earlier values obtained for the period 2000-2007. However, finding approximately the same lags in all IR bands for 2008-2013 differs from previous results at earlier epochs when the lag increased with increasing wavelength. Examples of almost the same lag in different IR bands are known for some other active nuclei. In the case of NGC 4151 it appears that the relative lags between the IR bands may be different in different years. The available data, unfortunately, do not allow us to investigate a possible change in the lags during the test interval. We discuss our results in the framework of the standard model where the variable infrared radiation is mainly due to thermal re-emission from the part of the dusty torus closest to the central source. There is also a contribution of some IR emission from the accretion disk, and this contribution increases with decreasing wavelength.

Some cosmological applications of obtained results are discussed.

Key words: AGN, optical and IR variability, time delay, data analysis, dust torus, cosmology.

1. Introduction

NGC4151 is one of the most popular and well studied AGNs. it is most bright and high variable object, which is very often used as an typical Sy1. The generally accepted model of an AGN is a supermassive black hole surrounded by an accretion disk (AD). The AD emits mostly soft X-ray, UV, optical continuum, and also gives some contribution to the near infrared. Above the AD dense clouds emit the broad emission lines. Outside this broad-line region is the narrow-line region. Variable near-IR radiation is associated with the region at a radius between the radii of the BLR and the NLR. This region is usually associated with the part of the optically-thick dusty torus closest to the central source (Hönig and Kishimoto, 2011). The presence of such a torus is the key to explaining of the observed differences in the spectra of type 1 and type 2 Seyfert nuclei by the torus eclipsing our direct view of the continuum radiation and the broad lines. It is also believed that the dusty torus radiates in the infrared, as a result of heating by shorter wavelength radiation from the central regions of the AD. Closer to the centre the dust is completely (or largely) sublimated and delayed infrared variability gives us the estimate of radius of the "dust holes" around the central source (Oknyanskij and Horne, 2001), i.e. the radius of the region where the dust is absent. The first measurement of the inner radius of the dust torus in NGC 4151 based on the cross-correlation analysis of IR and optical variability was obtained Oknyanskij (1993). Then, it was reviled that the inner radius varies depending on the luminosity of the central source (Oknyansky et al., 1989). However, these changes do not occur simultaneously, so as to restore the dust after the high luminosity states takes time. For NGC 4151 this time is at least a few years (Oknyanskij, 2006; 2008).

This work is a continuation of our series of papers in which we measure the inner radius of the dust torus in NGC 4151 and other AGNs from the delay of the variability in the near infrared to the optical (see details and references at Oknyansky et al., 2014). Despite the significant growth of theoretical and observational studies of AGN in the IR, our knowledge of the dust, its origin and the detailed morphology of these objects remain largely incomplete.
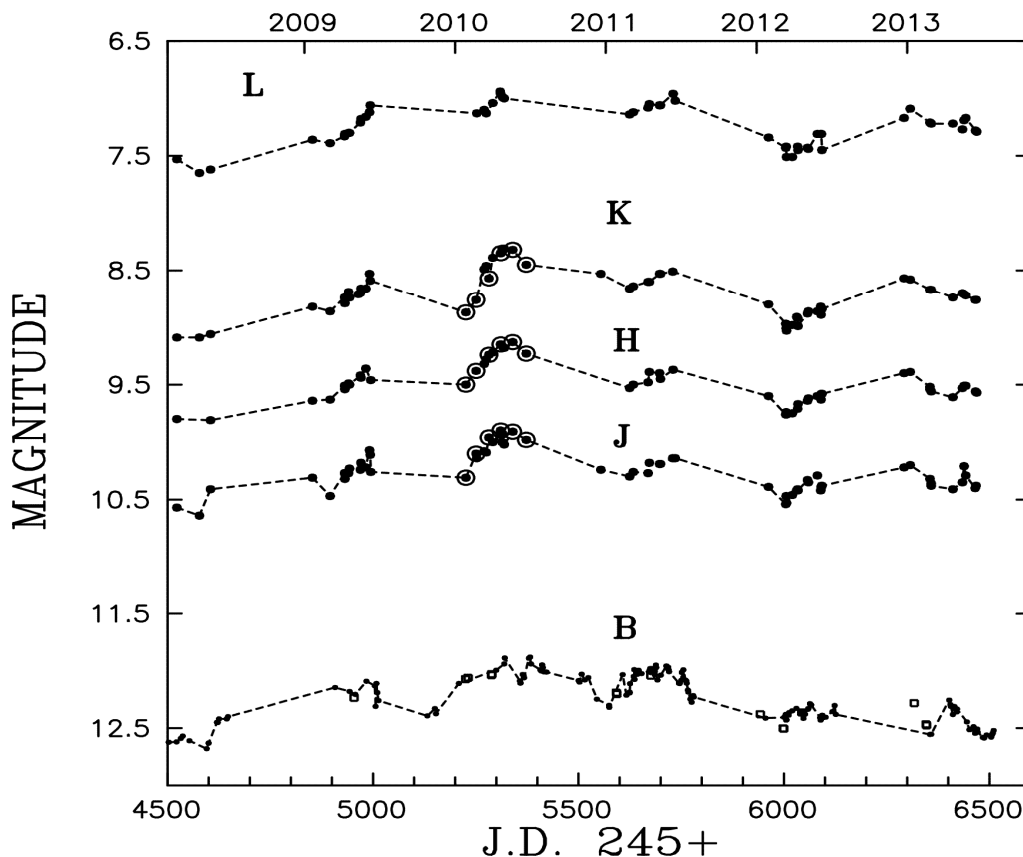
Figure 1: Infrared (***JHKL*** bands) and optical (***B***-band) light curves for 2008-2013. For the IR light curves the filled circles are our data and the open circles are the data of Schnülle et al. (2013) reduced to the same system. For the ***B***-band light curves the points are as follows: small filled circles – photoelectric and CCD measurements (our data and Roberts and Rumstey (2012), see details at Oknyansky et al. (2014)); open boxes – CCD photometry Guo et al. (2014) reduced to the same system.

2. Method of cross-correlation analysis

The inner radius of the dust torus in AGNs can be measured on the basis of cross-correlation analysis of near-infrared and optical variability. Cross-correlation analysis of astronomical time series is complicated because the sampling is usually uneven. As a rule, series of astronomical observations inevitably have gaps because of seasons when the object is invisible and interruptions due to the full moon, weather, and observing schedules. Classic cross-correlation analysis methods were developed only for uniformly sampled time series. The analysis of non-uniform astronomical series requires special techniques. At the present work we are using the method MCCF (see details and references at Oknyansky et al., 2014). At the heart of our method is the ICCF method (Gaskell and Spark, 1986), but we strive to reduce the contribution of the interpolation errors introducing certain limit *MAX* interval used for the interpolated points. We use only those interpolated points which are separated in time from the nearest observation points by no more than the value *MAX*.

3. Observational data

In this paper, we use the same observational data of IR and optical photometry for the interval 2008-2013, as in

Oknyansky (2014), but supplemented it with optical ***B*** data by Guo et al. (2014). These additional CCD observations were obtained on 15 nights using the 1.0-m telescope at Weihai Observatory of Shandong University (observed from 2009May to 2013 February). The data were reduced to the same system as in Oknyansky et al. (2014). The formal accuracy of the photoelectric and CCD measurements is not worse than 1-2%, but there may be systematic differences between measurements obtained on different instruments. We estimated that these errors do not exceed 10%. Our light curves in the *JHKL* infrared band and in the optical *B*-band are shown in Fig.1.

4. Cross-correlation analysis

Cross-correlation functions MCCF for the infrared *JHKL* bands versus the *B* band for 2008-2013 are presented in Fig. 2. It can be seen that the main peak for all of these cross-correlation functions in 36-44 days. The size of the lag between the *K* band and the optical remained almost the same as the lag we found for the period 2000-2007 (Oknyanskij et al., 2008), but the time delay for variability at ***L*** band before was significantly bigger – 105±5 days.

Figure 2: Cross-correlation functions calculated using the MCCF method with *MAX* = 30 days for *J* (dashed line), *K* (dots), *L* (solid line), versus ***B*** for 2008-2013.
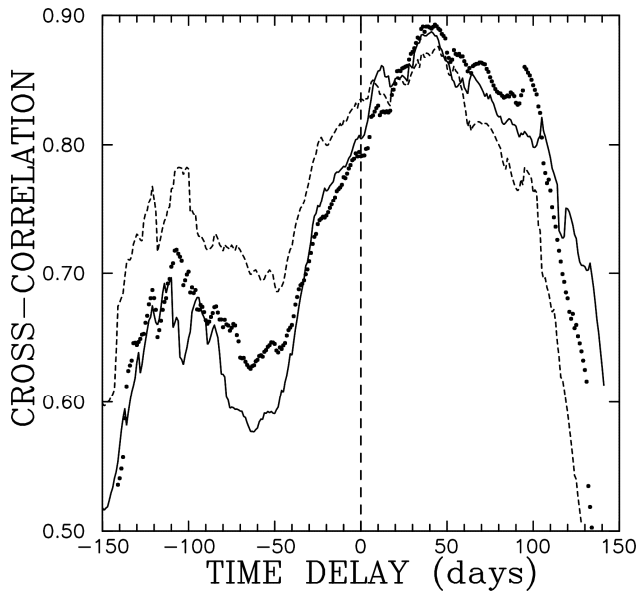
5. Cosmological applications

The ability to measure cosmological constants on the basis of the of delay of near-infrared variability relative to the optic was first mentioned by Kobayashi et al. (1998) and was independently proposed Oknyanskij (1999; 2002). At the same time it was first shown (Oknyanskij, 1999; 2002; Oknyanskij and Horne, 2001) that for a number of AGN the time delay of variability (in the ***K***-band) depends on the luminosity in the UV as $r_s \sim (L_{UV})^{1/2}$ in accordance with the theoretical result Barvainis (1987; 1992). In the recent publications Yoshii et al. (2014) and Hönig (2014) considered in details the possibility of measuring the cosmological constants on the basis of a study of delays in the IR variability. Of particular interest is the ability to measure distances to objects with large redshifts. For the case it is necessary to take into account the possible dependence of the delays from the wavelength in the IR range to make any appropriate reduction. The equation for such a reduction was derived by Oknyansky and Horne (2001) on the basis of the theory (Barvanis, 1987). However, IR delay may be not depending on the wavelength for the some part of the AGN, as well as it can be a temporary feature of a particular object, as it turned out in the case of NGC 4151. Accordingly, there is not exist any common rule for all objects to correct delays for redshift, in dispite to suggested by Oknyanskij and Horne (2001) and by Yoshii et al. (2014). Therefore, it is desirable to study variability of AGNs in several IR bands.

The presence of variability in AGNs is necessary for this method of measuring cosmological distances, although it is a particular problem, as the inner radius of the dust torus does not change in sync with changes in luminosity. Accordingly, the long-term photometric studies of objects is requested. Possible to measure the inner radius of a dust torus by infrared interferometry, but unfortunately it can be difficult or impossible for AGNs with high redshifts.

6. Conclusion

We firstly found that lags in different IR bands in NGC 4151 are approximately the same. This has been observed previously in some other AGNs, but for NGC 4151 it seems that it may be a temporary feature.

Using IR lags for cosmological applications is a very promising method, but it needs detailed investigations of optical and IR variability of selected AGNs as well as improved theoretical models.

References

Barvainis, R.: 1987, *Ap. J.* **320,**537.
Barvainis, R.:1992 *Ap. J.* **400**, 502.
Guo D.F. et al.: 2014, *Res. in A&A*., **14**, 923.
Gaskell, C. M; Sparke, L. S.:1986, *Ap. J.* **305**, 175.
Hönig S.F. ; Kishimoto M. 2011: *A&A,*. **524**, A121.
Hönig S.F.: 2014, *Ap. J.Lett.,* **774**, L4.
Kobayashi Y. et. al.:1998, *Proc. SPIE,* **3352**, 120.
Oknyansky V.L. et al.: 2014, *Astron. Lett.,* **40***,* 527.
Oknyanskij V.L. et al.: 2008, OAP, **21**, 79.
Oknyanskij, V. L.; Horne, K.:2001, *ASP Conf. Proc.* **224,** 149.
Oknyanskij V.L. et.al.:2006, *ASP Conf. Ser.* **360**, 75.
Oknyanskij, V.L:1993 *Astron. Lett.* **19**, 416.
Oknyanskij V.L. et.al.:1999, *Astron. Lett.* **25**, 483.
Oknyanskij V.L.:2002, *ASP Conf. Proc.*, **282**, 330.
Roberts C.A., Rumstey, K. R.:2012 *J. South. Associat. Res. Astron.* **6**, 47.
Schnülle A. et al.: 2013, *A&A*, **557,** L13.
Yoshii Y. et al.:2014, *Ap.J.Lett.*, **784**, L11.

PHOTOMETRICAL STUDY
OF OVERCONTACT BINARY SYSTEM V859 Cyg

E.A. Panko[1,2], O.G. Sergienko[1], A.V. Pomazan [3], D.V. Bodryagin[3]

[1] V.O. Suckomlinsky Nikolaev National University,
Nikolaev, Ukraine *panko.elena@gmail.com*

[2] Visiting Astronomer, Department of Astronomy, Saint Mary's University,
Halifax, Nova Scotia, Canada

[3] RI Nikolaev Astronomical Observatory, Nikolaev, Ukraine

ABSTRACT. We present the results of photometrical research of close binary system V859 Cyg with possible period variations. The light curve of the star was constructed using V-band magnitudes, obtained in 2007, 2009, 2014 years in Kalinenkov Astronomical Observatory of Nikolaev National University (Nikolaev, Ukraine). According our full light curve both eclipses are partial, the depths of primary and secondary minima in V-band are $0^m.38$ and $0^m.32$ respectively. We found 9 new time minima. However, the standard ephemeris of primary eclipse corresponds to our secondary minimum and vice versa during all observational seasons.

We obtained the parameters of binary system from light curve using Binary Maker 3 package. The inclination of orbit of V859 Cyg system is $64.°5$. The temperatures of components are $T_{effI} = 7100K$, $T_{effII} = 6850K$ and mass ratio is 0.35. Both components are deformed by mutual gravity and overfill own Roshe lobes, fillout factor is 0.875 for both stars. Mean radii of components are 0.51 and 0.33 of distance between stars. We attributed V859 Cyg as overcontact system with stable period $0.^d4050066$.

Key words: Stars: eclipsing: close binary stars: individual: V859 Cyg.

1. Introduction

Eclipsing binary system V859 Cyg ($RA_{2000} = 19^h27^m12^s.7$, $DEC_{2000} = +28°56'50''$, $V_{max} = 11^m.7$, $V_{min} = 12^m.2$, $JDH_{minI} = 2434629.4141 + 0.40500132E$, EW/KW-type) according to GCVS database (Samus et al., 2012) was described as variable by Wachmann (1963). We include the star V859 Cyg in our program of observations as scantily explored close binary system with possible period variations. The program stars were selected from 1140 eclipsing binaries with period variations, collected by Kreiner et al. (2000). The results of the investigation of some program binaries such as CU Peg, V609 Aql, BM UMa and V841 Cyg were published (Panko et al., 2006, Turner at al., 2008, Virnina et al., 2010, Sergienko et al., 2013). O–C diagram for V859 Cyg according to Kreiner et al. (2000) included only 17 time minima, but suggest some systematic period variations. In the "Up-To-Date Linear Elements of Eclipsing Binaries" (Kreiner, 2004) the 15 new time minima of the star were added and updated elements was calculated: $HJD_{minI} = 2452500.0759 + 0.4050066E$. The full set of time of minima collected in the "Variable Star and Exoplanet Section of the Czech Astronomical Society" database (O–C Gateway) includes 75 time minima and their O–C values according elements $HJD_{minI} = 2434629.4141 + 0.4050019E$. The full light curve of V859 Cyg was obtained in "The First INTEGRAL/OMC Catalogue of optically variable sources" (Alfonso-Garzon et al., 2012). From Optical Monitoring Camera (OMC) onboard INTEGRAL data they found the period of V859 Cyg, videlicet 0.40501036 with error 0.000017. Hoverer, full light curve of the star was not analyzed.

2. Observations

The observational data were obtained using the 70-cm telescope ZTS-702 of AOK, equipped with a SBIG ST-7 camera in an instrumental photometric system closely approximating the standard V-band. The focal length of the telescope is 2.806 m and CCD-frame corresponds to $5' \times 8'$ sky area. V859 Cyg was observed in July of 2007, 2009 and 2014. Frames were taken with 60 and 90 sec exposure time, S/N ratio for variable was in limits $14 - 45$. The standard reduction included dark signal and flat field correction was executed for all frames. Barycentric Julian Dates (HJD) were calculated using Eastman et al. (2010) code. We carried out the aperture photometry realized in the MUNI-
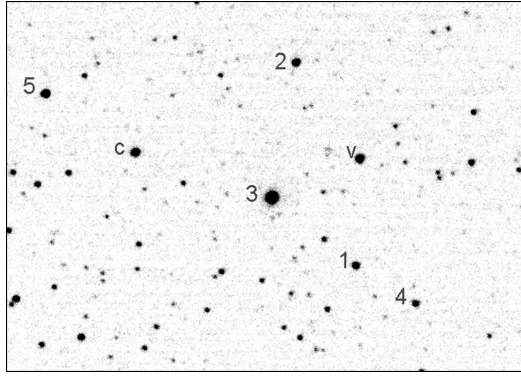
Figure 1: The reference stars in V859 Cyg frame.

Table 1: The reference stars for V841 Cyg frame.

N	TASS 4	V	SD
c	1839447	$11^m.901$	$0^m.101$
1	1839414	12.840	0.178
2	3488546	12.471	0.112
3	3136596	9.709	0.058
4	3136587	13.500	0.332
5	1839453	11.915	0.099

PACK software (Motl, 2003-2012). The package allows to determine the difference in magnitudes between comparison, control and variable stars. We assumed equal air mass for all stars in our small frames. The background has been estimated from neighboring pixels. The *SD* for individual relative magnitudes was not worse $0^m.040$. The reference stars were found in the TASS Mark IV photometric catalog, version 2 (Droege et al., 2007). The positions of variable, comparison and 5 control stars are shown in Fig. 1; the magnitudes and TASS Mark IV number of the stars are placed in the Table 1. The observed and synthetic light curves are shown in Fig. 2. The new time minima and their *O–C* according to elements from *O–C* Gateway are placed in the Table 2. The full light curve allows as to determine the depths of primary and secondary minima and to reconstruct of the system parameters. Our *O–C* values are in good agreement with Kreiner (2004) elements, but with 0.5-period correction, as it shown in Fig. 2. Note, modern set of observations gives linear dependence in *O–C* variations.

3. Light curve analyze and discussion

From the analysis of V859 Cyg light curve we obtained $\Delta m_I = 0^m.38$, $\Delta m_{II} = 0^m.32$ in *V*-band. The $B - V$ values of V859 Cyg varies from 0.1 (Hog et al.,
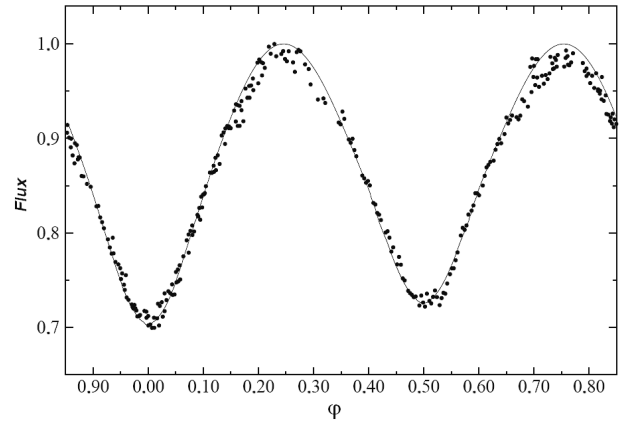
Figure 2: The light curve solution for V859 Cyg. Observational data are marked as dots, our final solution curve is line.

2000) to 0.224 (Kharchenko, 2009) and we assumed an initial effective temperature for the primary $T_{effI} = 7600K$. We modeled the light curve for V851 Cyg using Binary Maker 3 and *Catalog and Atlas of Eclipsing Binaries* (CALEB *http://caleb.eastern.edu/*) along with reasonable estimates for the properties of the two components. The temperature of the secondary of V859 Cyg was established through analysis of the light curve. The final solution was chosen in model grids calculated with steps: 0.01 in mass ratio and Ω-potentials, $50K$ in temperature and $0.25°$ in inclination. The linear limb darkening coefficients were assigned according to van Hamme (1993) as 0.598 for both components taking into consideration the final temperatures.

Table 2: V859 Cyg new time minima.

HJD_I	HJD_{II}
2454288.38378	2454291.42123
2454292.43403	2455033.39398
2455019.41972	2455041.49424
2455034.40568	2456868.47254
2456867.45999	

The best solution implies $T_{effI} = 7100K$ and $T_{effII} = 6850K$, mass ratio 0.35, mean radii of components are 0.51 and 0.33 of distance between stars. Both eclipses are partial and inclination of V859 Cyg system is $64.°5$. Both components are deformed by mutual gravity and overfill own Roshe lobes: fillout factor is +0.875 for both stars. The system reconstruction on phase 0.25 in shown in Fig. 3. We attributed V859 Cyg as overcontact system. In *A Catalogue of Approximate Photometric and Absolute Elements of Eclipsing Variable Stars* (Svechnikov & Kuznetsova, 1990) V859 Cyg is W UMa system with mass ratio 0.39 and inclination $73.°5$. Spectra SP1+SP2 are (F1)+[F2],
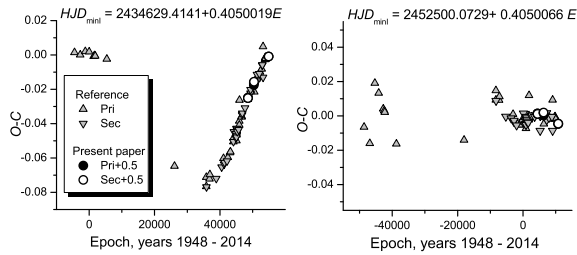
Figure 3: *O–C* variations of V859 Cyg system in 1948–2014 accoding to *O–C* Gateway (left panel) and Kreiner (2004) elements.

Figure 4: The view of reconstructed V859 Cyg system in phase 0.25.

and radii of the components 0.465 and 0.265 of the distance between stars. The data for V859 Cyg in the Catalogue by Svechnikov & Kuznetsova (1990) based on the GCVS and reference data have accuracy remark 1 in (0–9 scale), i.e. rough. Our reconstruction of the system improves the parameters of V859 Cyg.

4. Conclusion

From three seasons of observations we obtained 9 new time minima for W UMa type binary V859 Cyg. We found the positions of the primary and secondary minima of the light curve are checked on the 0.5 of period, so elements HJD_{minI} corresponds to secondary minima. The depths of minima in V-band are for primary $0^m.38$ and for secondary $0^m.32$. The inclination of orbit of V859 Cyg system is 64.°5. The temperatures of components are $T_{effI} = 7100K$, $T_{effII} = 6850K$ and mass ratio is 0.35. Both components are deformed by mutual gravity and overfill own Roshe lobes, fillout factor is 0.875 for both stars. Mean radii of components are 0.51 and 0.33 of distance between stars. We attributed V859 Cyg as overcontact system. The elements $HJD_{minI} = 2452500.0729 + 0.4050066E$ (Kreiner, 2004) give the best value of the period without systematical variations, but describe the secondary minima times.

References

Alfonso-Garzon J., Domingo A., Mas-Hesse J.M. et al.: 2012, arXiv:1210.0821v2, on-line data: *http://sdc.cab.inta-csic.es/omc/var/2137000064.html*

Binary Maker 3: *http://www.binarymaker.com/*

CALEB: *http://caleb.eastern.edu/*

Droege T.F., Richmond M. W., Sallman M. P. et. al.: 2006, *Publ. Astron. Soc. Pac.*, **118**, 1666, on-line data: *http://spiff.rit.edu/tass/patches/*

Eastman J., Siverd R., Gaudi B.S.: 2010, *Publ. Astron. Soc. Pac.*, **122**, 935.

Hog E., Fabricius C., Makarov V.V. at al.: 2000, *A&A*, **355** L.27.

Kharchenko N.V.: 2001, *KFNT*, **17**, 409.

Kreiner J.M., Kim C.H., Nha L.S. et al.: 2000, "An Atlas of *O–C* Diagrams of Eclipsing Binary Stars", Krakow, Poland, on-line data: *http://www.as.up.krakow.pl/o-c/index.php3*

Kreiner J.M.: 2004, *Acta Astronomica*, **54**, 207.

Motl D.: 2003-12, *http://c-munipack.souceforge.net O-C Gateway*, on-line data: *http://var.astro.cz/ocgate/*

Panko E., Flin P. & Pikhun A.: 2006, *ApSS*, **305**, 385.

Samus N.N., Durlevich O.V., Kazarovets E.V. et al.: 2012, *General Catalog of Variable Stars, GCVS (GCVS database)*, Version 2012 Feb., *http://www.sai.msu.su/groups/cluster/gcvs/gcvs/iii/html/*

Sergienko O.G., Bodryagin D.V., Panko E.A.: 2013, *Odessa Astron. Publ.*, **23**, 148.

Svechnikov M. A. & Kuznetsova E.F.: 1990, *A Catalogue of Approximate Photometric and Absolute Elements of Eclipsing Variable Stars*, Ural University Press, Sverdlovsk, *http://cdsarc.u-strasbg.fr/viz-bin/ftp-index?/ftp/cats/v/124*

Turner D.G., Panko E.A., Sergienko O.G. et al.: 2008, *The Observatory*, **128**, 2.

Virnina N.A., Panko E.A., Sergienko O.G. et al.: 2010, *OAP*, **23**, 148.

van Hamme W.: 1993, *AJ*, **106**, 2096.

Wachmann A.A.: 1963, *Astron. Abh. Hamburg. Sternw.*, **6**, 97.

Subsection　Virtual observatories are practice of application

COMPILATION OF CATALOG OF STELLAR EQUATORIAL COORDINATES AND B-MAGNITUDES USING UKRVO PLATE DATABASE

V.N.Andruk [1], V.V.Golovnya[1], G.A.Ivanov[1], E.M.Izhakevich[1], L.K.Pakuliak[1], Yu.I.Protsyuk [2], S.V.Shatokhina[1], A.I.Yatsenko[1], M.M.Muminov[3]

[1] Main Astronomical Observatory of the National Acad. of Sciences of Ukraine, 27 Akademika Zabolotnoho St., 03680, Kyiv, Ukraine, *andruk@mao.kiev.ua*

[2] Research Institute "Nikolaev Astronomical Observatory", 1 Observatornaya St., 54030, Mykolaiv, Ukraine, *yuri@mao.nikolaev.ua*

[3] Ulugh Beg Astronomical Institute of the Uzbek Academy of Sciences 33 Astronomicheskaya St., 100052 Tashkent, Uzbekistan

ABSTRACT. To ensure the rational use of informational resources generated by UkrVO in MAO NASU, a catalog of equatorial coordinates (α, δ) and B-magnitudes of stars was created by using plates obtained during observational campaign named FON (ukr., Photographic Sky Survey). 102 plates with field of view of 8° were processed. Digitization of plates with sizes of (30x30) cm or (13000x13000) px was performed by using resolution of 1200 dpi. The catalog contains astrometric data for 1,263,932 stars and galaxies with B $\leq$ 16.5^m at epoch 1984.76. The coordinates and B magnitudes were respectively obtained in the system of TYCHO-2 catalog and photoelectric standards. The internal accuracy of the catalog: for all objects is ±0.26" for coordinates and ± 0.17^m for magnitudes, and for stars in the range B = 8^m -13^m is ± 0.13" and ± 0.11^m. Convergence of coordinate with reference TYCHO-2 system is ±0.06" (for 93 925 stars), the convergence with the photoelectric stellar B-magnitudes is ±0.16^m (for 4458 stars). Errors relative to the UCAC-4 catalog are ±0.34". We identified 1099005 stars and galaxies.

Key words: virtual observatory tools – astrometry – techniques: photometric – methods: data analysis – catalogs

1. Introduction

At the end of 2013, more than 2000 astro negatives obtained during the program of Northern Sky Photographic Survey (FON) were digitized by using the UkrVO database (Kislyuk, 2000, Vavilova, 2012). Approximately one-third of the plates were digitized by the scanner Microtek ScanMaker 9800XL, others – on the scanner Epson Expression 10000XL (Andruk, 2005, Andruk 2007, Andruk, 2010, Golovnya, 2010). With the help of specially designed software for environment LINUX / MIDAS / ROMAFOT, we obtained rectangular coordinates and the photometric values for all objects and scans (www.eso.org/sci/software/esomidas). Basic software was developed by the Department of astrometry at the MAO of NASU in order to obtain the equatorial coordinates and magnitudes of astronomical objects, and has been successfully applied in practice described in a series of papers (Yatsenko, 2011, Protsyuk, 2014). As shown by subsequent experience of reduction of digitized plates, some astro negatives have to be rescanned and reprocessed. In part of this work, we studied the accuracy of astrometry and photometry.

On the base of 102 scans, we obtained the second version of the catalog of positions and B-values of stars (Yatsenko, 2011). The zone of 8° in declination along the 60° parallel was observed using the principle of quadruple overlap. The plates were exposed by using the Double Wide-angle Astrograph (D/F = 40/200, 103 "/mm) of the MAO of NASU. Most plates for this zone are (30x30) cm in size (8°x8°). All plates were scanned with a resolution of 1200 dpi by using Microtek and Epson scanners, the size of images was up to (13000x13000) px (1px = 2.17"). The second version of the catalog was derived from the processing of single scans without turning the plates on 90°. As the result, an amount of resources to store and process information was reduced twice without compromising the accuracy of the results.

2. Accuracy of scanners

We examined Microtek and Epson scanners to study the astrometric and photometric accuracy. Comparison of errors in the determination of equatorial coordinates for the two scanners gave the following result: astrometric and photometric errors of the Epson scanner is 25% less than of the Microtek scanner. Compiled catalog of Microtek and Epson scanners shows coordinate errors about 10% less than the expected errors and internal errors of convergence. Magnitude errors are a few times less than the expected errors and internal errors of convergence. Developed and applied software allows us to perform high-precision reduction of data to obtain equatorial coordinates and magnitudes.

3. The results of data processing

Normal scanning means that the Y-axis direction of movement is parallel to the axis of the equatorial coordinates of δ. When the plate is rotated on 90°, it implies that the Y axis is parallel to the axis of α. The

TYCHO-2 catalog was used as the reference system for the identification and correction of systematic errors caused by scanners and optical aberrations of telescopes. Normal scanning gives us the error for the equatorial coordinates about 25% less than for scanning with rotation on 90°. This is an expected result, since the scanning with rotation on 90° suggests that the uneven movement of the CCD line scanner (coordinate Y) coincides with the change in the scale of the plate by α relative to the lower and upper parts of the plate. For greater statistical reliability, the results were separately processed for scans of 23 plates with 4-fold overlap, i.e. we obtained two catalogs for testing on 437946 and 433726 stars for two positions of the plate. The overlap zone is 18h to 24h in α, 56° to 60º in δ. Third catalog was obtained by averaging the data of equatorial coordinates and magnitudes of the first two catalogs for 391852 stars. For the third catalog internal coordinate errors were decreased by about 40-50%, and internal magnitude errors were decreased by several times. All three test catalogs were compared with the TYCHO-2 as reference catalog. Number of common stars for them respectively: 28981, 28830 and 28758. Analysis of the errors gave us the following result: scanning the plates with rotation on 90° leads to an increase of errors by 20% in the determination of equatorial coordinates relative to the reference system of TYCHO-2. To check the error of the external convergence, we also made comparison of the three catalogs with the UCAC4 catalog (Zacharias, 2013). Number of common stars for the three catalogs are 372487, 369744 and 363584 respectively. Note that the external convergence of the coordinate errors for the averaged catalog about 10% less than for the individual catalogs. A separate analysis of the distribution of errors in determining the coordinates gave the following result: value of errors for faint stars is strongly dependent on the diameter (FWHM) of stellar images. The values of errors begin to grow for about 8 pixels in FWHM, which corresponds to B ≈ 12^m.

The plates obtained during the FON program were exposed for: 16 to 20 minutes and 30 to 60 seconds, long and short exposure respectively. To create a catalog, we must exclude the images with short exposure from data processing at an early stage, prior to the procedure of reduction of rectangular coordinates X, Y in the equatorial coordinates α, δ (Andruk, 2012).

We paid special attention to take into account the magnitude equation (mdtX, mdtY) for calculating tangential coordinates ξ, η. We took into account the magnitude equation for stars brighter than B ≈ 11^m. Analysis showed us that the magnitude equation is linear for brightness diameters and B-values and have second order for instrumental photometric values.

The combination of characteristic curves for both exposures allowed us to obtain the characteristic curve for the entire range of magnitudes. Photoelectric catalogs (Kornilov, 1991; Mermilliod, 1991) were used as the photometric standards. Stages and principles used to obtain the characteristic curve will be presented later due to the lack of space in this paper. The accuracy of the characteristic curve is σ = 0.115^m, a contrast ratio of emulsion is γ = -0.763 (37º).

4. Catalog

The second version of the catalog was created on the basis of data processing after the normal scanning. The first version of the catalog includes 1,108,603 stars and galaxies, and was created in 2011, using the combined data from the two versions of the scan (Yatsenko, 2011). The second version of this catalog contains 1,263,932 stars and galaxies up to $B_{ph} \leq 16.5^m$ (photographic magnitudes in the Johnson system) at epoch 1984.76 ± 0.50. The catalog was obtained after processing of 102 plates, mostly (30x30) cm in size or (13000x13000) px. Total number of objects (stars, galaxies, artifacts, etc.) were more than 7.2 million. Identification and selection of candidates for stars and galaxies for overlapping plates was carried out according to the following criteria: 1) objects should have the same equatorial coordinates ± half of the pixel size in seconds of arc (0.5px ≈ 1.1"); 2) magnitude difference of objects should not exceed ± 2^m. If the candidate met selection criteria for at least two plates, the object is counted in the catalog.

The internal accuracy of the catalog for all objects is ±0.26" for coordinates and ±0.17^m for magnitudes. For stars in the range of B= 8^m -13^m errors are ± 0.13" and ± 0.11^m. For the TYCHO-2 reference stars, astrometric error does not exceed the value of ±0.060".

Also, we made comparison of the equatorial coordinates between our catalog and UCAC-4 catalog. We identified 1099005 common stars and galaxies. Coordinate errors between our catalog and the UCAC4 is $\sigma_{\alpha\delta} = \pm 0.34$".

Photometry error was determined by comparing the magnitudes of our catalog with the photoelectric one of reference catalogs (4457 common stars). Photometry error is equal to ± 0.16^m.

References

Andruk V. et al: 2005, *Kinematika i Fizika Nebesnykh Tel*, **21, N5**, 396 (in Russian).

Andruk V.et al: 2007, *Journal of Physical Studies*, **11, N3**, 329.

Andruk V.M. et al: 2010, *Kinematics and Physics of Celestial Bodies*, **26, N3**, 146.

Andruk V.M. et al: 2012, *Kyiv Univ.Messenger. Astronomy*, **48**, 11 (in Ukrainian).

Vavilova I.B. et al.: 2012, *Kinematics and Physics of Celestial Bodies,* **28, N2**, 85.

Golovnya V. et al: 2010, *Journal of Physical Studies*, **14, N2**, 2902

Kislyuk V.S. et al.: 2000, *Kinematika i Fizika Nebesnykh Tel,*, **16, N6**, 483 (in Russian).

Protsyuk Yu.I. et al.: 2014, *Kinematics and Physics of Celestial Bodies*, **30**, **N6**, 296.

Yatsenko A.I. et al.: 2011, *Kinematics and Physics of Celestial Bodies*, **27, N5**, 249.

Kornilov V.G., Volkov I.M., Zakharov A.I., et al.: 1991, *Trudy GAIS*, **63**,1 .

Mermilliod J.C.: 1991, Homogeneous means in the UBV system.

Vavilova I.B., Pakuliak L.K., Protsyuk Yu.I., et al.: 2012, *Baltic Ast.*, **21, N3**, 356.

Zacharias N., Finch C.T., Girard T.M., et al.: 2013, *Astron. J.*, **145**, 44.

COMPARATIVE ANALYSIS OF PROPER MOTIONS OF STARS IN OPEN CLUSTERS BY USING VO TOOLS

A. Mazhaev [1], Yu. Protsyuk [2]

Research Institute "Nikolaev Astronomical Observatory", Mykolaiv, Ukraine
[1] *mazhaev@mao.nikolaev.ua,* [2] *yuri@mao.nikolaev.ua*

ABSTRACT. Astrometric catalogues such as Tycho2, Mobitel1, CSOCA, XPM, PM2000, SDSS-DR9 were used for cross identification of stars, visualization of proper motions and further data processing by using available Virtual Observatory (VO) Tools: cross-match service (CDS, Strasbourg), TopCat, Aladin. The coefficients of linear correlation for common stars as well as the standard deviations for differences of proper motions were determined for at least ten pairs of catalogues to compare the accidental errors and the systematic biases between the given data sets.

Key words: open clusters and associations: general – proper motions – virtual observatory tools

1. Introduction

Stars in open clusters of our Galaxy have been studied for more than fifty years to determine cluster membership probabilities for each star and astrophysical parameters for each cluster. Modern VO tools enable us to carry out quick and easy comparative analysis of stellar proper motions (PM) taken from different astrometric catalogues by using cross identification of stars, necessary data processing, graphic presentation of data, visualization of PM. The main aim of this work is to apply new possibilities in comparative analysis of stellar PM by using VO tools.

2. Cross Identification of Stars

There are several possible ways to carry out cross identification of stars by using VO tools such as xMatch, TopCat [5], Aladin [1]. New version of TopCat (version 4.2) released in July, 2014 contains the new CDS xMatch window, which enables us to match a loaded local table or catalogue against any VizieR or SIMBAD table.

3. Correlation of Proper Motions

Mobitel1 catalogue [3] contains astrometric data for 620 967 stars in the range of 8.0 to 17.5 for R magnitude. PM were derived from comparison of stellar positions taken from: USNO-A2.0 catalogue and CCD observations obtained with the Mobile Telescope (Mobitel) [4] in Mykolaiv in 2011-2012 years. TopCat helps us to obtain parameters of linear correlation (LC) for PM of stars in right ascension (RA) – $\mu_\alpha \cdot \cos\delta$ and declination (DE) – μ_δ for 550065 common stars. The coefficients of LC in $\mu_\alpha \cdot \cos\delta$ and μ_δ are equal to 0.9 meaning that 81% of common stars have the same direction of PM. The slopes of LC lines for $\mu_\alpha \cdot \cos\delta$ and μ_δ are 1.5 and 1.2 respectively.

It means that in general the XPM catalogue [2] has larger values of PM than Mobitel1 at 1.5 times in $\mu_\alpha \cdot \cos\delta$ and at 1.2 times in μ_δ. Aladin enables us to visualize PM of common stars for Mobitel1 and XPM catalogues and to check direction and value of PM for any of them (Fig. 1).
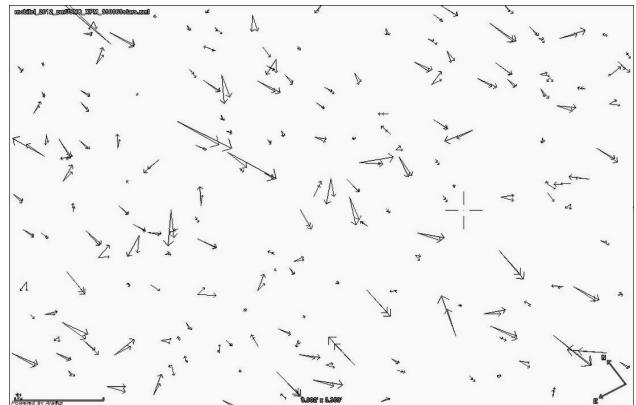
Figure 1: Visualization of PM for common stars

4. Differences of Proper Motions

TopCat facilitates us to compute and check differences of PM versus stellar magnitude, RA, and DE using its interactive possibilities. The synthetic column window easily enables us to compute the differences of stellar PM as well as to calculate any other value defined by any algebraic expression based on the values of other columns in the same row. The differences in the sense of Mobitel1 minus XPM were deliberately computed between absolute values of PM to show the systematic bias for the slope of LC lines in $\mu_\alpha \cdot \cos\delta$ and μ_δ (Fig. 2).

The so-called magnitude equation as the harmful function between PM (or positions) and stellar magnitudes may be caused by systematic errors such as: optical aberrations and guiding errors in combination with the nonlinear response of the photographic emulsion, charge transfer inefficiency (CTI) of the charge-coupled devices (CCD), image displacement due to curvature of star trails and drift rate variations during CCD observation in drift-scan mode with a stationary telescope, displacement of star image due to atmospheric differential refraction.

We have to check this function as the potential source of systematic bias. TopCat helps us to calculate the mean differences in $\mu\alpha \cdot \cos\delta$ – filled circles and $\mu\delta$ – empty squares (Fig. 3) and to graph them versus R magnitude.

The standard deviations are presented as the error bars for both mean differences: μα •cosδ and μδ.
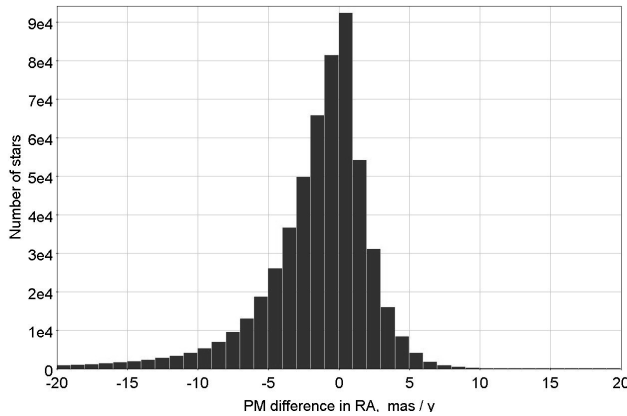
Figure 2: Differences of $\mu_\alpha \cdot \cos\delta$ vs number of stars

Figure 3: Mean differences in $\mu_\alpha \cdot \cos\delta$ and μ_δ vs R mag

Numbers of stars used for calculations of the mean differences are given on the left side from the mean values. The Mobitel1 catalogue was obtained using observations with CCD and photo plates. The XPM catalogue was obtained using observations with photo plates. Images of stars obtained with the CCD may be distorted in RA because of the CTI. At the same time, images of faint stars are less distorted due to smaller number of photons registered by the CCD. That is why the mean differences in $\mu_\alpha \cdot \cos\delta$ have a systematic trend with decreasing values for faint stars (Fig. 3). TopCat also enables us to calculate the mean differences between values of PM in $\mu_\alpha \cdot \cos\delta$ and μ_δ and to graph them as a function of declination (Fig. 4). The mean differences in the range of declinations from -5° to +30° are the smallest ones. Large differences in the range below -15° may be caused by atmospheric differential refraction and street light pollution in Mykolaiv. Large differences in the range above +33° may be caused by image displacements due to curvature of star trails and variations between apparent angular velocity of star and velocity of charge transfer during CCD observation. The velocity of charge transfer is constant for all columns of CCD pixels, and the apparent angular velocity of star is dependent on declination. Therefore, all stars within CCD frame were observed with the same velocity of charge transfer although the real angular velocities of stars are varied in declination. TopCat facilitates us to calculate the mean differences in $\mu_\alpha \cdot \cos\delta$ – filled circles and μ_δ – empty squares and to graph them as a function of declination (Fig. 4). The standard

deviations are presented as the error bars for both mean differences: $\mu_\alpha \cdot \cos\delta$ and μ_δ (Fig. 4).
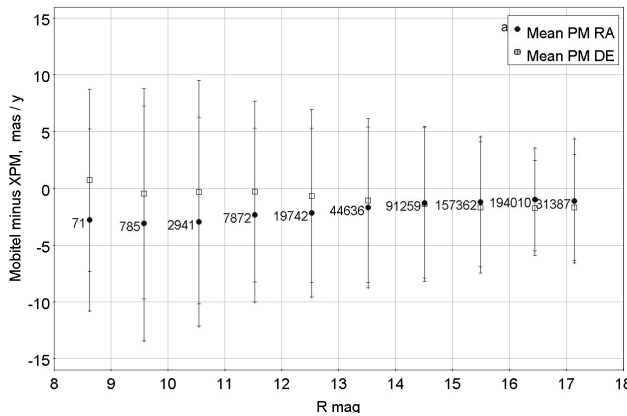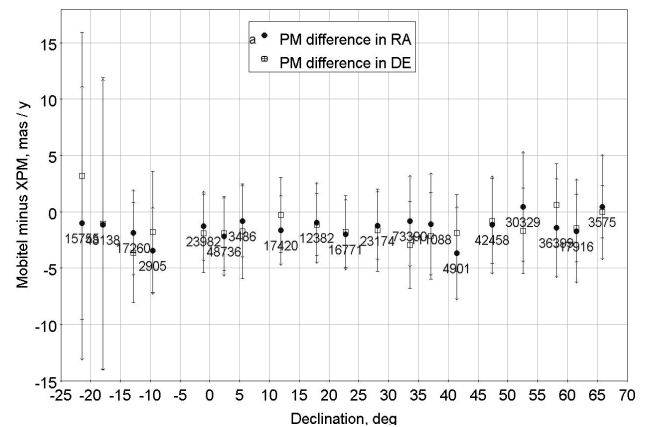

Figure 4: Mean differences in $\mu_\alpha \cdot \cos\delta$ and μ_δ vs DE

Numbers of stars used for calculations of the mean differences for each of 5° zone in declination are given below of the filled circles.

Conclusions

The main aim of this work was to apply new possibilities in comparative analysis of stellar PM by using VO tools. We have shown some results of comparative analysis for two astrometric catalogues. We also carried out comparative analysis for at least ten pairs of other catalogues, and the detailed results are not given in this paper due to the lack of place. Such catalogues as CSOCA and PM2000 have strong correlation with Tycho2 catalogue, because they were reduced in the system of the ICRS. The coefficients of LC in $\mu_\alpha \cdot \cos\delta$ and μ_δ are equal to 0.99, and the standard deviations for differences of PM are 0.8 mas/a for CSOCA and 2.4 mas/a for PM2000. The Mobitel1 and XPM catalogues have not such a strong correlation with the Tycho2 catalogue.

The work is conducted in frame of the UkrVO [6–9].

References

1. Bonnarel, F. et al.: 2000, *A&AS*, **143**, 33.
2. Fedorov P. N. et al.: 2010, *MNRAS,* **406**, 1734.
3. Protsyuk, Yu.I. et al.: 2014, *Kinematics and Physics of Celestial Bodies*, **30**, **N6**, 296.
4. Shulga A.V. et al.: 2012, *Kosmichna Nauka i Tekhno-logiyaKNiT*, **18**, 52.
5. Taylor, M. B. : 2005, *XIV ASP Conf. Series*, **347**, 29.
6. Vavilova, I.B. et al.: 2012*, Kinematics and Physics of Celestial Bodies*, **28**, 85.
7. Vavilova, I.B. et al.: 2012, *Baltic Astronomy*, **21**, 356.
8. Vavilova, I.B. et al.: 2011, *Kosmichna Nauka i Tekhno-logiya*, **17**, 74.
9. Vavilova, I.B. et al.: 2010, *Kosmichna Nauka i Tekhno-logiya*, **16**, 62.

ASTROMETRY OF X AND H PERSEI BASED ON PROCESSING OF DIGITIZED PLATES OF ARCHIVE OF THE ASTRONOMICAL INSTITUTE OF THE ACADEMY OF SCIENCES OF THE REPUBLIC OF UZBEKISTAN

M.M.Muminov [1], Q.X.Yuldoshev [1], Sh.A.Ehgamberdiev [1], B.B.Kahharov [1], V.N.Andruk [2], Yu.I.Protsyuk [3]

[1] Ulugh Beg Astronomical Institute of the Uzbek Acad. of Sciences,
33 Astronomicheskaya St., 100052 Tashkent, Uzbekistan, *muminov_mm@mail.ru*
[2] Main Astronomical Observatory of the Nat. Academy of Sciences of Ukraine,
27 Akad. Zabolotnoho St., 03680, Kyiv, Ukraine, *andruk@mao.kiev.ua*
[3] Research Institute "Nikolaev Astronomical Observatory",
1 Observatornaya St., 54030, Mykolaiv, Ukraine, *yuri@mao.nikolaev.ua*

ABSTRACT. Work is done with Epson Expression 10000XL scanner of Astronomical Institute (AI) of the Academy of Sciences of Uzbekistan. The plates were exposed with the Normal astrograph (D/F = 330mm / 3467mm, M = 59.56"/mm). The digitization of plates with (16x16) cm in size was made with resolution of 1200 dpi (1px = 1.25"). Test research was done using plates at first (1935.0) and second (1976.9) epochs in the sky area around the χ and h Persei clusters (field of view is 2°x2°). Coordinates and B-magnitude of stars were obtained using TYCHO-2 as the reference catalog. Errors of coordinate differences and proper motions for reduced and reference stars are respectively $\sigma_{\alpha\delta} = \pm 0.074"$ and $\sigma_{\mu\alpha\delta} = \pm 0.0018"$/year (655 stars). Errors of photometry are $\sigma_m = \pm 0.065^m$ and $\sigma_B = \pm 0.208^m$ for internal convergence and in comparison with TYCHO-2 catalog. Comparison with UCAC4 catalog for 8123 stars with $B \leq 17.5^m$ gave us errors of $\sigma_{\alpha\delta} = \pm 0.28"$, $\sigma_{\mu\alpha\delta} = \pm 0.0075"$/year and $\sigma_m = \pm 0.139^m$ for the equatorial coordinates, proper motions and magnitudes, respectively.

Key words: astrometry – methods: data analysis – proper motions – (Galaxy:) open clusters and associations: individual (χ,h Persei)

1. Introduction

Archive of Astronomical Institute (AAI) of the Academy of Sciences of Uzbekistan has about 10,000 plates. Astro negatives were exposed with the Normal astrograph from 1895 to 1976 and from 1976 to 1985 using the Double Zeiss Astrograph of Kitab Observatory. The archive contains about 3,000 plates produced before 1963, including the following observational programs: areas with galaxies – 1100 plates, minor planets – 1100, major planets – 60, planetary nebulae and star clusters – 150, comets – 200, variable stars – 200; other – more than 150 plates. Further work was carried out on the second epoch for favorites areas, such as open and globular clusters and in the areas of peculiar stars. Regular observations of the major planets

(Jupiter, Saturn and Uranus) and their satellites were carried out before the 1980s. Long exposures became impossible at this period of time due to a significant increase of light pollution in Tashkent. At one of the clear night in November 1976, M. M. Muminov received some great shots for the second epoch of χ and h Persei. It was the last observation with the Normal astrograph with long exposures. The Astronomical Institute carried out the next observations at Kitab Observatory using the Double Zeiss Astrograph (DAZ, D / F = 400mm / 3000mm), which was installed in 1975. The main scientific program of the DAZ was FON, which covered the equatorial zone of the sky (from -20° to +20°). More than 2,500 plates were obtained during the FON program. In addition, the plates of (30x30) cm in size: close open clusters (50 regions), young star-forming regions (50 plates) were obtained. Astro negatives are a valuable wealth of the Institute, as some of them contain dozens of previously unexamined open clusters. At the initiative of V. S. Schevchenko, this instrument captured many photos of areas with variable stars, star-forming regions in the Milky Way. The total volume of the DAZ archive has more than 6000 plates.

In order to obtain the equatorial coordinates α and δ, proper motions μ_α and μ_δ and photometric B-magnitudes of stars, the authors decided to start a pilot research using the field around the cluster of χ and h Persei. These clusters has been studied by Muminov (1982, 1996). Test research of scanner was made by Muminov in 2012. Experience of processing of digitized records in order to obtain the equatorial coordinates of stars and the photometric magnitudes was set out in (Andruk, 2005, 2007, 2010; Golovnya, 2010; Yatsenko, 2011; Vavilova, 2010, 2011, 2012a, 2012b; Protsyuk, 2014).

2. Processing of the digitized astroplates

The plates of the first and second epoch №76 (1935.0) and №4209 (1976.9) from the AAI were digitized with the Epson Expression 1000XL scanner. The plates were exposed with the

AI Normal astrograph, the digitization of plates was made with a resolution of 1200 dpi (1px=1.25"). Rectangular coordinates X and Y, instrumental photometric magnitude and FWHM were obtained by software in the environment LINUX/ MIDAS/ROMAFOT (www.eso.org/sci/software/esomidas). Reduction for the equatorial coordinates α, δ and stellar B-mag was carried in the system of TYCHO-2 catalog. To check overall accuracy characteristics of widely used TYCHO-2 and UCAC-4 catalogs (Zacharias, 2013), follow-up study was carried out. Internal errors of catalogs (for the equatorial coordinates σ_α and σ_δ, proper motions $\sigma_{\mu\alpha}$ $\sigma_{\mu\delta}$ and photometry σ_m) were found for a field of view of $3°$ with the center of the clusters χ and h Persei ($\alpha \approx 2^h20.7^m$, $\delta \approx 57°08'$). So, 1680 stars in the TYCHO-2 catalog have the following mean errors: $\sigma_\alpha = \pm0.060"$, $\sigma_\delta = \pm0.067"$, $\sigma_{\mu\alpha} = \pm0.0031"$/year, $\sigma_{\mu\delta} = \pm0.0032"$/year, $\sigma_B = \pm0.137^m$. Respectively, 41,726 stars in the UCAC-4 catalog are characterized by the following mean errors: $\sigma_\alpha = \pm0.053"$, $\sigma_\delta = \pm0.051"$, $\sigma_{\mu\alpha} = \pm0.0051"$/year, $\sigma_{\mu\delta} = \pm0.0049"$/year, $\sigma_{mu} = \pm0.157^m$. A comparison of the equatorial coordinates and proper motions of stars for these catalogs was made for the specified region of the sky. For 1496 common stars, the error of the differences for equatorial coordinates are $\sigma_\alpha = \pm0.072"$ and $\sigma_\delta = \pm0.068"$, the error of the differences of the proper motions are $\sigma_{\mu\alpha} = \pm0.0027"$/year and $\sigma_{\mu\delta} = \pm0.0031"$/year. The values of the above errors can be used as a reference in evaluating the similar values obtained for the presented catalog of positions and proper motions of stars.

3. Creating the catalog of positions and proper motions

Catalog of positions and proper motions of stars was obtained as follows. Equatorial coordinates of stars for the first epoch α_{1i}, δ_{1i} and the second epoch α_{2i}, δ_{2i} were obtained for epoch of exposures t_1 and t_2, but in the TYCHO-2 system on the equinox 2000.0. Differences of equatorial coordinates of stars $\Delta\alpha_i = \alpha_{2i} - \alpha_{1i}$, $\Delta\delta_i = \delta_{2i} - \delta_{1i}$, divided by the difference between the periods $\Delta t = t_2 - t_1 = 1976.9 - 1935.0 = 41.9$ years give us absolute proper motions $\mu_{\alpha i}$, $\mu_{\delta i}$. Equatorial coordinates of the stars for the epoch and equinox 2000.0 were obtained by adding the proper motions $\mu_{\alpha i}$, $\mu_{\delta i}$ (multiplied by $\Delta t' = 2000.0 - 1976.9 = 23.1$) to the equatorial coordinates for objects in 1976.9 The estimated accuracy of the equatorial coordinates and proper motions were derived from the comparison of similar values of the TYCHO-2 and UCAC-4 catalogs.

Comparison of the resulting equatorial coordinates α, δ and proper motions μ_α, μ_δ of our catalog (CAT), with the same data of TYCHO-2 gave the following results: errors of differences of the coordinates and the proper motions for calculated and reference stars are respectively $\sigma_{\alpha\delta} = \pm0.074"$ and $\sigma_{\mu\alpha\delta} = \pm0.0018"$/year. Errors of photometry are $\sigma_m = \pm0.065^m$ and $\sigma_B = \pm0.208^m$ for internal convergence and with comparison to TYCHO-2 B-mag. A similar comparison of our data with UCAC-4 catalog for the common 8123 stars with $B \leq 17.5^m$ gave errors of $\sigma_{\alpha\delta} = \pm0.28"$, $\sigma_{\mu\alpha\delta} = \pm0.0075"$/year and $\sigma_m = \pm0.139^m$ for the equatorial coordinates, proper motions and magnitudes respectively. Figure 1 shows the distribution of the proper motions μ_α, μ_δ for the region of the sky $2°\times2°$ (χh Persey, $\alpha \approx 2^h20.7^m$, $\delta \approx$

$57°08'$). The panels on the left and right show 655 common stars of TYCHO-2 catalog and created catalog.
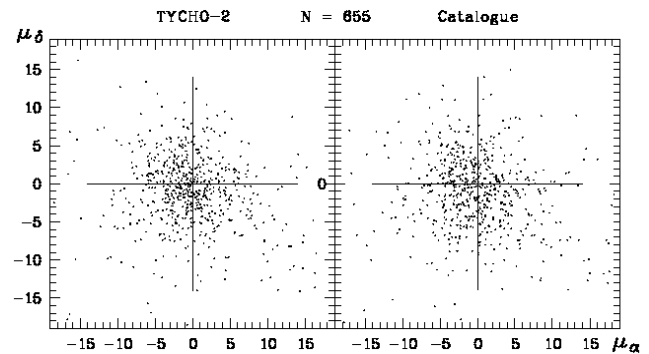
Figure 1: Distribution of the proper motions

4. Conclusion

For stars in the region of the sky around the clusters χ and h Persei (field of view $2°\times2°$), we obtained the following results for the accuracy of the equatorial coordinates: $\sigma_{\alpha\delta} = \pm0.085"$ and $\sigma_{\alpha\delta} = \pm0.056"$ for the first (1935.0) and second (1976.9) epochs, respectively.

Errors of coordinate differences and proper motions for common 655 calculated and reference stars are respectively $\sigma_{\alpha\delta} = \pm0.074"$ and $\sigma_{\mu\alpha\delta} = \pm0.0018"$/year.

Errors of stellar photometry are $\sigma_m = \pm0.065^m$ and $\sigma_B = \pm0.208^m$ for internal convergence and for comparison with TYCHO-2 B-mag.

Comparison of 8123 stars with $B \leq 17.5^m$ with stars of UCAC4 catalog gave errors $\sigma_{\alpha\delta} = \pm0.28"$, $\sigma_{\mu\alpha\delta} = \pm0.0075"$/year and $\sigma_m = \pm0.139^m$ for the equatorial coordinates, proper motions and magnitudes, respectively.

References

Andruk V. et al: 2005, *Kinematika i Fizika Nebesnykh Tel*, **21, N5**, 396 (in Russian).

Andruk V.et al: 2007, *Journal of Physical Studies*, **11, N3**, 329 (in Ukrainian).

Andruk V.M. et al: 2010, *Kinematics and Physics of Celestial Bodies*, **26, N3**, 146.

Golovnya V. et al: 2010, *Journal of Physical Studies*, **14, N2**, 1 (in Ukrainian).

Muminov M.: 1982, *Circular AI AN Uz.,* **N98** (in Russian).

Muminov M.: 1996, *Vizier Online data Catalog*, **5027**, 0.

Muminov M.M. et al.: 2012, *Izvestija GAO v Pulkovo,* **220**, 517 (in Russian).

Protsyuk Yu.I. et al.: 2014, *Kinematics and Physics of Celestial Bodies*, **30, N6**, 296.

Vavilova I.B. et al.: 2011, *Kosmichna Nauka i Tekhnologiya*, **17**, 74.

Vavilova I.B. et al.: 2010, *Kosmichna Nauka i Tekhnologiya*, **16**, 62.

Vavilova I.B. et al.: 2012a, *Kinematics and Physics of Celestial Bodies,* **28, N2**, 85.

Vavilova I.B., Pakuliak L.K., Protsyuk Yu.I., et al.: 2012b, *Baltic Ast.*, **21, N3**, 356.

Yatsenko A.I. et al.: 2011, *Kinematics and Physics of Celestial Bodies*, **27, N5**, 249.

Zacharias N., Finch C.T., Girard T.M., et al.: 2013, *Astron. J.* , **145**, 44.

SOFTWARE FOR PROCESSING OF DIGITIZED ASTRONEGATIVES FROM ARCHIVES AND DATABASES OF VIRTUAL OBSERVATORY

Yu. I. Protsyuk [1], V. N. Andruk [2], L.V. Kazantseva [3]

[1] Research Institute "Nikolaev Astronomical Observatory",
 1 Observatornaya St., 54030, Mykolaiv, Ukraine, *yuri@mao.nikolaev.ua*
[2] Main Astronomical Observatory of the Nat. Academy of Sciences of Ukraine,
 27 Akad. Zabolotnoho St., 03680, Kyiv, Ukraine, *andruk@mao.kiev.ua*
[3] Astronomical observatory of Taras Shevchenko Kyiv National University,
 Observatorna Str.,3, 04053, Kyiv, Ukraine

ABSTRACT. The paper discusses and illustrates the steps of basic processing of digitized image of astro negatives. Software for obtaining of a rectangular coordinates and photometric values of objects on photographic plates was created in the environment LINUX / MIDAS / ROMAFOT. The program can automatically process the specified number of files in FITS format with sizes up to 20000 x 20000 pixels. Other programs were made in FORTRAN and PASCAL with the ability to work in an environment of LINUX or WINDOWS. They were used for: identification of stars, separation and exclusion of diffraction satellites and double and triple exposures, elimination of image defects, reduction to the equatorial coordinates and magnitudes of a reference catalogs.

Key words: astrometry – methods: data analysis – virtual observatory tools – catalogs

1. Introduction

General algorithm of data processing was developed in 2010-2012 for photographic plates from the archives of Nikolaev Astronomical Observatory (Protsyuk, 2014). In the next years, the algorithm was almost not changed, capabilities of individual programs were just extended, automation of repetitive functions was added. The main processing steps are: initial data processing in MIDAS package, identification of stars, astrometric reduction of plate data, final data processing.

2. Initial data processing

Usually we scan 5-6 times every plate using 16 bit FITS format by **Scanfits** program (Barbieri, 2003). Scanning was made placing the negative with emulsion side down and choosing a linear gamma curve in the scanner settings. File name has the form of XXXX_N.fit or XXXX-N.fit, where XXXX – plate number and N – ordinal number of the scan. In principle, one can scan by standard scanner software using 16-bit gray TIFF format and with subsequent conversion to 16 bit FITS format by using the **ImageMagic** package (www.imagemagick.org). Scanned FIT files are copied to the folder on the computer with the Linux operating system and installed **MIDAS** package

(www.eso.org/sci/software/esomidas). This can be either a local computer or a virtual server or a remote computer, as on Figure 1. All of these options have been tested and have shown identical results. Option of remote access to the LINUX / MIDAS PC can be used for the collective processing of photographic plates by several observatories, for example within the framework of cooperation on UkrVO (Vavilova, 2010, 2011, 2012a, 2012b).
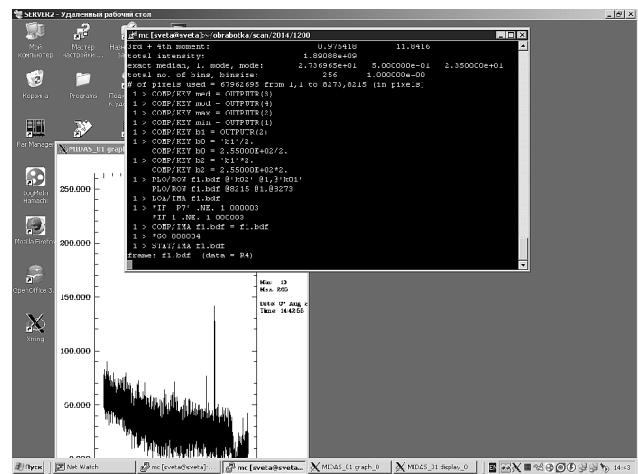
Figure 1: Remote access to Linux PC by using **Putty** and **Xming** programs and processing plate images in MIDAS environment.

In Linux PC we used program **full_pl** for forming sequential file list. The program renames all files in the current folder in names like 3333NNNN.fit, where NNNN file sequence number from 000 to 999. The numbers are based on the size of files, the smaller files are first in order. This is done for further batch processing of heterogeneous FIT files, which may be obtained with different values of dimensions for X and Y during scanning.

After that, we run the MIDAS package and program **00PLATE.PRG**, written in the internal language of package for image processing (Andruk, 2005, 2010, Yatsenko, 2011). The program processes all of the images in batch mode. Depending on the number of source files,

it can take up to several days. As the result of program work, we obtain: filtered FIT files, multiple DAT files with linear coordinates, intensity and other parameters of found objects. The large number of files for each plate (from 10 to 40 depending on the size of the source file) is generated due to limit of 20,000 objects per output file. DAT files contain information about objects on a strip of width of 500-700 pixels with an overlap of 50 pixels. After completing the program **00PLATE**, we again use *full_pl* program to restore the primary file names and copy all DAT files to Windows PC.

3. Stars identification

Using folder with DAT files on Windows PC, we run the program **dat2dir** for gluing strips of each processed plate in one file and for create the structure layout of data on disk. The program generates and executes the script that creates a folder XXXX by number of plate, then creates a sub-folder with the numbers from 1 to 6, in which the glued file **3000001.dat** is formed using the original DAT files (up to 43 strips on the plate).

For each record in the folder 1, we create file **coord.txt** with the initial coordinates of the plate center and the epoch of observation. In case of their absence, these values are entered by operator at the start of the program *plate_gr*.

In the folder with the number 1, we run the program **plate_gr** (Protsyuk, 2014), which is designed for identification of stellar images processed in the MIDAS package using the TYCHO2, UCAC4 catalogs (or another one). The program makes analysis of the quality of identification, taking into account the specific characteristics of the photographic observations in NAO, and calculates the coordinates of objects registered on the photographic plate. The program generates the sky image obtained on the plate in the left window and the image of the same area from the catalog in the right window by using the original DAT file and reference catalog. The brightness and size of stars in the windows is adjusted to achieve a visual correspondence between both images. The program may carry out:

-elimination of the image defects, such as spots, scratches, inscriptions,

-identification of stars in the image,

-allocation and exclusion from further processing of stellar images obtained during the second and the third exposures,

-exclusion of diffraction satellites of bright stars for images obtained with a diffraction grating,

-control of identification,

-reduction using models with different equations,

-analysis of the results.

After completion of data processing in folder 1, we use the script **2copy** to transfer data of identification and selection of exposure or diffraction satellites to folders with names from 2 to 6. In these folders, we also execute program **plate_gr**. Since they already have identification with the first folder, the abridged processing is carried out, which includes only cleaning of the image from defects and accurate snap of identified stars from image 1 to the current image. After that we made reduction of the current plate and exit the program.

When we make changes to the program or improve processing algorithms, all previously processed data can be reprocessed in a batch mode for a time from a few seconds to a few minutes for each frame according to the number of objects on the plate. We historically use the separate program for the final astometric reduction.

4. Astrometric reduction and usage of results

To carry out reduction of all processed plates in batch mode, we create file **lim.txt** in the root folder of all sub-folders with plate data. File **lim.txt** includes the input parameters for subsequent use by the program **00plate.exe** (Protsyuk, 2014), which makes final reduction. In root folder, we run the script **run00**, which performs the sequence data processing of all plates sub-folders by program **00plate**.

The obtained data can be used to compile catalog or to determine the coordinates of a selected object in a series of plates. For example, to create a catalog of positions of all stars in plates and to conduct data analysis we used **mid_an** program. To create a catalog of positions and proper motions of the two plates with a large difference of epochs, we used **plate_in_cat** program. Search for a specific object on all plates and determination of its average coordinates as well as the coordinates at the moment of observation, we implemented by programs **findobj** and **midobj**.

Also in the package of programs, we have a program for visualization of the magnitude equation, the systematic errors of the scanner, the functional connection of various parameters, aberrations of telescope optics, residual error of scan processing, etc.

5. Conclusion

We created the package of programs for image processing with the following parameters: images with resolutions from 600 to 2400 dpi, image size up to 20000x20000 pixels and up to 400,000 objects on the plate, field of view up to 20 degrees. PC with 2GB of RAM is enough to work in full mode.

The package has been successfully used for creation of several catalogs (Protsyuk, 2014) and determination of the coordinates of the planets of the Solar system.

References

Protsyuk Yu.I. et al.: 2014, *Kinematics and Physics of Celestial Bodies*, **30**, **N6**, 296.
Barbieri C., Blanco C., Bucciarelli B., et al: 2003, *Experimental Astronomy*, **15, N1**, 29.
Vavilova I.B., Pakuliak L.K., Protsyuk Yu.I.: 2010, *Kosmichna Nauka i Tekhn.*, **16, N5**, 62 (in Russian).
Vavilova I.B. et al.: 2011, *Kosmichna Nauka i Tekhnologiya*, **17**, 74.
Vavilova I.B., Pakuliak L.K., Protsyuk Yu.I., et al.: 2012a, *Baltic Ast.*, **21, N3**, 356.
Vavilova I.B. et al.: 2012b, *Kinematics and Physics of Celestial Bodies,* **28, N2**, 85.
Andruk V. et al: 2005, *Kinematika i Fizika Nebesnykh Tel*, **21, N5**, 396 (in Russian).
Andruk V.M. et al: 2010, *Kinematics and Physics of Celestial Bodies*, **26, N3**, 146.
Yatsenko A.I. et al.: 2011, *Kinematics and Physics of Celestial Bodies*, **27, N5**, 249.

METHOD FOR EVALUATING THE ASTROMETRIC AND PHOTOMETRIC CHARACTERISTICS OF COMMERCIAL SCANNERS IN THEIR APPLICATION FOR THE SCIENTIFIC PURPOSE

Yu.I.Protsyuk [1], V.N.Andruk [2], M.M.Muminov [3], Q.X.Yuldoshev [3], Sh.A.Ehgamberdiev [3], I.Eglitis [4], M.Eglite [4], O.E.Kovylianska [1], V.V.Golovnya [2], L.V.Kazantseva [5], S.G.Kashuba [6]

[1] Research Institute "Nikolaev Astronomical Observatory",
   1 Observatornaya St., 54030, Mykolaiv, Ukraine, *yuri@mao.nikolaev.ua*
[2] Main Astronomical Observatory of the Nat. Academy of Sciences of Ukraine,
   27 Akad. Zabolotnoho St., 03680, Kyiv, Ukraine, *andruk@mao.kiev.ua*
[3] Ulugh Beg Astronomical Institute of the Uzbek Academy of Sciences
   33 Astronomicheskaya St., 100052, Tashkent, Uzbekistan
[4] Institute of Astronomy, University of Latvia, 19 Raina blvd., Riga, LV-1586, Latvia
[5] Astronomical observatory of Taras Shevchenko Kyiv National University,
   Observatorna Str.,3, 04053, Kyiv, Ukraine,
[6] Astronomical Observatory, Odessa National University,
   Marazlieskaya St. 1v (Shevchenko park), 65014, Odessa, Ukraine

ABSTRACT. Method for estimating the accuracy of astrometric (rectangular coordinates) and photometric (diameters and magnitudes) characteristics of commercial scanners is proposed and applied. The method is demonstrated using an example of processing of sequential scans of plates, which were exposed with different telescopes and then digitized with resolution of 1200 dpi with several Epson scanners. Scanning operations were carried out in various observatories as part of development of the database of photographic observations for Virtual Observatories (Vavilova, 2012). Errors of studied scanners are equal to $\sigma_{x,\,y} = \pm$ 0.02-0.06px and $\sigma_m = \pm$ 0.015-0.024 mag for astrometry and photometry, respectively.

Key words: virtual observatory tools – astrometry – techniques: photometric – methods: data analysis

1. Introduction

We study the accuracy of commercial Epson scanners in terms of their practical application for astrometric and photometric tasks in astronomy. To capture images of star fields, six types of plates were exposed with six different telescopes:

1. Smidt Telescope (**ST**, 80/120/240) of the AO of the Inst. of Astronomy at the University of Latvia (Baldone), pl. N18103 (ORWO ZU21 + GG13), Exp = 4min, size = 24x24 cm, scale = 72"/mm; Epson Expression 10000XL.

2. Double Wide Angle Astrograph (**DWA**, 40/200) of the MAO of NASU (Goloseevo), pl. N219 (ORWO ZU21), Exp = 13.5min, size = 30x30 cm, scale = 103"/mm; Epson Expression 10000XL.

3. Zonal Astrograph (**ZA**, 12/204) of the RI NAO (Mykolaiv), pl. N4786 (ORWO ZU21), Exp = 20min, size = 24x24cm, scale = 101"/mm; Epson Perfection V750 Pro

4. Normal Astrograph (**NA**, 33/350) of Obs. AI Uz AS (Tashkent), pl. N76, Exp = 60min, size = 16x16cm, scale = 59 "/ mm; Epson Expression 10000XL

5. Wide Angle Astrograph (**WAA**, 12.5 / 170) of AO of T.Shevchenko Kiev National University, pl. NC-397-2, Exp=30min, size=24x24 cm, scale = 120 "/mm, Epson Expression 10000XL

6. Seven Wide Angle Astrograph (**SWA**, 12/60) of Astronomical observatory of Odessa National University, pl. N18303 (ORWO ZU21), Exp=30min, size=13x18 sm, scale = 313 "/ mm, Epson Perfection V700 photo

All plates were scanned sequentially six times with a resolution of 1200dpi in FITS or TIFF format. Conversion of files from TIFF to FITS format was carried out using the package GIMP (www.gimp.org) and package ImageMagic (www.imagemagick.org) (Golovnya, 2010). Processing of scans was performed in LINUX/ MIDAS /ROMAFOT (www.eso.org/sci/software/esomidas) environment by using the original software (Andruk, 2010), which was described in (Yatsenko, 2011, Muminov, 2012, Protsyuk, 2014).

2. Scan repeatability and internal accuracy

To estimate the astrometric and photometric errors of scanners, we made six scans for each of six plates. For all of 36 scans, we found rectangular coordinates X and Y, instrumental magnitudes and diameters for all objects. Then, for each of six plates we obtained averaged scan using six measurements for objects brighter than 14^m. Left part of the Figure 1 shows systematic differences in pixels of the rectangular coordinates Δx, Δy along the X-axis and Y-axis for six consecutive scans relative to the averaged scan. After correcting of systematic errors for each scan relative to the averaged scan, we obtained results, which

are presented on the same figures on the right. Columns 2, 3 of Table 1 show averaged residual errors, i. e. RMS values of differences between rectangular coordinates of objects (X, Y). Columns 3, 4 contain information about internal errors of the magnitudes and the diameter of the object. The expected errors for given angular scale of the plates are shown in the next three columns (in seconds of arc) for the coordinates and image diameters. In the Table 2, we present the astrometric and photometric errors in the TYCHO-2 system for six telescopes.
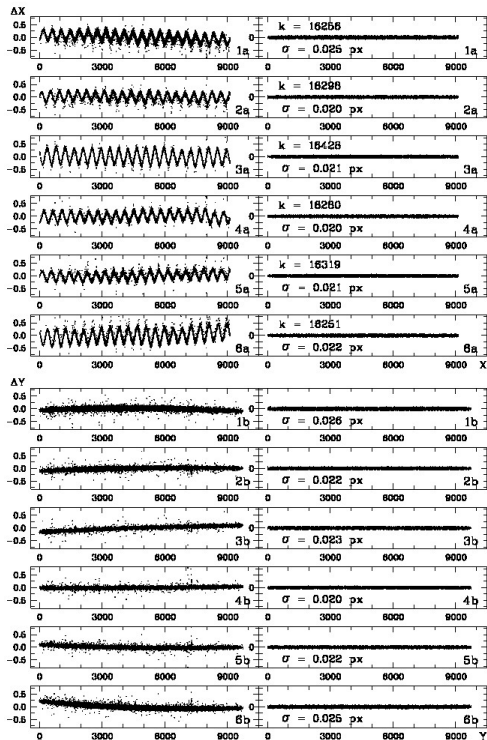

Figure 1. Systematic (left) and random (right) differences of the stellar coordinates ΔX, ΔY along the X and Y for six scans with respect to the averaged scan of one plate obtained with the Smidt Telescope (ST).

Table 1

Tel.	σX	σY	σ_m	σf	σ_α	σ_δ	σ_f
ST	0.022	0.024	0.015	0.030	0.040"	0.044"	0.055"
DWA	0.032	0.035	0.015	0.062	0.069	0.076	0.135
ZA	0.048	0.046	0.024	0.053	0.099	0.099	0.115
NA	0.037	0.039	0.015	0.040	0.047	0.049	0.050
WAA	0.061	0.064	0.030	0.074	0.156	0.164	0.189
SWA	0.029	0.053	0.023	0.059	0.213	0.388	0.432

Table 2

Tel.	σ_α	σ_δ	σ_B
ST	0.094"	0.070"	0.25^m
DWA	0.101	0.103	0.19
ZA	0.083	0.111	0.26
NA	0.113	0.098	0.30
WAA	0.174	0.190	0.26
SWA	0.440	0.375	0.35

3. Evaluation of the reduction accuracy

The accuracy of equatorial coordinates is given on Figure 2. Panels from top to bottom on the left show the systematic differences $\Delta\alpha$ and $\Delta\delta$ between the measured and TYCHO-2 catalog coordinates in the right ascension and declination (α,δ), which were obtained before the correction of scanner instrumental errors. The results of reduction of the measured coordinates after taking into account instrumental errors of scanner and aberrations of telescope optics are shown on the right panel.
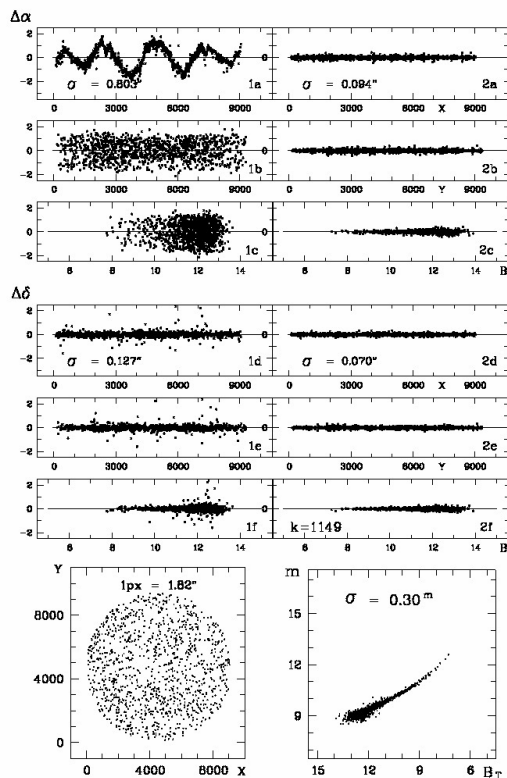
Figure 2. Systematic (left) and random (right) differences between measured and catalog coordinates $\Delta\alpha$ and $\Delta\delta$. At the bottom of the left – the distribution of TYCHO-2 stars on the plate field, on the right – the characteristic curves of plate.

4. Conclusion

Epson scanners and developed software allow us to digitize, process plates and obtain astrometric characteristics of objects with an internal accuracy better than $\sigma_{\alpha\delta} = \pm 0.1"$ for plates with angular scale up to 2.5"/px at a resolution of 1200 dpi. Internal accuracy of the determination of the magnitudes is $\sigma_m = \pm 0.025^m$.

References

Andruk V.M. et al: 2010, *Kinematics and Physics of Celestial Bodies*, **26, N3**, 146.

Vavilova I.B. et al.: 2012, *Kinematics and Physics of Celestial Bodies,* **28, N2**, 85.

Golovnya V. et al: 2010, *Journal of Physical Studies*, **14, N2**, 1 (in Ukrainian).

Muminov M.M. et al.: 2012, *Izvestija GAO v Pulkovo.* **220**, 517 (in Russian).

Protsyuk Yu.I. et al.: 2014, *Kinematics and Physics of Celestial Bodies*, **30, N6**, 296.

Yatsenko A.I. et al.: 2011, *Kinematics and Physics of Celestial Bodies*, **27, N5**, 249.

Vavilova, I.B., Pakuliak, L.K., Protsyuk, Yu.I., et al.: 2012, Baltic Astronomy, 21, N3, 356.

RESULTS OF PROCESSING OF ASTRONEGATIVES WITH COMMERCIAL SCANNER

Yu.I. Protsyuk [1], O.E. Kovylianska [1], S.V. Protsyuk [1], V.N. Andruk [2]

[1] Research Institute "Nikolaev Astronomical Observatory", 1 Observatornaya St.,
54030, Mykolaiv, Ukraine, *yuri@mao.nikolaev.ua*

[2] Main Astronomical Observatory of the Nat. Academy of Sciences of Ukraine,
27 Akad. Zabolotnoho St., 03680, Kyiv, Ukraine, *andruk@mao.kiev.ua*

ABSTRACT. Astrometric errors depending on the method of scanning with different spatial resolutions were studied with commercial scanner such as Epson Perfection V750 Pro. Accuracy, time of processing, volume of storage were tested using software package described in (Protsyuk, 2014). The best results of scanning were obtained with a resolution of 1200 – 1600 dpi.

Keywords: astrometry – methods: data analysis – virtual observatory tools – catalogs

1. Introduction

We used three photographic plates of (20x20) cm in size, taken from archive of the Zonal Astrograph (D= 120 mm, F= 2040 mm, FoV = 5° x 5°), which was in operation from 1929 to 1999 at Nikolaev Astronomical Observatory (NAO). The archive of plates with preview images is available online at the UkrVO website (http://ukr-vo.org) (Vavilova, 2012, Mazhaev, 2013).

We also used the EPSON PERFECTION V750 Pro scanner (made in 2011) with: A4 format in size, maximum dynamic range of 4.0D, optical resolution of 4800 x 9600 dpi, transparent area of 10" x 8" in size.

The current version of the software package for image processing has the following limitations: up to 400,000 objects on a plate, the size of a plate up to 20K x 20K pixel.

To choose optimal options for data processing, each of three plates was scanned six times in two modes:

• with resolution from 600 to 2400 dpi and increments of 300 dpi, with the signal to noise ratio of 3 in the MIDAS software;

• with resolution of 1800 dpi, with the signal to noise ratio from 3 to 12 in the MIDAS software.

Three personal computers (PC) on LINUX platform were used for data processing with the MIDAS software:

L1 – Main: Lubuntu 12.04 in a virtual machine (VM) with 2.5GB of RAM, disc volume (DV) of 20GB on host i3-2.4GGts, 16GB of RAM;

L2 – Lubuntu 12.04 in a VM with 2.5GB of RAM and DV of 80GB on host i5-3.2GGts, 8GB of RAM;

L3 – Mandriva 10.04 on Core Duo processor with a clock speed of 2.5GHz, 2GB of RAM, DV of 275GB.

Values of time for data processing are approximately equal for L1 and L2. The speed of data processing for L3 is less by 10-20% than for L1 and L2.

Three PC on Windows platform were used for data processing in the following configurations:

W1 – Main: i3 at 2.4GHz, 16GB of RAM;

W2 – i5 3.2GHz, 8GB of RAM;

W3 – Core2Duo 2.66GHz, 8GB of RAM.

Data processing on the L1/W1 was performed using: 5.5GB of RAM as cache of disk operations with delay in writing for 5 minutes. Volume of disk reading on L1/W1 during the test was 6.1TB including 4.4TB from the cache (more than 70%). Volume of recorded data was 19.1TB including physical data recording of 13.4TB, which is less on 30%.

We carried out image processing and obtained 17 catalogs of equatorial coordinates in the HCRF system for three given plates. Information about photometric precision of another commercial scanner was given by Andruk (2010).
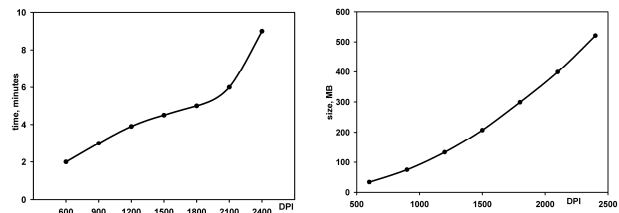
2. Results of testing

Figure 1: Time of plate scanning in minutes vs resolution – left, and size of image in MB vs resolution – right
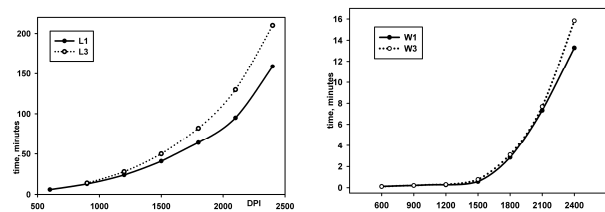

Figure 2: Time of one plate reduction in MIDAS vs resolution – left, and time of preparations for identification vs resolution – right
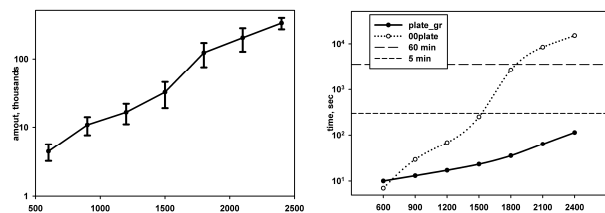

Figure 3: Number of objects on images vs resolution – left, and time of reduction in different programs – right
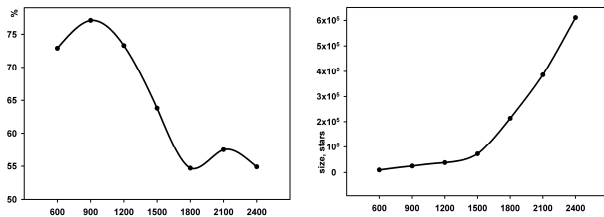
Figure 4: Percent of objects registered 5 or 6 times vs resolution – left, size of the catalog for three plates – right
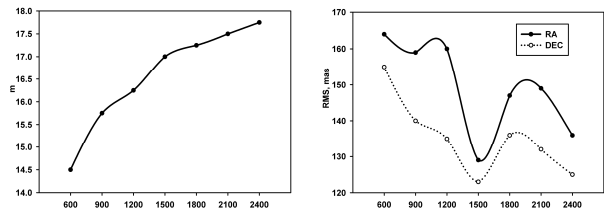

Figure 5: Limited magnitude in catalogs vs resolution – left, and mean RMS of catalogs vs resolution – right
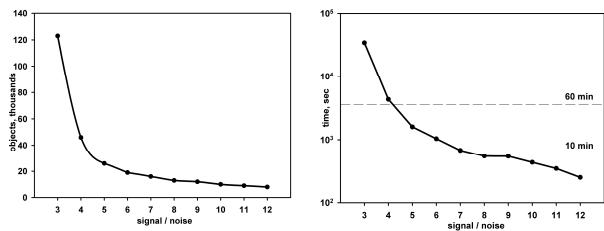

Figure 6: Number of detected objects for 1800dpi vs signal/noise – left, and time of reduction of 18 plates in 00plate program vs signal/noise – right
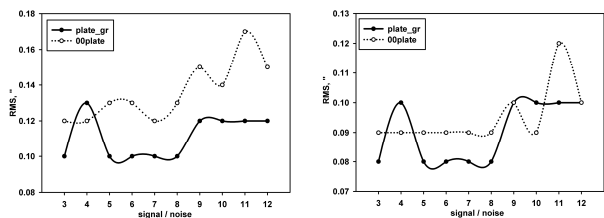

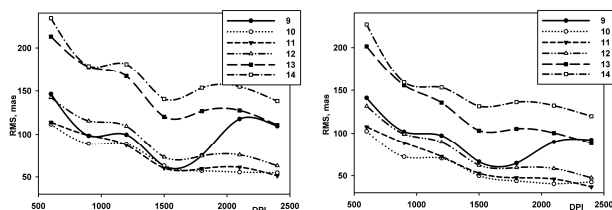Figure 7: Mean RMS of coordinates for 1800dpi using two programs in RA vs S/N – left, and in DEC – right

Figure 8: Distribution of the RMS in catalogs for different mag. in RA vs resolution – left, and in DEC – right

3. Determination of the processing time and the optimal processing options

If we have overlapping observation of the same sky region on 4 plates, we may make one scan for each plate. In other case, we must make 5 or 6 scans for one plate.

One scanner can approximately make 24 or 48 scans per day, respectively. We spend additional time in the first case for the search of plates, their preparation, removal of dust and inscriptions.

The volume of raw data for scanning with resolution of 600 to 2400dpi may amount from 2.4-4.8GB to 13-26GB. For processing in MIDAS, we must have the free space on the HDD in two times larger than initial data volume, and 0.5 to 5 GB for temporary files. With the current size of hard disks, daily work does not cause problems. To store the entire scan array obtained for a long period of time, we will need a special solution.

Usually, raw images must not be stored for more than two days without processing.

The processing time for all plates with scanning resolution of 600 to 2400 dpi consists of:

– preparation for initial data processing – from 20 to 100 minutes including time for making copy via the LAN;

– initial data processing in MIDAS – from 3 to 128 hours (over 5 days);

– preparations for identification – from 1 to 30 minutes;

– elimination of the image defects, image processing only for a single exposure, the identification of the several exposures and diffraction satellites – from 3 (8x6) to 6 (24x1) hours;

– reduction: by the program plate_gr – from 5 to 100 minutes; by the 00plate – 1 to 200 hours (over 8 days).

The analysis of the accuracy of data processing showed a bad result for resolutions less than 1200dpi, and we exclude resolutions of 600 and 900 dpi.

Eight working hours are enough for all steps that require a human attention, namely: preparation for initial data processing, preparation for the identification and identification.

We must select such resolutions that fit into the remaining 40 hours if 24h PC work is possible for batch processing. In this case we can use 3 resolutions: 1200dpi – with time processing of 11-21 hours, 1500dpi – 17-33 hours, 1800dpi – 27-53 hours.

The calculations were performed for plates of (20x20) cm in size. For other sizes, the results will be different.

5. Conclusion

If there is a possibility to use one PC for scanning for 8 hours and another PC for 24 hours of processing, we will use the resolution of 1500 to 1600dpi.

If we use single PC for scanning and processing, or one PC for scanning and one PC for processing during 8 hours per day, we should use the resolution of 1200dpi as the most balanced in terms of accuracy per unit of time.

References

Protsyuk Yu.I., Andruk V.N., Kazantseva L.V.: 2014, *Odessa Astr. Publ.*, in the current issue.

Mazhaev A., Protsyuk Yu.: 2013, *Odessa Astron. Publ.*, **26, N2**, 233.

Vavilova I.B., Pakuliak L.K., Protsyuk Yu.I., et al.: 2012, *Baltic Ast.*, **21, N3**, 356.

Protsyuk Yu.I. et al.: 2014, *Kinematics and Physics of Celestial Bodies*, **30**, **N6**, 296.

Andruk V.M. et al: 2010, *Kinematics and Physics of Celestial Bodies*, **26, N3**, 146.

THE SCIENTIFIC USE OF THE UKRVO JOINT DIGITAL ARCHIVE: GRBs FIELDS, PLUTO, AND SATELLITES OF OUTER PLANETS

I. Vavilova [1], V. Golovnya [1], V. Andruk [1], L. Pakuliak[1], O. Yizhakevych[1], S. Shatokhina[1], Yu. Protsyuk[2], L. Kazantseva[3], V. Lukianchuk[1,4]

[1] Main Astronomical Observatory NAS of Ukraine, Kyiv, Ukraine,
   golov@mao.kiev.ua, andruk@mao.kiev.ua,
[2] Nikolaev Astronomical Observatory, Mykolaiv, Ukraine,
[3] Astronomical Observatory, Kyiv Shevchenko National University, Ukraine,
[4] Kyiv Shevchenko National University, Ukraine

ABSTRACT. In the framework of UkrVO national project the new methods of plate digital image processing are developed. The photographic material of the UkrVO Joint Digital Archive (JDA – http://gua.db.ukr-vo.org/vo-mao/DB/archivespecial.php) is used for the solution of classic ast-rometric problem – positional and photometric determinations of objects registered on the plates. The results of tested methods show that the positional rms errors are better than ±150 mas for both coordinates and photometric ones are better than ±0.20^m with the Tycho-2 catalogue as reference.

Key words: virtual observatory, GRB, small Solar system bodies

1. Introduction

The national project of the Ukrainian Virtual Observatory (UkrVO) has breathed new life into the old observational archives. The Joint Digital Archive (JDA) of photographic observations has become the core of the UkrVO. JDA, which includes observational archives of five Ukrainian observatories and covers the observational period of around 100 years (http://gua.db.ukr-vo.org/archivespecial.php) [1–4]. The great part of JDA (about 70%) embraces archives of two Kyiv observatories: MAO NAS of Ukraine and AO of Kyiv national university. In the UkrVO framework, the digitizing of glass collections is conducted. At present, JDA controls 50 Kyiv observational archives with 40,000 metadata records and near 14,000 digital images. The JDA is supplemented by 14,500 digital images of observational logging records, identified with 23,000 photographic plates, included into the database, as well as about 6,000 arrays of coordinates and photometric data of objects, registered on the plates and derived in pre-processing procedures.

In addition to the direct images the photographic archive of MAO NASU contains about 50,000 photographic plates with spectra. This archive includes the material of a large number of observational projects and can be partly classified and digitized. We started the process of digitizing some collections of spectra, which are well documented and can be included into the spectral library (UkrVO SDL, http://ukr-vo.org/spectra).

Another form of archives representation is a standard format accepted for the Wide-Field Plate Database (WFPDB), which represents the largest archives of the world astronomical observatories. Catalogs have been transformed to this format and integrated to WFPDB (www.skyarchive.org) [5].

2. Astrometric solutions with the JDA

Plate digitizing is carried out using a flatbed scanner Epson Expression 10000XL with 16-bit gray levels, resolution of 1200 dpi. Digitized images are stored in TIFF and FITS formats. The results of digitizing are used for decision of the following scientific tasks: enrichment of FONAK astrometric catalogue (the photographic review of the northern sky) with data of objects, registered on the digitized images down to 16^m (B band) [6]; search of optical analogue of GRB and creation of catalogues of objects in the areas around GRBs; creation of astrometric catalogues of coordinates of Pluto and outer faint satellites of Jupiter and Saturn; elaboration of proper methods of treatment and obtaining astrometric coordinates for asteroids and comets [7]. The astrometric and photometric calibration procedures were developed on the basis of LINUX-MIDAS-ROMAFOT software [8, 9]. The improvements concern to the topocentric coordinates, their correction for scanner instrumental errors, the specific form of object image and application of different models for the final reduction in the Tycho-2 frame as reference. The comparison of obtained positions with ephemerides was made using IMCCE (Paris) [10].

2.1. The catalogs of objects in the areas around GRBs

The results of continuous GRB observations onboard spacecrafts are published in GCN Circulars and handed over to observatories for investigation of any objects in the sky areas around the GRB. The last task in addition can be solved using the JDA data. Objects, which potentially could appear on the archive plates, were selected in GCN Circulars published data. The positional accuracy of selected objects is between ±0.3″ and ±7.0″ and the range of magnitudes is 14^m–19^m. GRBs and all the objects are sought and identified on the digitized plates within the circle with the radius of dozens of arc minutes. Up to date the analysis of coordinates for 108 GRBs, taken place in 2003, 2009–2013, has been carried out. The bright objects with coordinates different from those of given to GRB but absent in vast stellar catalogues, were found in several

areas. Study of these objects is going on with attraction of other observational facilities [11]. The data of 26 areas are published in GCN Circulars [12–26]. Faint objects were found in the vicinity of two non-identified GRBs by the program of their positional data. We obtain catalogues of stars in the vicinity of GRB110213A (4′x4′), GRB101224A (10′x10′) and GRB090113 (8′x8′).

The work is in process. Catalogues are available on the web site of MAO NASU and UkrVO.

2.2. Astrometric solutions for Jupiter and Saturn satellites

The UkrVO JDA contains considerable observational material (more than 300 plates) on the main satellites of Saturn (S1–S8) and the outer satellites of Jupiter (J6–J8) obtained by four telescopes (DDA, DSHA, DAZ, TS600) during 1961–1993 [1–4]. In 1990 the reduction was carried out and partially published [27, 28]. At that time the measurement of negatives were realized using Askorekord and PARSEK instruments. Reference systems served the catalogues AGK3, PPM, CMC. At present, we start to reprocess all the observations using the scan processing method described in [8, 9]. As the reference frame the catalogue Tycho2 system was chosen. It has been already processed about 40% of the observational material. Simultaneously we carry out the comparison with the ephemeris [10] online. Standard error of deviation from the theory is about 0.20″–0.35″ in both coordinates. The work is in process too.

2.3. Catalogues of Pluto astrometric data

The JDA archives contains 77 digital images of plates with Pluto related to 1961–1990 years of observations. The main goals of their treatment were to determine whether the better positional accuracy could be achieved with those photographic material due to new methods of image processing and could the scanned images in general be used for the astrometric solutions with a high positional accuracy in applications for moving objects. Using the current results we obtain the joint catalog of Pluto positions. The part of plate sets was earlier used for positional determinations and the compilation of the Pluto positional catalogue. For current data rms errors of unit weight are 2 to 3 times better than that of classic methods [29– 31].

The comparison of results [31] for plates of different linear dimensions (13x13 cm to 30x30 cm), scales (38″ to 103″/mm) and exposures (5 to 60 minutes) permits to obtain the reliable material concerning the regularity of (O-C) in the system of planet coordinates in relation to appropriate values of different ephemerides in the specified time period. Digital images of plates and state-of-art stellar catalogues allow to improve the accuracy of positional determinations, using the earlier unusable photographic material for the enhancement of observational series with reliable results, and to involve more faint stars omitted previously into the processing of plates.

Conclusion

Our results suggest that the old observational archives, which are presented on the astroplates, can generate new knowledge in addition to current projects and new methods of observations [32–35]. One can register your archives on the WIKI [36].

References

1. Vavilova I.B. et al.: 2012, Kinematics and Physics of Celestial Bodies, **28**, 85.
2. Vavilova I.B. et al.: 2012, Baltic Astronomy, 21, 356.
3. Pakuliak L. et al: 2013, Odessa Astron. Publ., **26/2**, 236.
4. Vavilova I.B. et al.: 2010, *Kosmichna Nauka i Tekhnologiya*, **16**, 62.
5. Tsvetkov M.K. et al.: 1995, *Lect. Not. in Phys.*, **454**, Flares and Flashes, IAU Colloquium 151, Eds. J. Greiner, H.W. Duerbeck, R.E. Gershberg, Springer Verlag, p. 412.
6. Andruk V. et al: 2005, *Kinematika i Fizika Nebesnykh Tel*, **21, N5**, 396.
7. Golovnya V., Andruk V.: 2013, Odessa Astron. Publ., **26/2**, 226.
8. Andruk V.M. et al: 2010, *Kinematics and Physics of Celestial Bodies*, **26, N3**, 146.
9. Golovnya V. et al: 2010, *J. Phys. Studies*, **14**, 2902.
10. Natural Satellites Ephemeride (IMCCE.Paris) http://www.imcce.fr/hosted_sites/saimirror/nssephe.php
11. Golovnya V. et al: 2012, *Kyiv Univ. Messenger. Astronomy*, **49**, 36 (in Ukrainian).
12. Golovnya V.V.: 2011, *GCN Circul. Archive*, 12113.
13. Golovnya V.V.: 2011, *GCN Circul. Archive*, 12306.
14. Golovnya V.V., Kizyun L.N.: 2011, *GCN Circul. Archive*, 12586.
15. Golovnya V.V.: 2011, *GCN Circul. Archive*, 12680.
16. Golovnya V.V.: 2011, *GCN Circul. Archive*, 12786.
17. Golovnya V.V.: 2012, *GCN Circul. Archive*, 12807.
18. Golovnya V.V., Kizyun L.N., Pakuliak L.K.: 2012, *GCN Circulars Archive*, 12808.
19. Golovnya V.V.: 2012, *GCN Circul. Archive*, 12827.
20. Golovnya V.V.: 2012, *GCN Circul. Archive*, 12875.
21. Golovnya V.V.: 2012, *GCN Circul. Archive*, 12906.
22. Golovnya V.V.: 2012, *GCN Circul. Archive*, 12918.
23. Golovnya V.V.: 2012, *GCN Circul. Archive*, 13014.
24. Golovnya V.V.: 2012, *GCN Circul. Archive*, 13066.
25. Golovnya V., Yatsenko A., Pakuliak L.: 2012, *GCN Circul. Archive*, 13086.
26. Golovnya V.V.: 2014, *GCN Circul. Archive*, 16650.
27. Izhakevich E.M., Pakuliak L.K., Kulyk I.V.: 2012, *Proc. of the Conf. NAROO-GAIA, June 20- 22, 2012, France, Paris,* p. XX.
28. Izhakevich, E.M. et al.: 1994, *Kinematics and Physics of Celestial Bodies*, **10**, 88.
29. Shatokhina S., Yizhakevych O.: 2005, *Kinematika i Fizika Nebesnykh Tel*, Suppl, **5**, 570.
30. Telnyuk-Adamchuk V., Pasechnik S.: 1989, *Kyiv Univ. Messenger. Astronomy*, **31**, 82.
31. Shatokhina S. et al.: 2015, *Kinematics and Physics of Celestial Bodies*, **31** (accepted).
32. Golovnya V. et al.: www.astroplate.cz/wp-content/uploads/2014/01/Golovnya_UkrVO_new_life.pdf
33. Vavilova I. et al.: www.astroplate.cz/wp-content/uploads/2014/01/Prague-UkrVO-Vavilova-et-al.pdf
34. Protsyuk Yu. et al.: www.astroplate.cz/wp-content/uploads/2014/01/Protsyuk-NAO_2014-a.pdf
35. Vavilova I.B. et al.: 2011, *Kosmichna Nauka i Tekhnologiya*, **17**, 74.
36. Tuvikene T. et al.: www.plate-archive.org/wiki/index.php/Main_Page.

POSITIONAL CATALOGUES
OF SATURN'S AND JUPITER'S MOONS

O.Yizhakevych, V.Andruk, L.Pakuliak, V.Lukianchuk, S.Shatokhina

Main Astronomical Observatory NAS of Ukraine, Kyiv, Ukraine
izhak@mao.kiev.ua, pakuliak@mao.kiev.ua, andruk@mao.kiev.ua

ABSTRACT. In the framework of the UkrVO national project (http://ukr-vo.org/) we have started the processing of photographic observations of Saturn's (S1-S8) and Jupiter's (J6-J8) moons. Observations were conducted during 1961–1993 with three astrographs DLFA, DWA, DAZ and Z600 reflector. Plate images were digitized as tif-files with commercial scanners. Image processing was carried out by specific software package in the LINUX-MIDAS-ROMAFOT environment with Tycho2 as reference. The software was developed at the MAO NASU. Obtained positions of objects were compared with theoretically predicted ones in IMCCE (Paris) (www.imcce.fr/sat) online. Rms error of divergence between observed and calculated positions is of $0.20'' - 0.35''$.

Key words: UkrVO, JDA, LINUX-MIDAS-ROMAFOT

1. Introduction

Position coordinates of the Solar System bodies are the necessary basis for the solution of a number of scientific and applied problems. According to Harper & Taylor (1994), there are significant gaps in the coverage of observations of Saturn's satellites in the world, there are no published data on their observations in 1948-1966. Therefore, plates obtained in MAO NASU (Goloseevo) in 1961-1993 may occur of particular interest to fill up and complement the global database of their observations.

2. Observations

Observations were made with two refractors DLFA (D/F = 400/5500mm, scale = 37,5″/mm), DWA (D/F = 400/2000 mm, scale = 103″/mm), sited in Goloseevo and with DAZ (D/F = 400/3000 mm, scale = 103″/mm) in Kitab as well as with Z600 reflector (D/F = 600/7500 mm, scale = 27.5″/mm) at the mount Maidanak in Uzbekistan. We pay tribute to the most active observers E.A.Hertz, O.M.Yizhakevych, I.V.Ledovskaya (Kulyk), R.F.Ly- siakova, S.P.Major, G.V.Moroz, A.B.Onegina, E.M.Sereda, Yu.K.Philippov.

After creating the archive of the photographic observations DBGPA (http://gua.db.ukr-vo.org/vomao/DB/) an opportunity arises to expand the list of observations through the plates of expected satellite images from other observational programs. In addition, there were found 70 previously untreated observations of these objects. Currently observational material consists of more than 320 plates.

3. Reduction

In 1980th, as the observations were accumulated, the step-by-step processing of Saturn's moons was carried out (Yizhakevich et al. 1980, 1991, 1994, 2012; Natural Satellites Ephemeride (IMCCE.Paris) http://www.imcce.fr/hosted_sites/saimirror/nssephe.php; IMCCE (Paris), NSDC, Observations, Astronomical positions. http://www.imcce.fr/hosted_sites/saimirror/bsapomaf.htm). Then the measurements were made with the measuring machines of the ASCORECORD type, lately with the automatic measuring machine PARSEK. Reference systems were built using different catalogs: AGK3, PPM, ACT, Tycho2. Particular attention was paid to the choice of models for the reduction of wide-angle shots and for Z600 shots with a small field. Basically it was the third-order polynomial using distortion terms. Number of reference stars on the wide angle plates was approximately from 20 to 50. For the reduction of Z600 reflector observations the method of two-step binding was used.

After the implementation of digital techniques in the photographic images processing we decided to reprocess the total accumulated material in the unified reference system of Tycho2. Plates were digitized on the commercial scanners of two types: Microtek ScanMaker 9800XL TMA (MSM) and Epson Expression 10000XL (EE) with the image resolution 1200 dpi.

The new methods of plate reduction have been developed by V.N. Andruk at the (Andruk et al. 2005, 2010). The proposed algorithms and debugged programs were designed to work in the LINUX-MIDAS-ROMAFOT environment.

Initially programs were developed to work with wide angle plates of DWA having dot star images and one or two expositions per plate. To process DLFA plates with several expositions of different durations, this software required to be modified in order to separate object images on expositions.

The sequence of positional determinations on photographic observations is well developed: first the rectangular coordinates x_s, y of objects are determined, while program identifies and eliminates the errors for emulsion irregularities. Then Tycho-2 reference stars' identification in x,y array was made. The connection between tangential and measured coordinated is presented as infinite power series. The terms of polynomial depend on number of factors: quality of optical system, aberrations of the objective, scale and inclination of the plate to the focal plane and so on. The accuracy of the reduction also depends on errors of the measuring appliance and defects of the plate itself, as well as on the number of the polynomial terms. In our case for DWA plates (8°x8°) we use sixth-order

polynomial, and for DLFA plates (2°x2°) – third-order one. The accuracy of the reduction, or the r.m.s. error of unit weight over the whole plate field is 0.05″ – 0.15″. The number of reference stars is some hundreds for DWA and about 100 for DLFA plates. For the plates with small fields such as Z600 (0.5°x 0.5°) the method of two step binding is usually applied, using the plates with wide field as intermediate ones, DWA plates for example.

We demonstrate the accuracy of determination of equatorial coordinates as an example in Figure 1. In the left panel from top to bottom, respectively, it is shown the course of systematic differences $\Delta\alpha$ and $\Delta\delta$ between the measured and catalog coordinates for the right ascension and declination (α,δ) of TYCHO-2 before making the correction for scanners instrumental error for the studied astroplates. In the right panel, there are results of the reduction of the measured coordinates after correction for scanners instrumental error and accounting aberrations of telescope optics.
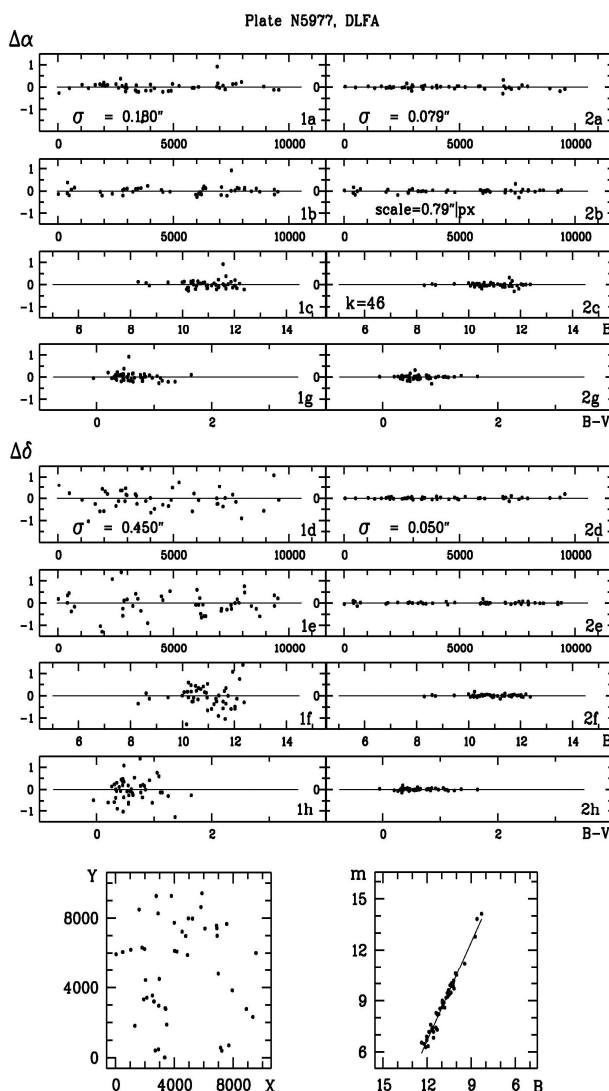

Figure 1: Systematic (left) and random (right) differ-ences between measured and catalog coordinates $\Delta\alpha$ and $\Delta\delta$. At the bottom of the left – the distribution of stars TYCHO-2 on the plate field, on the right – the characteris-tic curves of DLFA's plate №5977.

The project of positional catalogs of Saturn's and Jupiter's moons is starting. Thanks to IMCCE (Paris) [IMCCE (Paris), NSDC, Observations, Astronomical positions. http://www.imcce.fr/hosted_sites/saimirror/bsapomaf.htm) ephemerides: (O-C)α (O-C)σ and their rms. errors are derived simultaneously and the error range is 0.20-0.35″.

Brief summary

The archive of photographic observations accumulated at the MAO NASU embraces the information about near space events never occur again. One of the important problem is the processing of astronegatives to obtain positions of different objects including Saturn's and Jupiter's moons. While the planets at all times are subjects to perturbations by the giant planets and satellites neighbors, their orbit parameters constantly need to be improved. The proposed new method for the reduction of photographic observations qualitatively improves and facilitates the processing of photographic observations. It becomes possible to identify and treat those satellites, which images were previously inaccessible due to a poor separation of planetary images.The work is in process as well as it is a part of our UkrVO project (Vavilova et al., 2010, 2011, 2012a, 2012b; Pakuliak et al., 2013; Shatokhina et al., 2015).

References

Andruk V. et al: 2005, *Kinematics and Physics of Celestial Bodies*, **21**, N5, 396.

Andruk V.M. et al: 2010, *Kinematics and Physics of Celestial Bodies*, **26**, N3, 75.

Izhakevich E.M., Pakuliak L.K., Kulyk I.V.: 2012, *Proc. of the Conf. NAROO- GAIA,* June 20-22, 2012, France, Paris, p. 161.

Pakuliak L.K. et al.: 2013, *Odessa Astron. Publ.*, **26**, 236.

Shatokhina et al.: 2015, *Kinematics and Physics of Celestial Bodies*, **31**, No. 1 (accepted).

Vavilova, I.B. et al.: 2012, *Kinematics and Physics of Celestial Bodies*, **28**, 85.

Vavilova, I.B. et al.: 2012, *Baltic Astronomy*, **21**, 356.

Vavilova, I.B. et al.: 2011, *Kosmichna Nauka i Tekhnologiya*, **17**, 74.

Vavilova, I.B. et al.: 2010, *Kosmichna Nauka i Tekhnologiya*, 16, 62.

Yizhakevych O.M.: 1980, Scientific paper deposited in All-russian institute of scientific and technical information**, No. 4553-B91**, 1.

Yizhakevych O.M., Kaltygina S.V., Major S.P., et al.: 1991, *Kinematics and Physics of Celestial Bodies*, **7**, №2, 98.

Yizhakevych O.M., Kaltygina S.V., Ledovskaya I.V. et al.: 1994, *Kinematics and Physics of Celestial Bodies*, **10**, №1, 88.

RADIO-ASTRONOMY

USING THE METHODS OF WAVELET ANALYSIS AND SINGULAR SPECTRUM ANALYSIS IN THE STUDY OF RADIO SOURCE BL LAC

G.I.Donskykh[1], M.I.Ryabov[2], A.L.Sukharev[2], M.Aller[3]

[1] Department of Astronomy, I.I.Mechnikov Odessa National University, Odessa, Ukraine
[2] Odessa observatory "URAN-4" of the Radio-astronomical institute NAS, Odessa, Ukraine
[3] Radio observatory of Michigan University, Ann Arbor, USA

ABSTRACT. We investigated the monitoring data of extragalactic source BL Lac. This monitoring was held with University of Michigan 26-meter radio telescope. To study flux density of extragalactic source BL Lac at frequencies of 14.5, 8 and 4.8 GHz, the wavelet analysis and singular spectrum analysis were used. Calculating the integral wavelet spectra allowed revealing long-term components (~7-8 years) and short-term components (~ 1-4 years) in BL Lac. Studying of VLBI radio maps (by the program Mojave) allowed investigating features of components movement relatively to the VLBI core. The data of radio astronomy observations were also investigated using singular spectrum analysis. This method can solve the task of allocating trend, detection of periodic components and band-pass filtering (reconstruction of time series from quantity of main components, the last corresponds to individual bands of periods on time-frequency spectra or Fourier spectra). Singular spectrum analysis does not use the analyzing function, so its calculations allow to distinguish various components of investigated series with a high accuracy. To get spectral power distribution depending on time in the studied narrowband components obtained by singular spectrum analysis, short-term Fourier transformation was used.

Key words: BL Lac, jet.

1. Introduction

In this paper BL Lac is studied. The observations were taken by the radio telescope RT-26 Michigan Observatory, at frequencies of 14.5 GHz (1974–2011), 8 GHz (1968–2010) and 4.8 GHz (1980–2011). A graph of flux density BL Lac on three frequencies is presented at Figure 1. Details of the calibration methods and the methods of analysis are described in paper (Aller et al., 1985).

Considering the bright knots in the jets 3C120 and BL Lac according to the data from the Mojave data base (Lister et al., 2009), the existence of components receding gradually and components arising episodically at the same distances from the core was noted. In the articles of some authors (eg, Jorstad et al., 2001; Britzen et al., 2008; Alberdi et al., 2000), the existence of stationary component in the jets which are in a fixed position was discussed. These bright knots were explained as standing shocks caused by the interaction of the jet with the environment.

2. Data reduction

Based on daily observations of flux average values of 7 days with an irregular grid of counting are defined. According to the histogram of distribution of time intervals between counting the interpolation interval in 0.02 years (7.3 days) has been chosen. With using a polynomial moving average (half-width an interval of 5 points) reduction of noise has been reached and random emissions have been removed. By means of trigonometric interpolation the data have been reduced to an even step on time. Allocation of short component in signals against the main period Fourier filtering (O – C) was used (Gaydyshev, 2001).
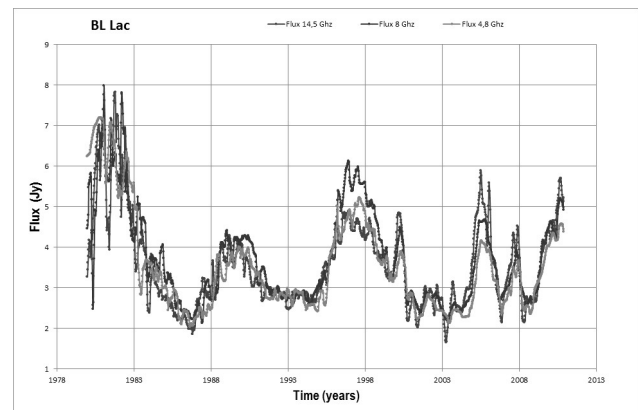
Figure 1: A graph of flux density BL Lac at three frequencies

3. Wavelet-analysis

Two-parameter analyzing function of one-dimensional wavelet transform is well localized both in time and frequency. This distinguishes it from the ordinary Fourier analyzing function which covers the entire time axis. Thus, it is possible to see the detailed structure of the process and the evolution of the harmonic components of the signal in time (Smolentsev, 2010). We used a continuous wavelet transform based on Morlet function. On the wavelet spectra of the harmonic components of the signal are visible as bright spots, stretching along the time axis. The example of the wavelet spectrum is shown in Fig. 2.

For a long-period component of the flux at all three frequencies the manifestation of periods 7.2-8.7 years and 4.1-4.7 years is marked. From short-period component periods of 1 to 3 years are marked. One of the short periods of 1-1.2 years, appears on all three frequencies, with maximum in 1982. The phases of activity in BL Lac for the long period component were at a frequency of 14.5 GHz – 1980 and 2006, at the frequencies of 8 GHz and 4.8 GHz – 1981. For

the short-period component phases of activity were at a frequency of 14.5 GHz – 1981 and 2006, at 8 GHz – 1975, 1980 and 2006, at 4.8 GHz – 1981 and 1996. From 1968 to 1974. at frequency of 8 GHz, blazar BL Lac showed the highest activity. We have no data on the other two frequencies for this time interval. Another peak of flux density at all three frequencies was observed from 1980 to 1982.

Figure 2: A continuous wavelet-spectrum of the initial smoothed data for BL Lac at a frequency of 8 GHz

4. Singular spectrum analysis

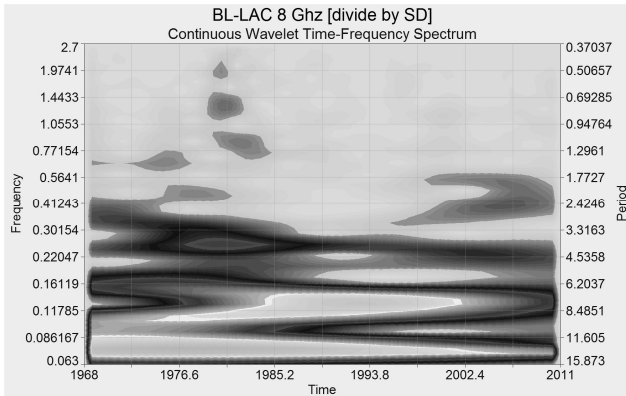Using the singular spectrum analysis we decompose the original signal into a set of narrow-band filters, which include trend components, periodic components and noise signal (Alexandrov, 2006). Using this set of narrow-band filters, the periods of sinusoidal oscillations in years were determined. To obtain spectral power distribution depending on time in study narrowband component obtained by analysis of a singular spectrum short Fourier transform was used, i.e. Fourier transform used a moving window where each window with overlaps calculated Fourier spectrum and as a result we get a step by step presentation of the temporal evolution of the spectral power and the frequency of the signal. Thus, it is possible to relate the formation of a certain period of time with the moment in which it was the highest. Examples of the obtained main components are shown in Figures 3 and 4.
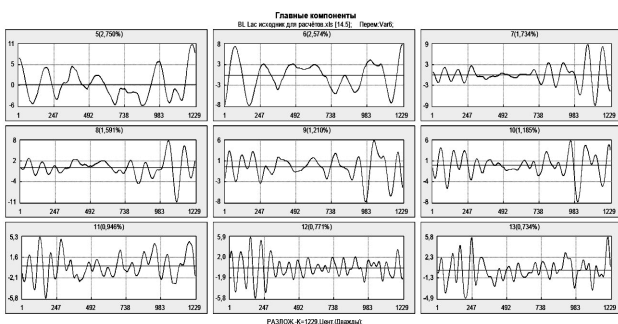

Figure 3: The main components for BL Lac at 14.5 GHz (1D)

The main drawback of this method with the analyzing function such as Fourier or wavelet analysis is that there is some test function used for comparison with the original series. Singular spectrum analysis allows to avoid the test function, so its calculations allow us within high accuracy distinguish various components of the test series.

The use of the singular spectrum analysis identified that the source BL Lac has periods of 4-5 years and 1.5-2 years at all three frequencies. There is a period of 7 years at 8 GHz. Periods obtained by analysis of the singular spectrum are shown in Table 1.

Table 1. Periods obtained by analysis of the singular spectrum for BL Lac

14.5 GHz	8 GHz	4.8 GHz
8	7	7
5 – 4	4.8 – 4	4
2.7 – 2.5	3.2	3
1.6 – 1.3	2	2.3 – 1.5
	1.3	
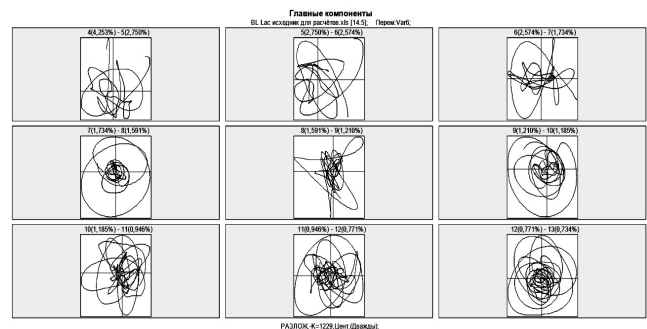
Figure 4: The main components for BL Lac at 14.5 GHz (2D)

Summary

Data processing using wavelet analysis indicates the presence of long-period component and short component, time of their existence and the main phases of activity in radio source BL Lac.

The use of the singular spectrum analysis identified:
– Blazar BL Lac has a long-period component of 7-8.7 and 4-4.7 years, as well as short component of 1 to 3 years.
– The source BL Lac has periods of 4-5 years and 1.5 -2 years at all three frequencies. There is a period of 7 years at 8 GHz.

The obtained data were compared with the results of VLBI monitoring MOJAVE during the period 1995-2012 at frequency 15.4 GHz, that allows us to investigate the structure of emissions during periods of maximum activity. In the jet of investigated source the existence of certain structures, moving with time and the existence of bright knots arising in the same distances from the core were indicated.

References

Alberdi A. et al.: 2000, *A&A*, **361**, 529.

Alexandrov F.I.: 2006, Development of software system for automatic selection and forecast of additive components of time series in the framework of the "Caterpillar SSA", Publishing House of St. Petersburg State University.

Aller H.D. et al.: 1985, *ApJS*, **59**, 513.

Britzen S. et al.: 2008, *A&A*, **484**, 119.

Gaydyshev I.: 2001, Analysis and data processing (the special directory), St.Petersburg Publishing house.

Jorstad S.G. et al.: 2001, *ApJS*, **134**, 181.

Lister M. L. et al.: 2009, *AJ*, **137**, 3718.

Smolentsev N.: 2010, *Veyvlet-analiz in MATLAB*, DMKPress.

DATA NETWORKING SUPPORT SERVICES OF PUSHCHINO RADIO ASTRONOMY OBSERVATORY, ASTRO SPACE CENTER OF LEBEDEV PHYSICAL INSTITUTE

D.V. Dumsky[1], E.A. Isaev[1,2,3], V.A. Samodurov[1,2], S.F. Likhachev[4],
M.V. Shatskaya[4], M.A. Kitaeva[1], A.Yu. Zaytcev[3], I.L. Ovchinnikov[1], V.V. Kornilov[2,3]

[1] Pushchino Radio Astronomy Observatory ASC LPI, Pushchino, Russia, *dumsky@prao.ru*
[2] National research university Higher school of economics, Moscow, Russia, *is@itaec.ru*
[3] Institute of Mathematical Problems of Biology, Russian Academy of Sciences,
    Pushchino, Russia,
[4] Astro Space Center LPI, Moscow, Russia

ABSTRACT. Growth of local area network Observatory associated with employee needs to access network resources has led to an increase in the number of computing and network devices. Until recently, we tested performance of these systems excellent manual and most of the problems and faults detected already on the fact the accident occurred. For a small number of network nodes, manual monitoring is not a significant problem, but with increasing the number of nodes troubleshooting becomes a very difficult task for network and system administrators and outage in work of netwok services Observatory may becomes critical. Therefore there was a need to automate the monitoring service network resources and servers.

Keywords: Telecommunications: networks: monitoring.

1. The choice of monitoring systems

The key to efficient network monitoring is to ensure that the selected instrument has been configured to monitor what, in fact, vital network availability, speed and utilization. Monitoring network availability allows both internal and external parties to access the services, including websites, DNS, databases and mail server. Monitoring network speed with bandwidth monitoring prevents our websites and other network services from losing visitors or frustrate users due to slow-loading pages, files or images. Finally, the use of monitoring allows to accurately estimate the load on the processor and find out just what type of work the servers are doing at different times of the day.

The criteria for selecting a new monitor for us were the ease of installation, intuitive setup, remote control via web browser, e-mail notifications about critical outages, free software and open source. That is why the choice was made in favor of Zabbix monitoring system. Zabbix is an enterprise-class open source distributed monitoring solution and uses a flexible notification mechanism that allows users to configure e-mail based alerts for virtually any event. This allows a fast reaction to server problems. Zabbix offers excellent reporting and data visualization features based on the stored data.

2. Monitoring LAN of PRAO ASC LPI

For load balancing, we have established a monitoring system on two servers of Observatory (Zabbix server and Zabbix proxy) thanks to its modular structure (Fig.1). As for implementation of the monitoring observatory network at the moment Zabbix server collects in one place and visualize a graphics and diagrams about utilization of RAM and CPU servers and network equipment, about free space remaining in file storages, about the temperature in the buffer data center. Information on the state and loading the main internal and external communication channels as well monitored by Zabbix. Monitoring keeps a history of all events occurred during his work and numerical values of monitored parameters in the MySQL database. User-friendly web-based administration interface allows us to flexibly configure the display of collected information and set how to alert if any error occurs. When thresholds of some critical parameters are exceeded or change the status of network interface, the administrator receive notification by e-mail and sound notifications in the browser web-based interface.

With the help of Zabbix agents that are installed on servers monitoring system collects basic and individually customized parameters for each server and services running on it. In particular mail queues being moni-
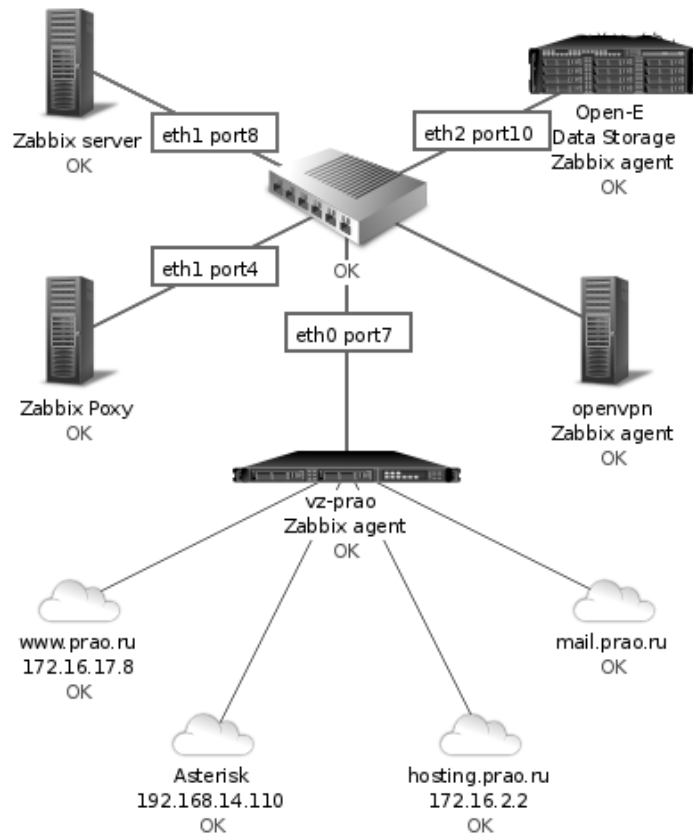
Figure 1: Zabbix monitiring servers map.

tored on the e-mail server and script that can check if the IP address of the e-mail server has been added onto a public DNS black lists what can lead to the inability to send emails from a domain prao.ru.

Zabbix proxy receives information about ethernet interfaces states, errors and utilization from a managed network equipment with the help of snmp (Simple Network Management Protocol) get request and snmp traps.

The current values of monitored parameters monitoring, as well as their changes can be viewed as separate graphs with variable scale from one hour to several weeks. We have split into groups monitoring data and formed so-called complex screens that allow one to display only currently interested graphics, information and network maps.

As a result of implementation a new system for monitoring the local network observatory we found the cause of frequent complaints of users on an error on delivery and sending of e-mails. And some other malfunction caused by network services as a large load on the equipment and malfunction of the individual hardware server components. By monitoring, we also fixed failure of one of the sections of the optical fiber at the territory of the Observatory and fiber breakage of communication channel allocated for data transmission from a space telescope in the experiment Radioastron.

PROSPECTS OF TRANSFERRIG THE LARGE VOLUMES OF RADIO ASTRONOMY DATA

E.A.Isaev [1,2,3], P.A.Tarasov [4]

[1] Pushchino Radio Astronomy Observatory, Astro Space Center, Russia
[2] National Research University "Higher School of Economics", Russia
[3] Institute of Mathematical Problems of Biology, Russia
[4] OOO «NPK-INFORM»

ABSTRACT. Shows the volume of scientific data generated by the leading radiostronomicheskimi projects. The methods of transmission of large amounts of data in the present time and in the future.

Key words: radioastronomy, data transfer.

Currently there has been a significant increase in the volume of experimental data in astronomy and astrophysics. A single observation that can last from several seconds to several minutes gives from a few megabytes up to several gigabytes of data or even more. There is a need for transfer of this information for filtering, storing and further studies [1].

Let's consider some of the largest astronomical research projects that operate with huge amounts of information.

An array of radio telescopes LOFAR is one of the largest international projects. Regular observations are being conducted from December 2012, but have not yet reached its full capacity [2]. This array of telescopes requires the bandwidth from 2 to 20 Gb/s to operate in the normal mode from the cable system that connects the stations. These stations will unite around 10,000 of radio antennas.

The largest global astronomical project under development is currently The Square Kilometre Array (SKA) [3]. This project is scheduled to reach the full capacity of data collection in 2024. It is expected that the SKA telescope will generate more than 1 exabyt of data per day upon reaching its full capacity, which is comparable to the volume of all Internet traffic existing at the moment.

The only technology that is currently capable of meeting the growing demand for the transfer of scientific data is fiber-optic communications. The fastest fiber optic data transmission was achieved by the Japanese companies Nippon Telegraph and Telephone Corporation (NTT). Their September 2012 experiment showed a record speed of data transfer. During the testing of a new link, the specialists have registered the data transfer speed of 1 petabit per second over fiber optic cable with 12 channels and the lightguide length of 52.4 kilometers [4]. In the summer of 2014 a team of researchers from the Danish Technical University has set a record for the fastest data transfer rates in the world with a single transmitter (43 Tb/s) [5].

The transmission of information using one of the quantum characteristics of photons – their "twist" – the orbital angular momentum of photons with respect to their direction of propagation – is currently being studied very intensively. It is currently prospected that in the near future it will allow a virtually unlimited expansion of data transmission bandwidth. It is this property of photons which allows the transmission of information through qubits in a quantum superposition, so an infinite number of states describing arbitrary points in a multidimensional space can be the units of data transfer. A recent experiment proved the reliability of a method even when information is transmitted through the atmosphere. Transfer rate is 4 pixels per second. Given the purpose of the experiment – to show that at large distances the turbulence of the atmosphere in the process of transfer has no significant impact on the reliability of data transmission – it is possible to draw a conclusion about the prospects of this method for the transmission of large amounts of information [6].

Thus, in order to maintain an efficient transmission, filtering and processing of the data received from the radio astronomy facilities, it is necessary to implement innovative technological solutions to significantly increase the speed of data transmission both through the existing communication networks and through the construction of the new channels of communication that will deal with the transfer of extra-large volumes of data while taking the projected rate of growth into account.

References

1. Isaev E. A., Kornilov V. V., Tarasov P. A., Samodurov V. A., Shatskaya M. V. Transmission, storage and processing of large amounts of astronomical data. Preprints. Physical Institute of the PN Lebedev, Russian Academy of Sciences. Series "Preprint". 2014. № 8.
2. The official site of the project LOFAR. URL: http://www.lofar.org/.
3. The official site of the project SKA. URL: http://www.skatelescope.org/.
4. World Record One Petabit per Second Fiber Transmission over 50-km. Официальный сайт NTT Group company. 2012. URL: http://www.ntt.co.jp/news2012/1209e/120920a.html.
5. The official website of the Danish Technical University. URL: http://www.dtu.dk/Nyheder/2014/07/Verdensrekord-i-dataoverfoersel-paa-danske-haender-igen.
6. e-print «Twisted light communication through turbulent air across Vienna».http://arxiv.org/abs/1402.2602.

TRACKING TYPE III RADIO BURST SOURCES IN THE SOLAR CORONA BY HELIOGRAPHIC MEANS

A.A.Koval[1], A.A.Stanislavsky[1,2], A.A.Konovalenko[1], Ya.S.Volvach[1]

[1] Institute of Radio Astronomy of NAS of Ukraine, 4, Chervonopraporna Str., 61002, Kharkiv, Ukraine, *akoval@rian.kharkov.ua*

[2] V.N. Karazin Kharkiv National University, Svobody Sq. 4, 61022, Kharkiv, Ukraine

ABSTRACT. We present the preliminary results of heliographic measurements of solar type III radio bursts in the low-frequency range (16.5-33 MHz) using the UTR-2 radio heliograph. The radio astronomy tools permit us to obtain two-dimensional spatial structures of burst sources in dependence of frequency and time. Each heliogram consists of 40 pixels (beams) as a result of the serial sweep in *UV*-plane wherein signals of each beam are recorded in a dynamic spectrum with both high temporal (~ 2.482 ms) and top spectral (~ 4 kHz) resolutions. The rate of output heliograph is one image per 3 seconds. Over a session in April, 2013 many type III radio and IIIb-III bursts were observed. On the heliograms the source motion direction in the upper corona is clearly detectable. The heliogram features are discussed.

Key words: Sun: radio emission – bursts: radio heliograph: UTR-2 radio telescope

1. Introduction

Solar bursts are important manifestations of solar activity because they are related to sporadic acceleration of enormous flows of solar plasma matter caused by release of energy stored in magnetic fields. The radio observations of bursts provide valuable information about solar plasma properties in the corona through which the bursts propagate. Many solar bursts reliably are identified with their sources from the study of frequency-time characteristics of these bursts that gives an indirect opportunity to specify parameters of their emitters.

Vast population or "zoo" of solar bursts manifests themselves in ground-based and space-based observations within wide frequency band. Such radio bursts were classified into several different types on the basis of their frequency drift rates df/dt (Wild, 1963). Solar emission in decameter wavelengths range (3-30 MHz) is abundant in bursts too. Recall a brief description of solar bursts characteristic for the decameter range. The type II and type IV bursts are often associated with coronal mass ejections (CMEs) which are generally attributed to solar flares or filament eruptions (Subramanian and Dere, 2001). The II type bursts are slowly drifting emission ($df/dt < 0.1$ MHz/s within 10-30 MHz) which is believed to be generated by shock waves traveling through the solar corona (Melnik et al., 2004). The broad continuum radia-

tion with varying the time structure relating to CME body itself is called the solar IV type burst.

The solar III type bursts are the most numerous events filling the low-frequency band (<100 MHz). In decameter wavelengths the type III bursts have typically drift rates about – (2−4) MHz/s (see, for example, Abranin et al., 1990). Such radio emission is associated with beams of fast electrons moving outward into interplanetary space along open magnetic field lines. Durations of these bursts can be up to 20 s, while the most are found in the range within 4-10 s in the frequency band 10-30 MHz. The energetic characteristics of decameter type III bursts is that their brightness temperatures can achieve to 10^8-10^9 K.

In many cases the conventional analysis of solar dynamic spectra is restricted by the determination of above-mentioned parameters of type III bursts. Unfortunately, there are no in-depth reports about spatial characteristics of type III bursts sources at low frequencies with the exception of space-based observations below 10 MHz (see, for example, Morosan et al., 2014). Particular estimations of spatial sizes of electron beams, which are sources of type III bursts, have been performed by Benz (2009). In decameter wavelengths the spatial structure of burst sources was studied by Abranin et al. (1976) as well as by Chen and Shawhan (1978). In general it was found that the angular width of type III burst sources increases inversely proportional to frequency.

One of the Ukrainian radio-astronomy projects developing on the basis of the UTR-2 telescope is a new radio heliograph aimed to study quiet-Sun radio emission and solar bursts activity in the wide low-frequency range 8-33 MHz. The instrument opens wide perspectives to fill the gaps in solar low-frequency data as applied to angular sizes of solar burst sources. In this paper we present preliminary results obtained by the UTR-2 radio heliograph to study the angular structure of type III radio bursts.

2. Instrument and observations

The radio heliograph based on the UTR-2 antenna system is an updated low-frequency instrument capable of measuring two-dimensional images of brightness distributions within 8-33 MHz (Stanislavsky et al., 2011). The dipoles (2040 units) of UTR-2 are divided on 12 sections forming three arms called North, South and West. The large total area of UTR-2 (~ 140000 m^2) permits us to investigate

both sporadic solar radio emission and continuum radiation of the quiet Sun in complicated interference conditions (Konovalenko et al., 2013). Recently, the heliograph has successfully proved itself in getting maps of quiet-Sun corona in the decameter range (Stanislavsky et al., 2013). The powerful back-end facilities of UTR-2 give opportunities to carry out observations with high time (from 0.2 msec up to 1 sec) and top frequency (~ 4 kHz) resolutions under wide dynamic range (over 90 dB). The present configuration of the radio heliograph is based yet only on a serial mode, i.e. an antenna pencil-beam changes its position consecutively along declination and hour angle, forming *UV*-images. Each image element is spaced on 30 minutes in declination and hour angle at 25 MHz. The angular field of heliograph view is about 2.5°×4.0°, and each frame consists of forty (5×8) pixels as an image matrix (Konovalenko et al., 2012).

The pilot heliographic observations of solar bursts have been fulfilled on 9-11 April 2013 in the frequency band 16.5-33.0 MHz. At that time the solar activity is accompanied by a large number of solar bursts, mainly IIIs type. In the observations the radio heliograph beam was formed with help of multiplying knife-pattern beams of North-South and West arms. The low-frequency operating range enables to study upper layers of the solar corona. Therefore, we can observe spatial and temporal peculiarity of coronal processes, particularly the evolution of angular structure of burst sources, in about 2-3 radii from the center of the Sun. At these heights the angular dimensions of type III burst sources correspond to about one solar radius and even more. The preliminary analysis of heliograms was performed for several III and IIIb-III bursts. The dynamic spectrum example of a type III burst is shown in Figure 1a. On Figure 1b the dynamic spectrum of this event recorded from the radio heliograph is presented. The consecutive record has the brightest vertical stripes being noise generator markers that indicate start/end instances of frames. The time between such two neighboring stripes (time of frame composition) is equal to 3 seconds. In the data processing the serial record was converted into a set of two-dimensional images. Consequently, the three-dimensional angular structure evolution of the type III solar burst source (*UV*-plane frames at selected frequencies in dependence of time) is obtained. It is quite visible that the burst duration expands with decreasing of frequency (see Figure 1a). Besides, the burst intensity peak moves towards low frequencies, i.e. the electron beam travels away from Sun to high altitudes in solar corona (see Figure 1c). The peak-in-time evolution from frame to frame indicates source-motion directions for this burst.

3. Summary and future work

The angular dimensions of sources of solar radio bursts are still not explored profoundly at low frequencies. Using the two-dimensional heliograph of UTR-2, we have shown that the tools allow us to get spatial information about sources of type III radio bursts within 16.5-33.0 MHz. Consequently, the three-dimensional evolution in time (so-called **3D+1** representation) of type III bursts spatial structures is obtained. A next step in the analysis of spatial features of IIIs bursts is the statistic estimation of angular sizes of their sources. The further researches will be focused on investigations of solar type II, IV bursts sources attributed to CMEs.
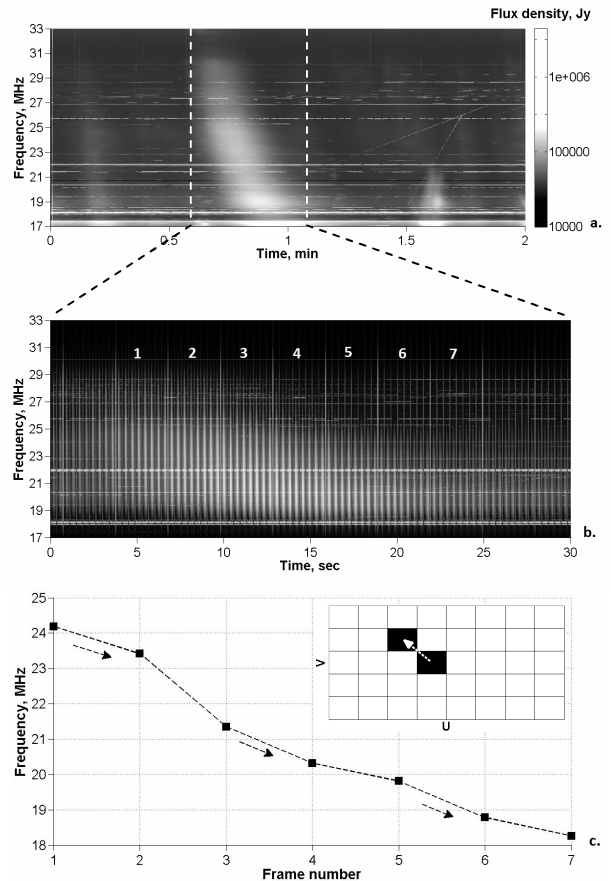

Figure 1: a) Dynamic spectrum recorded by UTR-2 at April 9, 2013. Time zero corresponds to 10:33:59 UT; b) Serial record obtained from heliographic measurements; c) Source position drift in *UV*-plane, frequency and time.

It should be also noticed that the measurement of burst source sizes can be carried out by two methods: either scanning by a radio telescope narrow beam or using interferometer tools. The facilities of UTR-2 enable to realize both methods simultaneously. This work plans to perform in the future too.

References

Abranin E.P. et al.: 1976, *SvA*, **19**, 602.
Abranin E.P. et al.: 1990, *SvA*, **34**, 74.
Benz A.O.: 2009, *LanB*, **4B**, 148.
Chen H.S., Shawhan S.D.: 1978, *Sol.Phys.*, **57**, 205.
Konovalenko A.A. et al.: 2012, *RPRA*, **3**, 1.
Konovalenko A.A. et al.: 2013, *Exp. Astr.*, **36**, 137.
Melnik V.N. et al.: 2004, *Sol.Phys.*, **222**, 151.
Morosan D.E. et al.: 2014, *A&A*, **568**, A67.
Stanislavsky A.A. et al.: 2011, *RPRA*, **2**, 197.
Stanislavsky A.A. et al.: 2013, *AN*, **334**, 1086.
Subramanian P., Dere K.P.: 2001, *ApJ*, **561**, 372.
Wild J.P.: 1963, *IAU Symp. Proc.*, **16**, 115.

THE DAILY 110 MHZ SURVEY (BSA FIAN) IN THE ON-LINE MODE: DATABASE AND PROCESSING METHODS

V.A.Samodurov [1,2], M.A.Kitaeva [1], S.V.Logvinenko [1], E.A.Isaev [1,2], D.V.Dumsky [1], V.D.Pugachev [1]

[1] Pushchino Radio Astronomy Observatory ASC LPI, Pushchino, Russia, *sam@prao.ru*
[2] National research university Higher school of economics, Moscow, Russia

ABSTRACT. From 2012 on radio telescope BSA FIAN multi beams diagram was started. It capable at July 2014 daily observing by 96 beams in declination -8 .. 42 degrees in the frequency band 109-111.5 MHz. The number of frequency bands are from 6 to 32, the time constant are from 0.1 to 0.0125 sec. In receiving mode with 32 band (plus one common band) with a time constant of 12.5 ms (80 times per second) respectively produced 33x96x80 four byte real and so daily we produced 87.5 Gbt (yearly to 32 Tbt). These data are enormous opportunities for both short and long-term monitoring of various classes of radio sources (including radio transients) and for space weather and the Earth's ionosphere monitoring, for search for different classes of radio sources, etc.

Key words: radio survey, monitoring, database.

1. Observation

From 2012 on radio telescope BSA of LPI multi beams diagram was started. It capable at July 2014 daily observing by 96 beams in declination $-8° < \delta <+ 42°$ in the frequency band 109.0 – 111.5 MHz (Oreshko et al., 2012).

The number of frequency bands are from 6 (417 kHz for each band, "small observational mode") to 32 (78 kHz for each band, that called "big observational mode") and the time constant of observational data from 0.1 sec ("small observational mode") to 12.5 ms ("big observational mode"). Thus continuous daily survey for most of the observed part of the sky is not yet over none observatories worldwide. Observations are carried out for more than two years, in a day is usually written from 2.3 GBT (small observational mode that have 6 bands and a time constant of 0.1 seconds) and per year – 0.8 TBT data. In big observational mode with 32 band (plus one common band) with a time constant of 12.5 ms (80 times per second) respectively produced 33x96x80 four byte real numbers and so daily we produced 87.5 GBT (yearly to 32 TBT).

In May 2014 work was completed for updating of our soft and multi-channel digital recording complex was rebuild. It is now possible to register at the same time in two different modes: small mode (6 bands of 10 times per second for 96 beams-channels) and big mode of observation (32 frequency bands 80 times per second for 96 beams-channels).

The big observational mode is need in the near future for the purpose of searching radio transients of different species. At the end of October 2014 we accumulated over three months of observations "heavy" format (total volume of about 10 TBT).

2. Database and data processing

The big observational data need in constructing special database. Already an experimental database for the period from 7 July 2012 up to the 20th of October 2013for more than 20 parameters are calculated for each beam for every 5 seconds (more than 8 million time points). By these data almost one million images was built (see Figure 1). By the end of 2014 will be finished work on the base data in on-line on the site http://astro.prao.ru/. From the database can be produce different ways of processing the observations, including by remote observers.

Highlight the fact that it was placing the compressed data in the sql database formats allows us to use the power of selection, sorting, matching, filtering and initial processing of data by means mechanism of standard sql commands. This will greatly simplify the interaction and the comparative analysis of the data for different sorts of data and their cross-temporal analysis, averaging etc. These data are enormous opportunities for both short and long-term
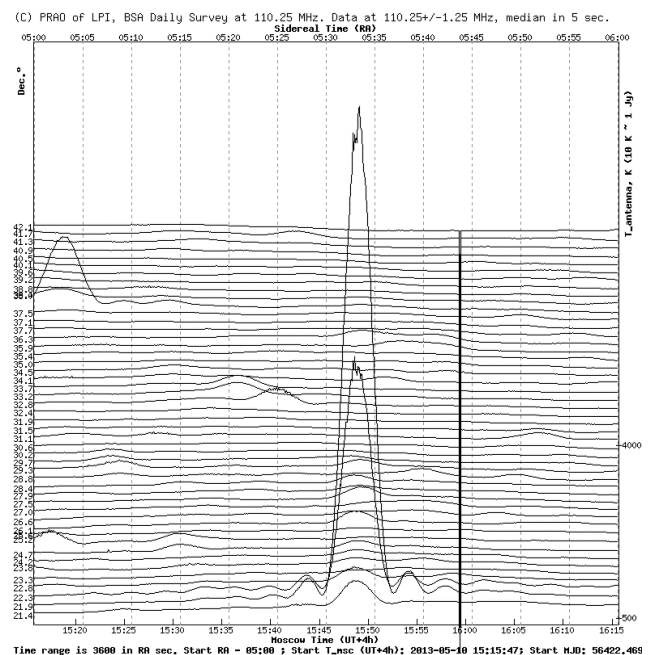

Figure 1: Example of multi beams observational data from BSA of LPI at 13 May 2013 (shows the source 3C 144 in bottom of the figure and calibrating signal to the right).

monitoring of various classes of radio sources (including radio transients) and for space weather and the Earth's ionosphere monitoring, for search for different classes of radio sources, etc.

As a result, as shown by preliminary estimates, we may reach the velocity of data processing practically in on-line mode (with a time lag of no more than 2-3 hours after the observations). All data – like the original observations and the results of processing on various scientific objectives will be continuously displayed on the PRAO of LPI website. For public use, it will be displayed in graphical form, as participants work will be available and the data in digital form.

In the total database and data reduction it can be also included on the basis of mutual benefit and the most low-frequency survey observations in word from the Ukrainian radio telescope UTR (Vasylieva I.Y. et al).

3. The future results of data processing and scientific aims

From a scientific point of view, the data held by the observations allow a high sensitivity to capture all sources of cosmic radio emission from a specified portion of the sky.

The classes of problems that can be solved in this monitoring system is unusually wide, and it is not only the fundamental scientific problems, but also problems of applied sciences. The proposed project allows to continuously monitor the celestial radio sources in most parts of the sky on time scales from milliseconds to years (this feature is implemented first time in the history of astronomy). Only briefly list the main science aims:

1) Monitoring of the ionosphere state and its fluctuations (with a characteristic time scale of tens of seconds). The task is closer to the applied sciences, but we will to solve it for searching the sources coordinate shifts in the process of solving the problem of monitoring radio sources fluxes.

2) Monitoring of active phenomena on the Sun (sporadic outburst on every some tens days, the time scale of outburst – from seconds to hours), and the state of the near-solar plasma. This broad class of problems of research on near-solar source flicker interplanetary plasma, and we will monitor and display in graphical form at least the most common parameters of its condition at the site PRAO of LPI.

3) Radio monitoring transient (flare) phenomena in the solar system, and ionospheres storm effects on the giant planets, tracking radio transients phenomena on the moon, other possible radio phenomena in the solar system. To our knowledge, the mass daily monitoring of such phenomena on the time scale of the order of years nobody has yet been made.

4) Monitoring of transient phenomena in our Galaxy: this class of problems is unusually wide – from studies of outbreaks of radio emission from cataclysmic variables to search for candidates in exoplanets (planets around other stars). Not all of them can be implemented on our radio telescope, but some events (for example it is flash cataclysmic variables on the scale of seconds) available to us.

5) Monitoring of extragalactic radio sources fluxes. In the literature, there are some indications of the variability of radio sources on scales of months at frequencies of hundreds of megahertz. However, work on long-term observations on the complete sample of radio sources at one hundred megahertz available not yet (only conducted studies of individual sources – see., Volvach A.E. et al). For aims of extragalactic radio sources monitoring (the 15 degrees from the plane of the Galaxy) inside the existing 96-beems diagram of BSA we can select about of 400-500 sources for daily monitoring.

6) Monitoring and searching of the many years variations of radio sources in our Galaxy. Although these variations are small enough (e.g., radio flux of the Crab Nebula in the year varies by about 0.3%), but based on the results of daily data statistics monitoring on the scale of months and years, can significantly clarify these data.

7) Extragalactic transient phenomena. The most interesting problems are searching of fast radio transients (on the scale of a few milliseconds) in other galaxies. Similar radio transients under some papers found in the decimeter range in the last few years. Theorists associated with them, such as the possible merger of neutron stars. Phenomena of this magnitude are energetic and highly to be detected in our antenna even for very distant galaxies at a distance of up to hundreds of Mpc. This problem is currently very topical for Astrophysics, meanwhile in the meter band fast radio transients no was looking.

In total multi beam observation on BSA of LPI will exploit the wide-field survey capabilities to enable the discovery and investigation of variable and transient phenomena from the local to the cosmological, including flare stars, intermittent pulsars, X-ray binaries, magnetars, extreme scattering events, interstellar scintillation, radio supernovae, and orphan afterglows of gamma-ray bursts. In addition, it will allow us to probe unexplored regions of parameter space where new classes of transient sources may be detected.

References

Oreshko V.V. et al.: 2012, *Transactions of the Institute of Applied Astronomy (Russia)*, **24**, 80.

Vasylieva I.Y. et al.: 2014, *Radio physics and radio astronomy (Ukraine)*, **19, № 3**, 197.

Volvach A.E. et al.: 2006, *Astronomical and Astrophysical Transactions*, **25, Issue 5**, 385.

VARIABILITY FEATURES OF THE RADIO SOURCE OT 081 IN CENTIMETER WAVELENGTH RANGE

Sukharev A.L.[1], Margo F. Aller [2]

[1] Radio Astronomical Institute of National Academy Sciences of Ukraine, Observatory "URAN-4"

[2] Radio astronomical observatory of Michigan University, Ann Arbor, USA

ABSTRACT. OT 081 – BL Lac object, intensively studied for many years in a wide range of the electromagnetic spectrum. We used observational data for 1999-2011 years, obtained on radio telescope at Michigan State University (UMRAO) at frequencies 14.5, 8, 4.8 GHz. For the study variability of the radio source used wavelet method of time series analysis. The values of main periods at three frequencies are ~2.6 and 1.2 years. The shortest periods with values ~0.9, 0.6, 0.4 years were shown in small time intervals (1.5 years). For harmonic components isolated by filtration, determined delay between radio frequencies. Obtained comparison of change between periods fluctuations of radio fluxes and dynamics in the radio jet (image VLBI Mojave, 15.4 GHz).

Introduction

Studied radio source OT 081 (1749+096) is a BL Lac objects, which are characterized by rapid and significant changes of luminosity over all range of electromagnetic spectrum, as well as a continuous optical spectrum and polarization. OT 081 is located in the constellation Ophiuchus, the redshift – 0.322 [1], distance – 1230 Mpc, the largest speed of jet component – 7.9c [2], radio spectrum is flat, OT 081 is a powerful gamma ray source.

Data processing

Original data on three frequencies (14.5, 8, 4.8 Ghz) were obtained on a 26-meter radio telescope of the University of Michigan. Methods of observations and data processing on RT-26 is described in article [3]. Observation period, 1999-2011 years (Figure 1). The average time interval between data points is 7 days. The correlation coefficients between frequencies: 0.90 (14.5-8 Ghz), 0.76 (14.5-4.8 Ghz), 0.92 (8-4.8 Ghz).

In the process of preparing data for analysis conducted smoothing by local spline regression method [4]. To search periodicities in the data used continuous wavelet analysis with the Morlet function and wavelet filtering, a detailed description of which is referred in literature [5, 6, 7]. Defining the time delay between the data at different frequencies is performed using cross-correlation method [8].
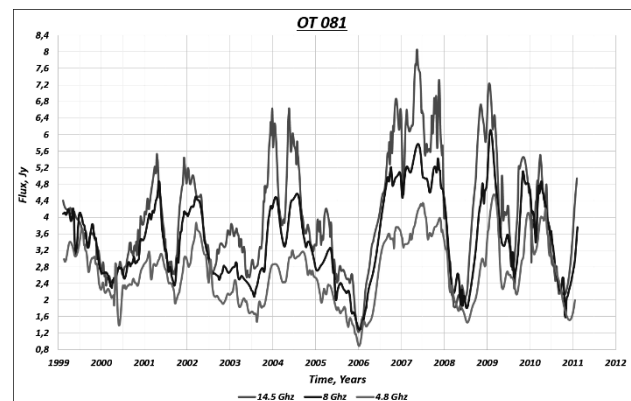

Figure 1: OT 081, graphs of radio fluxes at three frequencies of observations

Wavelet analysis

As a result of the analysis were obtained coefficient matrix of the continuous wavelet transform, representing a surface in three-dimensional space. Usually, they are replaced by projections on the plane "frequency-time" with the contour line, allows tracking changes over time in the frequency spectrum. Examples of wavelet spectra are shown in Figure 2.

By results of wavelet analysis, periods on three frequencies have similar values ~2.6 (main) and ~1.2 years. At frequencies of 14.5 and 8 Ghz, value of the main period is changes about ~0.3 years. At a frequency of 14.5 Ghz is allocated a weak five-year period (wave with two vertices 2002.1 and 2008.0), maybe it's the harmonic of main period. Elements of the spectra corresponding to the value of the period ~0.9-0.4 years represent sequentially located splash of radio flux with a decrease in the period to the end of time series.

Phase of activity defined by the time of maximum in global spectra averaged over frequency (show the distribution of total power spectral density of the signal over time), used for communication with variation of periods and change in VLBI structure of radio source. Below is a table of periods (Table 1).
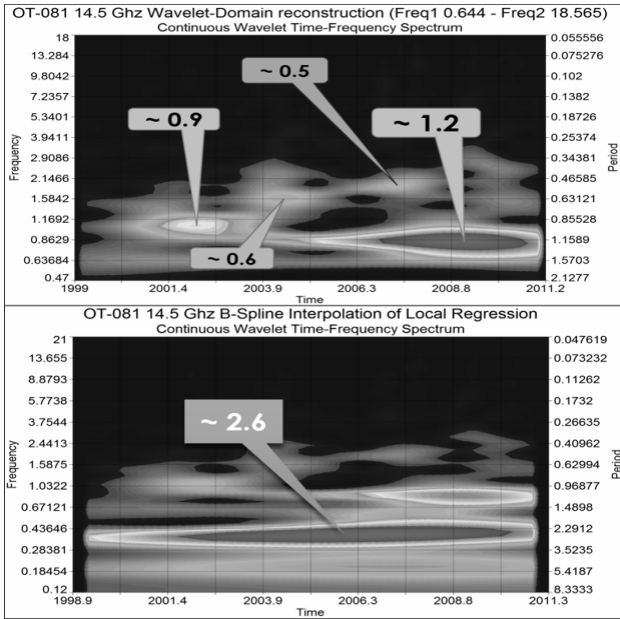
Figure 2: Wavelet spectra at a frequency of 14.5 GHz. The bottom graph – the original time series, the top – the short period allocated by filtration. Flags indicate periods in years.

Table 1. Table periods for radio source OT 081

OT 081							
Freq.	P_{max}	P_{min}	T_{start}	T_{end}	PSD_{max}	T, PSD_{max}	T, GWS_{max}
14.5	2.7	2.4	2000.2	2010.0	527	2006.1	2004.3
	1.2		2006.5	2010.6	250	2008.8	*2008.0*
	0.9	0.5	2001.5	2008.1	68	2002.0	
8	2.7	2.5	2000.4	2009.8	325	2006.0	2002.3
	1.2		2006.6	2010.7	137	2008.6	*2009.2*
	0.9	0.4	2001.4	2010.5	32	2002.5	
4.8		2.6	2000.3	2009.8	360	2006.2	2002.1
	1.2		2006.4	2010.5	162	2008.8	*2009.3*
	1.4	0.4	1999.7	2010.5	23	2003.1	

Designation: Freq. – frequency of observations (in Ghz); P_{max}, P_{min} – interval of period (in years) change; T_{start}, T_{end} – time interval of period existence; PSD_{max}, T, PSD_{max} – maximum value of the spectral power and the corresponding time; T, GWS_{max} – phase activity (main underlined).
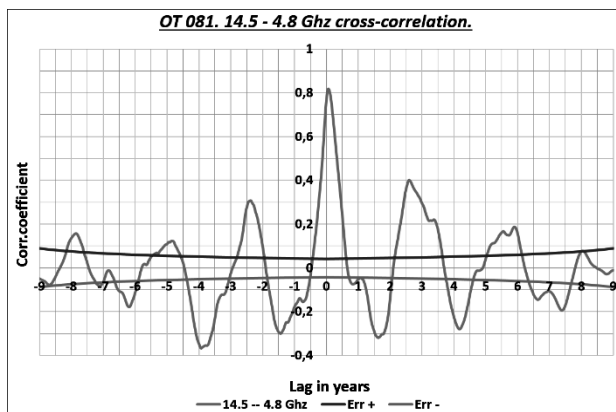

Figure 3: Cross-correlation function with the confidence intervals for frequencies pair 14.5 and 4.8 Ghz. The time delay – 22 days.

Table 2. Values of the time delay in days

Delay between frequencies, in days			
Freq. pair	Lag, orig	Lag, $P_{2.6}$	Lag, $P_{1.2}$
14.5 -- 8	14,5	22,0	22,0
14.5 -- 4.8	22,0	44,0	29,2
8 -- 4.8	7,3	29,2	7,3

Lag orig – delay for the original series; Lag, $P_{2.6}$ – delay in the period band 2.6 years; Lag, $P_{1.2}$ – delay in the period band 1.2 years.

Delay between frequencies

Using wavelet filter been allocated data for comparison in periods bands 2.6~1.2 years. Below chart shows an example of cross-correlation function (Figure 3) and a table of analysis results (Tabl.2).

Comparison of the radio emission variability with VLBI maps

In this work, we attempt to relate changes in quasi-periodic oscillation of radio flux with passage of bright spots in the jet. Each phase of activity correspond to forming her periods [9]. At times moments indicated in Table 1 were constructed local power spectra for each year individually. When comparing the local spectra with 15.4 GHz VLBI maps (MOJAVE Program [10]) evidently, that transit of each new bright spot on jet significantly alters the signal spectrum. Appropriate examples are given in Figure 4.

When the activity is low jet, intensity more at long period, when in jet appear bright components, increased intensity of a short period. When jet activity is high, intensity short period is greatest. Short splash may correspond to double components near the VLBI «core» source. Therefore most likely that the rapid variability of the radio emission forms a jet activity and long-term – core activity. Certain patterns can be extended to observation period when sessions VLBI measurements were not.

Results

Processing data showed the presence quasi-periodic components with periods ~2.6 and 1.2 years, as well as short-term fluctuations of flux with decreasing period of ~0.9-0.4 years, which appear on the tops of the main wave variability. Harmonic with 1.2 years period, intense in the second half of the investigated data. Period 2.6 years (14.5, 8 Ghz) slightly varies with time (0.2, 0.3 years). Obtained values of time delays. For original and filtered data in the period band 1.2 years for their sum frequency pairs 14.5-8 and 8-4.8 Ghz alike approximate delay between the extreme frequencies of 14.5-4.8 Ghz. At the time range trigonometric polynomials with periods found in good agreement with the original data, which shows their stability over time. The error in determining periods of ~0.08 years. A comparison of the periods of variability with changes VLBI structure showed that the bright
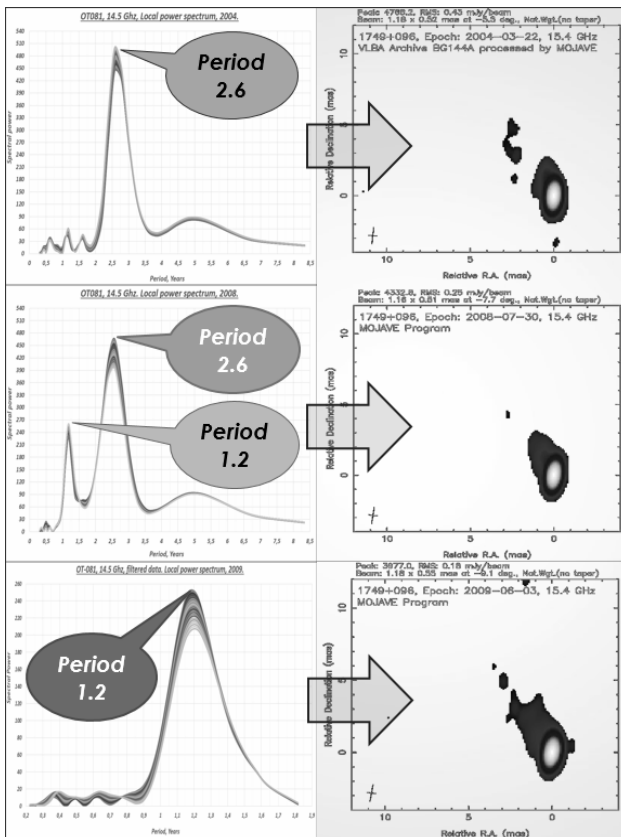
Fig.4. Changing periods and corresponding VLBI structure of radio source OT 081. In VLBI image (2004.03.22) activity jet weak and prevails during 2.6 years, the image (2008.07.30) is active new component in jet, to the period of 2.6 years, 1.2 years is added, the image (2009.06.03) activity jet high, 1.2 year period has the greatest spectral power.

components of the jet shape fast quasi-periodic variations in the radio flux. Longer flow changes, probably related to the activity of the nucleus of the radio source. Jet of radio source has a complicated, curved structure, perhaps a bimodal velocity distribution in the jet [11]. To explain the variability of BL Lac objects are often used models of shock waves interaction superluminal component with jet [12]. Motion of the components in the jet OT 081 on curved trajectory indicates the possible applicability of binary black hole model [13]. In this case, in addition to the precession of the jet, satellite can create tidal perturbations in the accretion disk and the vibrations that affect the variability of the radio flux [14].

References

1. Stickel et al.: 1988, *A&A*, **191**, 16.
2. Lister et al.: 2013, *AJ*, **146**, 120.
3. Aller M.F., Aller H.D., Hughes P.A.: 2001, *Bull. of the American Astronomical Society*, **33**, 1516.
4. William S. Cleveland: 1993, *Visualizing Data*, Hobart Press, Summit, NJ, ISBN 0-9634884-0-6.
5. Davidov A.V. Digital processing of signals: Thematic lectures. / Yekaterinburg: UGGU, IGIG, geoinformatics chair. – 2007.
6. Smolentsev N. Wavelet-analysis in MATLAB. DMK-Press, 2010.
7. Astaf'eva N.M.: 1996, *Uspekhi Fizicheskikh Nauk*, **166**, № 11.
8. Rosenberg G.S., Shitikov V.K., Brusilovsky P.M. Ecology Prediction (functional predictors of time-series). Tolyatti, 1994.
9. Ryabov M., Donskyh A., Sukharev A., Aller M.: 2012, Odessa Astron. Publ., **25/2**, 132.
10. Lister et al.: 2009, *AJ*, **137**, 3718.
11. Lu R.S., Zhen Z.Q. et al.: *http://arxiv.org/abs/1204.4150v2*.
12. Alan P.Marscher: 2008, *ASP conference series*, **386**.
13. Frank M.Rieger: *http://arXiv.org/abs/astro-ph/0506720v1*.
14. Optical monitoring of PKS 1510-089: a binary black hole system? *MNRAS*, 2005, **361 (1)**, 155.

PHYSICAL PARAMETERS OF HII/PDR COMPLEX IN ORION BAR ESTIMATED BY OBSERVATIONS OF 8 MM RECOMBINATION LINES. EFFECTIVE TEMPERATURE OF θ^1 C Ori STAR

A.P.Tsivilev [1], S.Yu.Parfenov [2], A.M.Sobolev [2]

[1] P.N. Lebedev Physical Institute, Academy of Sciences of Russia, Moscow, Russia, *tsivilev@prao.ru*
[2] Ural Federal University, 51 Lenin Str., Ekaterinburg 620000, Russia

ABSTRACT. Physical parameters of HII/PDR complex in Ori Bar were estimated using observations of recombination radio lines (RRL) of carbon (C), hydrogen (H) and helium (He) with RT-22 radio telescope in Pushchino. Possible structure of the complex is discussed. Effective temperature (T_{eff}) of the star ionizing Orion nebula was estimated. Obtained estimate provides additional constraint to existing "spectral class – T_{eff}" calibrations for O-stars indicating that the θ^1 C Ori star with ≈ O6.5 V spectral class has T_{eff} in the range 36 000–37 500 K.

Key words: Stars: OB stars, parameters – Interstellar medium: HII regions, PDR – Spectroscopy: RRL

1. Introduction

Hot OB stars emit amount of UV photons which is sufficient to form ionized hydrogen region (HII region). In a thin intermediate layer between the HII region and the cold natal molecular cloud (MC), called Photo Dissociation Region (PDR), molecules are destroyed and atoms with ionization potential lower than that of hydrogen, mostly carbon, are ionized. Hydrogen (H) and helium (He) recombination radio lines (RRLs) are formed in the HII regions in a wide wavelength range. The RRLs of carbon (C) are formed in PDR. Theory of RRL formation in HII regions is well known (Sorochenko, Gordon 2003). Determination of the PDR parameters using carbon RRL data complemented by the data on the infrared CII and OI lines was recently elaborated (Sorochenko & Tsivilev, 2000; 2010).

Modern radio instruments allow observation RRLs of H, He and C in a single band and, thus, information on both HII region and PDR can be obtained simultaneously. Orion Bar is a HII/PDR complex in the Ori A nebula, one of the most studied astronomical objects. The Ori Bar is located at about 2' to the south-east of the Ori A center.

2. Observations and results

In order to study this HII/PDR complex we performed observations of H, He and C RRLs in the 8 mm range. The observations were carried out with RT-22 telescope in Pushchino toward 4 positions of Ori Bar and in the direction to the center of Ori A (see Figure 1). Physical parameters of the Ori Bar HII/PDR complex estimated from these observations are given in Table 1.

Ori A HII region has a core-halo structure of "blister" type and is formed at the MC boundary closer to observer (Poppi et al. 2007; Tsivilev et al. 1986). Based on the data obtained in this work and the data from literature one can come to the following conclusions. The thin layer of PDR envelopes the core of HII region (Ori Bar outlines the core boundary and its ionization front) and extends further outside the Ori Bar as a boundary between HII region halo and the MC. Our estimates of the hydrogen number density in the Ori Bar PDR are in the range $\sim(1-3) \times 10^5$ cm^{-3}. Estimates of PDR extent along the line of sight (L) are in the range 0.006–0.04 pc. The maximum value of L is realized in direction toward Ori Bar. Our value is smaller than in the literature, which can be explained by the presence of clumps in PDR. The PDR temperature decreases from 210–230 K to 140–150 K with the distance from the ionizing star θ^1 C Ori which apparently heats PDR material. It is possible that HII region exerts pressure on the ambient
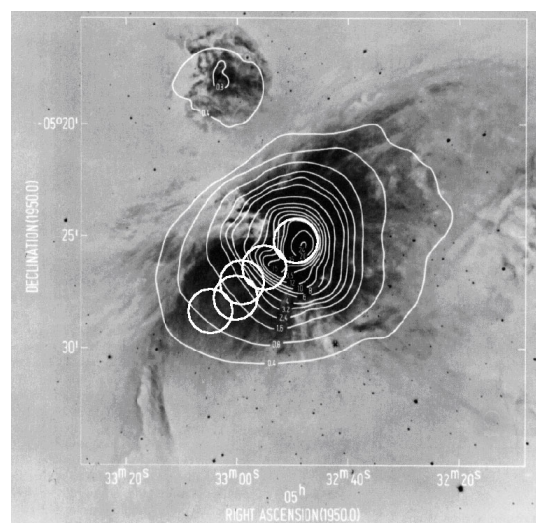

Figure 1: Optical image of Ori A region (in Hα and NII, Hua & Louise 1982). Contours (faint white lines) designate 23 GHz continuum (Wilson & Pauls 1984). White bright circles correspond to positions in which H, He and C RRLs were observed in this study. The size of white bright circles corresponds to the RT-22 telescope beam size

Table 1: Parameters of PDR and HII region in Orion A estimated in this study

Position of observations α_{1950} δ_{1950}	PDR				HII region	
	T_k K	n_H, $\times 10^5$ cm^{-3}	L , pc	ME cm^{-6} pc	T_e, K	$n(He^+)$ / $n(H^+)$, %
Orion Bar 5^{h}32^{m}55^s -5°26'30"	234 - 200	1.17 - 1.56	0.041- 0.036	37.1 - 60.0	8380 (200)	8.2 (±.55)
Ori Bar-2 5^{h}32^{m}59^s -5° 27'09"	196	3.03	.010	62.0	7330 (270)	7.3 (±.7)
Ori Bar-3 5^{h}33^{m}00^s -5° 27'50"	145	3.14	.0058	38.7	7000 (250)	5.7 (±.66)
Ori Bar-4 5^{h}33^{m}4.7^s -5° 28'27"	152	1.24	.010	10.4	6600 (170)	4.8 (±.8)
Ori A 5^{h}32^{m}49^s -5°25'16"	219	1.71	0.027	53.4	8170 (200)	8.3 (±.36)

MC. Data indicates presence of a gas density jump in the Ori Bar. This jump can result from interaction of HII region with MC and can initiate formation of new stars. Emission measure (EM) estimated from carbon RRLs is ~100±50 pc×cm^{-6} which puts restrictions on parameters of PDR represented by a two-component model (see details in the paper Tsivilev, 2014). Our estimates also show that θ^1 C Ori star alone has sufficient ionizing flux to provide ionization of the carbon in PDR.

Lines of the ionized gas formed in HII region are blue-shifted by 10–17 km/s with respect to the lines formed in PDR. This indicates that the hot ionized material is in motion relative to MC. This is expected in a blister-type model of Orion HII region. Electron temperature in the HII region decreases towards the periphery from 8 200–8 400 K to 6 600–7 000 K which was also confirmed by recent studies in the optics (Mesa-Delgado et al. 2008). Relative abundance of ionized helium to hydrogen decreases with the distance from the θ^1 C Ori star indicating that the size of ionized helium region is smaller than the ionized hydrogen one. This restricts the range of effective temperatures (T_{eff}) of the θ^1 C Ori star (Polyakov & Tsivilev 2007). Our model calculations show that T_{eff} of ionizing source is in the range 35 000–36 500 K. If we assume that the HII region is produced by a group of stars (Copetti & Bica 1983) then the actual T_{eff} of θ^1 C Ori should be higher by ~1000 K (Copetti & Bica 1983) and constrained by the range 36 000–37 500 K. Recent optical studies have shown that the spectral class of θ^1 C Ori is ≈ O7 V (Stahl et al. 2008). However, we think that the data of Stahl et al. (2008) clearly indicates that its spectral class is rather ≈ O6.5 V (see Figure 6 from Stahl et al. 2008). It is known that one of the important problems is calibration of OB stars, i.e. correspondence between the spectral class of a star and its T_{eff}. For example, for a star of O6.0 V spec-

tral class Vacca et al. (1996) assign T_{eff} ≈ 43 600 K while Pottasch et al. (1979) assign much smaller value T_{eff} ≈ 36 500 K. The important result of this study is that our experimental data complemented by the HII/PDR complex modelling provides constraint for the calibration by assigning T_{eff} range 36 000–37 500 K to the star of ≈ O6.5 V spectral class.

References

Copetti M. V. F. and Bica E. I. D.: 1983, *ApSS*, **91**, 381.
Hua C. T. & Louise R.: 1982, *A&A SS*, **88**, 477.
Mesa-Delgado A. et al.: 2008, ApJ., **675**, 389.
Polyakov A.M., Tsivilev A.P.: 2007, *Astron. Lett.*, **33**, 34.
Poppi S. et al.: 2007, *A&A*, **464**, 995.
Pottasch S.R. et al.: 1979, *A&A*, **77**, 189.
Sorochenko R.L., Gordon M.A.: 2003, Radio Recombination Lines. Physics and Astronomy (Fizmatlit, Moscow, 2003) [in Russian].
Sorochenko R.L., Tsivilev A.P.: 2000, *Astron. Rep.*, **44**, 426.
Sorochenko R.L., Tsivilev A.P.: 2010, *Kinem. Phys. Celest. Bodies*, **26**, 162.
Stahl O. et al.: 2008, *arXiv:0805.0701v2*.
Tsivilev A.P.: 2014, *Astron. Lett.*, **40**, 615.
Tsivilev A.P. et al : 1986, *Sov. Astron. Lett.*, **12**, 355.
Vacca W.D. et al.: 1996, *ApJ*, **460**, 914.
Wilson T.L. &. Pauls T.: 1984, *A&A*, **138**, 225.

SUN AND SOLAR SYSTEM

THE RESEARCH OF VARIATION OF THE PERIOD AND PRECESSION OF THE ROTATION AXIS OF EGS (AJISAI) SATELLITE BY USING PHOTOMETRIC MEASUREMENT

Burlak N., Koshkin N., Korobeynikova E., Melikyants S., Shakun L., Strakhova S.

Astronomical Observatory, Odessa National University
nikkoshkin@yahoo.com

ABSTRACT. The light curves of EGS Ajisai with temporal resolution of 20 ms referred to the time scale UTC (GPS) with an error of at most 0.1 ms were obtained. The observed flashes are produced when the mirrors which cover the spinning satellite's surface reflect off the sunlight. In previous paper the analysis of sequence of flashes allowed of reconstructing the arrangement and orientation of the mirrors, i.e. developing an opto-geometric model of the satellite (Korobeynikova et al., 2012), and to apply that model along with new photometric observations to determine the satellite's sidereal rotational period with an accuracy that was previously unachievable. A new technique for determination of the spin-axis orientation during each passage of the satellite over an observation site was developed. The secular slowdown of the satellite's spin rate (P_{sid} = 1.4858·EXP(0.000041099·T), where T is measured in days counted from the date of the satellite launch) and its variations correlating with the average duration of the satellite orbit out of the Earth's shadow were refined. New parameters of the spin-axis precession were estimated: the period P_{prec} = 116.44 days, α_{prec} = 18.0^h, δ_{prec} = 87.66°, the nutation angle θ = 1.78°.

1. Introduction

As noted in previous paper (Koshkin et al., 2010), the phase angle bisector position in the satellite-centric coordinate system determines which of those mirrors will reflect off the sunlight towards an observer. The mirrors in each ring should be considered in sets of three (Korobeynikova et al., 2012; Epishev et al., 2008) as all mirrors in each set are tilted at the same angle (which varies for different sets of three) to the central latitude of a certain ring. It was intended that while the Ajisai is spinning about its symmetry axis, any three mirrors with the same tilt can always reflect off sunlight towards an observer three times per rotation. If actual arrangement (orientation of the central normal) of the whole set of mirrors is available, it will enable the EGS spin period and orientation to be determined from photometric observations. As the spin axis of Ajisai is close to the celestial pole, the bisector declination in the equatorial coordinate system will be slightly different from the latitudes of the mirrors reflecting sunlight over a certain period of time.

2. Determination of the Ajisai spin-axis orientation

The time intervals between adjacent flashes over one rotation of the satellite allow to identify with confidence the corresponding set of three mirrors as well as to determine their satellite-centric latitude φ. When examining the differences of current declination of the bisector and latitudes of the reflecting mirrors, it can be seen that those differences at the instants of flashes for all three 'chains' merge with each other into a separate 'track' on the graph (see Fig. 1). Other 'chains' are figured by other tracks, which, as it was said above, overlap each other with time. Such geometric illustration reflects the fact that at a certain instant of time the plashes of sunlight on the satellite's surface moving in declination (δ), for instance, from south to north, reach the southern edge of a mirror (or to be more exact, of three mirrors), and respective flashes appear on the light curve up to the moment when the plashes have passed the northern edge of that mirror. It should be noted that if the Ajisai spin-axis orientation perfectly coincided with the celestial pole, then the differences ($\varphi - \delta$) would be within the range ±Δ where value Δ is dependant on the angular dimensions of the mirror and the light source. The actual observed differences ($\varphi - \delta$) also depend on the true spin-axis orientation in space. That enables to ascertain the current spin-axis orientation on the observation interval. For the true satellite spin pole, the differences ($\varphi - \beta$) where β – the bisector declination in the coordinate system related to the spin pole will be within the same range ±Δ. The flashes' amplitudes gradually change thereby defining the boundaries of 'chains'. Nevertheless, the beginning and the end of the chains are not strictly defined as a flash can be observed only upon reaching the corresponding phase of Ajisai's spinning; at that, the width of the plashes of sunlight, being continuously changed, could reach the edge of the mirror at the instant of time when it is out of sight of an observer.
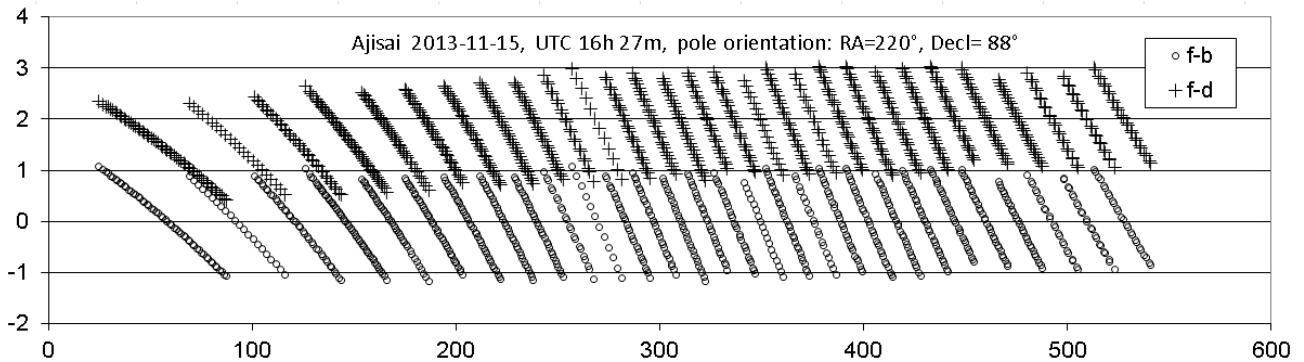
Figure 1: The time-dependent change in the differences between the mirrors' latitudes and bisector declination ($\varphi - \delta$) (marked with brown daggers) as well as the differences ($\varphi - \beta$) for the spin pole $\alpha_{pol} = 14.67^h$, $\delta_{pol} = 88.0°$, (marked with blue dots) during a passage of Ajisai on 15 November 2013. The X-axis represents the time in seconds since the measurements began; the differences in degrees are plotted in the Y-axis.
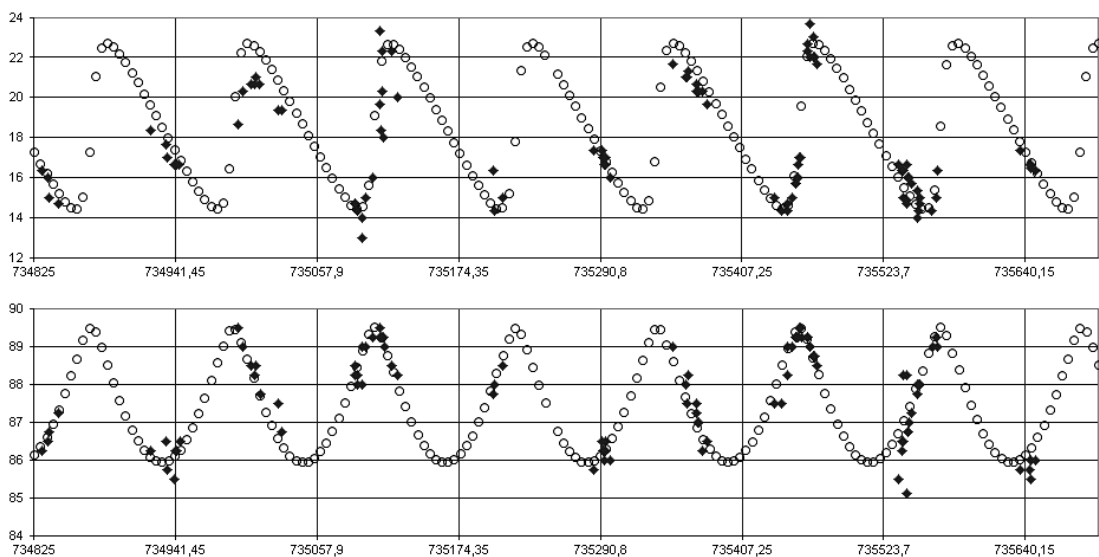

Figure 2: The Ajisai spin pole positions (indicated by solid circles), obtained from observations over the period of 2009-2014; the upper chart shows the right ascension of the pole (in hours); the lower chart represents the pole's inclination (in degrees). It also demonstrates the approximating trajectory of the spin-pole variations obtained with the following precession model: the pole is at the point $\alpha_{prec} = 18.0^h$, $\delta_{prec} = 87.66°$, the nutation angle is $\theta = 1.78°$ and nodal precession period is 116.44 days.

However, having examined numerous 'chains' during a satellite's passage over an observer, their boundary flashes can be definitely estimated in average that enables to determine the current position of the spin pole. Several tens of sets of three 'chains' (tracks on the graph "$\varphi - \delta$") can be observed with high-quality photometry during long-lasting well-observable passages. But when the observation conditions are unfavourable, the number of the observed chains is inadequate to definitely determine the spin pole position. The described technique of the spin-pole position determination implies that the spin axis in the satellite's solid almost coincides with its axis of symmetry (the mirrors' widths do not vary). It is possible that more thorough examination of the Ajisai light curve will allow of unravelling this and other thin effects in the satellite's spin-axis inclination variations.

Fig. 2 shows the results of our determination of the Ajisai spin-axis pole position on the time interval from November 2011 to February 2014. It also presents the approximating

trajectory of the spin-pole inclination variations, which was obtained applying the following precession model: spin pole is at the point $\alpha_{prec} = 18.0^h$, $\delta_{prec} = 87.66°$, the nutation angle $\theta = 1.78°$ and period of 116.44 days (while the Ajisai nodal precession period is 117.1 days).

The Ajisai nodal precession period which was 116.44 according to our determinations is almost perfectly coincides with the period estimated by Kucharski D. et al. (Kucharski et al., 2010; Kucharski et al., 2013). The phase of the spin-pole inclination variations is also practically the same (within the accuracy of the phase estimations reported in the paper referenced above). However, the precession axis is noticeably shifted in right ascension comparing to the data by Kucharski. It may be an actual axis shift as the authors' analysis of different measurement intervals resulted in the following estimates of the precession pole mean position:

Kucharski, 2010	2003-2009	$\alpha_{prec} = 14.9^h$,	$\delta_{prec} = 88.51°$
Kucharski, 2012	2003-2011	$\alpha_{prec} = 15.4^h$,	$\delta_{prec} = 88.05°$
This study	2009-2014	$\alpha_{prec} = 18.0^h$,	$\delta_{prec} = 87.66°$

For clarity, several dozen spin-axis pole positions on the sphere, which were obtained by us on different dates over the period from September 2009 to February 2014, are shown in Fig. 3. The spin-axis precession circular trajectory which approximates those data, as well as the circular trajectory according to the data by Kucharski et al. (Kucharski et al., 2010) obtained from the SLR observations in 2003-2011, is also plotted in the figure. It is obvious that our individual spin pole determinations can not be fitted by the precession pole from Kucharski et al.
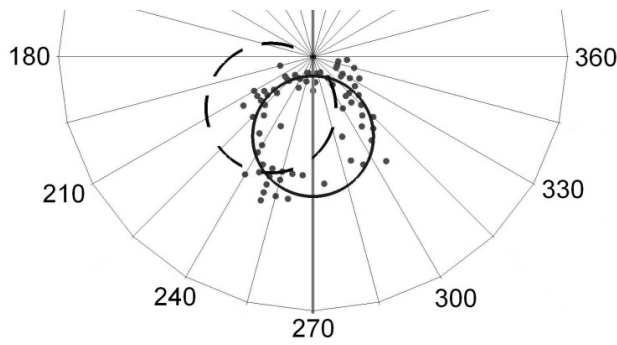

Figure 3: The spin-axis pole positions obtained on different dates over the period from September 2009 to February 2014, and the approximating circular trajectory of the spin-axis precession (indicated by the solid line). The dotted line indicates the spin-axis precession circular trajectory obtained by Kucharski et al. from the satellite laser range observations in 2003-2011.

3. Determination of the Ajisai spin period

The satellite's sidereal rotational period is determined based on the measurements of apparent (synodic) time intervals between individual flashes. Earlier, those measurements, being supplemented and checked at different passages of the satellite, were employed to develop a model for the mirrors' arrangement on the Ajisai's surface (Korobeynikova et al., 2012). And further, when determining the satellite's sidereal rotational period, the model is applied to compute the phase difference between any far off in time flashes from two different mirrors.

When the spin-pole orientation is not yet specified, we use the below-described quick-test which implies the neglect of the pole deviation from the celestial pole.

Let us consider four successive instants of flashes, which appear during one rotation of the satellite at the beginning of its passing above the observation site. The time interval between the fourth and first instants gives a preliminary estimate of the sidereal period P_1. By dividing three time intervals by that sidereal period we will determine approximate differences in longitudes of three reflecting mirrors. Based on those differences in longitudes, we can easily identify three corresponding mirrors in the model and hence to get to know their longitudes and common latitude on the satellite's surface.

Then, we can perform the similar identification of the mirrors for four successive flashes at the end of the satellite's passage. After that, we select two flashes from the examined eight ones (one of the selected flashes is in

the beginning of the satellite's passage, and another one is at the end of it), for which the respective mirrors' longitudes minimally differ from each other. Let us divide the time interval between those flashes by the estimated sidereal period P_1 mentioned above to find the number of complete revolutions N between the given instants, which is the nearest integer. Thereby, it is possible to determine the sidereal period as the mean value of several estimates resulted from the following formula:

$$P_{sid} = (t_{fin} - t_{beg})/[N - (\alpha_{fin} - \alpha_{beg}) + (A_{fin} - A_{beg})] \,,$$

where t_{beg} and t_{fin} – any pair of instants in the beginning and at the end of the satellite's passage; α_{fin}, α_{beg}, A_{fin} and A_{beg} – corresponding bisector right ascensions and mirrors' longitudes in the satellite's model expressed in fractions of rotation. The signs placed in front of corrections to the integer value of a number of rotations depend on the sense of the satellite's spinning; they enabled to find out that Ajisai is spinning in a clockwise direction (in the opposite direction to that of the Earth's rotation). The error in the period determination is caused by the errors in the obtained instants of flashes (<0.02 sec) and to the far smaller extent by the errors in the satellite's model and in the substitution the bisector right ascension for the bisector longitude in the coordinate system related to the satellite's spin axis. In our results, values N vary in the range from 50 to 320. Thus, the period's errors tend to be less than 0.0002 sec.

When the Ajisai spin-axis orientation is determined as it is described above, it is possible to ascertain the sidereal period for all available measurements of the instants of flashes:

$$P_{sid} = (t_i - t_1)/[N_i - (\lambda_i - \lambda_1) + (A_i - A_1)],$$

where t_1 and t_i – the first and all successive instants of Ajisai flashes during one passage; λ_1 , λ_i , A_1 and A_i – corresponding bisector longitudes in the coordinate frame related to the spin axis at the i-th instant of time and mirrors' longitudes in the satellite's model; N_i – the number of complete revolutions of the satellite over the interval $(t_i - t_1)$.

Thereby found values of the Ajisai sidereal rotational period are in good agreement with the most precise data by other authors (Kirchner et al., 2007; Vovchyk, 2003; Korobeynikova et al., 2012) – the duration of one rotation exponentially increases with time, i.e. the satellite slows down. Moreover, there is a well noticeable variation of the spin deceleration rate relative to the background of the secular slowing down of the satellite's spinning.

On the time interval 2009-2013, the increase in period can be approximately calculated by the linear formula (to visualize of the deceleration rate):

$$P_{sid} = 1.3596901371 + 0.0000879961 \cdot (t - 12\text{-}08\text{-}1986),$$

where t – the observation date counted from the date of the satellite launch on 12 August, 1986. However, to make the calculation more accurate for that time interval, the formula of the Ajisai deceleration looks as follows:

$$P_{sid} = 1.485802163871 \cdot EXP(0.015011430489 \cdot (t - 12\text{-}08\text{-}1986))$$

where 1.4858 – the initial spin period of the satellite just after launching obtained according to our data.
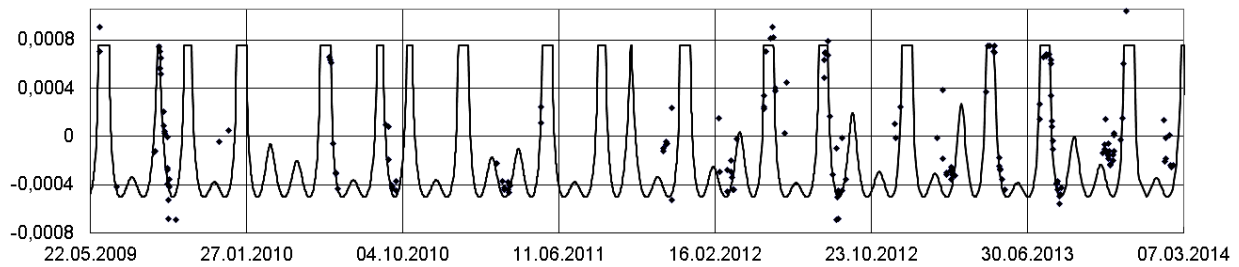
Figure 4: The Ajisai spin deceleration rate variations calculated from observations – the remainder after subtracting the exponential approximation (of the point). The solid-line curve is the renormed graph, which illustrates a part of the satellite's orbit out of the Earth's shadow (it occurs in the minimum of 0.7 and the maximum of 1.0).

Therefore, the Ajisai axial spin period, for instance, in 2013 was about 2.23 sec and it has been increasing on average by 0.00009 sec per day.

However, it is known that there are some non-periodic variations of the Ajisai spin deceleration rate (Kucharski et al., 2009), and that is completely borne out by our measurements. The variations of the Ajisai spin deceleration rate – the remainder after subtracting the exponential fit – are shown in Fig. 4 (of the filled point). The solid-line curve in the figure demonstrates the graph, renormed for the same range, which illustrates a part of the satellite's orbit out of the Earth's shadow (for Ajisai it occurs in the minimum of 0.7 and the maximum of 1.0).

It can be calculated rather easy by simple formulae for the circular orbit of Ajisai. If α is an angle between the normal to the orbit and the direction towards the Sun, then the illuminated part of the orbit is calculated as follows:

$$(\pi/2 + \arccos((R_E{}^2 - a^2{\cdot}\cos^2\alpha)^{0.5}/a{\cdot}\sin\alpha))/\pi,$$

where a – the semi-major axis of the satellite; R_E – the Earth's radius.

This graph demonstrated a noticeable correlation between the period of the satellite's illumination by the Sun and its deceleration rate (increase in the satellite's spin period) (Kucharski et al., 2010). Kucharski et al. suggested that such correlation can be caused by the Yarkovsky effect. However, it is known that for spherically symmetrical bodies there is no additional torque due to the YORP-effect on the rotating body. This observation fact provides a area for theoretical generalisation and interpretation of the obtained data.

4. Conclusions

A new technique for determination of the spin-axis orientation during each passage of the satellite over an observation site was developed. The secular slowdown of the satellite's spin rate ($P_{sid} = 1.4858{\cdot}EXP(0.000041099{\cdot}T)$ where T is measured in days counted from the date of the satellite launch) and its variations correlating with the average duration of the satellite orbit out of the Earth's shadow were borne out (Kucharski et al., 2009). New parameters of the spin-axis precession were estimated: the period $P_{prec} = 116.44$ days, $\alpha_{prec} = 18.0^h$, $\delta_{prec} = 87.66°$, the nutation angle $\theta = 1.78°$ and maximum value of $\delta_{pol} = 89.5°$ is achieved on 7.78 August 2013.

Regular photometric observations of the satellite are expected to clear up the physical nature of the discovered specific features of its rotation, enable to calculate the precise

ephemeris of its position in space and use this space object for communications between widely distant observation sites.

The described technique of the photometric observations and their processing aimed to determine the Ajisai rotation parameters enable to directly identify any mirror on the satellite's surface which produced a recorded flash. That considerably simplifies, first of all, the procedure of the spin period determination. The error in determination of the period δP linearly decreases with increasing number of rotations N on the interval of measurements ΔT between two flashes.

$$P \pm \delta P = \Delta T/(N{\pm}dN) \pm 2{\cdot}\delta T/(N{\pm}dN),$$

where δT – the error in measurement of the instant of flash.

The application of the model for the mirrors' arrangement opens the way to ascertain dN and determine the spin period with high accuracy not only during one passage of the satellite, but also to proportionally increase the accuracy of period determination by calculating it on the interval of either two successive passages (with the spin period formal error is $\delta P \sim 0.00001$ sec) or a 24 hours-period ($\delta P \sim 0.000001$ sec). As the characteristic time of the change in the period variation rate equals to several days, this method allows of studying minute particulars of those variations.

References

Sasaki M., Hashimoto H.: 1987, *IEEE Trans. Geosci. Remote Sens.*, **25 (5)**, 526.

Kirchner G., Hausleitner W., Cristea E.: 2007, *IEEE Trans. Geosci. Remote Sens.*, **45 (1)**, 201.

Koshkin N.I., Korobeynikova E.A. et al.: 2010, *Odessa Astron. Publ.*, **22**, 36.

Korobeynikova E., Koshkin N. et al.: 2012, *Odessa Astron. Publ.*, **25/2**, 216.

Kucharski D., Kirchner G., Otsubo T. et al.: 2009, *Adv. Space Res.*, **44 (5)**, 621.

Kucharski D., Otsubo T., Kirchner G., Koidl F.: 2010, *Adv. Space Res.*, **46 (3)**, 251.

Kucharski D., Kirchner G., Otsubo T. et al.: 2010, *IEEE Trans. Geosci. Remote Sens.*, **48 (3)**, 1629.

Kucharski D., Otsubo T., Kirchner G., Lim H.-C.: 2013, *Adv. Space Res.*, **51**, 162.

Vovchyk Ye., Blagodyr Ya., Bilinsky A. et al.: 2003, *Astron. and Astrophys. Transactions*, **22**, **No. 4–5**, 645.

https://directory.eoportal.org/web/eoportal/satellite-missions/e/egs

Epishev V., Isak I. et al.: 2008, *http://lfvn.astronomer.ru/report/0000027/Uj/index4.htm*

HEAT MODELS OF ASTEROIDS AND THE YORP EFFECT

O.Golubov[1, 2, 3]

[1] Institute of Astronomy of V. N. Karazin Kharkiv National University,
 35 Sumska Str., 61022, Kharkiv, Ukraine, *golubov@astron.kharkov.ua*
[2] School of Physics and Technology, V. N. Karazin Kharkiv National University,
 Svobody Sq. 4, 61022, Kharkiv, Ukraine
[3] Department of Aerospace Engineering Sciences, University of Colorado at Boulder,
 429 UCB, Boulder, CO, 80309, USA.

ABSTRACT. The Yarkovsky–O'Keefe–Radzievski–Paddack (YORP) effect is a torque of light pressure recoil forces acting on an asteroid. We show how this torque can be expressed as an integral of a universal function over the surface of an asteroid, and discuss generalizations of this expression for the case of non-Lambert's scattering laws, non-convex shapes of asteroids, and non-zero heat conductivity. Then we discuss tangential YORP (TYORP), which appears due to uneven heat conductivity in stones lying on the surface of an asteroid. TYORP manifests itself as a drag, which pulls the surface in the tangential direction. Finally, we discuss relation and interplay between the normal YORP and the tangential YORP.

Keywords: Asteroids: dynamics – Galaxy: abundances – stars: late-type

1. Introduction

The YORP effect was first introduced by Rubincam (2000) as the torque experienced by an asymmetric asteroid due the recoil forces created by the scattered or re-emitted light.

It was soon recognized to be the major factor causing evolution of rotation state of kilometre-sized asteroids. The YORP torque alters the distribution of asteroids over rotation periods and rotational axis orientations. Via centrifugal forces it alters shapes, and for most rapidly rotating asteroids YORP creates binaries via rotational fission. Via changing period and rotation axis orientation, YORP also changes Yarkovsky effect experienced by an asteroid (Bottke, 2006). YORP effect already turns to be necessary for precise light-curve fitting, and has thus been detected for 5 asteroids.

2. YORP as Surface Integral

The YORP torque can be conveniently represented as an integral over the asteroid's shape of a universal function $f(\psi,\varepsilon)$, which determines the average YORP torque created by a surface element located at latitude ψ of an asteroid with obliquity ε. This approach was first pre-sented in Golubov & Krugly (2010) and Steinberg & Sari (2011). Their analysis had some important limitations due to the assumptions used in the model, the most important of which were:

1. Lambert's scattering law;
2. Convex shapes of asteroids;
3. Zero heat conductivity.

Our current analysis shows, that abandoning Lambert's scattering law does not substantially change the results. Substituting Lambert's law with Lommel-Seeliger law causes no substantial change in $f(\psi,\varepsilon)$.

Applying this treatment to non-convex asteroids shows results close to the ones obtained via rigorous ray tracing, if only the concavity of the asteroid is not too extreme. Thus convexity is also not a crucial assumption.

Finally, this treatment can be generalized for non-zero heat conductivity, if heat propagation is considered in a semispace under the surface. This model leads to the same expressions with only the universal function f depending not on 2, but on 3 parameters, the third one being thermal parameter of the soil θ.

Still, this model does not exhaust all possible physics of the process. It turns out, that if non-flat surface is considered, a qualitatively new effect turns in, which we call tangential YORP or TYORP, to distinguish it from normal YORP or NYORP introduced by Rubincam (2000).

3. Tangential YORP

Tangential YORP is due to heat conductivity fluxes going through centimetre- to metre-sized structures on the surface of the asteroid, such as stones or grooves. Under some conditions, it turns out that western slopes of structures are on average slightly warmer than their eastern slopes, which causes the preferential emission of light in the western direction, and the accelerated rotation of the asteroid. These additional forces produced by the fine structure of the surface are directed tangentially to the global gross-scale surface of the asteroid.

TYORP was first studied by Golubov & Krugly (2012) in the simplest model, with stones approximated via vertical walls on the surface of an asteroid. Although the

model allowed to give a rough order-of-magnitude estimate of TYORP, it used numerous assumptions, the most limiting of which were

1. One-dimensional geometry of the wall.
2. Mirror reflection of light from regolith to account for self-illumination.
3. Zero obliquity.
4. Circular orbit of the asteroid.

Golubov & Krugly (2014) could get rid of the first two assumptions. They considered spherical stones lying in regolith on the surface of the asteroid. Ray tracing technique was used to account for multiple scattering of light by the stones and the regolith. The model included more free parameters, which made parametric study of the effect more complicated, but the general result was consistent with the estimate of the effect given by Golubov & Krugly (2012).

TYORP is substantial only in a relatively narrow area, where the size of the stone is of the order of the thermal wavelength, and the thermal parametre is of the order of unity. TYORP rapidly vanishes as one goes away from this area. It means, that only stones within some size range substantially contribute to the TYORP force. Moreover, this size range changes with changing rotation rate of the asteroid.

Incorporating non-zero obliquities and non-zero eccentricities into the theory of TYORP still remains an important problem to solve.

4. Conclusions

The YORP effect has two components: the normal YORP is caused by scattering and emission of light normally to the overall asteroid's surface, while tangential YORP is caused by preferential emission of light by small structures on the surface westward rather than eastward.

For each surface element the NYORP force is much bigger than the TYORP. But after integration over a symmetric surface NYORP torque vanishes, so that only asymmetry of the asteroid contributes to the total torque. In contrast, TYORP can produce torque even for a symmetric asteroid. As most asteroids are only moderately asymmetric, NYORP and TYORP torques can be comparable.

References

Bottke W.F. et al.: 2006, *AREPS*, **34**, 157.

Golubov O. et al.: submitted, *MNRAS*.

Golubov O. et al.: 2014, *ApJ*, **794**, 22.

Golubov O. & Krugly Yu.N.: 2012, *ApJL*, **752**, 11.

Golubov A.A. & Krugly Yu.N.: 2010, Protecting the Earth against Collisions with Asteroids and Comet Nuclei, St. Petersburg, 90.

Rubincam D.P.: 2000, *Icarus*, **148**, 2.

Steinberg E. & Sari R.: 2011, *AJ*, **141**, 55.

INFLUENCE OF SPACE WEATHER EFFECTS ON THE UPPER ATMOSPHERE ACCORDING TO THE DRAG OF ARTIFICIAL EARTH SATELLITES

Komendant V.H.[1], Koshkin N.I.[2], Ryabov M.I.[3], Sukharev A.L.[3]

[1] Astronomy Department of Odessa I.I.Mechnikov National University
[2] Research Institute "Astronomical Observatory" of Odessa I.I.Mechnikov National University
[3] Odessa observatory of Radioastronomical Institute of Ukrainian National Academy of science

ABSTRACT. The applying of the method of time-frequency analysis allows to reveal the detailed structure of the manifestations of the influence of the space weather's state on the upper atmosphere of the Earth. The sensitive indicator of such changes are low-orbit satellites. The drag dynamics of five low–orbit satellites was viewed as indicators manifestations of the influence of space weather on the Earth upper atmosphere. The study period includes phases of decay and a long minimum of 23-rd solar cycle, phases of growth and maximum of 24-th solar cycle. In drag dynamics of all the analyzed satellites strongly marked regular drag effects with long periods (2-4 years) and short-period effects with periods less than one year. The satellites with orbital inclinations close to the equator shows periods with trend from 25 days to 1,3 months.

1. Introduction

Evolution of the orbit and satellite's drag variations depend on: gravitational perturbations (the gravitation of the Sun, moon and other planets); oblateness of the Earth; the Earth's magnetic field; light pressure; charged and neutral particles (the effect is small and therefore neglected); aerodynamic disturbances (Earth's atmosphere). The atmosphere density variations cause a change in the height of the satellite [1, 2]. The density of the atmosphere is constantly changing and not only depends on the latitude and height above the Earth's surface, but also on the solar activities and space weather conditions. In this work, satellites are used as indicators of the impact of space weather and manifestations of solar activity on the upper atmosphere of the Earth.

2. Observational data

For analysis were taken five satellites with NORAD numbers: 25860, 27700, 12054, 25064, 23757. These satellites have the following elements of the orbits: Polar: №5860: i=98[0]; e=0.0002; a=655 km; №27700: i=97[0]; e=0.005; a=486 km. Midlatitude: №12054: i=65[0]; e=0.007; a=522 km. Equatorial: №25064: i=34.9[0]; e=0.0007; a=507 km; №23757: i=22.9[0]; e=0.0009; a=499 km. All satellites were observed during 9 years (2005-2013). Satellite 27700 were observed during the 8 years (2005-2012). Study's satellites moved in unmanaged mode and the satellite 27700 by the end of the observation period was burned in the atmosphere. Observations of these satellites fall to decay phase of solar cycle 23 and the beginning of solar cycle 24, and the minimum phase between them.

3. Spectral analysis

Spectral analysis – is one of the signal processing methods, which allows to describe the frequency content of the measured signal. The basis for this analysis is the Fourier transform. It binds the values of the time series with their representation in the frequency domain. Disadvantage of this method is that if the amplitude of any harmonic changed in a certain period of time, this method will not be able to show at what time it happened. One option to eliminate these disadvantages, it was proposed to use the method not to the entire process, but to the process within a certain time window, which gradually shifts [3]. To recalculate the coefficients of the resulting series use the algorithm of fast Fourier transform (FFT). In this work, to build the spectrograms were used algorithm "Winograd". This algorithm has a significant advantage over the other, when the multiplication operation is more difficult than addition [4].

4. Results

For preprocessing data used STATISTICA 8. The data on changes in the atmospheric drag coefficient of satellites (Bstar) were analyzed. Due to the fact that the data series are presented on an uneven timeline, we used the interpolation B-spline. Figure 1 shows an example graph of the change of the drag coefficient of satellite 25064 in the investigated time interval.

From the resulting graphs can be seen that in the phase of minimum solar activity there are quasi-periodic oscillations with an interval of 27 to 30 days. In addition to these observations are marked sudden (abnormal) periods of braking with a period of about three months. As observation of satellites cover different periods of solar activity state, their observations were divided into two periods: 2005-2009 and 2010-2013. Using Fourier analysis, we

constructed periodogram for these intervals. An example of periodogram shown in Figure 2.
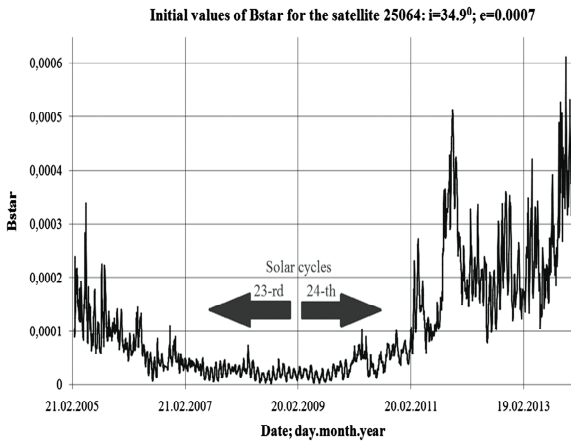

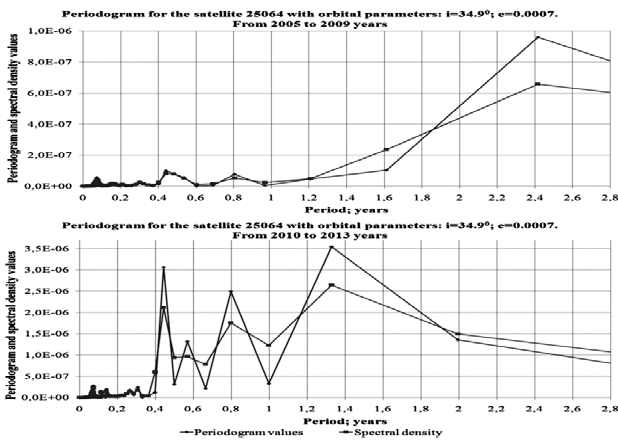Figure 1: Initial values for equatorial satellite 25064

Figure 2: Periodogramm for two time periods for the Equatorial satellite 25064

Table 1.

Number of satellite	25860		27700		12054		25064		23757	
Period of periodogramm	Date 2005-2009	Date 2010-2013	Date 2005-2009	Date 2010-2013	Date 2005-2009	Date 2010-2013	Date 2005-2009	Date 2010-2013	Date 2005-2009	Date 2010-2013
Periods; Year - *, Months - **, Days - ***.	2,4*	5,3**	2,4*	1,2*	2,4*	2*	2,4*	1,3*	2,4*	5,3**
	5,27**	9,6**	1,2*	5,8**	9,6**	5,32**	5,27**	5,3**	9,7**	~1,3*
	9,7**	2*	5,3**	~27***	5,27**	6,8**	9,7**	9,6**	5,3**	9,57**
	2,5*	6,8**	26***	22***	6,44**	9,6**	~27***	6,8**	25,6***	6,8**
	14,6***	3,2**	3,2**	1,7**	2,4*	4,35**	29,4***	~27***	3,6**	3,6**
	~1**	3,7**	2,1**		3,62**	3,68**	3,6**	3,68**	26,7***	~27***
	20,7***	26,5***	~27***			2,4**		1,7**	2,2**	1,7**
	1,8**		~30***					3,2**	~9***	
	3,4**		4,1**							
			~9***							

In the resulting periodogram presented periods ranging from 9 days and ending 1.3-2.4 years. Some periods are shown in Table 1. In periodogram, built in the period of 2005-2009, for all satellites is present the maximal period of variations is equal to 2.4 years. While for periodogram, built in the time period 2010-2013, the periods with the maximum amplitude is different. For example, for equatorial orbit – 1,3 years. To identify the time of existence of

periodic components used program PSELab [5]. The result of its application to the equatorial satellite 25064 shown in Figure 3.

The periods trend from 25-28 days to 1.3 months were detected. Table 2 shows some detected periods of variations for all of the studied objects. The semi-annual period is present for all satellites throughout the time range of observation, while periods more than one year are present not for all satellites.

The following steps assume comparison of the received data with the manifestations of solar activity and magnetic storms. This have the practical importance for determine the complex influence of various manifestations of space weather on the state of Earth's upper atmosphere, creating the basis for its forecasting.
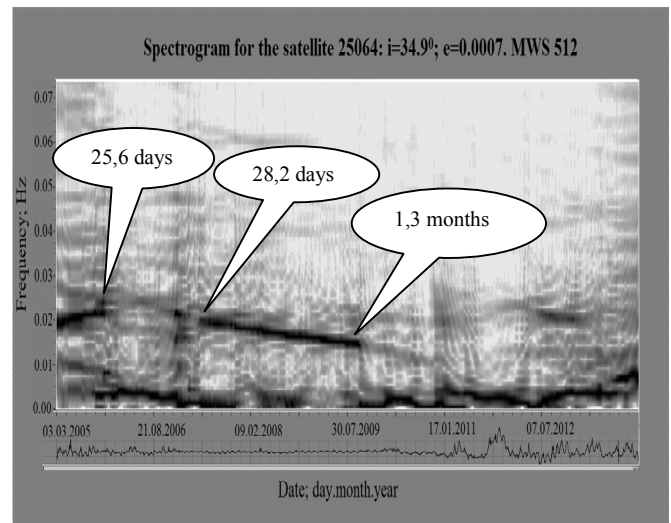

Figure 3: Spectrogram for the equatorial satellite 25064

Table 2.

Number of satellite	25860		27700		12054		25064		23757	
MWS	512	2048	512	2048	512	2048	512	2048	512	2048
Periods; Year - *, Months - **, Days - ***.	3,4*	2,5*	2,6*	2,9*	2,4*	2,4*	3,4*	3,6*	3,3*	3,7*
	7,4**	1,4*	7,1**	1,7*	7,4**	1,4*	7,2**	2,1*	7,7**	1,9*
	1,8**	5,9**	4,4**	6,8**	5,2**	8,5**	5,4**	11,7**	4,5**	1,05*
	25,9***	1,5**	1**	1,1**	3,3**	5,8**	1,3**	5,8**	1**	6,1**
	14,5***	27,1***	16,3***	1**	2,2**	3,7**	28,2***	1,5**	27,4***	1,6**
		14,5***	10,7***	16,3***	25,6***	2,9**	26,4***	29,9***	24,4***	27,4***
			8***	10,9***		1,4**				
							27,4***			

References

1. Beletsky V.V. The motion of an artificial satellite about the center of mass. Moscow, 1965, 416 p.
2. Roy A. Orbital motion. Moscow: Mir, 1981, 544 p.
3. Marple S.L., Jr. Digital spectral analysis with applications. Moscow: Mir, 1990, 584 p.
4. Oppenheim A., Schafer R. Digital signal processing. Moscow: Technosphere, 2006, 856 p.
5. PSELab [web resource] / POWER SPECTRUM ESTIMATION LABORATORY. – Access mode: http://pselab.ru/.

PROGNOSES AND ANOMALY OF 24TH CYCLE
OF SOLAR ACTIVITY

V.G.Lozitsky, V.M.Efimenko

Astronomical Observatory of Taras Shevchenko National University of Kyiv,
Observatorna 3, Kyiv, 04053, Ukraine,
lozitsky@observ.univ.kiev.ua, efim@observ.univ.kiev.ua

ABSTRACT. Development of solar activity in 24th cycle has specific peculiarity – non-monotonous increasing of solar activity on grown phase which occurs for 1/3 number of all cycles. The modification of Waldmayer's method was applied for forecasting 24th cycle which bases on a connection between maximum sunspot number and speed of increasing of activity on grown phase of cycle. If we compare 24th cycle with previous similar cycles Nos. 1, 5, 6, 9, 12, 15 and 16, we can conclude that this cycle will be weak, with maximum sunspot number W_{max} (24) = 73 ± 10 in 2014–2015, most likely – in first half of 2014. Current cycle could be considered as anomaly by three criterions: a) sharp slowdown in growth after the 30th of the month cycle, b) two-humped peak cycle with a significant predominance of the second peak height and c) the emergence of a giant sunspot with a diameter of about 170 Mm.

Key words: Sun: Solar activity – Sunspot number: Solar activity – Prognoses: Peak of 24th cycle – Anomaly.

1. Introduction

The current cycle No. 24 began in December, 2008. Some tens of forecasts of solar activity in this cycle were proposed; we will mention only some of them. According to Badalyan et al. (2001), the current cycle was expected as very weak – with the maximum averaged sunspot number on level of $W_{max} \approx 50$. The similar forecast is offered also by Svalgaard et al. (2005) – $W_{max} = 75\pm8$. Kane (2007), on the contrary, concluded that this cycle will be with $W_{max} = 142\pm24$. According to Dikpati et al. (2006), the 24th cycle will be rather powerful – on 30-50% higher, than the previous cycle No. 23. Years of cycle peak also significantly differ by different authors – from 2010 to 2014. In the present work, we use the modification of Waldmayer's method for forecasting the current cycle.

2. Method and Results

We used two working hypothesis. Our first hypothesis was following. It is necessary take into account that solar activity appears as partly determined, and partly stochastic phenomenon. We can expect that owing to stochastic component our forecasts of solar activity should be the worse the longer time interval is between the latest observational data and the forecast. In that case, the most successful forecast can be make according to latest data about the actual changes of solar activity.

Being based on this thesis as on working hypothesis, authors showed earlier that if to proceed from rise speed of activity between 20th and 32th months of development of a cycle (i.e. a little to modify Waldmayer's method), the maximum of averaged sunspot number turns out $W_{max} = 120 ± 17$ – as in middle cycle (Lozitsky and Efimenko, 2012).

It illustrates Fig. 1 based on data placed on site http://www.solen.info/solar/ . One can see that for the majority of cycles there is close connection between W_{max} and an increment of activity between 32th and 20th months of a cycle, $W_{32} - W_{20}$ (correlation coefficient r = 0.91 ± 0.03). Smooth curve provided in Fig. 1 is approximated by formula

$$W_{max} = 19.0 \times (W_{32} - W_{20})^{0.496} \qquad (1)$$

From (1) follows that W_{max} is approximetely proportional to scquare root from difference $W_{32} - W_{20}$. Also, one can see that the largest deviations from (1) demonstrate cycles Nos. 9, 19 and 3 (data for named cycles is pointed on Fig. 1 by corresponding numbers). If we substitute in (1) observed value $W_{32} - W_{20} = 42$ for 24th cycle then we obtain $W_{max} \approx 120$.

Similarly, the time of cycle peak was considered, and the coclusion was made that this peak should be in second half 2012 or first half 2013.
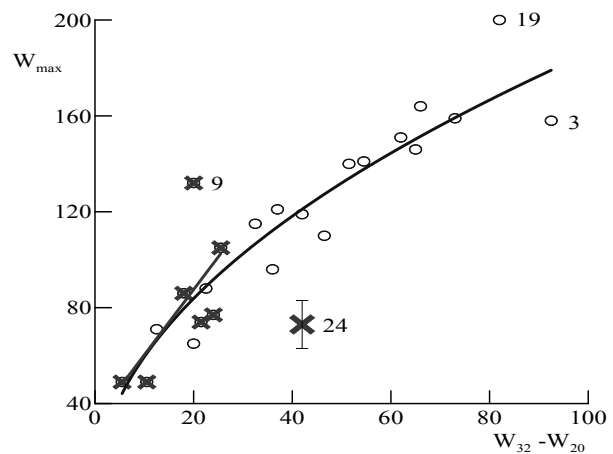

Figure 1: Maximum averages sunspot number, W_{max} , vs. speed of increasing of activity between 32th and 20th months, $W_{32} - W_{20}$, for 23 previous cycles (see text).

This forecast was not come true. The main cause of this failture is that the approximation presented by formula (1)

is suitable for cycles with monotonous curve of grown phase. But, as it was observed after 32th month of current cycle, this cycle has namely non-monotonous grown phase. In particular, after 32th month the development of solar activity slowed down. In fact, following two years after 32th month the sunspot number was almost the same - in range of 58–67 units. But later solar activity increased, in general, monotonically and this increasing is in progress till 64th month. This is obvious evidence that 24th cycle has non-monotonous grown phase. Among 23 previous cycles, number of similar cycles was 7 (approximately 1/3), namely Nos. 1, 5, 6, 9, 12, 15 and 16.

Second our working hypothesis was following. For more exact forecast, we should compare the cycles with non-monotonous grown phase only.

Figure 2 presents the comparison of W_{max} vs. W_{52}, i.e. sunspot number on 52th month. In fact, W_{52} is averaged by 4,33 years speed of increasing of solar activity which well averages local temporal changes of sunspot number.
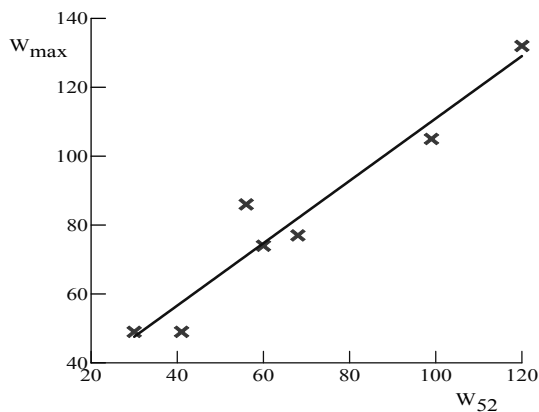

Figure 2: Maximum averages sunspot number, W_{max}, vs. sunspot number on 52th month, W_{52}, for cycles with non-monotonous increasing of solar activity on grown phase.

As it follows from Fig. 2, dependence W_{max} vs. W_{52} is enough close and almost linear. It has not any sizable deviations from linear trend that allow to prognose the peak of current cycle with confidence. So long as for 24th cycle $W_{52} = 58$, we obtain by this method: $W_{max}(24) = 73\pm10$. Time of peak – likely, first half of 2014.

3. Anomaly Cycle

There are three evidences that current cycle is anomaly.

Firstly, corresponding value $W_{max}(24) = 73\pm10$ on Fig. 1 has practically the same largest deviation from averaged curve (1) as cycle No. 9. However, data for cycles Nos. 9 and 24 are located on opposite sides of this curve. This means that cycle No. 9 had sharp increasing of solar activity before the maximum, whereas cycle No.24 has, on the contrary, sizable slowing down. In this connection, current cycly can be considered as cycle with destroyed peak. It is interesting to note that all 'irregular' cycles (with non-monotonous grown phase) excluding No.9 were weak. Such cycles are pointed on Fig. 1 by crosses. As it follows from this Figure, forecast of W_{max} via $W_{32} - W_{20}$ for such cycles is unreliable.

Secondly, current cycle should have two splitted peaks, and second peak is expected to be higher than the first. In fact, two or three past cycles had such peculiarity, namely Nos. 5, 12 and perhaps 16.

Let us illustrate this anomaly using number data. Denote $W_2 - W_1$ second maximum height difference relative to the first, and through $T_2 - T_1$- time (in months) between the first and second maximum. Comparison from this point of view cycles Nos. 5, 12, 16 and 24 is given in Table 1.

Table 1: Some characteristics of cycles 5, 12,16 and 24

No. of cycle	$W_2 - W_1$	$T_2 - T_1$
5	4	31
12	11	24
16	5	17
24	≥ 15	≥ 26

From Table 1 follows, that current cycle has the largest difference $W_2 - W_1$ and second (from all named cycles) time interval $T_2 - T_1$ between splitted peaks.

Thirdly, namely in the current cycle a giant sunspot had occurred in October 2014 (Fig. 3). Similar sunspots with penumbra diameter of 150-170 Mm were observed in cycles Nos. 17, 18 and 22. It was shown that such sunspots present a unique separate statistical ensemble of especially large spots (Babij et al, 2011). Strictly speaking, the existence of such an ensemble is determined not only by the diameter of sunspots, but by the index of integral distribution in the range of 50-90 Mm. Authors plan to do this study in the future.
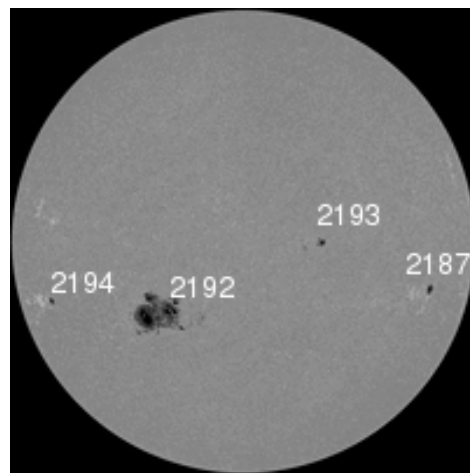

Figure 3: Sun's image in white light observed 22 October 2014 using SDO/HMI (http://spaceweather.com/).

References

Badalyan O.G. et al.: 2001, *Sol. Phys.*, **199**, 421.

Svalgaard L. et al: 2005, *Geophys. Res. Lett.*, **32**, L01104.

Kane R.P.: 2007, *Solar Phys.,* **243**, 205.

Dikpati M. et al.: 2006, *Geophys. Res. Lett.*, 33, L05102.

Lozitsky V.G., Efimenko V.M: 2012, *Izv.Crim.Astrofiz. Obs.*, **108**, 312.

Babij V.P. et al.: 2011, *Kinem. Phys. Celest. Bodies.*, **27**, 191.

DIAGNOSTICS OF LOCAL MAGNETIC FIELDS IN SOLAR FLARES USING FeI 5383 AND MgI 5528 LINES

V.G.Lozitsky[1], O.V. Lozitsky[2]

[1] Astronomical Observatory of Taras Shevchenko National University of Kyiv,
Observatorna 3, Kyiv, 04053, Ukraine, *lozitsky@observ.univ.kiev.ua*
[2] Physical Phaculty of Taras Shevchenko National University of Kyiv,
Prosp.Acad. Glushkova, 2, Kyiv, 03022, Ukraine, *olozitsky@gmail.com*

ABSTRACT. Main purpose of the present work is to estimate upper limit of the local magnetic field strength in solar flares using spectral lines FeI 5383 and MgI 5528. These lines like FeI 5233 have low Landé factors (1.12 and 1.00, respectively) and relatively large spectral width (0.2–0.3 Å). On this account, even in a case of very strong fields (3-4 kG) they must show the simple picture of the Zeeman splitting, with parallel to each other the bisectors of profiles I+V and I − V. In actual fact, another picture was found for nine flares: bisectors of these lines have maximums of splitting on certain distances from line center, what must not be in the homogeneous magnetic field. In particular, both lines have peak of bisector splitting on distance 150–170 mÅ from line center. If we assume the Zeeman nature of named peculiarities then necessary fields are 11.2 kG for FeI 5383 and 10.5-11.2 kG for MgI 5528. Likely, this agreement of field values is a new argument to reality of such very strong magnetic fields in flares.

Keywords: Sun: magnetic fields – solar flares: spatially unresolved structures – spectral diagnostics: local strength

1. Introduction

At present it is not clear what is the maximum possible magnetic field strength in the photosphere. More recently, van Noort et al. (2013) analysed SOT/SP observations of a sunspot penumbra in Fe I 6301.5 and 6302.5 Å. lines and found indications of magnetic field of around 7 kG. Lozitsky (2009, 2014) considered the fine structure of Zeeman splitting in Fe I lines with very small Landé factors (about 0.01) and found direct indications that magnetic field up to ~10^4–10^5 G might be present in the solar flares. Likely, such lines allow to estimate the order of field strength – no exact field values. For the named purpose, it is necessary to use the spectral lines with larger magnetic sensitivity. Lozitsky and Staude (2008) had used FeI 5233 line (g_{eff} = 1.26) and found narrow extremums of bisector splitting of $I ± V$ profiles which indicate the unacceptability of weak field approximation in case of two solar flares. An alternative is that such peculiarities present the observational evidences of multi-component magnetic field structures with strengths 1.3–1.5, 3.9–4.0 and 7.4–7.8 kG at level of middle photosphere in the spatially unresolved magnetic elements.

From this point of view, it is interesting to use another non-blended spectral lines like FeI 5233 to exclude possible instrumental effects (e.g. narrow molecular blends). This is main reason why we use FeI 5383 and MgI 5528 in the present work.

2. Observations and Selected Lines

We have used observational data obtained with the Echelle spectrograph of horizontal solar telescope of the Astronomical Observatory of Taras Shevchenko National University of Kyiv (Kurochka et al., 1980). In this short paper, we do not point list of observed flares; some data on these flares are presented in Table 1 in article by Lozitsky (2014). More exactly, the following nine flares were studied from this Table: Nos. 1,2,4,5,6,7,8,9 and 10. These flares had importance from C5 to X1.4. It is useful to remember, in article by Lozitsky (2014) the FeI 5123.7 and 5233 lines were studied (no FeI 5383 and MgI 5528). In all nine cases the spectra were taken in locations with highest Hα intensities. All these locations were outside sunspot umbras, where the observed Zeeman splittings measured by $I ± V$ 'centers of gravity' method were found to be in the range about several hundred of gauss.

Some parameters of two selected spectral lines are presented in Table 1 below.

Table 1: List of selected spectral lines

Wave-length (Å)	Element and multiplet number	Equiva-lent width W (mÅ)	Excita-tion po-tential (eV)	Effec-tive Landé factor
5383.380	FeI-1146	204	4.31	1.124
5528.418	MgI-9	293	4.34	1.000

According to Moore et al. (1966), these lines do not have intensive spectral bleds in range ±300mÅ from line center. In particular, first line has nearest blends 5383.07 and 5383.766 Å with equivalent width W =1 an 2 mÅ, respectively; second line has nearest blends 5528.086 and 5528.905 Å (W = 3 an 22 mÅ, respectively).

3. Method and Results

We found that in all flares both lines have nearly normal Fraunhofer profiles without emission peaks in their cores. However, their observed Zeeman splitting was found, in general, some different on different distances from line center (Fig. 1). Obviously, this can reflect two effects simultaneously: a) possible presence of Zeeman perturbations and b) noise effects. As for Zeeman perturbations, they should occur at the same distances from the line center for different flares if magnetic field strengths in different flares are the same. As to noise effects, they should be irregular, and their influence is expected to be decreasing if we average large volume of observational data.

Analysis of bisector splitting in both lines was made similarly to described by Lozitsky (2014). As first step, the bisector splitting function (BSF) was found and its linear trend (see, for instance, Fig. 2). Then we find the standard deviation of the local values of BSF from the linear trend (SDFLT) and averaged them over all nine flares. The noise effects were estimated by telluric line H_2O 5919.644 Å observed in the case of big air mass (≈ 20). Fig. 3 presents the example of comparison of SDFLT for MgI 5528 line for nine flares (solid line) and errors of measurements (dashed). One can see that for distances from line center $\Delta\lambda < 120$ mÅ , perturbations of bisectors in flares correspond to expected errors, but in range $120 < \Delta\lambda < 230$ mÅ observed effect in flares exceeds the error level. Theoretically, in a case of quasi-homogeneous and moderate magnetic field (< 1 kG), standard deviation from linear trend should be similar to distribution for errors of measurements.
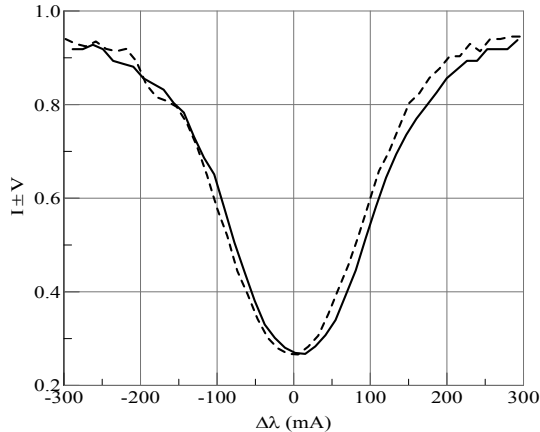

Figure 1: $I + V$ (solid lines) and $I - V$ (dashed lines) profiles of Fe I 5383 observed in 1B flare of 14 July 2000.
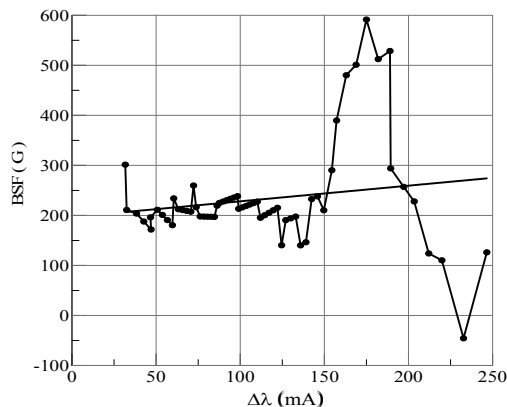

Figure 2: Bisector splitting function (BSF) of $I \pm V$ profiles for 1B flare of 14 July 2000.
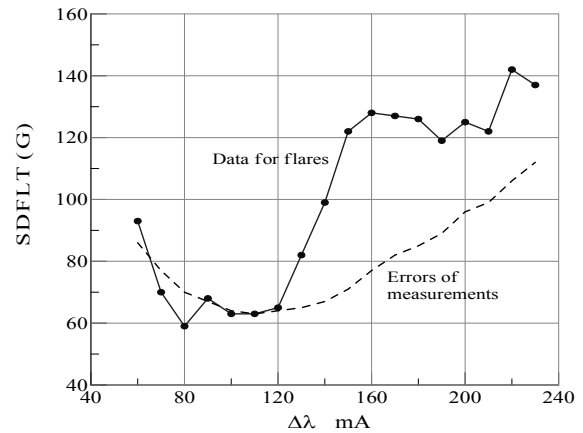

Figure 3: Comparison of SDFLT for MgI 5528 line for nine flares (solid line) and errors of measurements (dashed line).
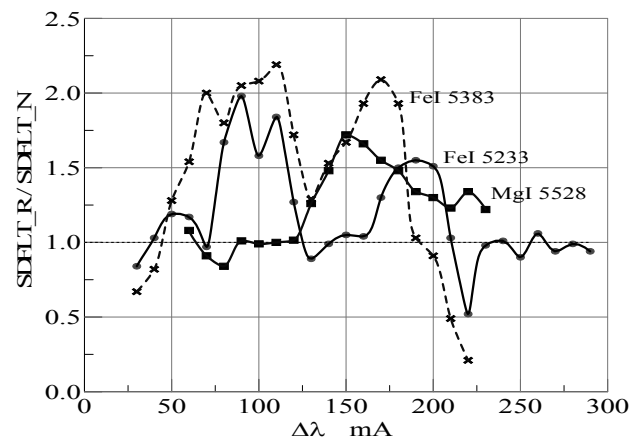

Figure 4: Flares-to-noise ratio for averaged SDFLT.

Flares-to-noise ratio for averaged SDFLT for both lines together with similar data for 5233 according to Lozitsky (2014) is given on Fig. 4. One can see that both FeI lines demonstrate similar distributions with two peaks on about 70-120 mÅ and 170–190 mÅ. MgI line has one single peak on 150–160 mÅ. It is interesting to note that second peaks (placed on 150–190 mÅ) correspond to approximately the same magnetic field strengths by all lines, namely 11.8 kG and 11.2 kG by FeI 5233 and 5383, and 10.5-11.2 kG by MgI 5528. Likely, this agreement is a new argument to reality of such very strong magnetic fields in flares.

References

Van Noort M. et al: 2013, *A&A*, **557**, id.A24.
Lozitsky V.G.: 2009, *J. Phys. Stud.*, **13**, 2903-1.
Lozitsky V.G.: 2014, *Adv.Spac.Res.*, doi: *http://dx.doi.org/* 10.1016/ j.asr.2014.09.028.
Lozitsky V.G. and Staude J.: 2008, *J. A & A*, **29**, 387.
Kurochka E.V. et al.: 1980, *Vest.Kiev.Univ.*, *Astr.*,**22**, 48.
Moore Ch.E. et al.:1966, "The solar spectrum 2935 A to 8770 A"*Nat.Bur. Stand. Monogr. 61*,349 p.

UNSTABLE ANGINA TREATMENT IN VARIOUS PERIODS OF GEOMAGNETIC ACTIVITY

Parshina S.S.[1], Tokayeva L.K.[1], Afanas'yeva T.N.[1], Samsonov S.N.[2], Petrova V.D.[1], Dolgova E.M.[1], Manykina V.I.[2], Vodolagina E.S.[1]

[1] Saratov State Medical University n.a. V.I. Razumovsky of the Ministry of Health of Russia, St. B. Kazach'ya, 112, Saratov, Russia, *parshinasvetlana@rambler.ru*
[2] Institute of Cosmophysical Research and Aeronomy n.a. U.G. Shafer, Russian Academy of Sciences, Lenin Avenue, 31, Yakutsk, Russia, *s_samsonov@ikfia.ysn.ru*

ABSTRACT. In 145 patients with unstable angina (UA) there was analized an efficiency of a drug therapy at different types of heliogeophysical activity (HA) during the 23th solar cycle. 83 patients were examined at the period of a lower HA (Kp-index 16,19±0,18), and 62 patients – at the period of a higher HA (Kp-index 17,25±0,21, p<0,05). Baseline severity of patients' condition with UA at the moment of hospitalization at the studied periods did not differ, but the effectiveness of the therapy depended on the period of HA. At the period of a higher HA antianginal effect was stronger than at the lower period of HA (2,27±0,16 points and 1,75±0,12 points, p<0,05), and the need in nitroglycerin on the background of a drug therapy disappeared for 5-7 days quicker than at the period of a lower HA.

Maximal hypotensive effect at a higher HA was achieved quicker – on the 3rd day of the treatment, and at a lower HA – only up to hospital discharge (p<0,05). Blood viscosity did not normalize in both of the studied periods, but in small vessels there was noted a decrease of a BV (p<0,05). So, at a higher HA the effectiveness of a drug therapy in patients with UA is higher than at the period of a lower HA.

Key words: heliogeophysical activity, solar cycle, unstable angina.

1. Introduction

It is known that a cardiovascular system is the main target for heliogeophysical activity influence (Breus, 2003, Samsonov et al., 2013). Tense magnification of magnetic field of the Earth caused by flashes in the Sun is one of the facts of the adaptation failure and flare-up of chronic conditions. The study aimed the research of clinical picture and a course of unstable angina, hemorheologic disorders and the effectiveness of a drug therapy at the periods of a low and a high solar activity during the 11-year solar cycle.

2. Results and discussion

In 145 patients with unstable angina (UA) there was analized an efficiency of a drug therapy at different types of heliogeophysical activity (HA) during the 23th solar cycle. 83 patients were examined at the period of a lower HA (Kp-index 16,19±0,18), and 62 patients – at the period of a higher HA (Kp-index 17,25±0,21, p<0,05). The groups were matched in age and sex characteristics.

The patients' clinical condition was estimated according to a number of pain episodes per day and a daily demand of nitroglycerine. Effectiveness of treatment was evaluated in points.

It was found out that the severity of the patients with UA at the moment of hospitalization at the studied periods of higher and lower the HA did not differ. So, the frequency of pain episodes was 8,88±0,06 at a LHA and 8,98±1,14 at a HHA (p>0,05) (Table1). The duration of deterioration before the moment of hospitalization also did not differ (9,06±0,87 days at the period of a LHA and 9,86±1,16 days at the period of HHA, p>0,05).

Table 1: Indices of a clinical condition and central hemodynamics in patients with UA at the moment of hospitalization at periods of various types of geomagnetic activity (M±m)

Indices	LHA (n = 83)	HHA (n = 62)
The number of pain episodes per day	8,88±0,064	8,98±1,14
The number of nitroglycerine pills per day	10,74±1,08	8,83±1,17
HBR (beats/min)	75,90±0,07 *	76,47±0,27
BP systolic (mm of mercury)	147,7±2,4 *	156,2±3,1
BP diastolic (mm of mercury)	89,1±1,2	91,8±1,5

Note: * – the difference between the periods of a lower and a higher HA is statistically valid, < 0,05.

At the same time, there are differences in parameters of hemodynamics and fats: at the period of a LHA angina develops at lower heartbeat rates (HBR) and blood pressure (BP), and at less evident fats disorders. Systolic BP and a HBR at the period of a lower HA were lower than at the period of a higher HA (p<0,05) (Table 1). Diastolic BP did not statistically differ (p>0,05) (Table 1).

The level of β-lipoproteins and triglycerids in patients with UA at a LHA was lower than at the period of a HHA

(p<0,05) (Table 2). Cholesterol parameters at various periods of HA statistically did not differ (p>0,05) (Table 2).

Table 2: Parameters of lipid metabolism in patients with UA at periods of various geomagnetic activity (M±m)

Parameters	LHA (n = 83)	HHA (n = 62)
Cholesterol (mmol/L)	5,64 ±0,12	5,93±0,18
β- lipoproteins (units)	39,82±0,12 *	43,46± 1,76
Triglycerids (mmol/L)	1,52±0,07 *	1,86±0,15

Note: * – the difference between the periods of a lower and a higher HA is statistically valid, p< 0,05.

The received data display unstable condition of patients at the period of LHA, as an acerbation goes at lower parameters of BP, HBR and blood lipids level.

We found out that the effectiveness of a drug therapy depends on a period of HA: at a HHA antianginal effect was stronger than at a LHA (2,27±0,16 points and 1,75±0,12 points, p<0,05).

Besides, at the period of HHA and drug therapy the number of episodes of UA decreased maximally up to hospital discharge (p<0,05), and the number of nitroglycerine pills per day practically had not been changing up to the 5th day (p<0,05) and hospital discharge (p>0,05 with the parameter of the 5th day). It means that at a HHA the number of severe episodes decrease up to the 5th day, and there is no need in nitroglycerine, and then the number of UA episodes decreased, they disappear without any treatment.

At a HHA is accompanied as with maximal decrease of angina episodes as with a daily demand of nitroglycerine happen only up to hospital discharge, it means that severe angina episodes can be cortared only by the end of hospitalization.

Thus, at a HHA there was noted more serious antianginal effect (by the 5th day) at severe angina episodes needed nitroglycerine. At a LHA maximal decrease of angina episodes needed nitroglycerine was noted only by hospital discharge. This means that at the period of a HHA the demand of nitroglycerine on the background of a drug therapy disappeared 5-7[t] days quicker than at the period of a LHA.

Moreover, at a LHA the frequency of angina episodes and nitroglycerine demand for the 5th day of treatment and at the moment of hospital discharge was lower than at the period of a HHA (p<0,05).

Maximal hypotensive effect at HHA was achieved quicker (bt the 3rd day), and at LHA – only be the day of hospital discharge (p<0,05).

So, antianginal effect of a drug therapy at HHA is more serious and achieved quicker than at LHA, which is accompanied by stronger hypotensive effect.

Analysis of an influence of a drug therapy on rheological blood properties displayed that there is no normalization of a blood viscosity in any of the studied periods of a drug therapy (p<0,05 comparing with healthy persons). At the same time there are some positive results: a decrease of a blood viscosity in small vessels: at LHA – from 13,74±0,88 to 11,45±0,66 mPa·c (p<0,05), at HHA – from 10,79±0,74 to 9,89±0,58 mPa·c (p<0,05).

It is found that a drug therapy does not influence aggregation erythrocytes properties and transporting of the oxygen into tissues at LHA, as well as at HHA (p>0,05).

A drug therapy does not effect on erythrocytes deformability at the period of HHA. At the period of LHA on the background of a drug therapy there is a decrease of erythrocytes deformability ability, but erythrocytes deformability stays compensated high, comparing with parameters of healthy persons (1,51±0,08 and 1,14±0,04, p<0,05), which displays high erythrocytes deformability as adaptation response.

The results of the research show that the effectiveness of treatment of patients with unstable angina depends on parameters of geomagnetic activity. Antianginal effect and hypotensive effect of a drug therapy are more evident at the period of HHA then at the period of LHA.

References

Breus T.K.: 2003, *Thesis of a Doctor of Physics and Mathematics*, Moscow, 45.

Samsonov S.N. et al.: 2013, *Odessa Astron. Publ.*, **26**, 300.

GEOMAGNETIC ACTIVITY AND EFFECTIVENESS OF MILLIMETER ELECTROMAGNETIC RADIATION IN UNSTABLE ANGINA TREATMENT

Parshina S.S.[1], Samsonov S.N.[2], Afanas'yeva T.N.[1], Tokayeva L.K.[1], Petrova V.D.[1], Dolgova E.M.[1], Manykina V.I.[2], Vodolagina E.S.[1]

[1] Saratov State Medical University n.a. V.I. Razumovsky of the Ministry of Health of Russia, St. B. Kazach'ya, 112, Saratov, Russia, *parshinasvetlana@rambler.ru*
[2] Institute of Cosmophysical Research and Aeronomy n.a. U.G. Shafer, Russian Academy of Sciences, Lenin Avenue, 31, Yakutsk, Russia, *s_samsonov@ikfia.ysn.ru*

ABSTRACT. There had been performed a research of an effectiveness of millimeter electromagnetic radiation (MM EMR) use in patients with an unstable angina (UA) at periods of a lower (daily value of Kp-index 16,19±0,18) and a higher (daily value of Kp-index 17,25±0,21, p<0,05) gemagnetic activity (GA). It was found that involving of the MM EMR (the wave length 7.1 mm) into the treatment of the patients with an UA, enhances an antianginal effect of a drug therapy independently on the period of GA. The MM EMR at the period of a lower geomagnetic activity (LGA) enhances the decrease of diastolic blood pressure (BP), and at the period of a higher geomagnetic activity (HGA) – the decrease of systolic BP. At a HGA there were noted: a quick and more serious antianginal effect, maximal antihypertensive effect was achieved quicker, but (as opposed to the period of a LGA) there was no a pulse slowing effect of a MM EMR. Including the MM EMR into the treatment accelerates stabilization of the patients' condition only at a LGA. Positive effect on blood rheological properties is an independent effect of MM EMR, and it is in blood viscosity reduce in microcirculatory at both of the periods of GA. Normalization of blood viscosity under the MM EMR is only at the period of a LGA. So, the effect of MM EMR on a clinical condition of the patients is more evident at the period of a HGA, blood viscosity – at the period of a LGA.

 Key words: heliogeophysical activity, unstable angina, millimeter electromagnetic radiation, rheology, blood viscosity

1. Introduction

The effectiveness of millimeter electromagnetic radiation (MM EMR or extremely-high frequency therapy) in patients with an ischemic heart disease is described in many studies: there is noted its antianginal, hypotensive, antioxidant, hypocoagulative effect, positive effect on blood rheological properties, normalization of kininogenase system activity and tissue perfusion amendment (Lebedeva 1997, Parshina 2006, Vodolagin 2008). Though, there are no researches of the effectiveness of MM EMR dependent on changes in heliogeomagnetic activity – a component of the space weather.

The research aimed studying of an effect of heliogeophysical activity on the effectiveness of a complex therapy with the use of millimeter electromagnetic radiation in patients with unstable angina during 11-year solar cycle.

2. Results and discussion

An efficiency of MM EMR was estimated in 65 patients with unstable angina, who got a complex therapy (medications + additional MM EMR therapy): at the period of a lower GA (Kp-index 16,19±0,18) – in 45 persons, at the period of a higher GA (Kp-index 17,25±0,21, p<0,05) – in 20 persons during the 23rd solar cycle. There were estimated: antianginal effect, influence on perameters of haemodynamics and blood rheology (blood viscosity (BV), aggregation index of erythrocytes and erythrocytes deformability, transporting of oxygen into tissues). The course of MM EMR (wave length 7.1 mm) included 10 sessions of intermittent radiation mode.

145 patients with UA on the background of a drug therapy were in the group of compare: 83 patients at the period of a LGA and 62 – at the period of a HGA. The groups of a drug therapy (DT) and a complex therapy (DT+MM EMR) were comparable by essential data at the proper periods of GA.

It was found that an additional use of MM EMR forces antianginal effect of a drug therapy independently on the period of GA (p<0,05). At the period of a LGA the effectiveness of a complex therapy was 2,40±0,09 points, at a drug therapy 1,75±0,12 points (p<0,05). At the period of a HGA the effectiveness of a complex therapy was also higher then the effect of a drug therapy (2,85±0,08 and 2,27±0,02 points respectively, p<0,05). But the influence on the parameters of the central haemodynamics depends on the period of a GA: at a LGA the MM EMR potentiates medicamental reduce of diastolic BP, and at a HGA – decrease of systolic BP.

Changes in GA influence on the terms of stabilization of patients' condition with UA. Stabilization of condition

at the period of a LGA at the use of MM EMR was 7,96±0,52 days, at a drug therapy – 9,82±0,79 days (p<0,05); at the period of a HGA at a complex therapy – 7,95±0,86 days, at a drug therapy – 8,24±0,59 days (p>0,05). So, addition of MM EMR accelerates stabilization of the patients with UA at a lower GA.

We had established that rheoprotective effect of a combined therapy with the use of MM EMR is stronger than the effect of a drug therapy at the period of a HGA, as well as a LGA.

At the period of a LGA a complex therapy (as opposed to a drug therapy) favored the decrease of a BV 100 sec^{-1} (in medium vessels) (from 11,11±0,83 to 8,73±0,63 mPa·c, p<0,05), but this parameter was higher then in healthy persons (7,06±0,40 mPa·c, p<0,05). And in a microcirculation area (BV20 sec^{-1}) blood viscosity at the moment of hospital discharge corresponded with parameters of healthy persons (10,36±0,52 and 9,62± 0,46 mPa·c, p>0,05), but after a drug therapy BV20 sec^{-1} was higher comparing with the group of healthy persons (11,45± 0,66 and 9,62± 0,46 mPa·c, p<0,05).

At the period of a LGA including of MM EMR to a drug therapy did not influence the dynamicsof a fibrinogen level, functional erythrocyte properties and transporting of oxygen into tissues (p>0,05). By the moment of hospital discharge deformation activity of erythrocytes stayed compensatory high comparing with the group of healthy persons (1,39±0,09 and 1,14±0,01 c.u., p<0,05), transporting of oxygen into tissues was reduced (7,11±0,42 and 11,20±0,95 c.u., p<0,05).

Thus, at the period of a LGA positive effect from the use of MM EMR was in normalization of a BV in a microcirculation area and decrease of a BV in medium vessels.

At the period of a HGA including of MM EMR did not effect on a dynamics of BV parameters in big and medium vessels, as on the background of a drug therapy (p>0,05). Althou, in small vessels there was a decrease of a BV (from 10,99±0,85 to 8,89±0,43 c.u., p<0,05). Nevertheless, BV20 sec^{-1} at the moment of hospital discharge was high comparing with parameters of healthy persons (11,45±0,66 and 5,29±0,33 mPa·c, p<0,05).

At the period of a HGA, as well as a LGA, there were no differences in indices of aggregation and erythrocytes deformability and transporting of oxygen into tissues at the use of complex and drug therapy.

There were not found any significant differences in influence of MM EMR on blood rheological properties at the periods of LGA and HGA: the basic additional effect of MM EMR (comparing with a drug therapy at the period of LGA and HGA) is a positive effect on microcirculatory component of hemostasis system – BV in small vessels. Normalization of BV20 sec^{-1} at the use of MM EMR goes only at the period of a LGA, and at the period of a HGA there is only a statistically valid decrease of BV20 sec^{-1}.

At comparing the effects of MM EMR at various periods of GA there was found that at the period of a HGA there is more significant antianginal effect then at a LGA (2,85±0,08 and 2,40±0,09 points respectively, p<0,05). Hypotensive effect of MM EMR at a HGA develops 2 days quicker.

As we can see, the effect of MM EMR on clinical condition of the patients is more evident at the period of a HGA, on BV – at the period of a HGA.

The presented studyings show that the use of MM EMR in patients with UA is reasonable at any periods of geomagnetic activity.

The revealed dependence of the use of MM EMR on the state of the external magnetic field of the Earth is very significant. The retention of therapeutic effects of MM EMR at an increase of geomagnetic activity displays that the reception of MM EMR is more serious then the reception of external geomagnetic activities.

References

Lebedeva A.Yu.: 1997, *Millimeter waves in medicine and biology*.
Parshina S.S.: 2006, *Author's abstract*.
Vodolagin A.V.: 2008, *Author's abstract*.

INFLUENCE OF SPACE WEATHER ON A CARDIOVASCULAR SYSTEM OF A HUMAN BEING DURING VARIOUS SOLAR CYCLE PHASES

Samsonov S.N.[1], Manykina V.I.[1], Krymsky G.F.,[1], Parshina S.S.[2], Petrova P.G.[3], Palshina A.M.[3], Strekalovskaya A.A.[3], Shadrina L.P.[4], Vishnevsky V.V.[5]

[1] Yu.G.Shafer Institute of Cosmophysical Research and Aeronomy of Siberian Branch of the Russian Academy of Sciences, Russia, *s_samsonov@ikfia.ysn.ru*

[2] V.I.Razumovsky Saratov Medical University, Russia

[3] Medical Institute of M.K.Ammosov North-Eastern Federal University, Russia

[4] Academy of Sciences of Republic of Sakha (Yakutia), Russia

[5] Institute of Mathematical Machines and System Problems of the National Academy of Sciences, Ukraine

ABSTRACT. The study of relationship of dynamics of space weather parameters to changes of cardiovascular system state of a human being was carried out by data of measurements of volunteer groups in October – December 2009 and March-April, 2011 by data of Yakutsk and Tixie carried out according to the program of Russian-Ukrainian "Geliomed" project.

It is shown that during a phase of minimum (2009) and growth phase (2011) of the 11-year solar activity a distinction in the response of cardiovascular system of a human being connected with the level of geomagnetic activity, latitude of residing of a human being and his/her age is observed.

Key words: solar wind, interplanetary magnetic field, geomagnetic disturbance, cardiovascular system of a human being.

1. Introduction

It is known that cardiovascular diseases are one of principal causes of physical disability and death rate of the population. Now it is also known that the considerable contribution to this process is brought by disturbances of space weather parameters and, first of all, parameters of geomagnetic disturbance. The peak absolute values of such disturbance are manifested at high latitudes. So, an experiment on the study of influence of space weather parameters on a cardiovascular system of human being was carried out within the framework of international "Geliomed" project (Vishnevsky et al., 2003) with the participation of volunteer groups in the auroral (settlement of Tixie) and subauroral (city of Yakutsk) zones. The intensity of geomagnetic disturbance changes in the 11-year cycle, so in this work the results of experiments obtained during a phase of minimum and growth phase of the 11-year solar activity cycle are given.

2. Experimental data and methods of registration

The experiment on the study of state of the cardiovascular system of volunteers depending on space weather parameters with the express – cardiograph ("Fazagraf") was carried out with groups of volunteers in Yakutsk and Tixie during the following time periods: October-December, 2009 (phase of the 11-year solar activity (SA) cycle minimum) and March-April, 2011 (growth phase of SA).

Measurements were carried out every day at two points of the city of Yakutsk: at Yu.G.Shafer Institute of Cosmophysical Research and Aeronomy (IKFIA) and Medical Institute of M.K.Ammosov North-Eastern Federal University (MI), and also at the Polar Geophysical Observatory belonging to IKFIA in the settlement of Tixie using the same equipment (a Fazagraf complex) according to a common report of investigation with a group of volunteers enrolled at each point of observation. Data of the first lead of volunteers' electrocardiograms (ECG) with a subsequent calculation of T-wave symmetry coefficient (TSC) characterizing a functional state of cardiovascular system of a human being (Fainzilberg, 1998) was used. The data of the solar wind (speed, density, and dynamic pressure), interplanetary magnetic field (magnitude and three orthogonal components), and geomagnetic activity (Kp-index) were used as an index of space weather parameters.

The total number of volunteers participated in the experiment of 2009 was 45 persons, and in 2011 there were 47 persons of various age, sex and physical health. During the experiments on working days the volunteers' ECG were carried out with the Fazagraf device.

3. Results and Discussion

The experiment of 2009 showed that the considerable number of maxima and minima of space weather parameters coincided in time of occurrence with the same maxima and minima in a group response of volunteers' TSC. In particular, 88 % of maxima and minima of Kp-index coincided in time of occurrence with the same maxima and minima in a group response of volunteers' TSC. Such almost complete coincidence was observed for a half of volunteers' groups in Yakutsk (14 persons of middle age of 35-years old from a group of 29 persons). Another half of volunteers (15 persons of middle age of 48-years old) showed a partial coincidence of TSC with space weather parameters. The best coincidence was observed for TSC with the magnitude of interplanetary magnetic field, dynamic pressure of the solar wind and Kp-index of geomagnetic disturbance. For example, the correlation coefficient between TSC in Yakutsk and Kp-index was 0.6, and it was on condition that TSC represented not the index of one person but the averaged value (group parameter) of a half of volunteers participating in the experiment. In this case, in Tixie the coincidence of maxima of the Kp-index and TSC accounted for 66%. Conceivably a lower percent of coincidence in Tixie (auroral zone) might be connected with the fact that the highest absolute values of geomagnetic disturbance were observed there, and a part of volunteers living there did not yet attain a sensitivity threshold to the external action.

It is known that an organism of a human being responds to changes of usual ground weather. In order to be convinced that in the given investigation the usual ground weather influenced or did not influence on a cardiovascular system of volunteers, we have compared their changes with changes of usual ground weather parameters. Such a comparison and low values of correlation coefficient have shown that just those parameters of space weather, not of usual ground weather influenced on the cardiovascular system state of volunteers (Samsonov et al., 2013).

The experiment of 2011 (growth phase of the solar activity cycle) was carried out in March-April at values of a 24-hourly coefficient of geomagnetic disturbance up to 35 units, i.e. the geomagnetic disturbance was higher than in 2009. In this case the coincidence of temporary changes of TSC of volunteers in the group of MI (87 % of coincidences) in Yakutsk (middle age of participants is 22 years) and TSC of a half of volunteer group in Tixie (80 % of coincidences; middle age is 40 years) with Kp-index changes was observed. Another half of participants in Tixie (middle age is 43 years) showed only a partial coincidence. A group of IKFIA (middle age is 48 years) in Yakutsk showed only a partial coincidence of dynamics of changes of TSC of volunteers with changes of space weather parameters.

It is known that external actions on biological objects are manifested in the form of quasi-logarithmic dependence (Garkavi et al., 1998). Moreover, this dependence describes experimental data observed by us very well.

The Figure presents a supposed dependence of cardiovascular system state of a human being on the level of geomagnetic disturbance. It consists of three sections. In the first section the change of geomagnetic disturbance leads to a similar change in the response of cardiovascular system (TSC) of a human being so in 2009 we observed a coincidence of changes of the level of geomagnetic disturbance with TSC in Yakutsk and Tixie both for young people and people of elder age.
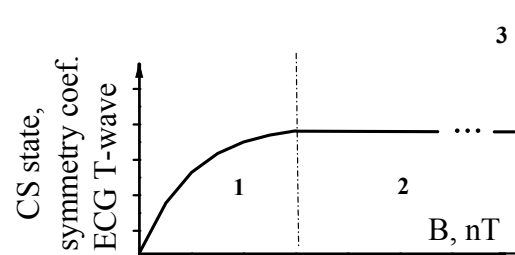

Figure: Dependence of cardiovascular system state of a human being on the level of geomagnetic disturbance

The increase of geomagnetic disturbance leads to the section 2 at which TSC does not increase with the growth of geomagnetic disturbance. Perhaps, it is connected with the attainment of maximum permissible parameters of the cardiovascular system state allowing it to function in a safe regime for life. In this case, in 2011 the coincidence of changes of geomagnetic disturbance only with the MI group (average age is 22-years old) in Yakutsk and a half of younger part of group in Tixie was observed. It means that younger people in Yakutsk and Tixie are in the section 1, and people of elder age are in the section 2. If the geomagnetic disturbance will attain the section 3, then the adaptive capacities of organism cannot cope with such external action and catastrophic consequences for the cardiovascular system of a human being can occur.

Thus, one can assert that the response of cardiovascular system of a human being is connected with the level of geomagnetic activity, latitude of residing of a human being and his/her age.

References

Vishnevsky V.V. et al.: 2003, *Biomedical technologies and radioelectronics*, **3**, 3.
Garkavi L.Kh. et al.: 1998, Moscow.: IMEDIS, 656.
Fainzilberg L.S.: 1998, *Operating systems and machines*, **4**, 40.
Samsonov S.N. et al.: 2013, Odessa Astron. Publ., **26/2**, 300.

EARTH'S MAGNETIC FIELD DYNAMICS: SPACE WEATHER AND SOLAR CYCLE EFFECT EXHIBITING

A.L.Sukharev [1], L.I.Sobitnyak [1], M.I.Ryabov [1], M.I.Orlyuk [2], I.M.Orliuk [2], A.A.Romenets [2]

[1] Odessa observatory "URAN-4" Radio Astronomy Institute
of the National Academy of Sciences of Ukraine
[2] Institute of Geophysics of the National Academy of Sciences of Ukraine

ABSTRACT. According to the "Odessa" and "Kiev" observatories total vector magnetic field variations data for 2008-2010 period, dynamics of the space weather manifestations were considered. Wavelet analysis application made the determination of structure changing in circadian period possible. The features of displaying 12, 8 and 6 hour periods are shown. The nature of their correlation and modulation in solar and geomagnetic activity changing is seen. Two stations changes differences that can result from the latitudinal dependence are examined. The existence of "Odessa" magnetic anomaly located on land and at sea is reviewed.

Introduction

The study of solar-terrestrial relations is a fundamental scientific problem. Solar activity affects not only on magnetosphere and the ionosphere of the Earth but it also leads to large changes in the troposphere and influences on the climate (temperature fluctuations, the formation of cloud cover, etc.). In this work, we have used a geomagnetic field variations observational data (full magnetic induction vector) for 2010 year, obtained by magnetic observatories, located near Odessa and Kiev cities (Institute of Geophysics NASU).

Observation and data processing

Observational data – every minute counts of full induction vector of the geomagnetic field (in nT) during the year 2010, received at magnetic observatories near Odessa and Kyiv cities (see fig. 1). Odessa and Odessa region is one of the biggest magnetic anomalies located on the territory of Ukraine. Original data is very noisy and to remove noise and drop-down point and to fill small gaps in the data, we used the method of Fourier-smoothing and approximation, linear trends were also removed.

Two-parametrical analyzing function of one-dimensional wavelet-transformation is well localized in both, on the time and on frequency. That is distinguished from Fourier's usually applied transformation which analyzing function covers the all-time base. Thus it is possible to see detailed structure of process and evolution of a harmonious signal component in time. Continuous wavelet-transformation on the basis of Morlet function was used.
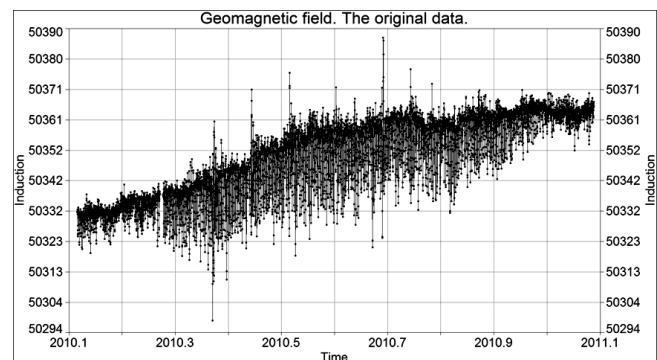

Figure 1: The "Kiev" observatory geomagnetic field original data example

Wavelet and FFT filtering and reconstruction for the isolation of the total spectrum of individual harmonic components corresponding to the bands with the highest spectral power was used. It allowed the detailed consideration of changes in the geomagnetic field oscillation periods, depending on seasons and magnetic storms, and a change in the annual and semi-annual fluctuations in the Black Sea level, which are influenced by the temperature, rainfall and river flow. Numerical used methods are described, for example in the following papers [1, 2].

Geomagnetic field fluctuations

Time series variation of the geomagnetic field induction shows an increasing of linear trend during a year of observation (2010-2011). Wavelet spectra according to "Kiev" and "Odessa" magnetic stations (see fig. 2) show a strong high-frequency part (with the values of 24 hours or less periods) and a weak low-frequency part (with the values of a few tens of day's periods). In addition to the daily period are also highlighted values of 12 and 8 hours periods, data on Kiev – 6 hours (Odessa data is almost invisible during this period). Spectral power of these periods are not evenly distributed in time, it is seen that the oscillation amplitude is low at the beginning and in the

end of the year (winter), increases in spring, peaks in summer and fades in autumn [3,4]. 6 hours period has maximum intensity in summer and autumn. It can be seen that values of the periods are unstable and vary greatly in some moments (magnetic storm).
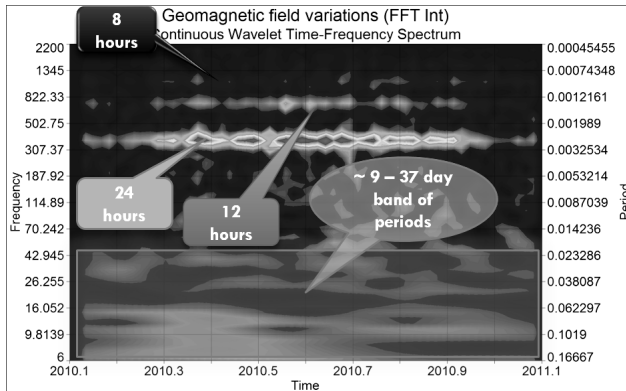

Figure 2: The "Odessa" observatory wavelet spectrum example. Bands of main periods are marked by flags.
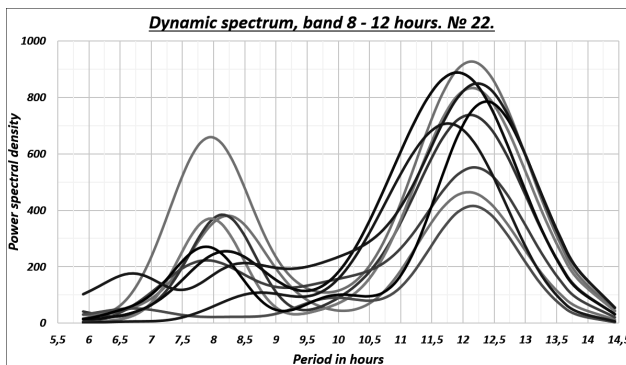

Figure 3: Local wavelet power spectrum example shows changes periods over 10 days. "Odessa" observatory, 8 – 12 hours band.

The greatest changes in the moments of magnetic storms occur in daily (5.5 hours) and semi-diurnal periods (4.7 hours) (see fig. 3). 8 hours period varies less (about 1 hour), 6 hours in Kyiv observations show greater stability, their values vary slightly with time (less than 1 hour) [5].

There are slow changes of the geomagnetic field, for Odessa observations 37, 10 days, and 87, 50 days in Kyiv, and the period of changing this value from 25 to 14 days. With reduction of the oscillation period, amplitude modulation increases.

Conclusions

Geomagnetic field oscillations occur with 24, 12, 8 and 6 hours periods. The period of 6 hours is almost imperceptible for the Odessa data. Fluctuations are unevenly distributed by the time, at the beginning and in the end of the year their amplitude is very weak, in spring the amplitude increases and reaches the maximum in summer decreasing to autumn. The 6 hours period has maximum intensity in summer and autumn.

The founded periods do not have constant values which can change at some hours for some time interval (10 days). The strongest period's jumps are observed at magnetic storms. When disturbance ends, the value of periods comes back to the previous. The greatest changes in values occur in Kyiv data – 21.5-27 hours daily period (Odessa 21-24.5 hours). Values for a twelve hours period for Odessa vary within 12-16.7 hours (Kyiv 12-13.5 hours), shorter periods – about an hour.

Except fast variability of daily scale according to stations of Odessa and Kyiv, there are slower changes of geomagnetic field at more than 10 days scales. For Odessa observations it is 37, 10 days, for Kyiv – 87, 50 days, and also the period with changing value from 25 to 14 days.

The observed periods (6 – 24 hours) belong to solar-daily variations, the period of 25 – 14 days is close by values to the period of planetary scale waves ~ 18 days. The 10-87 days periods are close to the corresponding in solar activity ~ 10, 34, 50, 90 days periods.

Reference

1. Smolentsev N.: 2010, *Wavelet analysis in MATLAB*, St.-Petersburg.
2. Davydov A.V.: 2005, *Digital Signal Processing,* Ekaterinburg.
3. Yanovsky B.M.: 1978, *Terrestrial magnetism,* Leningrad University.
4. Samoylova O.M.: 2012, *Studing's results of magnetic field variations in observatory "Paratunka"*, Kamchatka Vitus Bering State University.
5. Rivin Y.R.: 1989, *Cycles of the Earth and the Sun*, Moscow.

LARGE-SCALE BIOPHYSICAL EXPERIMENT "GELIOMED-2"

V.Vishnevskey [1], E.Gromozova [2], M.Ragoulskaya [3]

[1] Institute of mathematical machines and systems problems of Ukrainian NAS,
Kiev, Ukraine

[2] Institute of Microbiology and Virology im.D.K.Zabolotnogo NAS of Ukraine, Kiev

[3] N.V.Pushkov IZMIRAN, Troitsk, Russia, *vit@immsp.kiev.ua*

ABSTRACT. Results and new design of large-scale biophysical experiment "Geliomed 2" discusses.

Key words: Solar-terrestrial relations, magnetic storms, monitoring, Chizhevsky-Velhover effect, metachromasia

As we reported earlier, the project "Geliomed" was started by a group of Russian and Ukrainian researchers in 2006, the year as a proactive and dedicated to the study of the impact of space weather on biological systems [1]. In the period from 2006 to 2010 have been successfully carried a series of synchronous monitoring, new experiments on the measurement of the same type equipment ECG signal 1st diversion that centrally processed using an original technique [2].

Data already conducted monitoring studies that were performed synchronously in Yakutsk (Samsonov SN), Troick (Ragulskaya MV), Simferopol (Grigoriev PE) and Saratov (Rogacheva SM) revealed several specific especially the effect of external factors on the human body and to develop an algorithm of automatic detection of group effects.

The existence of several fixed universal individual programs for adaptation to Cosmo and geophysical factors proved. The peculiarities of individual heliobiological reactions depending on the season and the phase of the cycle of solar activity on the basis of data at nearly the full period of solar activity proved. We prove the existence of group and population effects. Questions of nonlinear dynamics and stability of biosystems to periodic external force and parametric noise considered with the help of a new theoretical model.

In 2010, the authors extended the telecommunications large monitoring experiment "Geliomed" released book "Biotropic impact of space weather", which sets out the main results of the project [3].

In 2014, a new joint Russian-Ukrainian project "Role of normal and extreme heliogeophysical processes in the evolution of the biosphere" started. The project aims to study the dynamic co-evolution of the Sun and the biosphere in terms of early and modern sun and consists of two blocks of research: theoretical (the study of modern solar-terrestrial relationships and processes in the heliosphere epoch of formation and development of the early biosphere) and experimental (based on modern biological systems and databases Information about the dynamics of the factors cosmogeophysical 23-24 solar activity cycle). The experimental part of project is based on block-oriented technology internet portal "Geliomed» (http://geliomed.immsp.kiev.ua) and therefore we have named "Geliomed-2."
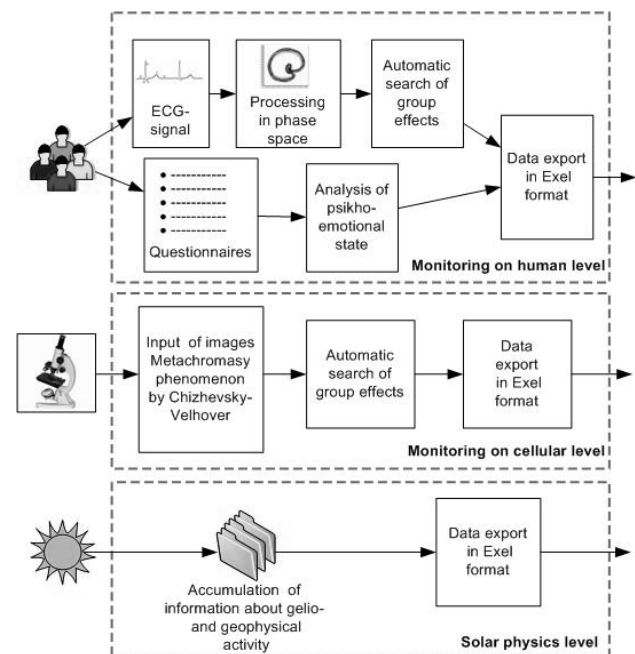

Figure 1: Design of experiment "Geliomed 2"

The overall design of the experiment Geliomed-2 is clear from Figure 1. The technique of monitoring experiments at the level of assessment of people using Internet-based portal technologies in the project "Geliomed-2" are complemented by monitoring at the cellular level for the reference cell culture Accharomyces cerevisiae.

It is known that for a given cell culture Ukrainian microbiologists perfected and adapted method of estimating the metahromasia effect of volyutin grains, known in the literature as "planetary Chizhevsky-Velhover effect" [4].

In our project, we plan to standardize the technique of coloring volyutin grains of yeast Saccharomyces cerevisiae and complete development of automated methods for quantifying this reaction.

Visual readout of the reaction in the study of metachromasia Chizhevsky-Velhover effect is formulated as:"change of color volutin grains from blue to red through purple". It is clear that for "immersion" in this study project "Geliomed" it was necessary to formalize a procedure for evaluating the effects of metachromasia terms of analysis of digital images.
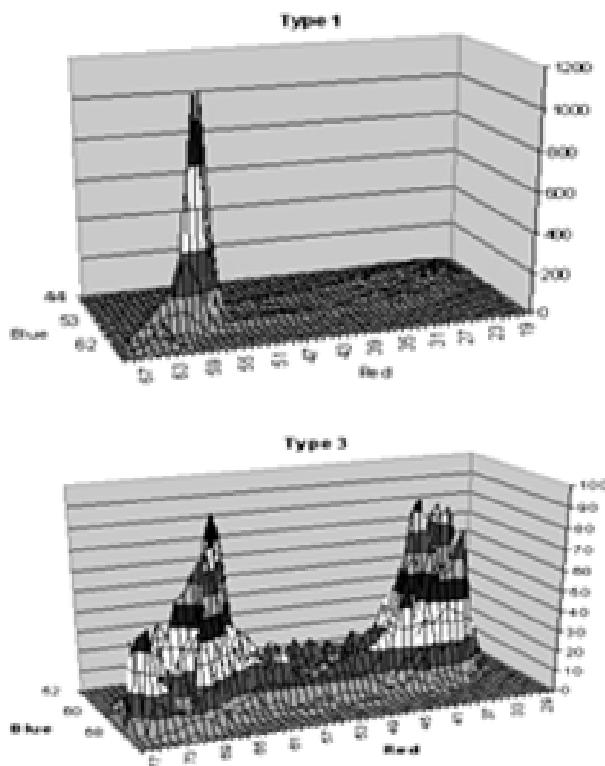
The first experiments with the "dissection" of digital images of volyutin granules of Saccharomyces cerevisiae yeast cells UKM-517 yielded new information understanding of the phenomenon metachromasia and possible to formulate a number of issues and hypotheses.

The figure 2 Up shows the typical histogram of pixels in the grain volutin red-blue plane RGB-image model for the phenomenon of lack of metachromasia. On the Down figure 2 – similar histogram for the most obvious manifestation of metachromasia volutin grain. It is evident that the phenomenon of metachromasia is the presence of two stable states volutin grain, which resembles a phase transition.

Automated estimation algorithm metachromasia reaction is based on results of statistical processing of such histograms for daily studies metachromasia effect. Currently specified thresholds for images that experts refer to a state of "no effect metachromasy, Type 1" and "on-metachromatic effect is observed, Type 3".

The resulting long rows biotropic effects at different levels of organization of the biosphere will be used to develop new synthetic indexes of space weather, which could well reflect actual biotropic effects caused by the Helios factors.

Figure 2: Histograms for two states volutin grains

References

1. Vishnevskiy V.V., Ragulskaya M.V. Samsonov S.N.: 2007, *Live System Technologies*, **4**, 55.
2. Vishnevskiy V.V., Faynzilberg L.S., Ragulskaya M.V.: 2003, *Biomedical Technologies and Radioelectronics*, **3**, 3.
3. Biotropic impact of space weather (based on the Russian-Ukrainian monitoring "Geliomed" 2003-2010 g) / Ed. by MV Ragul'skii. Moscow, Kiev – St. Petersburg, VVM, 2010, 312 p.
4. Gromozova E.N, Kachur T., Voychuk S.: 2009, In: *VIII International Crimean Conference "Cosmos and Biosphere", Sudak, Crimea, Ukraine, Sept. 28 – October 3*, 70.